Understanding Catalyst Structural Effects on the Ring-Opening Polymerization of Cyclic Esters

A Dissertation
SUBMITTED TO THE FACULTY OF THE
UNIVERSITY OF MINNESOTA
BY

Anna Marie Luke

IN PARTIAL FULFILLMENT OF THE REQUIREMENTS
FOR THE DEGREE OF
DOCTOR OF PHILOSOPHY

William B. Tolman, Theresa M. Reineke, Advisors

July 2020

Anna Marie Luke © 2020

Acknowledgements

I would first like to thank my advisors, William B. Tolman and Theresa M. Reineke for their constant support and encouragement. Bill, you were the reason I first believed that I could succeed in graduate school. It has been an absolute honor to work for and with you all these years. Theresa, you gave me a chance when I needed it most. I will forever be grateful for your graciousness; I have loved being a part of your research group.

I would like to thank my collaborators, past and present, for their scientific contributions and more. To Dr. Letitia Yao, Dr. Daniel Stasiw, Hanna Macaranas, Morgan Young, Appie Peterson, Dr. Yanay Popowski, Dr. Christopher De Rosa, Mukunda Mandal and Sina Chiniforoush, thank you for being a significant part of my scientific story.

To my close friends and colleagues that I've met along the way, thank you for being an integral part of this journey. I need to thank Dr. Courtney Elwell, Caitlin Bouchey and Hussnain Sajjad for being my people through thick and thin. Your love, laughter and continuous support through the years has made graduate school the best place to be. To Dr. Megan Fieser, Dr. Lauren Mitchell and Dr. Wilson Bailey, thank you for being incredible mentors along the way. You taught me so much about becoming a great scientist, and I appreciate that more than you'll ever know.

Thank you to all members of the Tolman and Reineke groups that I've had the pleasure of working with through the years. You have become a family to me and have fostered a wonderful environment for the pursuit of science.

Thank you to my parents and my brother for believing in me, even when I couldn't. Thank you for being my support system and for always pushing me to do and be my best. I love you so much. I dedicate this thesis to you.

And finally, to Billy: I love you and I appreciate you. You have celebrated me every step of the way and have been my light in the darkest of times. I hope you know how much you mean to me.

To my family.

Abstract

Materials derived from biomass feedstocks are considered sustainable substitutes for some of the petrochemically-derived products used in commercially relevant polymers. One option for synthesizing polymers from these feedstocks involves the ring-opening polymerization (ROP) of cyclic esters, ultimately yielding degradable, aliphatic polyesters. While it is generally accepted that these polymerizations follow a coordination-insertion mechanism, by which the monomer first binds to a Lewis acid before being ring-opened via nucleophilic attack, a deeper and more fundamental mechanistic understanding of these reactions is still needed for improved catalyst design. In this work, ROP reactions are performed via a variety of Zn and Al-based catalysts with modular ligand frameworks, allowing for mechanistic investigation as a function of catalyst structure. In combination with theoretical calculations, results from these experimental works yield a better understanding of how these catalysts operate, allowing for rational catalyst design for the future.

Table of Contents

List of Tables

Chapter 1

Chapter 2

Chapter 3

Chapter 4

Chapter 5

Chapter 6

List of Figures

Chapter 1

Chapter 2

Chapter 3

Chapter 4

Chapter 5

Chapter 6

List of Schemes

Chapter 2

Chapter 4

Chapter 5

List of Equations

Chapter 1

Chapter 2

List of Abbreviations
(in alphabetical order)

$[X]_0$	initial concentration of X
°/deg	degree(s)
°C	degrees Celsius
^{13}C NMR	carbon nuclear magnetic resonance
^{1}H NMR	proton nuclear magnetic resonance
Å	angstrom
a.u.	arbitrary unit
Ad	adamantyl
Al	aluminum
$Al(Et)_3$	triethylaluminum
$Al(O\mathit{i}Pr)_3$	aluminum isopropoxide
AlOR	aluminum-alkoxide
app	apparent
Ar	aryl
atm	atmosphere
BDI	*β*-diketiminato
BL	*γ*-butyrolactone
Bn	benzyl
BnOH	benzyl alcohol
Br	bromo
bs	broad singlet
CaH_2	calcium hydride
cat	catalyst
CD_2Cl_2	deuterated dichloromethane
$CDCl_3$	deuterated chloroform
CEM	chain-end control
CH_2Cl_2	dichloromethane
$CHCl_3$	chloroform
Cl	chloro
CL	*ε*-Caprolactone
CO_2	carbon dioxide
conv.	conversion
COSY	correlated spectroscopy
Cu	copper
Cy	cyclohexyl (diamine)
d	day(s)
D	diffusion constant
d	doublet
Đ	polymer dispersity
ddd	doublet of doublet of doublets
DFT	density functional theory
DMSO-d_6	deuterated dimethyl sulfoxide
DOSY	diffusion ordered spectroscopy
DSC	differential scanning calorimetry
dt	doublet of triplets

E	electronic energy
Ed	ethylene (diamine)
EDG	electron-donating substituent/group
Eq.	equation
equiv.	equivalent(s)
ESC	enantiomorphic site control
Et	ethyl
Et_2AlOEt	diethylaluminum ethoxide
EtOAc	ethyl acetate
EtOH	ethanol
EWG	electron-withdrawing substituent/group
EXSY	exchange spectroscopy
FDE	framework distortion energy
G	best-estimate free energy
G	gradient field strength
g	gram
γ	gyromagnetic ratio for a proton
h	hour
H_2O	water
HR-ESI-MS	high resolution electrospray ionization mass spectrometry
HSQC	heteronuclear single quantum coherence spectroscopy
Hz	hertz
I	intensity
INT	intermediate
*i*Pr	isopropyl
IR	infrared
J	coupling constant
K	Kelvin
k_2	insertion rate constant
k_B	Boltzmann constant
kcal	kilocalorie(s)
kDa	kilodalton
K_{eq}	equilibrium constant
K_M	saturation substrate binding constant
k_{obs}	pseudo-first order rate constant
k_p	propagation rate constant
LA	lactide
L_n	ligand
m	*meso* relationship
M	metal ion/molarity, moles/liter
m	multiplet
m/z	mass to charge ratio
Me	methyl
MeOH	methanol
mg	milligram
MHz	megahertz
min	minute
mL	milliliter

mM	millimolar
mmol	millimole
M_n	number average molecular weight
Mo	molybdenum
mol	mole
M_w	weight average molecular weight
n	number of repeat units in polymer chain
$N(Me)_2$	dimethylamino
N_2	dinitrogen
Na_2SO_4	sodium sulfate
$NaBH(OAc)_3$	sodium triacetoxyborohydride
$NaBH_4$	sodium borohydride
NEt_3	triethylamine
NMR	nuclear magnetic resonance
NO_2	nitro
NOESY	nuclear Overhauser effect spectroscopy
η	viscosity
OBn	benzyloxy/benzyloxide
O*i*Pr	isopropoxy/isopropoxide
OMe	methoxy/methoxide
OR	alkoxide moiety
p	percent monomer conversion
P	polymer chain
PBr_3	phosphorus tribromide
PCL	poly(ε-caprolactone)
PE	poly(ethylene)
PET	poly(ethylene terephthalate)
Ph	phenyl
Ph_3Si-	triphenylsilyl
PLA	poly(lactic acid) or poly(lactide)
PLLA	poly(L-lactide)
P_m	percent *meso* character in polymer chain
PP	poly(propylene)
ppm	parts per million
P_r	percent racemic character in polymer chain
PS	poly(styrene)
PU	poly(urethane)
PVC	poly(vinyl chloride)
Py	pyridyl
q	quartet
r	racemic relationship
r_1	metal-OR bond distance in the catalyst
r_2	metal-carbonyl bond distance
RDS	rate-determining step
r_H	hydrodynamic radii
ROP	ring-opening polymerization
s	second(s)/singlet
SCRF	self-consistent reaction field

SEC	size exclusion chromatography
Sn	tin
$Sn(Oct)_2$	tin(II) 2-ethylhexanoate
sp	square pyramidal geometry
t	time/triplet
T/Temp.	temperature
tbp	trigonal bypyramidal geometry
TBS	*tert*-butyldimethylsilyl
*t*Bu	*tert*-butyl
$t\mathrm{BuPh_2Si}$	*tert*-butyldiphenylsilyl
td	triplet of doublets
T_g	glass transition temperature
THF	tetrahydrofuran
THF-d_8	deuterated tetrahydrofuran
Ti	titanium
TiOR	titanium-alkoxide
T_m	polymer melting temperature
TMS	trimethylsilyl
TMTAA	dibenzotetramethyltetraazaannulene
tol-d_8	deuterated toluene
TS	transition state
TSG	transition state geometry
V_max	reaction rate upon reaching saturation
VT	variable temperature
X	generic substituent
X_n (where X = P, Q, R)	linking tether differing in length
Zn	zinc
$ZnEt_2$	diethyl zinc
ZnOR	zinc-alkoxide
δ	chemical shift/diffusion gradient length
Δ	delta/diffusion delay
$\Delta G^\ddagger$	activation free energy
ΔG°	standard-state free energy
$\Delta H^\ddagger$	enthalpy of activation
$\Delta S^\ddagger$	entropy of activation
$\Delta\Delta G^\ddagger$	difference in activation free energy
Λ	lambda
µL	microliter
µmol	micromole
π	pi
ρ	sensitivity constant, slope of line in Hammett plot
σ_para	Hammett *para* parameter
τ	tau, universal geometric index

1. Ring-Opening Polymerization of Cyclic Esters to Form Sustainable Polymers: Understanding Mechanism as a Function of Catalyst Structure

1.1 The Importance of Sustainable Plastics

"The Earth is a fine place worth fighting for..."

– Ernest Hemingway, *For Whom the Bell Tolls*, 1940

"It is the worst of times, but it is the best of times because we still have a chance."

– Sylvia Earle, *Twitter*, 2019

Undoubtedly, the famous American author and decorated marine biologist who spoke these words in vastly different times meant to convey different things. Yet, their sentiment is the same: our planet deserves a fighting chance. Today, one of our Earthly battles revolves around a dependence on single-use plastics and the inevitable pollution that follows their use. This environmental fight is made difficult by the fact that plastic is everywhere. Our heavy and prolonged use of these products is evident by the sheer amounts of plastics observed in our water systems, soil, and organisms[1] all across the globe.[2] And while efforts to eliminate pollution and expand recycling capacity are feasible ideas to combat this problem, our dependence on these products means that annual plastic production will only rise with time, as will its eventual environmental discard.[3]

Steady increase in plastic production would not be such an issue if our current global plastic flow was cyclic. Yet, today, we observe a largely linear plastic flow - meaning that the vast majority of post-consumer plastics are not recycled. In 2016, global plastic packaging production reached 78 million tons, with 40% of that going to landfill, 32% leaking into the environment and only 14% being collected and subsequently incinerated for energy recovery. Of that 78 million tons, a mere 14% was collected for recycling, only 2% of that belonging to a closed-loop recycling regime.[4] Even predictive models that anticipate higher levels of incineration and recycling in years to come forecast that by 2050, there will be 26 billion tons of plastic waste in the world, almost half of which will be thrown into either landfills or the environment.[3] If true, this model indicates that in 30 years, the mass of plastics and fish in the ocean will be nearly equal.[4]

Moving toward a cyclic plastic flow (i.e., closed-loop recycling) through the use of compostable polymers is thus an important goal.[5] Closed-loop recycling embodies the idea that polymeric materials made from renewable resources can be used, collected, composted, and returned to basic building blocks (CO_2 and H_2O, the feedstocks for biomass), which in turn can be used to generate more renewable resources (Figure 1.1). From production to end-of-life, these materials remain in a continuous loop, inhibiting deleterious environmental impacts. Any nonrenewable resources used to make plastic products would be a break in the circle, as would the incorporation of plastics that cannot be composted into feedstocks for eventual plant growth.

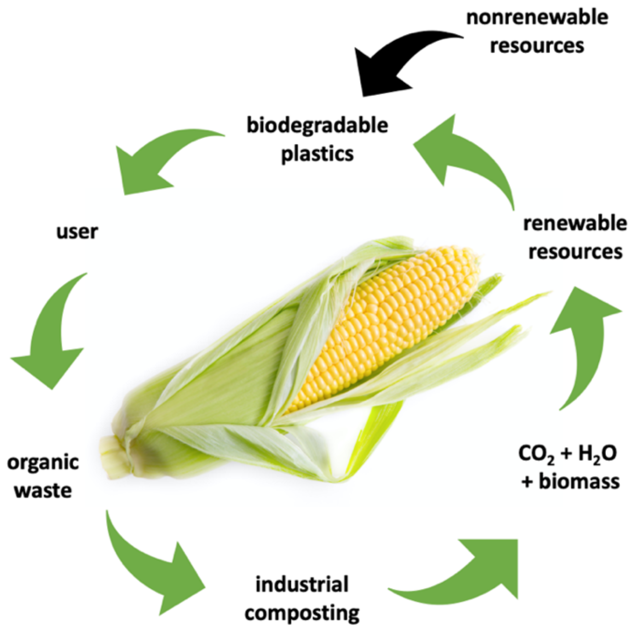

Figure 1.1. Depiction of closed-loop recycling. Adapted from reference 6.

Most industrial plastics are petroleum-derived and are challenging to degrade, making them inadequate materials for closed-loop recycling. In fact, synthetic polymers including poly(ethylene) (PE), poly(propylene) (PP), poly(vinyl chloride) (PVC), poly(ethylene terephthalate) (PET), poly(styrene) (PS), and poly(urethane) (PU), which make up over 90% of all plastics ever made,[3] are non-degradable (even by abiotic degradation), and their lifetime in landfills can be indefinite.[7]

A major goal is thus to generate new and useful materials derived from renewable resources.[8–10] Linear, aliphatic polymers made from the ring-opening polymerization (ROP) of cyclic esters from biomass are examples of such sustainable materials. The most prominent compostable polymer on the market, poly(lactide) (PLA),[1] is synthesized through ROP from lactide (LA), a monomer derived from lactic acid, a widely occurring carboxylic acid in nature.[11] However, to polymerize materials such as PLA with robust properties, a high level of understanding for the ring-opening mechanism by which it is polymerized is required.

This thesis will examine such ROP reactions through fundamental investigation of detailed mechanisms and how those mechanisms are influenced by catalyst structure. Both LA and *ε*-caprolactone (CL, a monomer that is not made from biomass directly, but has been demonstrated to be bio-derived[12–14]) are used as featured monomers in these studies (Figure 1.2), due to their relevance within the field as model substrates for the generation of biodegradable polyesters. From this work, information regarding rational catalyst design for the future of sustainable polymerizations is gained.

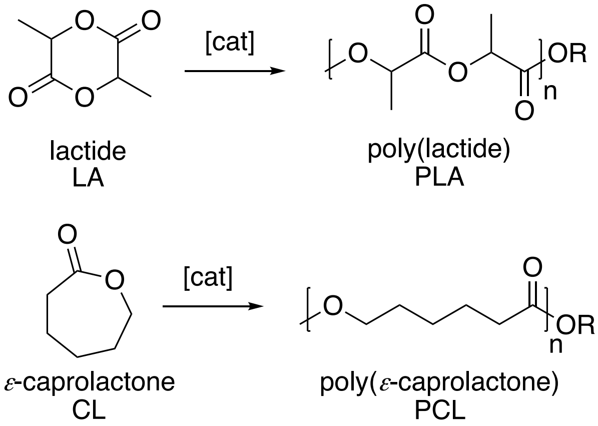

Figure 1.2. Generic polymerization schemes of LA (top) and CL (bottom) via catalysis, where n = number of repeat units, or degree of polymerization.

1.2 Metal-Alkoxide Catalyzed Ring-Opening Polymerization of Cyclic Esters

ROP of cyclic esters can be performed by several methods including anionic[15,16] and cationic polymerization,[17,18] and by using organocatalysts paired with various nucleophilic initiators.[19,20] This thesis however, will focus on ROP catalyzed by single-site metal-alkoxide initiators. These discrete catalysts offer high levels of polymerization control[12,21,22] (i.e., less evidence of transesterification within the polymer), and, in some cases, conveniently measurable polymerization rates, making them ideal candidates for mechanistic study. An aspect of particular mechanistic importance, especially for the polymerization of LA, involves understanding the basis for observed control of polymer microstructure, such as polymer tacticity (stereocontrol).

1.2.1 *rac-Lactide Polymerization and Polylactide Microstructure*

PLA is the most prominent biodegradable polymer in the world today.[1] On the industrial scale, it is produced on the order of ~200,000 tons per year,[23] while trajectories indicate this number to increase as demand for bio-based polymers grows. While broadly used in food packaging applications and cutlery, PLA's inherent brittleness makes it a difficult material to use in a variety of applications, especially those that require temperatures exceeding its glass transition temperature (T_g, temperature at which the polymer chains are mobilized, which for PLA is 55 °C).[24] Much work has been done to try and improve the overall mechanical properties of PLA, either by copolymerizations or polymer blending with more elastic/rubbery polymers with lower T_gs,[25–27] or through attempts at altering PLA's microstructure, which dictates its overall mechanical properties.[28]

A key aspect of PLA microstructure is its tacticity, the stereochemical relationship between consecutive stereocenters in the molecule. Two proximal stereocenters bearing the same stereochemistry share a *meso* relationship, while those with opposite stereochemistry are racemic. Polymer tacticity is controlled by the manner in which a monomer inserts itself onto the catalyst center. This process may be classified in two ways: either enantiomorphic site control (ESC), whereby the physical structure and environment of the metal complex dictates which way the monomer binds and inserts,[29] or chain-end control (CEM), where subsequent monomer insertion is dictated by the stereochemistry of the previously inserted monomer.[29] Due to the difference in propagation between these two stereochemical mechanisms, if an "error" occurs via ESM, it can be "fixed" by subsequent monomer insertions. If an "error" occurs via CEM however, it is propagated throughout the polymer chain until the next "error" occurs[29] (Figure 1.3).

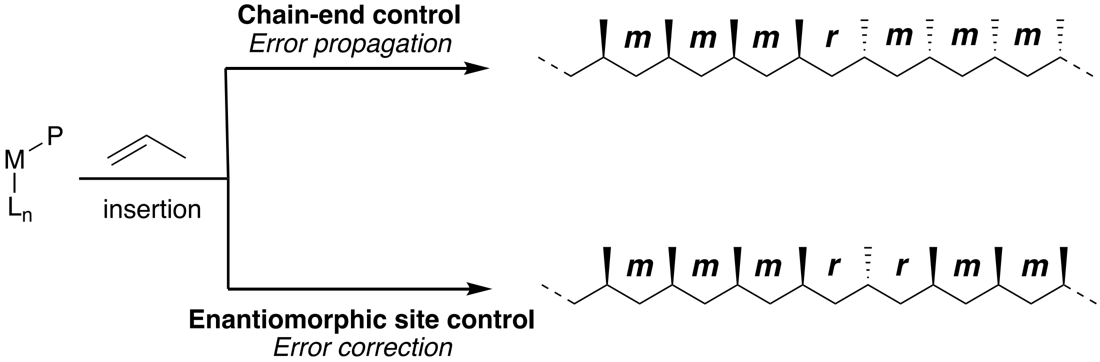

Figure 1.3. Representations of both CEM and ESC mechanisms using PP as a model polymer, where M is the metal center, L_n is the ligand framework, P is the polymer chain, m = *meso* relationship and r = racemic relationship.

PLA polymerized from a racemate (*rac*-LA, a 50:50 mixture of its individual enantiomers, L-LA and D-LA) can be observed to have any one of three variants of polymer tacticity: isotacticity, heterotacticity, and atacticity. Isotactic polymers are those that contain mainly *meso* relationships between monomer units, while heterotactic polymers are those that contain mainly racemic relationships. Atactic PLA is a product of random stereochemical relationships throughout the polymer chain (Figure 1.4).

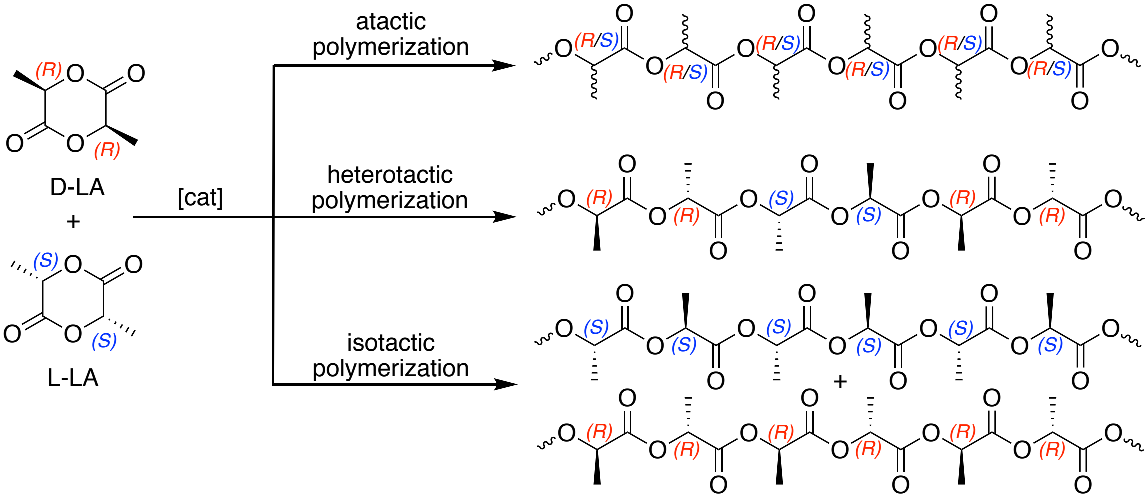

Figure 1.4. Examples of polymer microstructure via atactic, heterotactic and isotactic polymerization of *rac*-LA.

Heterotactic PLA is typically amorphous,[30] whereas isotactic PLA has attractive physical characteristics such as high crystallinity and high polymer melting temperatures, T_ms, as a result (see Table 1.1 for examples of T_m as a function of PLA tacticity[31–34]). PLA polymerized from single enantiomers of LA (such as PLLA, polymerized from L-LA) is isotactic by nature. Yet stereocontrol in the polymerization of *rac*-LA is highly coveted, because isotactic polymer chains of both D- and L-LA bear stereochemical appendages (methyl groups) that can co-crystallize together, driving up the T_m of the polymer as a result of stereocomplexation.

Table 1.1. Examples of polymer T_m as a function of tacticity and crystallinity, where PLA is synthesized from *rac*-LA, and PLLA from L-LA.

Polymer	**Degree of Crystallinity**	**T_m (°C)^a**
atactic PLA	amorphous	–^{b}
heterotactic PLA	semi-crystalline to amorphous	–^{c}
isotactic PLA	crystalline	175^d
isotactic (stereocomplexed) PLA	highly crystalline	209^e

[a]Values obtained from differential scanning calorimetry (DSC). [b]Reference 31. [c]Reference 32. [d]Reference 33. [e]Reference 34.

The level of polymer tacticity within a polymer chain may be measured by homonuclear decoupled NMR spectroscopy, whereby the individual tetrads (four consecutive stereocenters within the polymer chain) of the polymer are analyzed by integration to determine their relative concentrations. Each tetrad is denoted by the stereochemical relationship between monomer units (m = *meso* and r = racemic character). In the case of PLA, there are five potential tetrads (rmr, rmm, mmr, mmm, and mrm). The relative concentrations of these tetrads lead to calculations of isotacticity or heterotacticity, by way of Eqs. 1.1 and 1.2 (assuming CEM mechanism).[35] The terms P_m and P_r denote polymer tacticity, indicating the measurement of percent *meso* or racemic character within the polymer, respectively; a P_m = 1.00 signifies perfect isotacticity, where only *meso* enchainment is observed, while the opposite is true for a P_r = 1.00. For atactic PLA, the probability of having either racemic or *meso* enchainment is equal, so $P_m = P_r = 0.5$.[36]

$$P_r = \sqrt{2 \text{ x } [rmr]} \qquad \textbf{Eq. 1.1}$$

$$1 - P_r = P_m \qquad \textbf{Eq. 1.2}$$

Depending on the mechanism by which tacticity is implemented in the polymer (ESM or CEM), different statistical models are used, inevitably leading to variations in Eq. 1.1. While several examples in the literature that observe polymerization stereocontrol claim control through only one mechanism,[37–39] it is possible that a polymer's tacticity is a result of both CEM and ESC. As others have noted,[40–42] it can be difficult to determine whether one or both mechanisms are responsible for polymerization stereoselectivity. Typically, the determination of the relative ratios of the tetrad species serves as the manner for determining whether ESC or CEM is at play in the polymerization. Thus, a ratio of [mmr]:[mrm]:[rmr]:[rmm] = 1:2:1:1 indicates ESC, whereas a ratio of 1:1:0:1 is consistent with CEM.[43] However, sometimes these specific tetrad ratios do not match well with what is predicted for either the ESC or CEM mechanism.[44] For simplification, tacticity measurements within this thesis are based on calculations via the CEM mechanism, due to similarities between the systems presented herein and other catalytic systems that claim CEM control.[34] It is noted, however, that ESC is a likely contributor to the tacticity values presented.

While isotactic/stereocomplexed PLA is a key target, relatively few catalysts control polymer stereocontrol well enough to lead to stereocomplexed PLA, and even fewer do so under more industrially relevant conditions (sans solvent, in the bulk, at high temperatures). Catalysts that exert stereocontrol typically bear chiral ligands,[43,45,46] although there are few reports of achiral, yet fluxional catalysts that are able to achieve high levels of isotactic stereocontrol, as well.[34,47] Design of effective ROP catalysts that exhibit such stereocontrol hinges on a detailed understanding of the chemical reaction mechanism.

1.2.2 *Coordination-Insertion Mechanism*

ROP of cyclic esters via metal-alkoxide catalysts is largely understood to follow a coordination-insertion mechanism (Figure 1.5). While a recognized paradigm, this mechanism is not fully understood with molecular level detail. According to this mechanism, the monomer's carbonyl moiety reversibly binds to the Lewis acidic metal center, ultimately activating the carbonyl for attack by a nucleophilic substituent (an alkoxide moiety, -OR, in the context of this work). The resulting four-membered tetrahedral intermediate then undergoes ring-opening to generate a new alkoxide nucleophile, belonging to that of the last inserted monomer. Repeating the process (propagation) yields the final polymer.

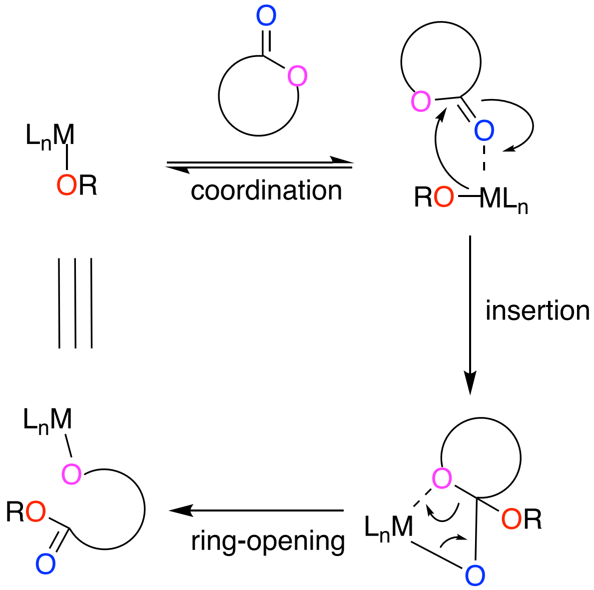

Figure 1.5. Coordination-insertion mechanism of a generic lactone, where L_n = ligand, M = metal center, and OR = alkoxide moiety.

In the absence of polymerization terminators, ROP is a living polymerization, in which the molecular weight of the polymer grows linearly with time. Polymerization termination is invoked by either quenching with protic solvent, which releases the polymer chain from the metal. In the case of air-sensitive catalysts, quenching can be achieved with air.

The coordination-insertion model is a simplified representation of the process of monomer enchainment which does not elucidate key details involving the separate reaction steps (i.e., monomer binding and nucleophilic insertion). Elucidating these constituent steps and better understanding how catalyst structure affects them is a goal that will allow for improved ROP catalyst design.

1.2.3 *Catalyst Development*

Many types of metal-based catalysts have been studied for ROP capability (largely Sn,[48–50] while other Lewis acids such as Al,[34,45,51,52] Zn,[30,53,54] Ti,[55,56] and various lanthanides[57,58] have also been thoroughly studied). Studies of ligand variation have led to increased understanding of how catalyst structure affects polymer microstructure and overall polymerization capability. Interested readers are pointed to these reviews for a more encompassing interpretation of these works.[59–64]

Among the various catalysts thoroughly explored, ones with Al and Zn metal ions have particular advantages that make them amenable for study. As such, we have chosen to focus on studying ligand structural effects on ROP by selected Al- and Zn-alkoxide complexes in an effort to probe the ROP mechanism, ultimately uncovering mechanistic questions that still remain. These rationales are described in more detail in the following sections.

1.2.3.1 *Targeted Ligand Variations of Al-Alkoxide Catalysts*

Aluminum-alkoxide (AlOR) catalysts have been well-studied in terms of ligand variation and corresponding ROP efficacy. Spassky and coworkers were among those who set the precedent for polymerization study as a function of Al catalyst structure.[45,65] In 1996, they developed an achiral Al catalyst (Figure 1.6) bearing a salen-type ligand and an alkoxide initiator (denoted as (salen)AlOR) for the polymerization of *rac*-LA. While it showed a slight preference for isotactic PLA (P_m not calculated, but T_m = 141 °C), another complex, bearing a chiral backbone, (Figure 1.6), exhibited much higher levels of selectivity (T_m = 187 °C). Their work raised the question of how structural changes in complexes could lead to different polymerization capabilities and diverse polymer microstructures and served as a basis for similar studies.

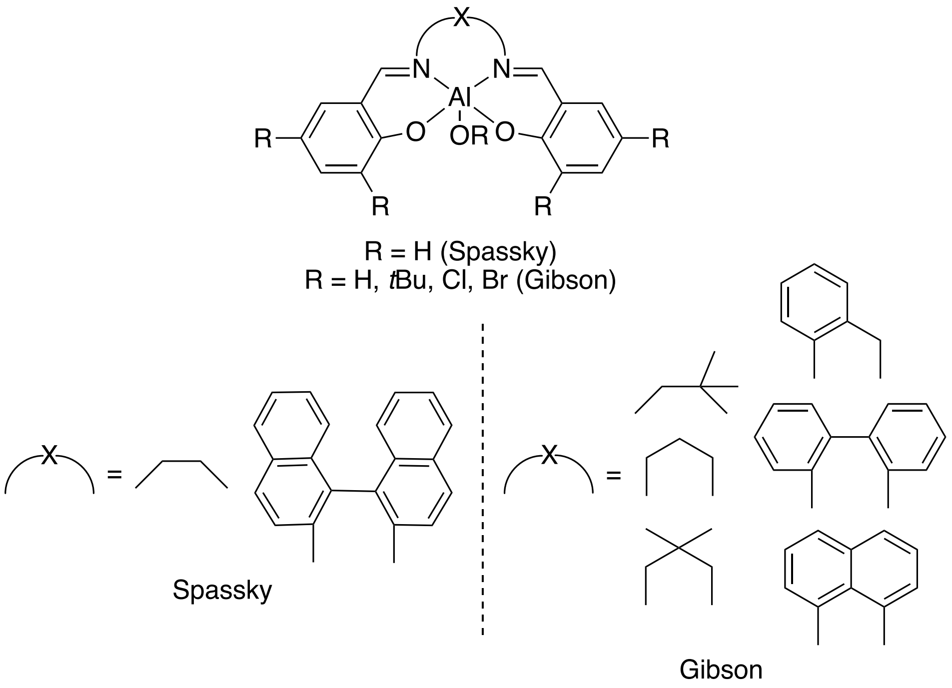

Figure 1.6. Ligand variations as performed by Spassky and Gibson. Spassky's achiral catalyst and chiral variant (left) and library of ligand backbones generated by Gibson (right).

In 2006, Gibson and colleagues compared the polymerization capability of a series of (salen)AlOR complexes that differed with respect to ligand backbone and electronics of the supporting ligand (Figure 1.6).[51] Kinetic experiments indicated that complexes with more electron-withdrawing substituents (EWGs) on the phenolate ring and longer, more flexible backbones led to faster polymerization rates. Two hypotheses were invoked to explain these observations: 1) EWGs on the phenolate rings of the ligand framework enhance metal electrophilicity, thereby strengthening the binding between it and the carbonyl of the monomer and 2) increased flexibility of the catalyst led to facilitation of favorable interactions during the rate-determining step (RDS) of the polymerization. PLA microstructure as a function of these ligand variations was noted (P_m values shifted between those of atactic and isotactic nature, 0.50–0.88), but no significant trend was observed and rationales for the stereocontrol were not offered.

In separate work, Nomura et. al. examined the effects of varying the steric bulk in the *ortho* position on ROP rates and stereocontrol (Figure 1.7).[34] While very large substituents (R_1 = Ph_3Si, *t*$BuPh_2Si$) inhibited polymerization (likely due to the inability for the monomer to bind to the metal center effectively), a general trend of increased steric bulk leading to greater polymerization stereoselectivity (maximum stereocontrol: R_1 = TBS, P_m = 0.98) was observed. Yet, relatively sluggish polymerization rates (p = 96 after 14 h, in toluene at 70 °C) were observed for the catalysts with the highest selectivity.

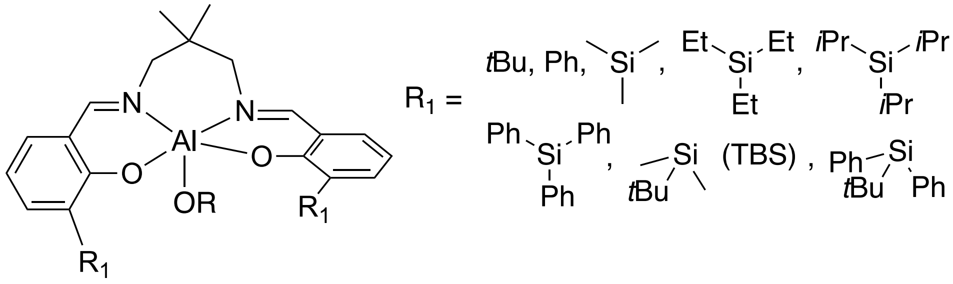

Figure 1.7. Nomura's library of (salen)AlOR catalysts, varied in terms of steric encumberment.

Impressively, polymerizations using the complex with R_1 = TBS produced T_m values of 209 °C, a clear indication of chain stereocomplexation. This T_m is among the highest reported for PLA synthesized via metal-catalyzed ROP. Probing the reason behind the stereoselectivity observed, the authors noted that the crystal structure of the catalyst lacked symmetry, despite its NMR characterization data suggesting otherwise. From subsequent, in-depth ^1H NMR studies, Nomura et. al. concluded that the catalyst was fluxional, and hypothesized that this fluxional nature, along with the level of steric encumberment in the *ortho* position of the ligand, were significant contributors to the high stereoselectivity observed. While postulated in this work, we further explore these hypotheses through the study of related catalysts, the results of which are described in detail in *Chapter 4*.

While these studies examining ROP capabilities as a function of ligand structural alterations are helpful in identifying general ROP trends and have contributed to the evolution of polymerization catalysis in general, intrinsic mechanistic nuances were not studied in-depth. Moreover, kinetic analyses were accomplished using generic rate constants (k_{obs}), which are helpful for examining relative rates, but are less useful when trying to study the constituent steps of monomer binding and insertion. These drawbacks were addressed in studies of CL polymerization by Al complexes using a methodology exploiting saturation kinetics. While briefly described in the following sections, this approach is also applied in *Chapter 3*.

In contrast to typical kinetic approaches that yield a simplified pseudo-first order rate constant k_{obs} (a product of the propagation rate constant, k_{p}, and [cat]), these CL ROP reactions were studied under saturation conditions, ultimately allowing k_{obs} to be separated into its more elementary and descriptive kinetic parameters of binding (K_{eq}) and insertion (k_2) (distinguished from k_{obs} in Figure 1.8). By studying polymerizations at $[\text{monomer}]_0 >$ 2.0 M, saturation behavior is achieved, and the Michaelis-Menten rate equation (Eq. 1.4) can be used in substitution for the more typical first-order rate equation (Eq. 1.3). Modification of the Michaelis-Menten equation, allows substitution for the parameters of V_{max} and K_{M} (reaction rate upon reaching saturation and saturation substrate binding constant, respectively), and subsequently, the propagation rate constant can be broken down into individual reaction steps (Eq. 1.5).

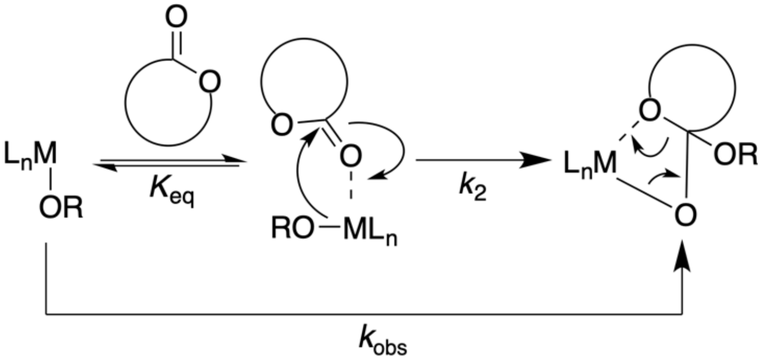

Figure 1.8. ROP mechanism depicted by different kinetic parameters via a generic cyclic ester, where L$_n$ = ligand, M = metal center, and OR = alkoxide moiety.

$$-\frac{d[\text{monomer}]}{dt}=\frac{d[\text{polymer}]}{dt}=k_{\text{obs}}[\text{monomer}] \qquad \textbf{Eq. 1.3}$$

where $k_{\text{obs}} = k_{\text{p}}[\text{cat}]$

$$-\frac{d[\text{monomer}]}{dt}=\frac{d[\text{polymer}]}{dt}=\frac{V_{\text{max}}[\text{monomer}]}{K_{\text{M}}+[\text{monomer}]} \qquad \textbf{Eq. 1.4}$$

where $K_{\text{M}} = \frac{k_{-1}}{k_1} = \frac{1}{K_{\text{eq}}}$ and $V_{\text{max}} = k_2[\text{cat}]$

$$-\frac{d[\text{monomer}]}{dt}=\frac{d[\text{polymer}]}{dt}=\frac{k_2[\text{cat}][\text{monomer}]}{\frac{1}{K_{\text{eq}}}+[\text{monomer}]} \qquad \textbf{Eq. 1.5}$$

Such saturation behavior is confirmed via excellent fits to the Michaelis-Menten kinetic expression (and poor fits to those of first- and second-order kinetic expressions). Using COPASI software,[66] fits to Michaelis-Menten kinetics allow for the extrapolation of the specific rate constants K_{eq} and k_2, ultimately allowing for the study of these kinetic parameters as a function of catalyst structure.

Using this approach, (salen)AlOR catalysts, bearing either a 2 or 3-carbon backbone (named **1.1** and **1.2**, respectively, Figure 1.9) with substituents varied in electron withdrawing or donating capabilities at the *para* position of the phenolate rings (R_1 = NO_2, Br, or OMe, Figure 1.9), were synthesized and used for the polymerization of CL.[67,68]

Kinetic analyses of **1.1** and **1.2** resulted in several major realizations. Both extended backbone linker length and the presence of EWGs (NO_2 > Br > OMe) resulted in increased ROP rates, and k_2 was the kinetic parameter which most contributed to polymerization rate.[67,68] The latter conclusion was drawn on the basis of analysis of Eyring (Figure 1.10, top left) and van't Hoff (Figure 1.10, top right) plots that indicated unlike k_2, K_{eq} is relatively unaffected by variation of electronic substituents or backbone linker lengths. Thus, it was concluded that ROP rate depends more on the alkoxide nucleophilic attack to the substrate and relative to monomer binding.

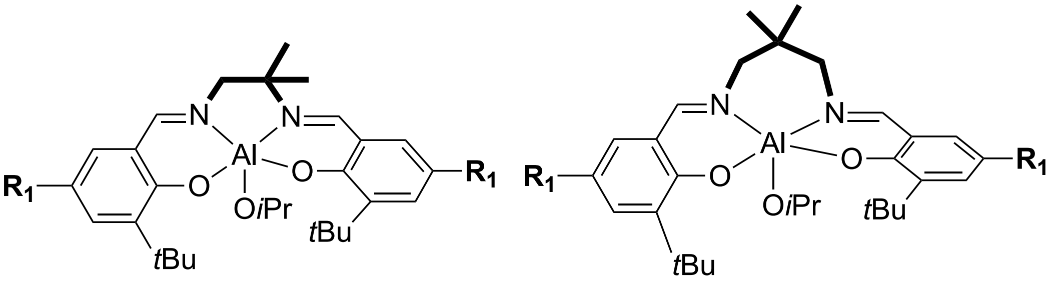

1.1 **1.2**

Figure 1.9. Catalysts **1.1** and **1.2**, where $\mathbf{R_1}$ = either NO_2, Br or OMe.

Ligand variations had a significant effect on k_2, such that the fastest catalyst studied within the context of this work (**1.2**, R_1 = NO_2) yielded polymerization rates over three orders of magnitude faster than the slowest catalyst studied (**1.1** R_1 = OMe, see Figure 1.10, bottom). To better understand why extension of backbone linker length and inclusion of EWGs increased rate of polymerization so considerably, the structures of the catalysts and the molecular mechanism were evaluated using synergistic experiment and theory.

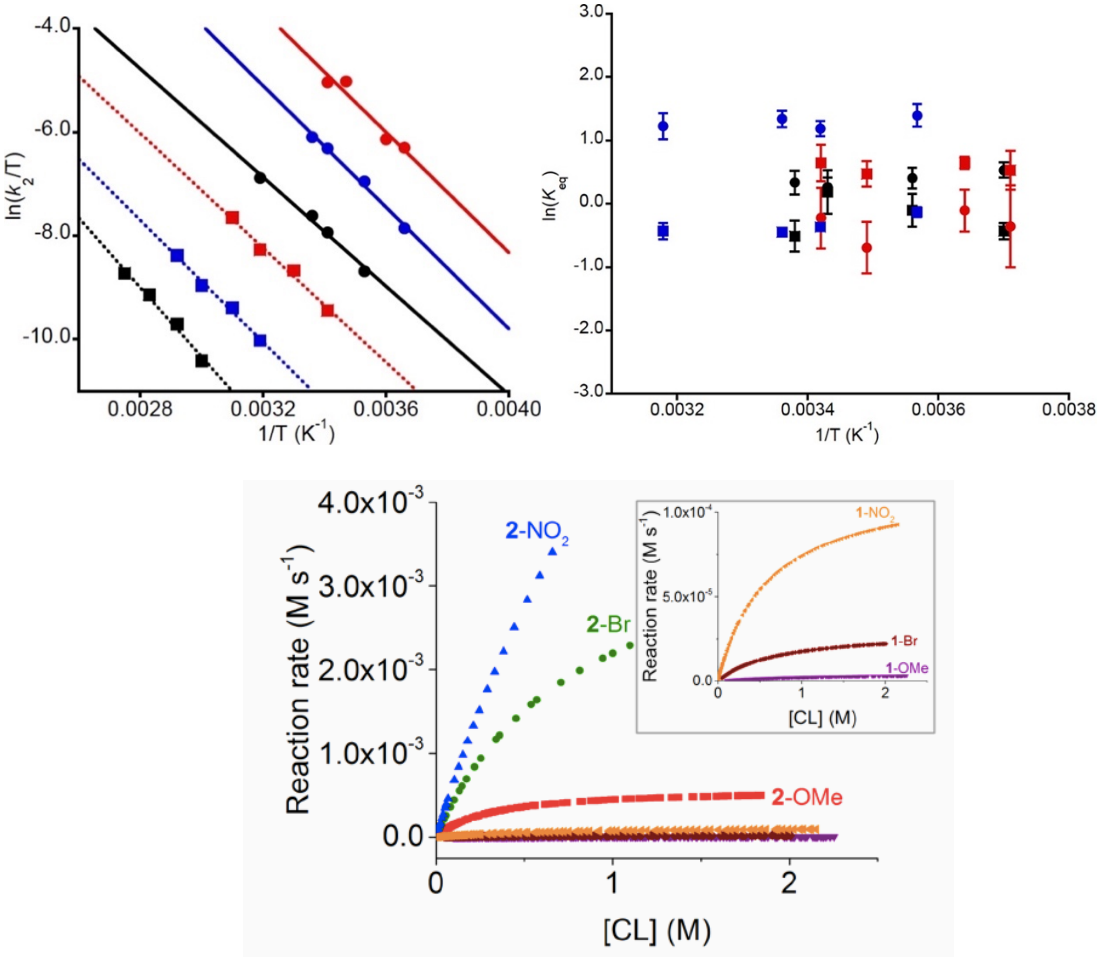

Figure 1.10. (Top left) Eyring analysis of **1.1** (squares, dashed lines) and **1.2** (circles, solid lines) for R_1 = OMe (black), Br (blue), and NO_2 (red). (Top right) van't Hoff analysis of **1.2** variants for R_1 = OMe (black), Br (blue), and NO_2 (red). (Bottom) comparison of ROP rates produced by **1.1** and **1.2**, where variants of catalyst **1.1** are denoted as **1**-R_1 and **1.2** as **2**-R_1. Top images reproduced with permission from reference 68, https://pubs.acs.org/doi/abs/10.1021/acscatal.5b02607, further permissions related to the material should be directed to the American Chemical Society.

Density functional theory (DFT) calculations showed that EWGs attached to the salen ligand strengthened the bond between the alkoxide moiety and carbonyl of the monomer in the transition state, resulting in quicker nucleophilic attack, and overall faster polymerization rates. The calculations also revealed that the transition state geometries (TSGs) for the various complexes were quite similar, suggesting that the differences in rate should be attributed to differences in the energy of the ground state structures. X-ray diffraction studies of **1.1** and **1.2** revealed significant differences quantified by the parameter and universal geometric index τ_5, where a value of 1 is representative of a perfectly trigonal bypyramidal geometry (tbp), while a value of 0 is representative of a perfectly square pyramidal geometry (sp).[69] Complexes **1.1** and **1.2** bore τ_5 values of 0.52, and 0.84, respectively, indicative of a more tbp structure for the faster catalyst, **1.2**. This finding is consistent with previous reports that corroborate that tbp geometries enhance ROP rates compared to their sp counterparts.[51]

In a further analysis, the energies required for **1.1** and **1.2** to adopt their respective TSGs (denoted as "framework distortion energy", FDE, a contributor to the overall activation energy, $\Delta G^{\ddagger}$) were estimated. The value calculated for **1.1** (calculated $\Delta G^{\ddagger}_{(TSG)} = 14.1$ kcal/mol) was larger than that for complex **1.2** (calculated $\Delta G^{\ddagger}_{(TSG)} = 10.3$ kcal/mol), corroborating their differences in ROP rates. Correlations between rate and FDE requirements of other published catalytic systems used for ROP of lactones were observed,[51] setting the stage for the use of this method for predicting new catalysts.

Having examined both the electronics and flexibility of the backbone of the parent (salen)AlOR ligand and its effect on the polymerization of CL, the question of how the steric crowding of the ligand framework would affect the rate of polymerization was raised. This question was addressed by replacing the *ortho*-*t*Bu substituent on the parent ligand with a more sterically encumbered adamantyl (Ad) group.[70] Each catalyst studied within the context of this work bore a Br substituent in the *para* position, in order to ignore the effects of electronics on the ligand and focus entirely on the variable of significance.

As with complexes **1.1** and **1.2**, the catalysts bearing Ad substituents (**1.3** and **1.4**, Figure 1.11) showed saturation behavior, allowing for determination of K_{eq} and k_2. Similar to previous systems, K_{eq} values remained relatively invariant for both **1.3** and **1.4**, while k_2

values changed significantly, signifying that ROP rate differences arose from the differences in rates of nucleophilic insertion onto the monomer, rather than the thermodynamics of monomer binding.

A key finding was that the CL ROP rates by **1.3** and **1.4** were faster than the less sterically hindered congeners. Computations indicated that these rate differences could be linked to the twisted resting state geometries of the catalysts due to the larger steric profile of their *ortho* substituents ($\tau_5 = 0.63$ for **1.3** and 0.81 for **1.4**). As a result, these complexes had lower FDE values (10.0 and 11.0 kcal/mol, for **1.3** and **1.4**, respectively) compared to that of **1.1** and **1.2** (15.5 and 12.4 kcal/mol, respectively). The largest rate difference observed between the four catalysts was between that of **1.1** and **1.4** (over five orders of magnitude difference in ROP rate when R_1 = Br) indicating that *both* increased flexibility in the backbone and increased steric encumberment in the *ortho* position of the framework have a positive effect on ROP rate, albeit for different reasons; a longer carbon backbone (increased complex flexibility) enables conformational change more easily, while Ad substituents prime the complexes' geometry to be closer to that of the TSG, minimizing FDE requirements.[70]

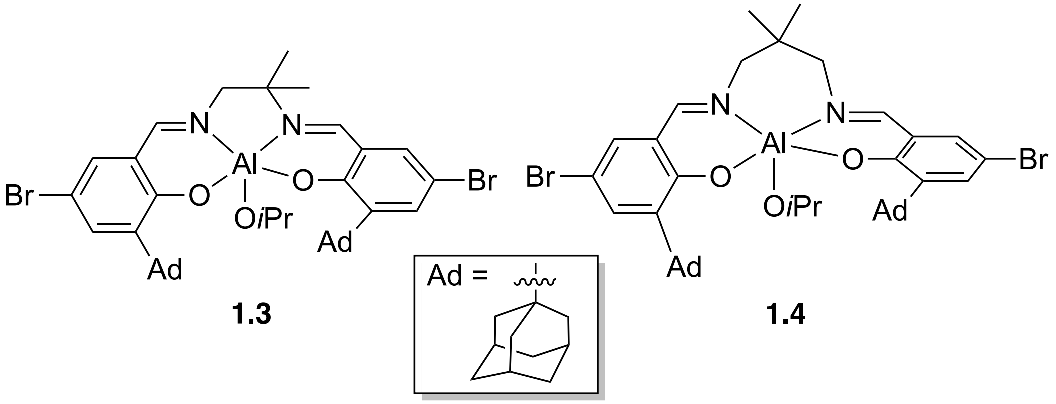

1.3

1.4

Figure 1.11. Catalysts **1.3** and **1.4**.

1.2.3.2 *Zinc-Alkoxide Ring-Opening Polymerization Catalysts*

Zinc-alkoxide (ZnOR) catalysts with variable supporting ligands have also been thoroughly studied for their ROP capabilities. For example, Lin et. al. studied salan-like dimeric Zn complexes with tridentate ligand frameworks with differing sterics and electronics (Figure 1.12, left) to better understand the effects of these ligand structural variations on ROP rate.[71] Kinetic analyses of L-LA polymerization indicated that larger substituents on the backbone (R_1 = Ph), along with the presence of electron-donating groups (EDGs) on the ligand framework led to faster rates. Both observations were postulated to derive from stabilization of the intermediate produced upon ring-opening.[71]

In addition, Lin and colleagues explored di- and trimeric Zn catalysts featuring *β*-diketiminato (BDI) ligands (Figure 1.12, right).[72] Again, EDGs were found to enhance the polymerization rate. This result was rationalized by postulating decreasing electrophilicity at the Zn center, which resulted in a weaker bond between the Zn atom and the alkoxide initiator, leading to greater nucleophilicity and faster polymerization rates.

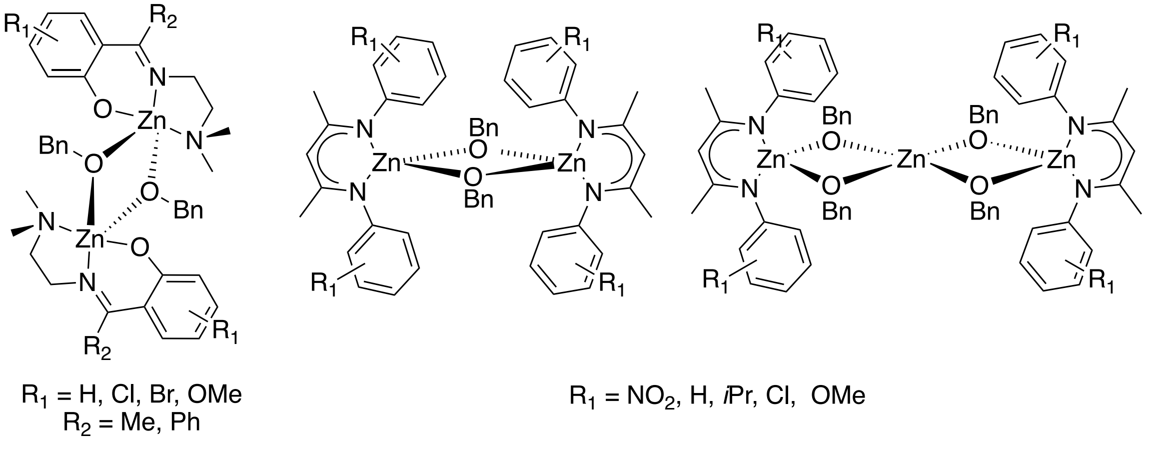

Figure 1.12. Lin's multinuclear Zn complexes, featuring a variety of substituents.

In separate work, Tolman and Hillmyer studied a Zn catalyst supported by a tridentate ligand. This catalyst was found to polymerize 650 equiv. of *rac*-LA in under 5 min (Figure 1.13) with moderate levels of polymerization control (polymer dispersity, *Đ*, measure of uniformity of polymer chain length = 1.42).[54] The resulting polymers were atactic, and the tendency for the complex to dimerize when introduced to exogenous alcohol (Figure 1.13, left), complicated mechanistic studies. Subsequently, Kol and coworkers modified the ligand by attaching a pyridyl substituent which prevented dimerization of the complex (Figure 1.13, right). This catalyst, while more sluggish (300 equiv., $p > 95\%$ in 15 min), allowed for the synthesis of moderately isotactic PLA ($P_m = 0.70$) with narrower polymer dispersities ($Đ = 1.10$).[30] In order to understand the different behaviors of these catalysts, mechanistic studies were needed, in particular to evaluate how electronic variability of the salan-like ligand affected both the tacticity of the resulting polymer and the ROP rates. Our studies of these issues are described in *Chapter 2*.

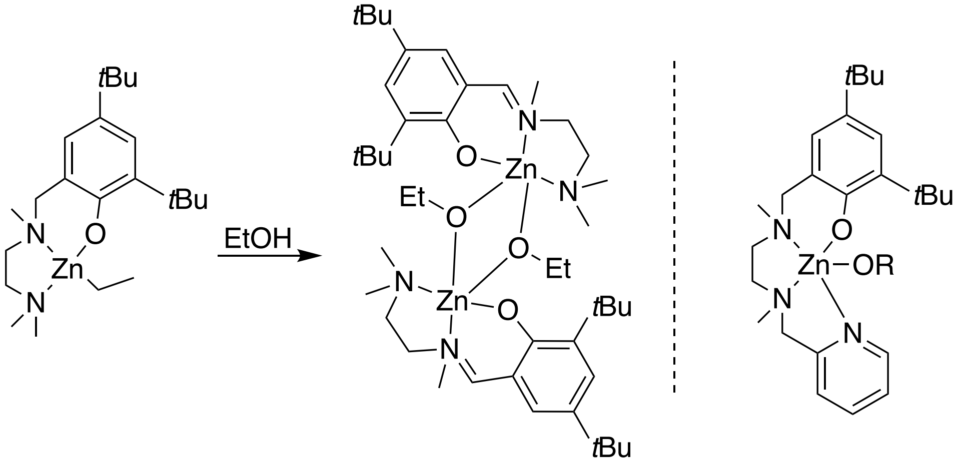

Figure 1.13. Tolman's and Hillmyer's Zn-alkyl complex and subsequent dimer species (left) and Kol's modified Zn complex (right).

1.3 Overview and Brief Description of Chapters

Despite progress in understanding ROP mechanisms, many unanswered questions remain. These questions are important to address in order to develop fundamental insights for use in future catalyst development. For example, this thesis aims to address questions such as: How does electronic variation of the ligand affect fast, monomeric Zn catalysts in terms of ROP rate and stereocontrol? Can the FDE model be used to design a new catalyst with high efficacy for ROP? How does catalyst fluxionality play a role in polymerization stereoselectivity? Can we better understand the ROP mechanism through stoichiometric studies of the postulated elementary reaction steps, such as initiation? Is the synthesis of monomeric catalysts bearing very flexible backbones (i.e. > 3 carbons) possible? If so, how does this increase in flexibility affect ROP capability?

We aimed to address these and related questions through modulation of catalytic complexes encompassing a number of variables, including, but not limited to length/flexibility of the backbone linker chain, change in the electronics of the ligand substituents and modulation of steric bulk (illustrated with regard to a salen-type ligand in Figure 1.14).

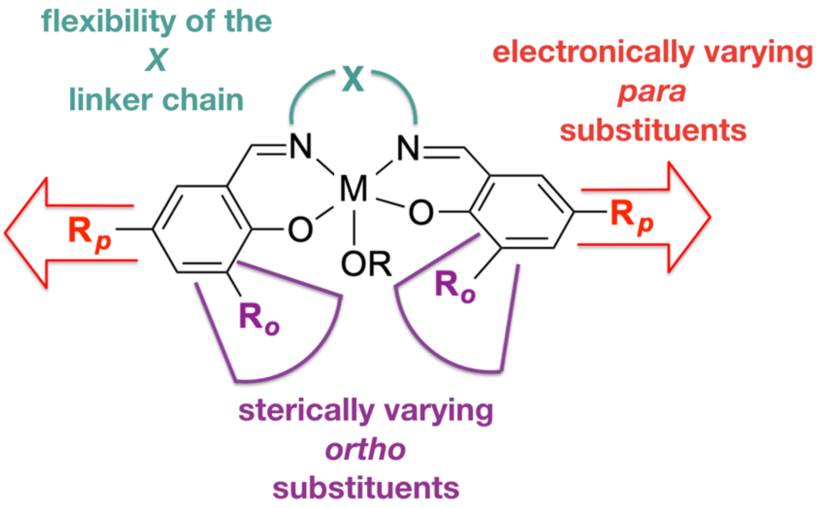

Figure 1.14. Example of general salen-type catalyst with ligand variability indicated.

The following chapters describe how catalyst modulation and its effect on ROP were evaluated. *Chapter 2* examines asymmetric Zn catalysts analogous to those previously published by Tolman, Hillmyer and Kol.[30,54] In-depth characterization of these complexes revealed an induction period due to slow formation of the active catalyst. Full formation of the alkoxide species allowed for significantly improved polymerization rates. In addition, electronic effects for the salan-like ligands were found to minimally influence ROP rate, in contrast to similar Al counterparts. Theoretical studies helped elucidate the reasons behind these observations.

Chapter 3 delves further into the FDE predictive model by way of a synergistic approach between experimental and theoretical work. In this chapter, studies of a new, indolide-based Al catalyst (designed via the FDE model, *in silico*) are described. The validity of the FDE model was probed by comparisons of experimental and theoretical results.

Chapter 4 examines the same Al catalyst as was introduced in *Chapter 3*, but here for the polymerization of *rac*-LA. Characterization of the catalyst revealed fluxional behavior. Polymerization stereoselectivity as a function of fluxionality was explored, and stoichiometric reactions led to the isolation of polymerization initiation products. A combination of X-ray crystallography and NMR spectroscopy revealed a high level of enantioselective polymerization initiation. This work inspired the study of two, new catalysts bearing similar indolide-type frameworks, differing in their backbone structure. *Chapter 5* studies these catalysts in-depth, with the aim of better understanding how fluxionality (or lack thereof) affects *rac*-LA polymerization and PLA microstructure. Careful initiation studies akin to what was presented in *Chapter 4* are also discussed.

Finally, *Chapter 6* examines a multitude of catalysts with various metal ions and ligand structures, with an emphasis on new complexes that bear extremely flexible ligand backbones. While fully characterized, these complexes were not studied in detail in terms of ROP, the reasons for which are discussed.

Taken together, the work described in this thesis has provided new insights into molecular mechanism of ROP by Al- and ZnOR catalysts. Better understanding of ligand structural effects on ROP rates and stereochemistry was obtained, and this knowledge provides the basis for future catalyst design efforts.

2. Mechanism of the Polymerization of *rac*-Lactide by Fast Zinc-Alkoxide Catalysts

Reproduced in part with permission from:

Stasiw, D. E.[†]; Luke, A. M.[†]; Rosen, T.; League, A.; Neisen, B. D.; Cramer, C. J.; Kol, M.; Tolman, W. B. *Inorg. Chem.,* **2017**, *56* (22), 14366–14372. [†]Authors contributed equally.

Copyright 2017 American Chemical Society.

2.1 Overview

In this work, ROP of *rac*-LA using (salan)L^XZn catalysts with variable *para* substituents X on the bound phenolate donor (X = NO_2, Br, *t*Bu, OMe), was evaluated and comparisons to aforementioned (salen)AlOR systems[67,68] were drawn. Detailed kinetic experiments and DFT were employed, with the aim of determining how electronic modulation of the ligand framework influences polymerization rate, selectivity, and control for fast Zn catalysts. After finding that L^XZnEt pre-catalysts required 24 h of reaction with BnOH to convert to active complexes for ROP initiation, the subsequently formed species (L^XZnOBn) proved to be active and fairly selective, polymerizing up to 300 equiv. of *rac*-LA in 6–10 min while yielding isotactic PLA (P_m = 0.72–0.78) with narrow polydispersities ($Đ$ = 1.06–1.17). In contrast to previous work with Al catalysts for which electronic effects of ligand substituents were significant (Hammett ρ = +1.2–1.4),[67] the L^XZn systems exhibited a much smaller effect (ρ = +0.3). Density functional calculations revealed details of the initiation and propagation steps, enabling insights into the isotacticity and the insensitivity of the rate on the identity of X.

2.2 Introduction

As stated previously in *Chapter 1*, new catalytic synthetic methods are needed for the development and broader implementation of sustainable polymers that are both derived from renewable feedstocks and readily degraded after use.[7,73] Understanding the mechanisms by which existing catalysts operate is a key prerequisite for addressing this goal. As a privileged class of bioderived monomers, cyclic esters undergo ROP to yield useful sustainable materials, with catalysis by metal-alkoxide complexes serving as a pervasive route.[62,74–77] There is wide agreement that these systems follow a coordination-insertion mechanism involving initial binding of the monomer to the catalyst followed by nucleophilic attack and ring-opening by an alkoxide ligand. However, purposeful catalyst design is hindered by a general lack of knowledge of many details of the process, including the nature of the coordination and insertion steps and the fundamental reasons for changes in rates and selectivity observed upon varying the supporting ligand and/or metal ion.

Significant insights into these issues have been obtained from kinetic studies of ROP of LA or CL by AlOR complexes.[51,67,68,78–84] Such catalysts exhibit high molecular weight control and modest rates that are convenient for monitoring by NMR spectroscopy, and typically feature easily synthesized supporting Schiff-base ligands that are readily structurally modified so that steric, overall geometric, and electronic influences may be evaluated.[63,85] Notably, previous studies of AlOR systems revealed significant rate changes upon variation of the electron withdrawing/donating power of substituents on otherwise identical supporting ligands. For example, EWGs in (salen)AlOR catalysts enhanced the rate of ROP of CL (for the insertion rate constant k, Hammett $\rho \sim +1.3$, $\Delta\Delta G^{\ddagger} = 1.6$–$2.6$ kcal/mol between systems with NO_2 and OMe substituents). Analysis by DFT pointed to changes in the bonding in the insertion transition state as being responsible for the rate differences (greater electron withdrawal shortens the Al-O(carbonyl) and C(carbonyl)-O(alkoxide) interactions). On the other hand, there are reports of other AlOR catalysts that exhibit the reverse trend, where ROP is inhibited by EWGs and enhanced by EDGs.[83,84]

While these and other results from studies of well-controlled but relatively slow AlOR catalysts ($k \sim 10^{-2}$ s^{-1}) provide useful insights, it is unclear whether they are transferable to catalysts that perform ROP at much faster rates (i.e. Zn-based catalysts).[86–88] A notable example of the latter is complex **2.1** (Figure 2.1), which was found to polymerize up to 500 equiv. of *rac*-LA in under 5 min at room temperature (k_p = 2.2 $M^{-1}s^{-1}$).[54] This system produced atactic PLA with moderate polydispersities ($Đ$ = 1.3–1.4). Unfortunately, its dimeric nature rendered detailed mechanistic analysis challenging compared to that of single-site metal alkoxide catalysts. Recently, a modified version of the ligand in **2.1** **(**incorporating a pyridyl group to help prevent dimerization) was found to yield an exclusively monomeric (salan)L^XZnEt species (**2.2**, Figure 2.1, X = *t*Bu). This complex is a fast, controlled, and selective pre-catalyst for the polymerization of *rac*-LA (300 equiv.) using BnOH as initiator, reaching > 95% conversion in ~30 min at ambient temperature with moderate isotacticity (P_m = 0.7–0.8).[30]

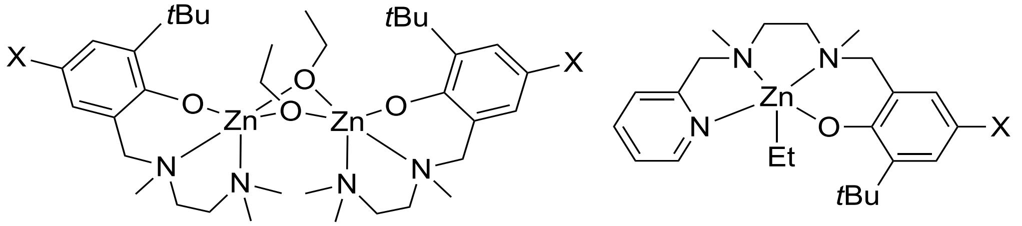

2.1
(X = *t*Bu or Me)

2.2
(X = *t*Bu, OMe, Br, NO_2)

Figure 2.1. Zn complexes used for the polymerization of LA.

Intrigued by these results, we sought to investigate the effects of varying the electron donating propensities of substituents X (**2.2**, Figure 2.1) on the ROP kinetics and stereocontrol. We report the synthesis and characterization of new variants with X = NO_2, Br, and OMe, and a full experimental kinetic analysis of ROP of *rac*-LA by all four derivatives. Key findings include discoveries that pre-conditioning of the complexes with BnOH results in very high ROP rates (significantly faster than what is observed via Zn-alkyl species and exogenous BnOH in the polymerization system), that all catalysts yield PLA with similar isotacticity, and that the polymerization rates are relatively *insensitive* to the nature of substituent X, in contrast to what was observed with AlOR catalysts. The bases for these results was evaluated through analysis of the reaction pathway by DFT calculations, which provided insights into the high isotacticity of the system and a rationalization for the lack of significant rate changes upon varying X.

2.3 Results and Discussion

2.3.1 *Synthesis and Characterization of Complexes*

Using the same method reported previously for the synthesis of the proligand and complex **2.2** (X = *t*Bu),[30] the respective proligands and complexes **2.2** (X = NO_2, Br) were prepared by coupling the appropriate bromomethylphenol with the pyridyl-amine fragment followed by treatment with $ZnEt_2$. A different route was used to produce the proligand with X = OMe, involving reductive amination of the indicated aldehyde (Figure 2.2, see Scheme 2.1, section 2.5.2 for additional detail). Each ligand was fully characterized by ^1H, ^{13}C, COSY, and HSQC NMR spectroscopy, as well as high resolution electrospray ionization mass spectrometry (HR-ESI-MS; details provided in section 2.5.2). The ^1H NMR spectra of the proligands resulted in unique resonances for each proton (attributing to the asymmetry of the molecules), and in the case of X = Br, a broad O-H peak was observed (~3.3 ppm, Figure 2.15, section 2.5.2), but the same resonance was buried in the baseline for X = NO_2, *t*Bu, and OMe. The subsequent complexes (**2.2**) were obtained as crystalline solids in good yields (85–93%), and were characterized by ^{1}H, ^{13}C, COSY and HSQC NMR spectroscopy, CHN analysis, HR-ESI-MS, and, for **2.2** (X = Br), X-ray crystallography. The ^{1}H NMR spectra of complexes **2.2** featured significantly shielded ethyl peaks (resonances ranging from –0.5–1 ppm) and for the case of X = Br, a notable disappearance of the O-H resonance, indicating full metalation had occurred. Similar to other reported structures with analogous ligands,[30] **2.2** X = Br was mononuclear with a distorted sp geometry characterized by $\tau_5 = 0.24$. Albeit, both the Zn-O1 and Z-NX bond distances for **2.2** are notably longer than that of similar bonds in other mononuclear, tetradentate Zn complexes (bond lengths ranging between 1.93–1.97 Å for Zn-O and 2.01–2.11 for Zn-N for selected examples).[89–91]

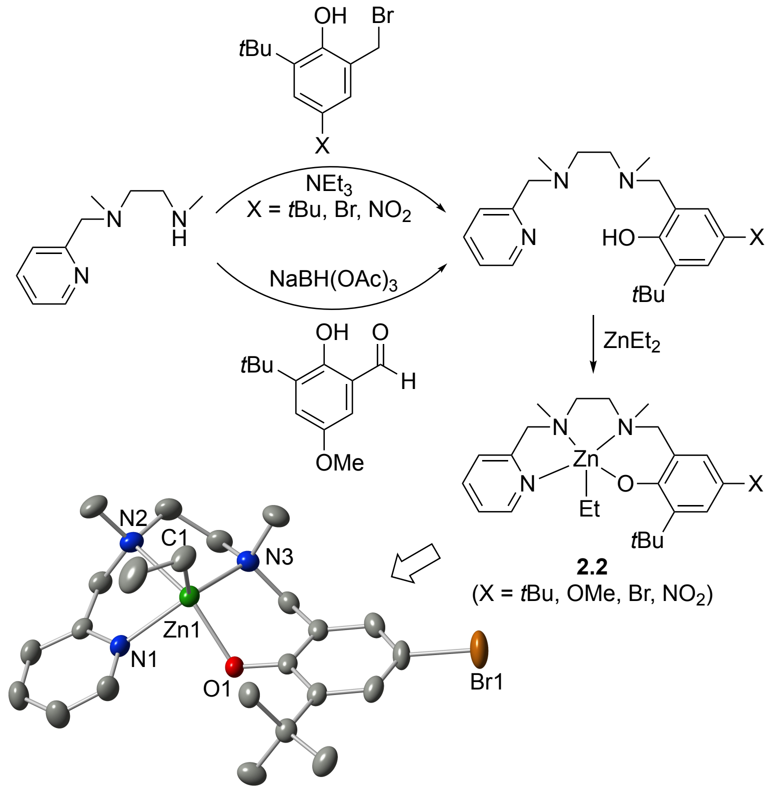

Figure 2.2. Synthesis of proligands and complexes, and a representation of the X-ray crystal structure of **2** (X = Br), showing all nonhydrogen atoms as 50% thermal ellipsoids. Selected distances (Å) and angles (deg): Zn1-O1, 2.0473(11); Zn1-N1, 2.1407(14); Zn1-N2, 2.4348(14); Zn1-N3, 2.1999(15); Zn1-C1, 2.0059(17); C1-Zn1-O1, 114.67(6); C1-Zn1-N1, 113.30(7); C1-Zn1-N2, 104.29(6); C1-Zn1-N3, 116.42(7); O1-Zn1-N1, 87.43(5); N1-Zn1-N2, 73.24(5); N2-Zn1-N3, 76.93(5); N3-Zn1-O1, 88.89(5); O1-Zn1-N2, 140.84(5); N1-Zn1-N3, 126.62(5).

2.3.2 *Polymerization Kinetics: Monitoring via ^{1}H NMR Spectroscopy*

Polymerization of *rac*-LA was initially monitored by ^{1}H NMR spectroscopy with fixed concentrations of *rac*-LA (0.9 M < [*rac*-LA]$_0$ < 1.2 M), pre-catalyst **2.2** (3 mM < [**2**]$_0$ < 4 mM), and BnOH (3 mM < [BnOH]$_0$ < 4 mM) in CD_2Cl_2, using 1,4-bis(trimethylsilyl)benzene (8.33 mM) as an internal standard (conditions matched what had been previously studied with the original L^{tBu}ZnEt + BnOH system). In the experiments, BnOH was added last, at which point data collection was initiated. Upon inspection of the ^{1}H NMR spectroscopy data for the polymerization of *rac*-LA by **2.2** (X = NO_2), evidence of an induction period near the beginning of the polymerization array was observed (Figure

2.3; note the overall sigmoidal form of the curves). Based on the general reactivity/oxophilicity of Zn-alkyl species,[92,93] we assumed that once the exogenous alcohol was introduced to the system, rapid exchange between the ethyl substituent and BnOH would occur to yield a ZnOR complex, L^XZnOBn, (**2.2'**) which then initiated ROP. To explain the apparent induction period observed under the aforementioned reaction conditions, however, we hypothesized that the conversion of **2.2** to **2.2'** was slow, and that the overall polymerization rate observed under these conditions (> 95% conversion in 2.5 h) was in fact slower than if formation of **2.2'** was instantaneous.

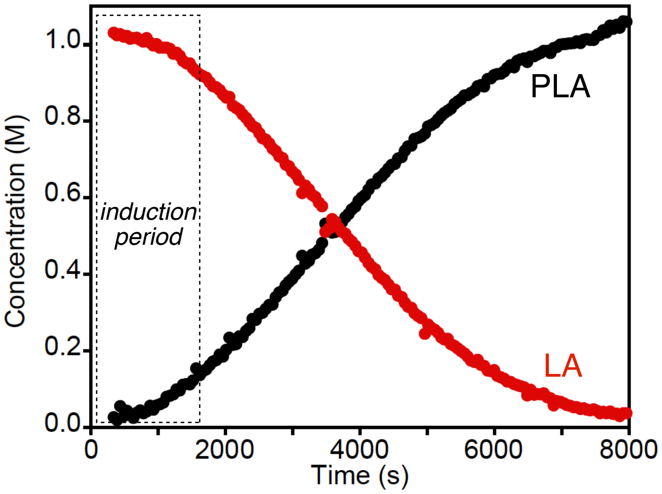

Figure 2.3. Concentration vs. time plot for polymerization of *rac*-LA (300 equiv., 1 M) by **2.2** (X = NO_2, 1 equiv., 3.33 mM) and BnOH (1 equiv., 3.33 mM) as monitored by ^{1}H NMR spectroscopy. Data collection was started soon after addition of BnOH.

To test the above hypothesis and determine the mixing time required for full formation of **2.2'**, exchange experiments were performed, in which a solution of **2.2** (X = NO_2, 3.33 mM) in CD_2Cl_2 was added to an NMR tube with an equimolar amount of BnOH and the decay of the ethyl peaks associated with **2.2** (X = NO_2) was monitored. Total disappearance of the peaks (labeled O and N, Figure 2.4) from the NMR spectrum of the L^XZnEt + BnOH mixture signifying complete conversion to the L^XZnOBn complex occurred only after 24 h.

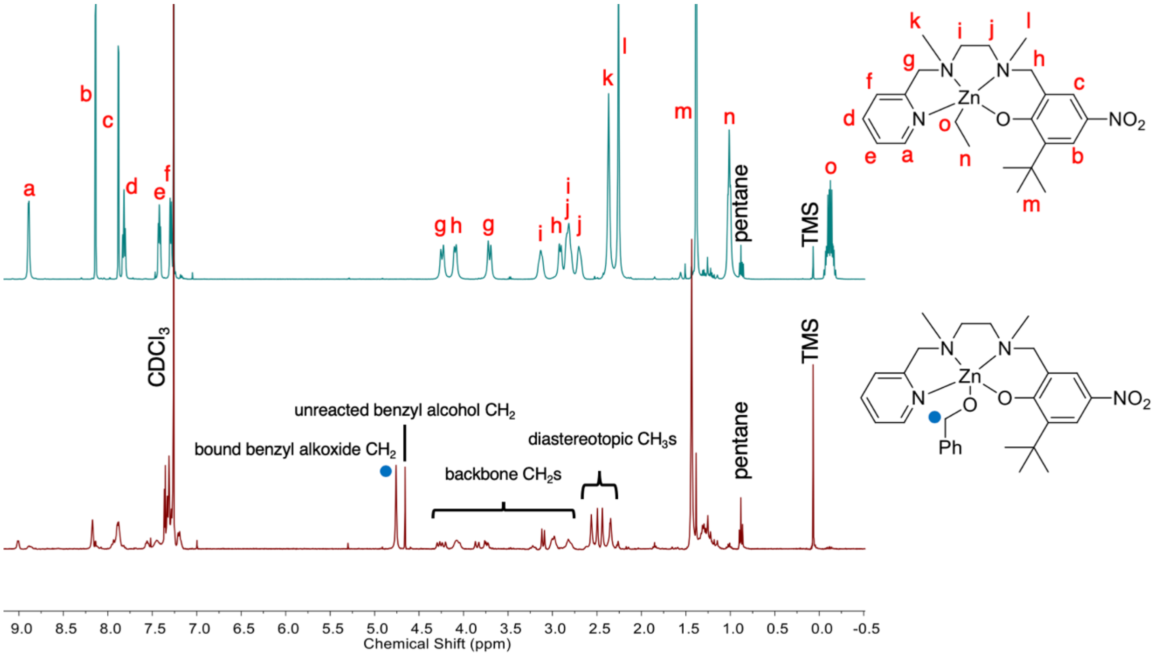

Figure 2.4. (Top) assigned spectrum of **2.2** (X = NO_2) (see Figure 2.14, section 2.5.2 for comparison). (Bottom) ^{1}H NMR of *in situ* generated **2.2’** (X = NO_2) after 24 h of mixing with ~1 equiv. BnOH. Addition of the OBn substituent to the Zn complex causes resolution of two diastereomers as seen in splitting of the N-CH_3 and backbone CH_2 protons.

Although the slow reaction of **2.2** with the BnOH was initially unexpected, there is literature precedent for slow Zn-alkyl and alcohol exchanges.[94] While NMR data support the formulation of **2.2’**, efforts to isolate the complexes were not successful. Nonetheless, we confirmed that the active species were likely mononuclear in solution by using diffusion ordered spectroscopy (DOSY) on **2.2'** (X = NO_2). From these experiments, hydrodynamic radii r_H for **2.2** and **2.2’** were found to be 6.22 Å and 6.98 Å, respectively, via the Stokes-Einstein equation (Eq. 2.1, where k_B = Boltzmann's constant, T = temperature, η = viscosity and D is the diffusion constant), which measures the diffusion of particles through a liquid.[95] See Figure 2.5 and section 2.5.3 for additional detail.

$$r_H = \frac{k_B T}{6\pi\eta D} \qquad \textbf{Eq. 2.1}$$

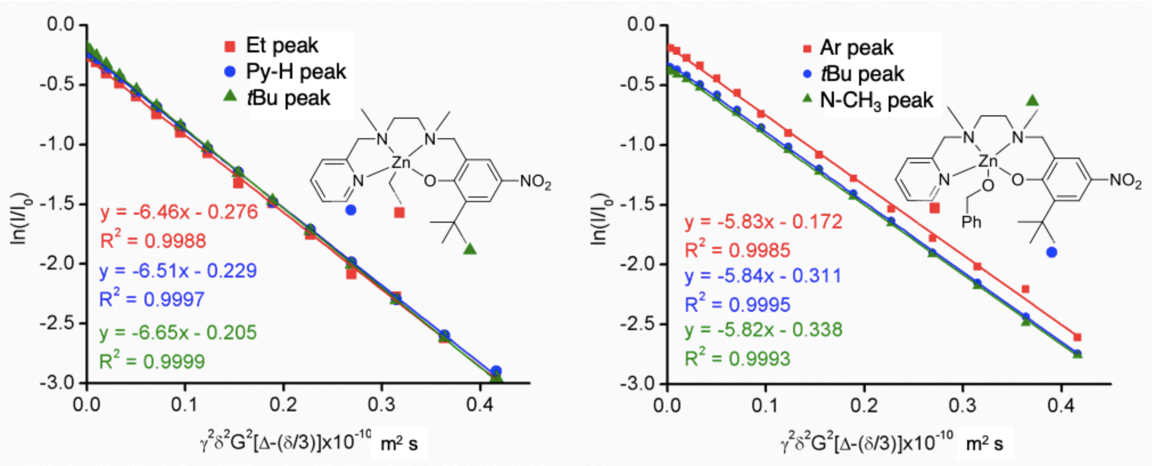

Figure 2.5. Plot of ln(I/I0) vs. $\gamma^2\delta^2G^2[\Delta-(\delta/3)]\text{x}10^{-10}$ (where I = intensity, γ = gyromagnetic ratio for a proton, δ = diffusion gradient length, G = gradient field strength, and Δ = diffusion delay) for **2.2** (X = NO_2) (left) and **2.2'** (X = NO_2) (right).

With the knowledge that conversion from the L^XZnEt species to a L^XZnOBn complex was slow, we 'pre-conditioned' the catalysts by first stirring **2.2** with BnOH for 24 h to fully convert them to **2.2'** before adding *rac*-LA. Subsequent ROP was then monitored via ^{1}H NMR spectroscopy using the same fixed conditions as previously described. Significantly faster polymerizations were observed; complexes **2.2'** (X = NO_2 or Br) reached > 95% monomer conversion in just under 400 s (~6 min), with the same conversion reached with **2.2'** (X = *t*Bu or OMe) in ~8 and ~10 min, respectively. These enhanced rates support the hypothesis that slow conversion from **2.2** to **2.2'** underlies the induction period and that full conversion to the active L^XZnOBn catalyst is necessary for rapid ROP. However, due to the timescale for the reactions, these new polymerization rates rendered monitoring of the polymerizations by traditional ^{1}H NMR spectroscopy methods challenging, so we turned to an alternative methodology.

2.3.3 *Polymerization Kinetics: Monitoring via React-IR Spectroscopy*

In view of the fast conversions observed for the ROP reactions performed by first allowing **2.2** to react 24 h with BnOH, we used *in situ* IR monitoring by React-IR to obtain accurate kinetic data. Kinetic measurements of ROP of LA using Sn(Oct)$_2$ were previously measured with React-IR using single wavelength analysis.[96–98] Preliminary experiments using this method yielded variable and inconsistent results depending on the IR peak selected. This problem was avoided by using spectral deconvolution and global fitting in the 1900 cm^{-1} to 900 cm^{-1} region of the spectra to obtain relative amounts of *rac*-LA and PLA per spectrum collected. Known issues with non-linear absorption response vs. analyte concentration[96,99] were addressed by use of calibration curves for both *rac*-LA and PLA (~50 kDa average M_w), which established correlation of integrated area under the 1900 cm^{-1} to 900 cm^{-1} region of interest to known concentrations (Figure 2.6).

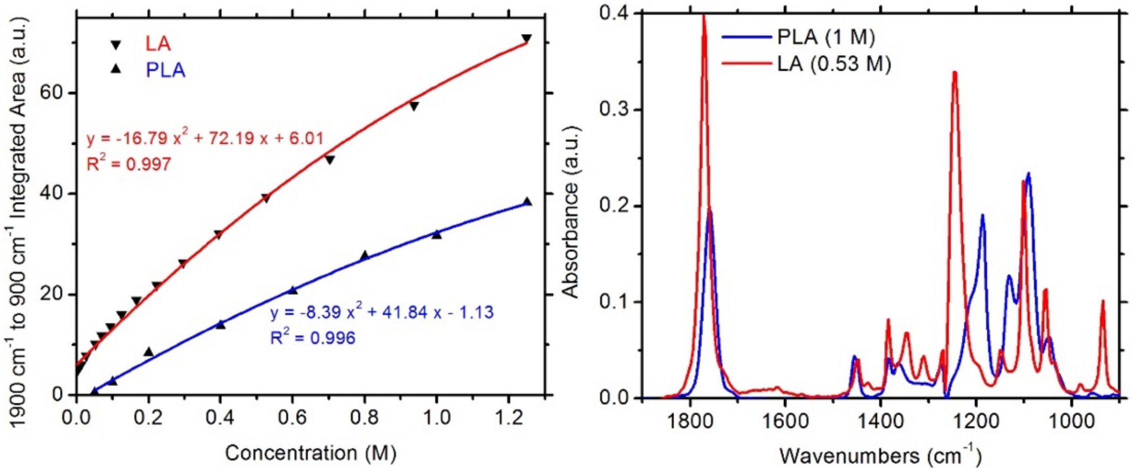

Figure 2.6. (Left) *rac*-LA and PLA concentration calibration curves for React-IR 1900 cm^{-1} to 900 cm^{-1} integrated area. Non-zero intercepts are an artifact of instrument noise. (Right) overlay of spectra of pure LA (0.53 M) and PLA (1 M).

Polymerizations of *rac*-LA to PLA were performed in triplicate and monitored by React-IR at fixed concentrations of *rac*-LA (0.5 M < [*rac*-LA]$_0$ < 1.5 M) and **2.2'** (1 mM < [**2.2'**]$_0$ < 4 mM). The series of spectra (illustrative data shown in Figure 2.7, left) were separated into two components, *rac*-LA and PLA, through spectral deconvolution analysis.[100] Relative concentrations of *rac*-LA and PLA vs. time as well as absolute concentration (using the calibration curves) vs. time data were fit with COPASI software.[66] Excellent agreement with a first-order fit by all **2.2’** species showed that the polymerizations follow a pseudo-first order rate expression: rate law = k_{obs}[*rac*-LA] where k_{obs} = k_p[**2.2’**] (see section 2.5.6, Figures 2.19–2.20 for more detail, illustrative data shown in Figure 2.7, right). The spectral data were also fit to a pseudo-first order rate law by Olis GlobalWorks spectral fitting software.[101] Comparison of the three fitting methods revealed results in close agreement (within 20%; Table 2.4, section 2.5.6); we arbitrarily chose to provide those obtained by COPASI fitting to calibrated data in Table 2.1.

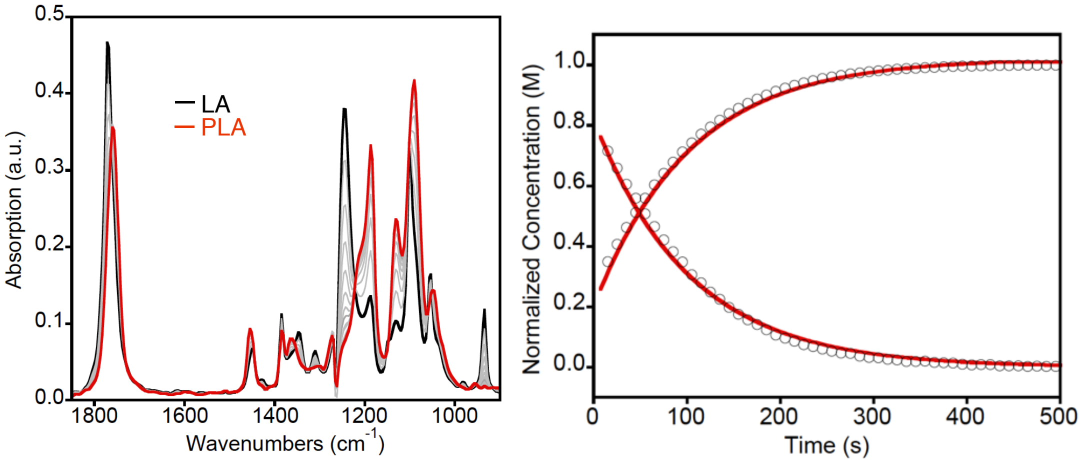

Figure 2.7. (Left) stacked IR spectra at 30 s intervals for polymerization of *rac*-LA (black) to PLA (red) to > 95% conversion using **2.2’** (X = NO_2; intermediate spectra in gray). (Right) illustrative plot of experimental data (circles) and corresponding COPASI fit (red line) for the ROP of *rac*-LA by **2.2’** (X = NO_2). See Figures 2.19–2.20 for data plots by other L^XZnOBn catalysts.

Comparison of the k_{obs} values as a function of *para* substituent (Table 2.1) reveals a negligible trend, as illustrated by only ~2–fold difference in rate constants. Also, a small ρ value of +0.3 is seen in a Hammett plot of the log(k_p) values (black line, Figure 2.8). This finding differs significantly from that seen for ROP of CL by (salen)AlOR catalysts (red and blue lines), which exhibited ρ = +1.2 or +1.5, respectively (where k_p refers to the catalytic rate constant k_2 in the Michaelis-Menten expression, applicable for these catalysts because they exhibit saturation kinetics). In addition, the polymerization rates for the Al catalysts (also at 293K) varied by approximately an order of magnitude (NO_2 > Br > OMe).[67] In section 2.3.5, we turn to DFT calculations in order to better understand why a significantly less pronounced trend in rate as a function of phenolate substituent was observed for the Zn catalysts as compared to the previously studied (salen)AlOR systems.

Table 2.1. Rate constants and PLA characterization data.

Complex	k_{obs} (s^{-1})^a	M_n (kDa)^{b,c}	$P_m{}^d$	$Đ^c$
2.2’ **(X = NO_2)**	0.014(1)	53.8	0.72	1.17
2.2’ **(X = Br)**	0.010(1)	61.4	0.76	1.15
2.2’ **(X = *t*Bu)**	0.0102(8)	35.5	0.78	1.15
2.2’ **(X = OMe)**	0.006(1)	39.2	0.75	1.06

[a]Conditions: $[LA]_0$ = 1 M: $[\mathbf{2.2'}]_0$ = 3.33 mM (300:1) in CH_2Cl_2 at 25 °C. [b]Theoretical M_w = 43.3 kDa. [c]Values were determined by SEC using light scattering detection with THF eluent. [d]Determined by homonuclear decoupled ^1H NMR spectroscopy.

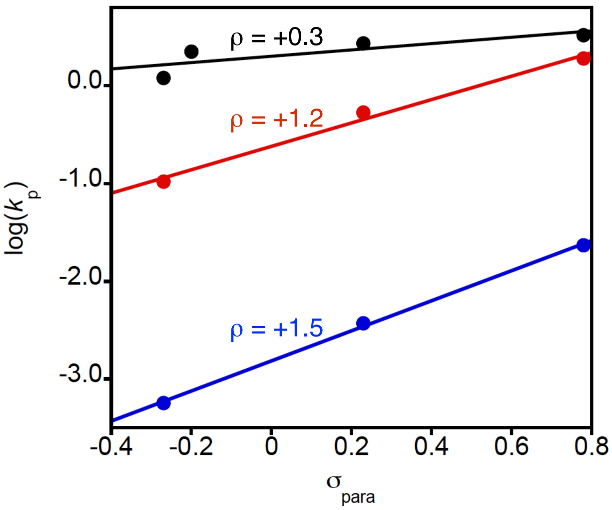

Figure 2.8. Hammett plots of log(k_p) vs. σ_{para} for **2.2’** (X = NO_2, Br, *t*Bu, OMe; black data and linear fit, $R = 0.825$), with data and fits reported previously for ROP of CL by AlOR catalysts supported by salen ligands with a 3-carbon backbone (red, $R = 0.995$) or a 2-carbon backbone (blue; $R = 0.999$) at 298 K. The slopes of the lines corresponding to the Hammett ρ values are shown.

2.3.4 *Polymer Characterization*

Kinetic experiments were exposed to air to quench the polymerization reaction within ~30 min of completion and PLA was precipitated by addition to cold MeOH, collected, and dried via Schlenk line for ~48 h. Size exclusion chromatography (SEC) using a dynamic light scattering detector was used to determine M_w and $Đ$ of the resulting polymers (Table 2.1). Even at the rapid polymerization rates observed by **2.2’**, polymerization control is maintained, indicated by narrow polydispersities ($Đ$ = 1.06–1.17). A sample of dry PLA from each kinetic experiment was dissolved in $CDCl_3$ and used to determine P_m via homonuclear-decoupled ^1H NMR spectroscopy. Using the methine region of the subsequent NMR spectrum, the different tetrad concentrations were integrated so that the *meso* and racemic character of the polymer could be determined (Figure 2.22, section 2.5.7).[35,102–104] An isotactic preference for PLA by all catalysts studied was observed, with P_m values reaching as high as 0.78 (Table 2.1).

2.3.5 ***Density Functional Theory Calculations*** (performed by Aaron B. League, Mukunda Mandal and Christopher J. Cramer).

Quantum chemical modeling, which has previously offered important insights into the metal-catalyzed ROP of LA in other systems,[105–111] was undertaken to 1) offer insight into the observed isotacticity in the polymer product, and 2) rationalize the insensitivity of the reaction rate to *para* substitution of the phenoxide moiety in the catalyst. This section briefly describes some of the theoretical modeling involved in this project, while more details are available in published work.[44]

A detailed survey of stereodistinct isomers for relevant insertion and ring-opening transition state structures in the parent system was done using the M06 family of density functionals (see section 2.5.8 for additional detail), and the reaction coordinate (Figure 2.9) was found to have the lowest barriers for the initiation step of the proposed polymerization mechanism. The ring opening transition state (TS4-5) was predicted to be rate limiting for both enantiomers of *rac*-LA, with the *S,S* enantiomer having a significantly higher barrier than the *R,R* enantiomer (16.1 vs. 14.0 kcal/mol, respectively) for the catalyst configuration used. While it is noted that the flexibility of the growing polymer chain, together with the structural similarity of O*i*Pr to the portion of the growing polymer chain coordinated to the metal, suggests that similar differential energetics may be expected for subsequent propagation steps, it is also recognized that some degree of chain-end control of polymer stereochemistry likely occurs and is not addressed by our calculations. The observed ratio of tetrad peaks in the homonuclear decoupled ^{1}H NMR spectrum of the PLA product reported herein and that which was previously reported[30] do not match either predicted ratio, (1:2:1:1 for ESC vs. 1:1:0:1 for CEM).[43] Critically, the *rmr* peak was of significant intensity, indicative of the importance of site control in the polymerization mechanism.

While calculations here only delve into the basis for this path, it is recognized that a complete analysis would have to take into account chain-end effects by replacing the isopropoxide with a more accurate model of the growing polymer chain. Such extensive calculations were beyond the scope of this work, which is more focused on the influence of the substituents on ROP rate.

Working under the assumption that site control is important, it is hypothesized that the difference in activation free energies between the two LA enantiomers is one key determinant of the isotacticity observed in the polymer (noting that changing the configuration at Zn requires a quite high-energy dissociation/re-coordination of the growing polymer chain from the metal center). The origin of the 2.1 kcal/mol energy difference is associated with the boat-like geometry of the 6-membered LA ring in this ring-opening transition state structure. The boat is preferred because it permits both methyl groups of the LA to be pseudo-equatorial while their corresponding geminal hydrogen atoms are pseudo-axial (the planarity of the ester linkages that comprise the other 4 atoms of the ring also contribute to stabilizing the boat ring form in this transition state structure). For the specific $L^{X}Zn$ catalyst configuration chosen, the alternative boats have differing steric interactions. For the *S,S* case, a methyl group of the LA ring is close to and clashes with the *t*Bu group of the aryloxy ring and the alkylamino portion of the ligand linker, whereas these interactions are lessened considerably for the *R,R* isomer. Moreover, the methyl group from the alkylamino portion of the ligand linker points directly towards the unperturbed ester linkage of the LA ring for the *S,S*-case, whereas these interactions are absent in the *R,R* variant. It is hypothesized that these differences in steric interactions and/or unfavorable changes in electronic interactions associated with geometry relaxation to ameliorate the steric clash underlie the transition state energies and are at least partially responsible for the observed isotacticity in the polymerization.

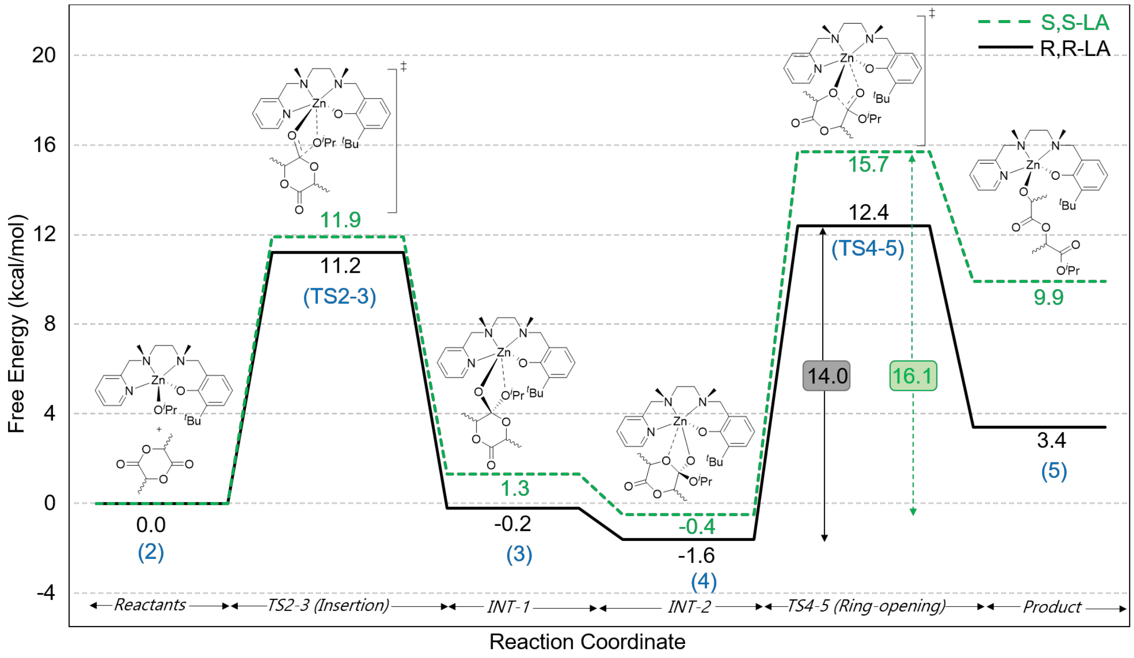

Figure 2.9. M06-2X//M06-L reaction coordinate standard-state free energies for LA opening (kcal/mol) relative to separated species with line drawings of relevant stationary points, where TS indicates a certain transition state. Results for pathways involving both *S,S-* (green dotted line) and *R,R*-LA (black solid line) are shown with adoption of a particular configuration at Zn in the pre-catalyst differentiating these two paths.

To assess substitution effects, all of the stationary points in Figure 2.9 were substituted at the *para* position. Relative energetics for TS4-5, along with CM5 charges on the Zn atom, are shown in Table 2.2 for all of the reaction coordinates (taking the specific configuration at Zn that favors *R,R* reactivity). Slightly lower reaction barriers were predicted for EWGs than for H or EDGs, in good agreement with experimental observations, but the overall sensitivity to *para* substitution was predicted to be slight. Consistent with this observation is the very small variation in Zn CM5 charges that is predicted over the range of substituents. Thus, from *para*–N(Me)$_2$ to *para*–NO$_2$, there is an increase in the Zn charge of only 0.008 a.u., i.e., its Lewis acidity is modulated very little by *para* substitution of the phenol. It is not entirely trivial, of course, to explain why something does *not* happen, but we speculate that the extensive nitrogen functionality about Zn buffers the phenol *para* substitution effect so that its influence is more limited than it might otherwise be expected to be.

Table 2.2. DFT predicted reaction barriers and Zn charges in TS4-5.

	***R,R*-LA**		***S,S*-LA**	
Substituent	**$\Delta G^{\ddagger}_{rxn}$ (kcal/mol)**[a]	**$Q_{Zn,\ CM5}$**	**$\Delta G^{\ddagger}_{rxn}$ (kcal/mol)**[a]	**$Q_{Zn,\ CM5}$**
$-NO_2$	13.3	0.733	15.4	0.722
–Br	12.9	0.728	16.9	0.718
–H	14.0	0.729	16.1	0.717
–*t*-Bu	14.0	0.727	16.9	0.716
–OMe	14.0	0.726	16.9	0.715
$-N(Me)_2$	14.6	0.725	17.0	0.714

[a] Computed as $G_{TS4\text{-}5} - G_4$ using M06-2X//M06-L free energies.

Additional insights into the basis for the ligand substitution effects may be attained by comparing the transition state structures calculated here to those previously reported for the (salen)Al system with the 2-carbon backbone (Figure 2.10).[67] As illustrated for selected bond distances (Table 2.3) the largest change in transition state structure bond lengths for the (salen)Al system is found for the O_2-C_1 bond, which is the bond that forms in this mechanistic insertion step (0.057 Å; O_2 is the alkoxide oxygen nucleophilically attacking the carbonyl carbon of CL, C_1). Given such a large change in the position of the transition state, it is not particularly surprising that a significant variation in $\Delta G^{\ddagger}$ is also observed for polymerization in this system (Figure 2.8, blue), presumably reflecting the influence of the varying basicity of the phenolates in the ligand (of which there are two). By contrast, for the L^XZn system, there is quite little variation in the lengths of the key bonds being made or broken as a function of *para* substitution in the single phenol ring in these catalysts (0.009 Å for O_2-C_1 in the insertion step, TS2-3, Table 2.3). The variation is similarly small for O_5-C_1 in the ring-opening step (0.013 Å, TS4-5). Interestingly, in both transition state structures, there *are* significant variations in heteroatom-Zn bond distances associated with *para* substitution of the L^X phenolate, but these do not seem to significantly influence the reacting partners (consistent with the observed lack of much charge variation at the Zn center described above). We postulate that these findings derive from the fact that 1) there is only a single phenol in the L^XZn system compared to the two in the (salen)Al system and/or 2) the Zn–O bonds are intrinsically about 0.2 Å longer than analogous Al–O bonds, thereby making Zn less sensitive to substitution effects than Al simply from the r^{-1} dependence of purely electrostatic effects.

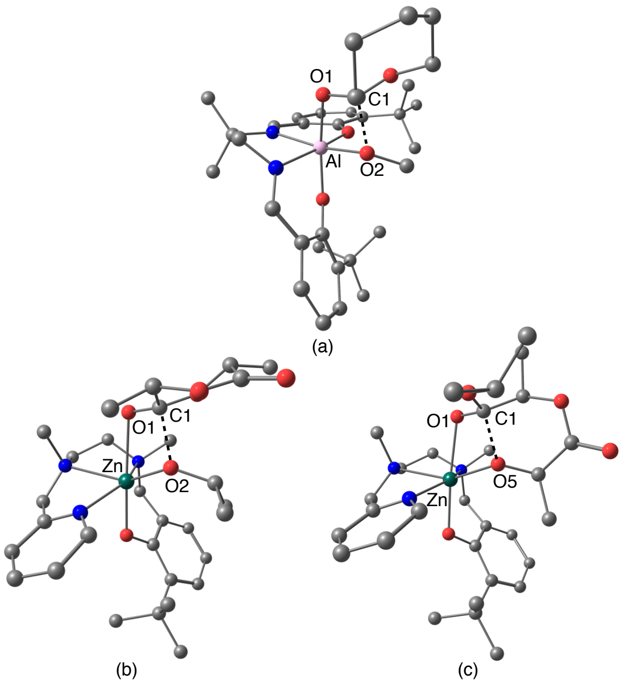

Figure 2.10. Optimized transition state structure geometries, with selected atoms identified. (a) previously reported transition state structure for nucleophilic attack on CL by coordinated alkoxide for (salen)Al catalyst analogous to the Zn catalysts reported here, (b)transition state structure for nucleophilic attack on *R,R*-LA with (salan)Zn catalyst (TS2-3), and (c) ring-opening transition state structure for the tetrahedral intermediate in the *R,R*-LA/(salan)Zn system (TS4-5). Select geometric details are recorded in Table 2.3.

Table 2.3. Selected bond lengths (Å) and bond length variations in calculated transition state structure for nucleophilic attack on CL or *R,R*-LA by coordinated alkoxide as a function of *para* substitution of the phenolate group(s).[a]

Bond	NO_2	Br	H	OMe	Range
(salen)Al					
Al-O_1	1.893	1.912	1.927	1.929	0.036
Al-O_2	1.900	1.900	1.905	1.904	0.005
O_1-C_1	1.302	1.295	1.289	1.291	0.013
O_2-C_1	1.744	1.769	1.801	1.784	0.057
L^XZn					
Zn-O_1	2.245	2.283	2.291	2.285	0.046
Zn-O_2	2.061	2.067	2.065	2.076	0.015
O_1-C_1	1.255	1.253	1.252	1.252	0.003
O_2-C_1	1.874	1.870	1.876	1.879	0.009

[a]Bond labels refer to structures in Figure 2.10 (a) and 2.10 (b), respectively. Data for Al bonds from reference 68.

2.4 Concluding Remarks

In this collaborative work, we prepared and characterized a series of complexes **2.2** akin to previously reported efficient ROP catalysts,[30] but here featuring *para* substituents with variable electronic influences. We found that pre-conditioning the L^XZnEt complexes with BnOH yielded putative alkoxide species (**2.2'**) that gave fast and reproducible rates of ROP of *rac*-LA ($p > 95\%$ in 6–10 min, depending on the catalyst used). Analysis of kinetic data acquired using *in situ* React-IR revealed a pseudo-first order rate expression, while analysis of NMR data indicated formation of polymer enriched in isotactic sequences. In contrast to previous work on Al systems which showed that variation of the electronic influences of *para* phenolate substituents has a significant effect on ROP rate,[67,68] the effects were found to be significantly attenuated for the Zn catalysts studied herein. DFT calculations shed important light on the reasons for the moderate isotacticity and the lack of sensitivity of the ROP rate on the nature of *para* substituents X. Key findings were 1) the ring-opening TS, TS4-5, is rate-determining, and its energy is significantly different for opening the *R,R*- and *S,S*-isomers of LA as a result of multiple steric interactions, thus helping to explain the observed isotacticity of the product polymer, and 2) the attenuated effect of *para* substituent variation is reproduced, and attributed to lesser charge variation at Zn and small differences in key interatomic distances in the transition state structures relative to those seen for Al systems.

2.5 Experimental

2.5.1 *General Considerations*

All air- and water-sensitive reactions were performed under inert atmosphere using standard Schlenk techniques. All chemicals were purchased from Sigma-Aldrich and used as received unless otherwise noted. Tetrahydrofuran (THF), diethyl ether, and toluene were each freeze-pump-thawed, dried over sodium metal and benzophenone, and vacuum distilled onto 3 Å activated molecular sieves where they were stored prior to use. Dichloromethane (CH_2Cl_2) was dried with an alumina column followed by calcium hydride (CaH_2) and vacuum distilled onto 3 Å activated molecular sieves where it was stored prior to use. Pentane was dried with an alumina column and stored over 3 Å activated molecular sieves prior to use. Deuterated solvents were purchased from Cambridge Isotope Laboratories, Inc., dried over CaH_2 and vacuum distilled onto activated 3 Å molecular sieves where they were stored prior to use. *rac*-LA was purchased from Sigma-Aldrich and sublimed three times prior to use. NMR spectra were obtained on either a Bruker Avance AV-500, a Bruker Avance HD-500, or a Bruker Avance AX-400 spectrometer. NMR chemical shifts (δ) are reported as parts per million (ppm) and coupling constants (*J*) in Hertz (Hz). ^{1}H NMR spectra are referenced to the residual solvent peak at $\delta = 7.26$ for

CDCl$_3$, δ = 5.32 for CD$_2$Cl$_2$, or δ = 2.50 for DMSO-*d*$_6$. ^{13}C NMR spectra are referenced to the residual solvent peak at δ = 77.23 for CDCl$_3$ or δ = 39.52 for DMSO-*d*$_6$. Molecular weights (M_n and M_w) and polydispersity (*Đ*) of the PLA samples were determined in THF at 25 °C with a flow rate of 1 mL/min on an Agilent 1260 Infinity HPLC with Waters Styragel (HR6, HR4, and HR1) columns connected to a Wyatt DAWN Heleos II light scattering detector and a Wyatt OPTILAB T-rEX refractive index detector. X-ray diffraction measurements were collected with Cu Kα radiation and a Bruker D8 Photon II CPAD diffractometer using normal parabolic mirrors as monochromators. Elemental analysis was performed by Roberson Microlit Laboratories. 4-bromo-2-(bromomethyl)-6-(*tert*-butyl)phenol (**4b**),[112] 3-(*tert*-butyl)-2-hydroxy-5-nitrobenzaldehyde,[113] 3-(*tert*-butyl)-2-hydroxy-5-methoxybenzaldehyde,[114] and N^1,N^2-dimethyl-N^1-(pyridin-2-ylmethyl)ethane-1,2-diamine[30] were synthesized according to published procedures.

2.5.2 *Synthetic Procedures*

Scheme 2.1. Synthesis of precursors, **2.2** complexes and **2.2'** catalysts.

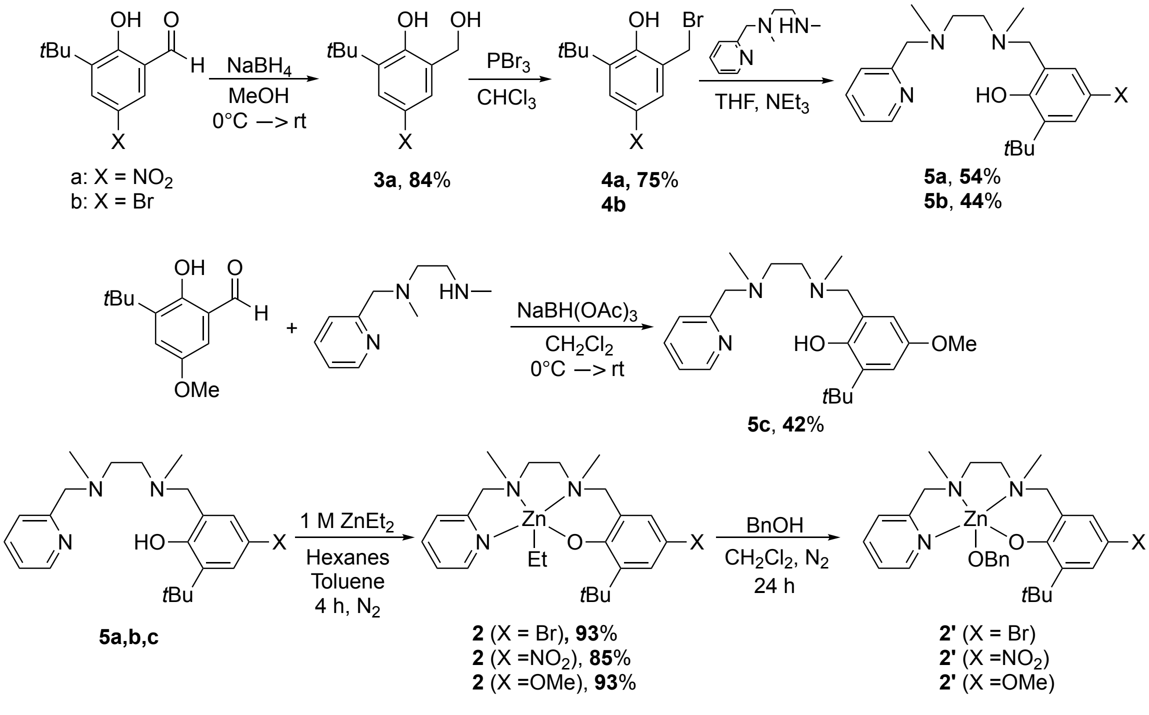

Synthesis of 2-(*tert*-butyl)-6-(hydroxymethyl)-4-nitrophenol (3a). A 100 mL round bottom flask was charged with 590 mg (2.64 mmol) 3-(*tert*-butyl)-2-hydroxy-5-nitrobenzaldehyde, dissolved in 50 mL MeOH, and chilled to 0 °C. With vigorous stirring, 353 mg (9.33 mmol) $NaBH_4$ dissolved in 10 mL MeOH was added slowly, then warmed to room temperature and stirred for 24 h. The solvent was removed under reduced pressure to yield a yellow, oily residue, to which ~5 mL H_2O and ~2 mL glacial acetic acid was added. The product was extracted with CH_2Cl_2 (3 x 50 mL), dried over Na_2SO_4, and the solvent removed under reduced pressure to yield 501 mg (84%) crude **3a**, which was used without further purification to synthesize **4a**. ^1H NMR (400 MHz, $CDCl_3$, δ): 8.17 (d, *J* = 2.8 Hz, 1H, Ar-*H*), 7.84 (d, *J* = 2.8 Hz, 1H, Ar-*H*), 4.98 (s, 2H, Ar-*CH*$_2$-OH), 2.11 (s, 9H, Ar-*tBu*). ^{13}C NMR (125 MHz, $CDCl_3$, d): 161.92, 140.21 138.72, 124.36, 123.36, 121.78, 65.24, 35.30, 29.31. HRMS (ESI/Q-TOF) *m*/*z*: $[M+Na]^+$ Calcd. for $C_{11}H_{15}NO_4Na$, 248.0899; found, 248.0890.

Synthesis of 2-(bromomethyl)-6-(*tert*-butyl)-4-nitrophenol (4a). A 100 mL round bottom flask was charged with 500 mg (2.22 mmol) **3a**, which was dissolved in 15 mL $CHCl_3$, chilled to 0 °C, and placed under N_2. Using an N_2 purged syringe, 0.3 mL (2.22 mmol) PBr_3 was added dropwise with stirring. The reaction was allowed to warm to room temperature and stirred for 18 h followed by addition of ~ 10 mL cold H_2O with vigorous stirring. The product was extracted with $CHCl_3$ (3 x 25 mL), dried over Na_2SO_4, and the solvent removed under reduced pressure to yield 481 mg (75%) crude **4a**. ^1H NMR spectroscopy indicated the compound was present, but with unknown impurities. The crude material was used in the next synthetic step without further purification. ^1H NMR (500 MHz, $CDCl_3$, δ): 8.23 (d, *J* = 2.7 Hz, 1H, Ar-*H*), 8.08 (d, *J* = 2.7 Hz, 1H, Ar-*H*), 4.56 (s, 2H, Ar-C*H*$_2$-Br), 1.46 (s, 1H, Ar-*tBu*).

Synthesis of 2-(*tert*-butyl)-6-((methyl(2-(methyl(pyridin-2-ylmethyl)amino)ethyl)amino)methyl)-4-nitrophenol (5a). A 100 mL round bottom flask was charged with 484 mg (1.67 mmol) **4a**, which was dissolved in 25 mL THF. To this stirring mixture, 301 mg (1.67 mmol) N^1,N^2-dimethyl-N^1-(pyridin-2-ylmethyl)ethane-1,2-diamine dissolved in 5 mL THF and 0.9 mL NEt_3 was added dropwise. The reaction was stirred for 2 h then filtered through Celite and the solvent removed under reduced pressure to yield a dark yellow oil. The crude product was re-dissolved in CH_2Cl_2, passed through a 0.5" neutral alumina plug and finally purified by flash chromatography (5% MeOH in CH_2Cl_2) to yield 348 mg (54%) pure **5b** as a yellow oil. ^{1}H NMR (500 MHz, $CDCl_3$, δ): 8.53 (d, *J* = 5.5 Hz, 1H, Py-*H*), 8.13 (s, 1H, Ar-*H*), 7.80 (s, 1H, Ar-*H*), 7.63 (t, *J* = 7.6 Hz, 1H, Py-*H*), 7.56 (d, *J* = 7.6 Hz, 1H, Py-*H*), 7.17 (t, *J* = 5.5 Hz, 1H, Py-*H*), 3.76 (s, 2H, Py-*CH₂*-N), 3.73 (s, 2H, Ar-*CH₂*-N), 2.70 (s, 4H, N-*CH₂*-*CH₂*-N), 2.28 (s, 6H, N-*CH₃* x2), 1.43 (s, 9H, Ar-*tBu*). ^{13}C NMR (125 MHz, $CDCl_3$, □): 164.03, 148.99, 139.14, 137.51, 136.55, 123.32, 122.78, 122.58, 121.93, 64.20, 60.66, 54.31, 53.89, 42.25, 41.24, 35.02, 29.07. HRMS (ESI/Q-TOF) *m*/*z*: $[M+H]^+$ Calcd. for $C_{21}H_{31}N_4O_3$, 387.2396; found, 387.2423.

Synthesis of 2.2 (X = NO_2). A 50 mL Schlenk flask was charged with 292 mg (0.75 mmol) **5a**, pump/purged with N_2 three times, and dissolved in 5 mL dry toluene. Using an N_2 purged syringe, 0.75 mL $ZnEt_2$ (1 M in hexanes) was added dropwise then allowed to stir at room temperature for 2 h. The solvent was removed under reduced pressure and the flask transferred to a nitrogen glovebox. The residual solids were dissolved in minimal toluene, transferred to a 20 mL vial, layered with diethyl ether, and cooled to –20 °C for 48 h. The resulting yellow precipitate was collected on a medium frit and dried under vacuum to yield 309 mg (85%) pure **2** (X = NO_2). ^{1}H NMR (500 MHz, $CDCl_3$, δ): 8.88 (1 H, s, Py-

H), 8.12 (s, 1H, Ar-*H*), 7.86 (s, 1H, Ar-*H*), 7.82 (t, *J* = 7.2 Hz, 1H, Py-*H*), 7.42 (t, *J* = 7.2 Hz, 1H, Py-*H*), 7.30 (d, *J* = 7.3 Hz, 1H, Py-*H*), 4.23 (d, *J* = 14.4 Hz, 1H, Py-C*H*$_2$-N), 4.09 (d, *J* = 10.2 Hz, 1H, Ar-C*H*$_2$-N), 3.71 (d, *J* = 14.4 Hz, 1H, Py-C*H*$_2$-N), 3.12 (m, 2H, N-C*H*$_2$-CH$_2$-N), 2.90 (d, *J* = 10.2 Hz, 1H, Ar-C*H*$_2$-N), 2.82 (m, 2H, N-CH$_2$-C*H*$_2$-N), 2.36 (s, 3H, N-C*H*$_3$), 2.24 (s, 3H, N-C*H*$_3$), 1.39 (s, 9H, Ar-*tBu*), 1.01 (t, *J* = 10.4 Hz, 3H, Zn-CH$_2$-C*H*$_3$), -0.13 (q, *J* = 10.4 Hz, 2H, Zn-C*H*$_2$-CH$_3$). ^{13}C NMR (125 MHz, CDCl$_3$, δ): 176.24, 149.72, 149.63, 139.19, 138.61, 133.14, 126.50, 124.14, 123.84, 123.01, 117.47, 62.60, 60.83, 55.92, 54.71, 44.06, 43.94, 35.15, 29.32, 13.70, –2.30. HRMS (ESI/Q-TOF) *m*/*z*: [M-Et]$^+$ Calcd. for $C_{21}H_{29}N_4O_3Zn$, 449.1531; found, 449.1540. Anal. Calcd for $C_{23}H_{34}N_4O_3Zn$: C, 57.56; H, 7.14; N, 11.67. Found: C, 57.32; H, 7.29; N, 11.29.

Synthesis of 4-bromo-2-(*tert*-butyl)-6-((methyl(2-(methyl(pyridin-2-ylmethyl)amino)ethyl)amino)methyl)phenol (5b). A 100 mL round bottom flask was charged with 400 mg (1.24 mmol) **4b** and dissolved in 20 mL THF. To this stirring mixture, 224 mg (1.24 mmol) N^1,N^2-dimethyl-N^1-(pyridin-2-ylmethyl)ethane-1,2-diamine dissolved in 5 mL THF and 0.8 mL NEt$_3$ was added dropwise. The reaction was stirred for 2 h then filtered through Celite and the solvent removed under reduced pressure to yield a yellow oil. The crude product was re-dissolved in CH$_2$Cl$_2$, passed through a 0.5” neutral alumina plug and finally purified by flash chromatography (75% EtOAc, 25% Hexanes, neutral alumina) to yield 226 mg (43%) pure **5b** as a pale yellow oil. ^{1}H NMR (500 MHz, DMSO-*d*$_6$, δ): 8.45 (d, *J* = 5.5 Hz, 1H, Py-*H*), 7.68 (t, *J* = 7.6 Hz, 1H, Py-*H*), 7.56 (d, *J* = 7.6 Hz, 1H, Py-*H*), 7.24 (t, *J* = 5.5 Hz, 1H, Py-*H*), 7.14 (s, 1H, Ar-*H*), 7.07 (s, 1H, Ar-*H*), 3.69 (s, 2H, Py-*CH*$_2$-N), 3.63 (s, 2H, Ar-*CH*$_2$-N), 3.34 (bs, 1H, Ar-*OH*), 2.59 (m, 4H, N-*CH*$_2$-*CH*$_2$-N), 2.18 (s, 3H, N-*CH*$_3$), 2.15 (s, 3H, N-*CH*$_3$), 1.33 (s, 9H, Ar-*tBu*). ^{13}C NMR (125 MHz, DMSO-*d*$_6$, δ): 159.61, 156.54, 149.04, 138.51, 136.71, 129.35, 128.24, 125.40, 123.13, 122.53, 109.74, 64.08, 60.08, 42.26, 42.09, 34.95, 29.46. HRMS (ESI/Q-TOF) m/z: [M+H]$^+$ Calcd. for $C_{21}H_{31}BrN_3O$, 420.1651; found, 420.1675.

Synthesis of 2.2 (X = Br). Inside a nitrogen filled glovebox, a sample of 214 mg (0.51 mmol) **5b** was added to a 20 mL vial and dissolved in 3 mL dry toluene. Using a syringe, 0.52 mL $ZnEt_2$ (1 M in hexanes) was added dropwise with stirring. The reaction was capped with a plastic screw cap, stirred for 2 h at room temperature, and the solvent was removed under reduced pressure to yield 243 mg (93%) **2** (X = Br). X-ray quality crystals were collected from the recrystallization of **2** (X = Br) in toluene layered with pentane at –40 °C. ^{1}H NMR (500 MHz, $CDCl_3$, δ): 8.81 (d, *J* = 4.3 Hz, 1H, Py-*H*), 7.75 (t, *J* = 7.7 Hz, 1H, Py-*H*), 7.35 (m, 2H, Py-*H*), 7.19 (d, *J* = 2.0 Hz, 1H, Ar-*H*), 6.91 (d, *J* = 2.0 Hz, 1H, Ar-*H*), 4.33 (d, *J* = 10.0 Hz, 1H, Py-CH_2-N), 4.21 (bs, 1H, N-CH_2-CH_2-N), 3.65 (d, *J* = 10.0 Hz, 1H, Py-CH_2-N), 3.24 (bs, 1H, Ar-CH_2-N), 2.73 (m, 3H, N-CH_2-CH_2-N, N-CH_2-CH_2-N,), 2.62 (bs, 1H, Ar-CH_2-N), 2.30 (s, 3H, N-CH_3), 2.23 (s, 3H, N-CH_3), 1.39 (s, 9H, Ar-*tBu*), 0.96 (t, *J* = 7.3 Hz, 3H, Zn-CH_2-CH_3), -0.20 (m, 2H, Zn-CH_2-CH_3). ^{13}C NMR (125 MHz, $CDCl_3$, δ): 149.39, 141.24, 137.80, 136.74, 135.39, 130.97, 130.75, 129.15, 123.27. 122.91, 103.23, 63.18, 59.90, 55.22, 55.15, 44.09, 43.28, 35.13, 29.37, 13.60, –2.55. HRMS (ESI/Q-TOF) *m*/*z*: [M-Et]$^+$ Calcd. for $C_{21}H_{29}BrN_3OZn$, 482.0785; found, 482.0794. Anal. Calcd for $C_{23}H_{34}BrN_3OZn$: C, 53.76; H, 6.67; N, 8.18. Found C, 53.71; H, 6.60; N, 7.95.

Synthesis of 2-(*tert*-butyl)-4-methoxy-6-((methyl(2-(methyl(pyridin-2-ylmethyl)amino)ethyl)amino)methyl)phenol (5c). A 250 mL round bottom flask was charged with 1.00 g (4.80 mmol) of 3-(*tert*-butyl)-2-hydroxy-5-methoxybenzaldehyde dissolved in 20 mL CH_2Cl_2. To this, 861 mg (4.80 mmol) N^1,N^2-dimethyl-N^1-(pyridin-2-ylmethyl)ethane-1,2-diamine dissolved in 40 mL CH_2Cl_2 was added. After stirring for 2 hours, the reaction mixture was brought to 0 °C and 1.32 g (6.24 mmol) sodium triacetoxyborohydride was added. The reaction was stirred for 4 h and then quenched with $NaHCO_3$. The product was extracted with CH_2Cl_2 (3 x 50 mL) and the solvent was removed under reduced pressure to yield a dark brown oil. The crude product was re-dissolved in CH_2Cl_2, passed through a 0.5" neutral alumina plug and finally purified by flash chromatography (gradient, 100% CH_2Cl_2 to 10% EtOAc in CH_2Cl_2, SiO_2) to yield 748 mg (42%) pure **5c.** ^{1}H NMR (500 MHz, $CDCl_3$ δ): 8.59 (ddd, *J* = 4.9, 1.8, 0.8 Hz, 1H, Py-*H*), 7.73 (td, *J* = 7.8, 1.6 Hz, 1H, Py-*H*), 7.38 (dt, *J* = 7.8, 0.8 Hz, 1H, Py-*H*), 7.33 (ddd, *J* = 7.8, 4.9, 1.3 Hz, 1H, Py-*H*), 6.80 (d, *J* = 3.0 Hz, 1H, Ar-*H*), 6.42 (d, *J* = 3.0 Hz, 1H, Ar-*H*), 4.13 (d, *J* = 13.5 Hz, 1H, Py-CH_2-N), 4.05 (d, *J* = 13.5 Hz, 1H, Py-CH_2-N), 3.75 (s, 3H, OCH_3), 3.74 (app s, 1H, Ar-CH_2- N), 3.70 (d, *J* = 13.5 Hz, 1H, Ar-CH_2-N), 3.06 (m, 4H, N-CH_2-CH_2-N), 2.65 (s, 3H, N-CH_3), 2.37 (s, 3H, N-CH_3), 1.35 (s, 9H, Ar-*tBu*). ^{13}C NMR (125 MHz, $CDCl_3$, δ): 151.98, 150.87, 150.36, 149.95, 138.04, 137.03, 127.17, 124.21, 122.03, 113.16, 111.26, 64.61, 62.39, 57.38, 55.80, 50.19, 48.81, 42.12, 34.92, 29.49. HRMS (ESI/Q-TOF) m/z: $[M+H]^+$ Calcd. for $C_{22}H_{34}N_3O_2$, 372.2651; found, 372.2659.

Synthesis of 2.2 (X = OMe). Inside a nitrogen filled glovebox, a sample of 104 mg (0.279 mmol) **5b** was added to a 20 mL vial and dissolved in 3 mL dry toluene. Using a syringe, 0.56 mL $ZnEt_2$ (1 M in hexanes) was added dropwise with stirring. The reaction was capped with a plastic screw cap, stirred for 2 h at room temperature, and the solvent was removed under reduced pressure to yield 120 mg (93%) **2** (X = OMe) which was recrystallized from toluene layered with pentane at –40 °C. ^{1}H NMR (500 MHz, CD_2Cl_2, δ): 8.75 (d, *J* = 3.7 Hz, 1H, Py-*H*), 7.77 (t, *J* = 6.7 Hz, 1H, Py-*H*), 7.40 (bs, 1H, Py-*H*), 7.34 (t, *J* = 4.0 Hz, 1H, Py-*H*), 6.74 (d, *J* = 2.0 Hz, 1H, Ar-*H*), 6.43 (d, *J* = 2.0 Hz, 1H, Ar-*H*), 4.34 (bs, 1H, Ar-CH_2-N), 4.21 (bs, 1H, Py-CH_2-N), 3.69 (s, 3H, OCH_3), 3.35 (bs, 1H, N-

C*H*$_2$-CH$_2$-N), 2.86 (bs, 1H, N-CH$_2$-C*H*$_2$-N), 2.70 (app bs, 3H, Ar-C*H*$_2$-N, Py-C*H*$_2$-N, N-C*H*$_2$-CH$_2$-N), 2.56 (bs, 1H, N-CH$_2$-C*H*$_2$-N), 2.27 (s, 3H, N-C*H*$_3$), 2.24 (s, 3H, N-C*H*$_3$), 1.37 (s, 9H, Ar-*tBu*), 0.97 (t, *J* = 7.2 Hz, 3H, Zn-CH$_2$-C*H*$_3$), -0.22 (m, 2H, Zn-C*H*$_2$-CH$_3$). ^{13}C NMR (125 MHz, CD$_2$Cl$_2$, δ): 161.83, 155.43, 149.71, 147.69, 139.56, 138.10, 124.89, 123.66, 123.50, 113.94, 113.94, 64.14, 60.42, 56.47, 56.01, 55.57, 44.63, 43.23, 35.50, 29.83, 14.05, –2.15. HRMS (ESI/Q-TOF) *m*/*z*: [M-Et]$^+$ Calcd. for $C_{22}H_{32}N_3O_2Zn$, 434.1786; found, 434.1809. Anal. Calcd for $C_{24}H_{37}N_3O_2Zn$: C, 62.00; H, 8.02; N, 9.04. Found: C, 60.16; H, 7.66; N, 8.77. Two separate attempts for elemental analysis resulted in percentage matches for hydrogen and nitrogen atoms, but both attempts yielded slightly lower percentages for carbon atoms than calculated. This is likely due to incomplete combustion during the experiment, as the high purity of the complex was confirmed via ^{1}H NMR spectroscopy and HRMS.

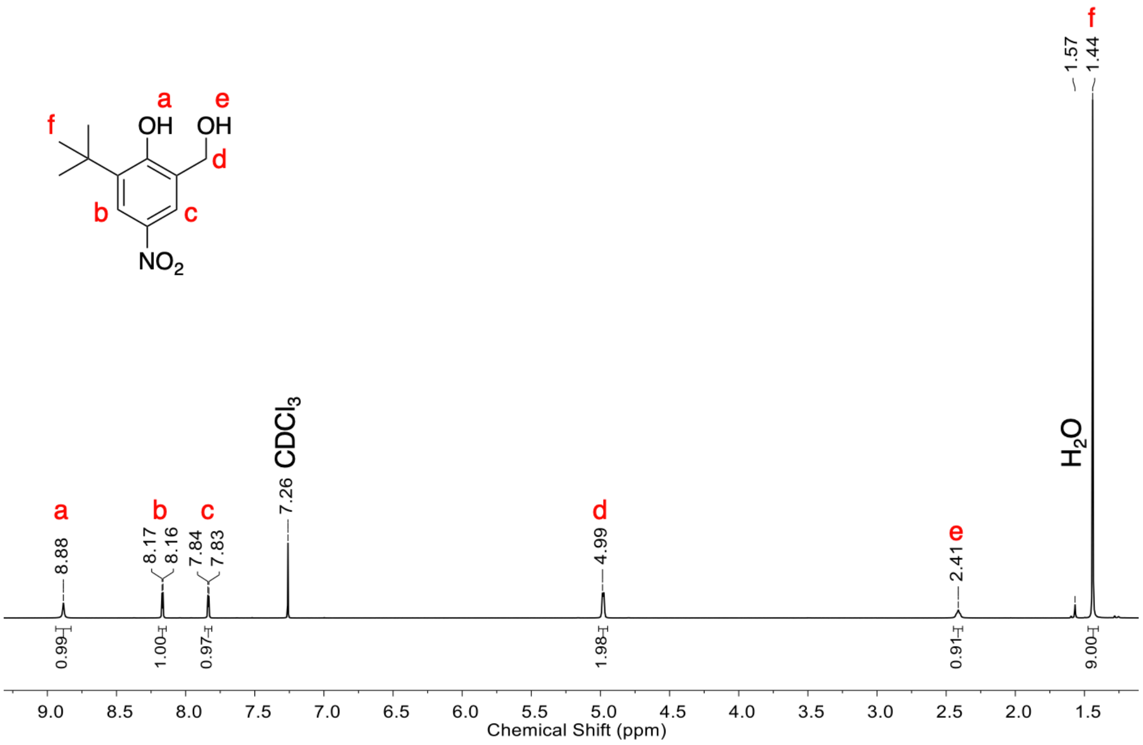

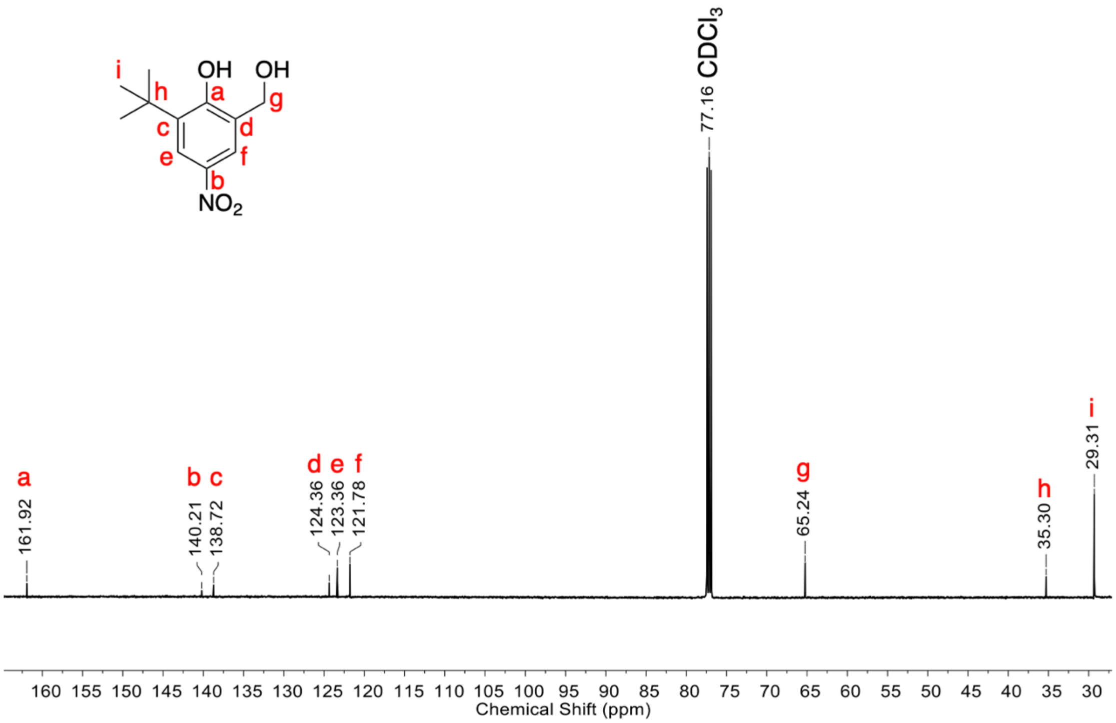

Figure 2.11. ^{1}H (top) and ^{13}C (bottom) NMR spectra of **3a**.

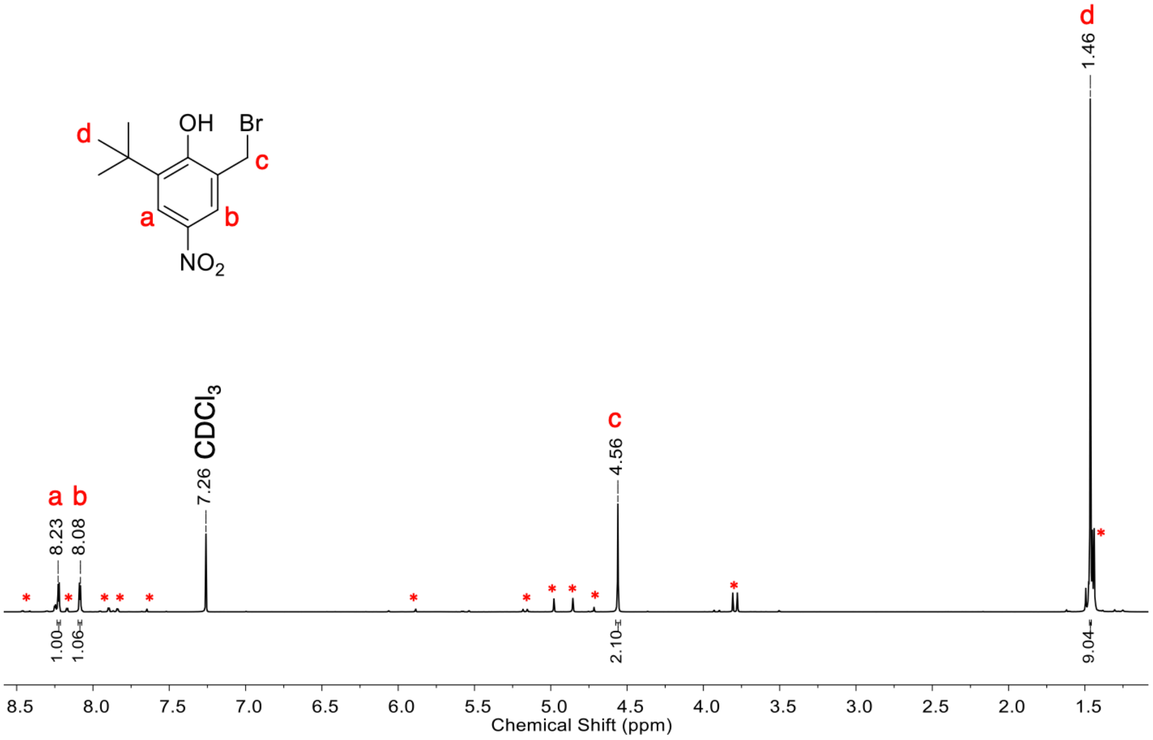

Figure 2.12. ^{1}H NMR spectrum of **4a**. Impurities are denoted by red asterisks (purification was not required before subsequent synthetic step).

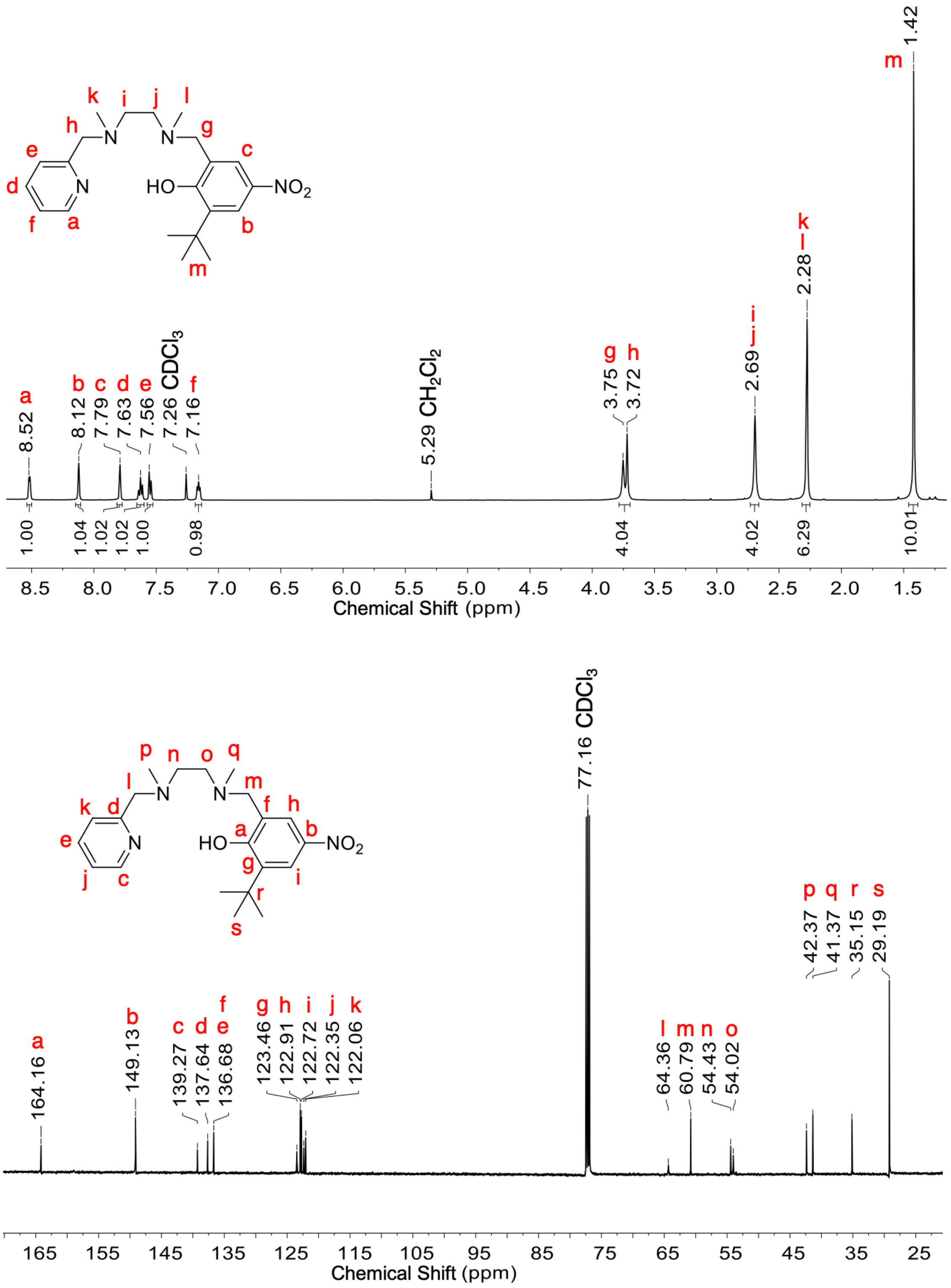

Figure 2.13. ^{1}H (top) and ^{13}C (bottom) NMR spectra of **5a**.

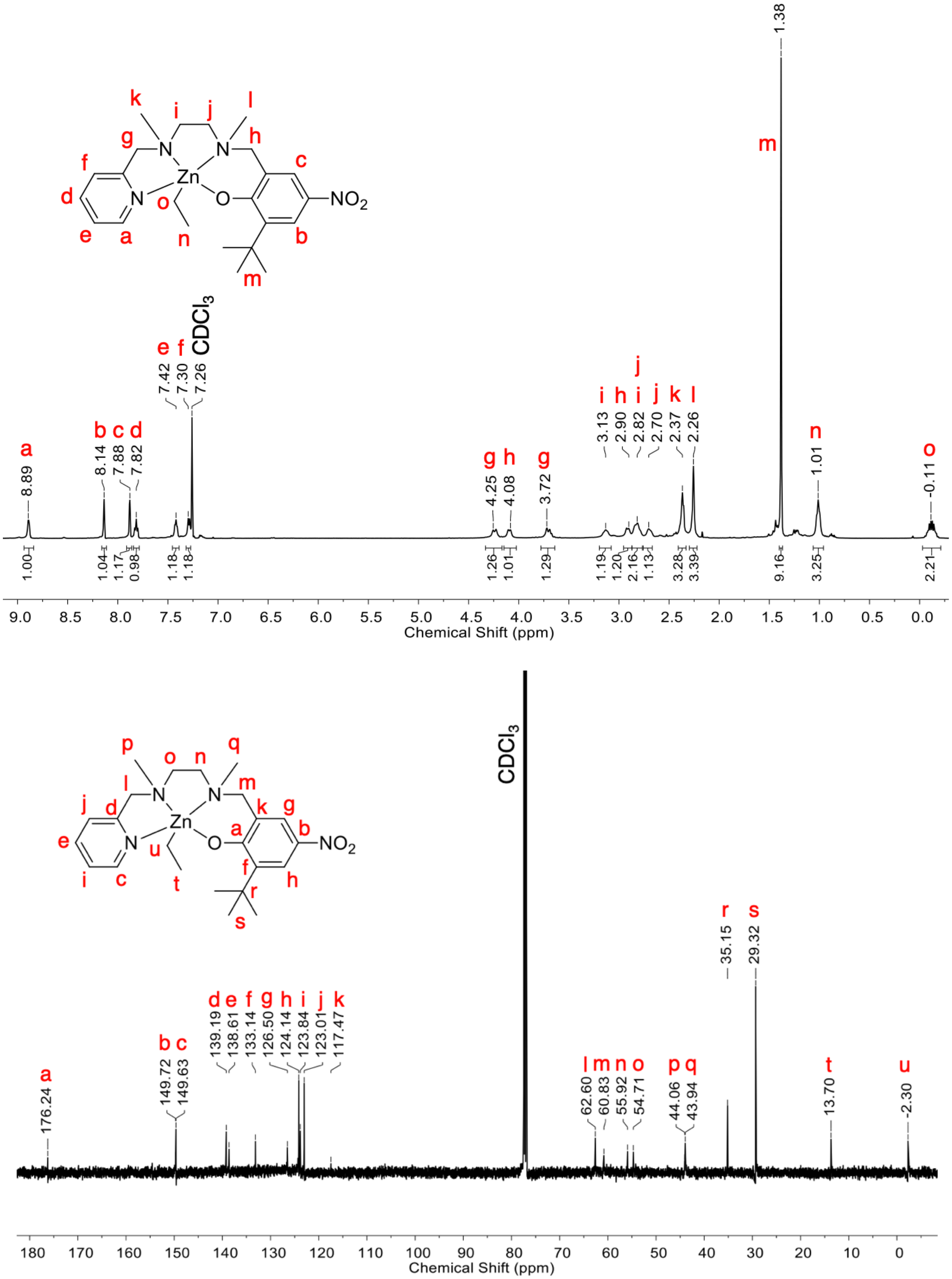

Figure 2.14. ^{1}H (top) and ^{13}C (bottom) NMR spectra of **2.2** (X = NO_2).

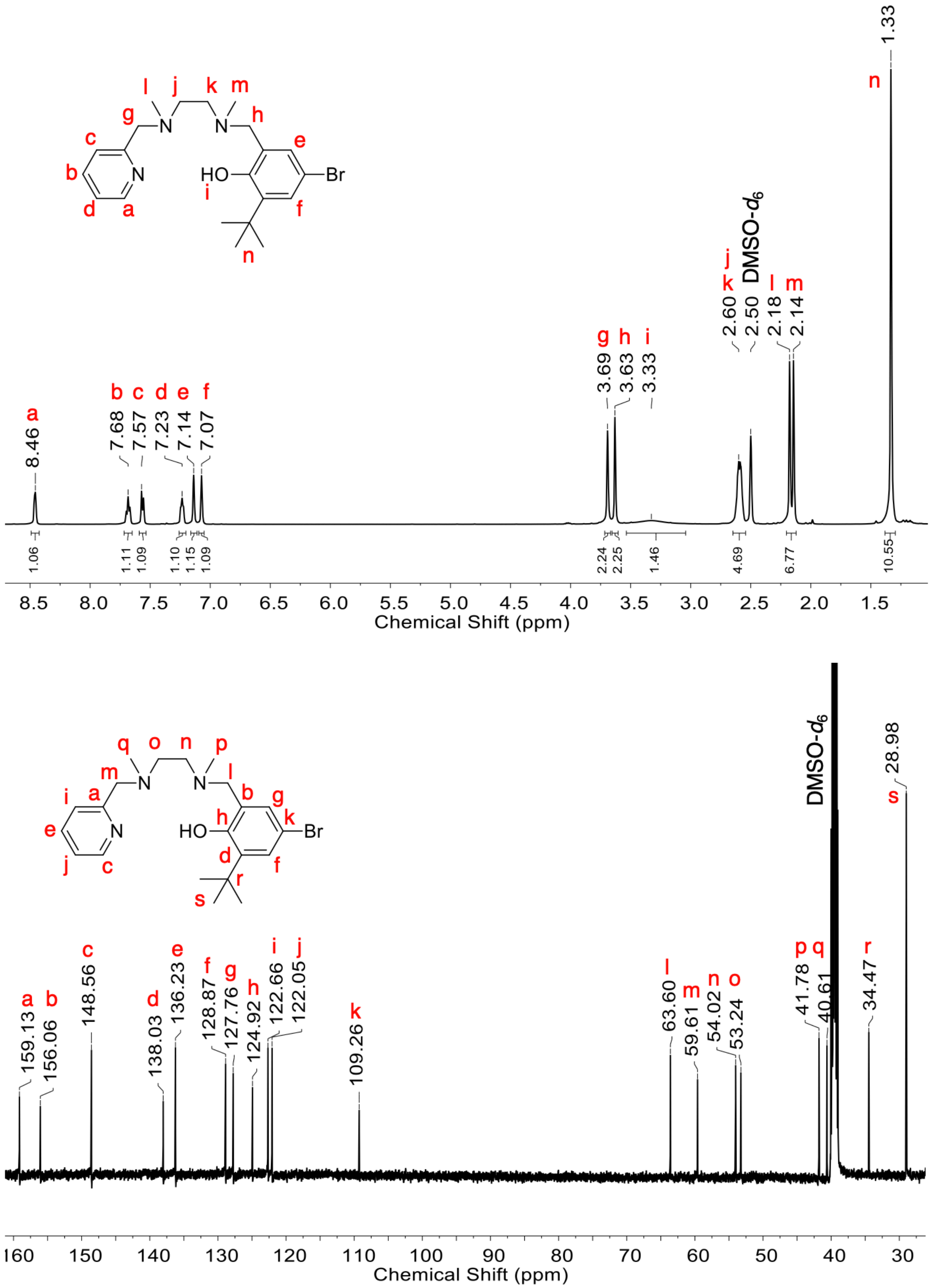

Figure 2.15. ^{1}H (top) and ^{13}C (bottom) NMR spectra of **5b**.

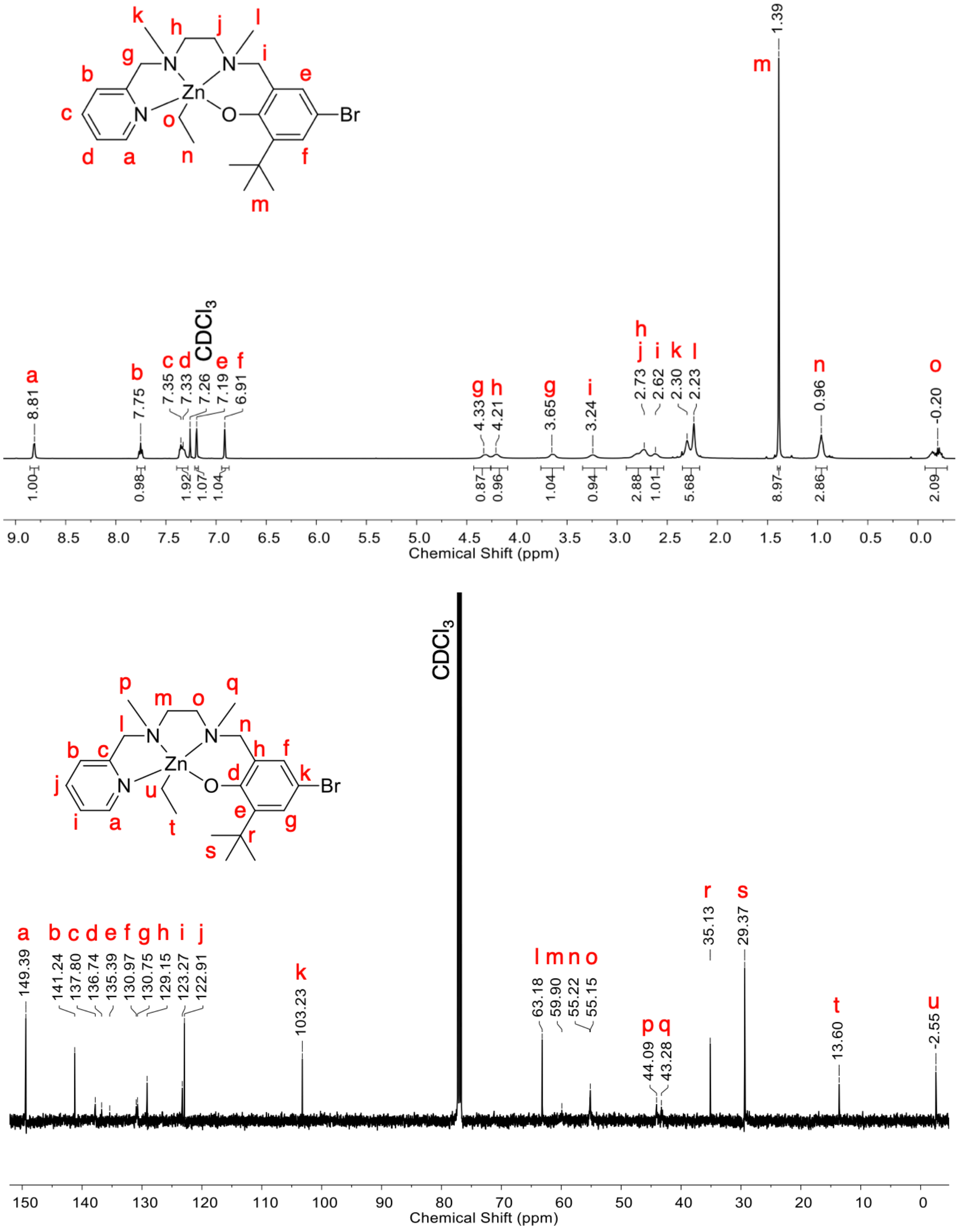

Figure 2.16. ^{1}H (top) and ^{13}C (bottom) NMR spectra of **2.2** (X = Br).

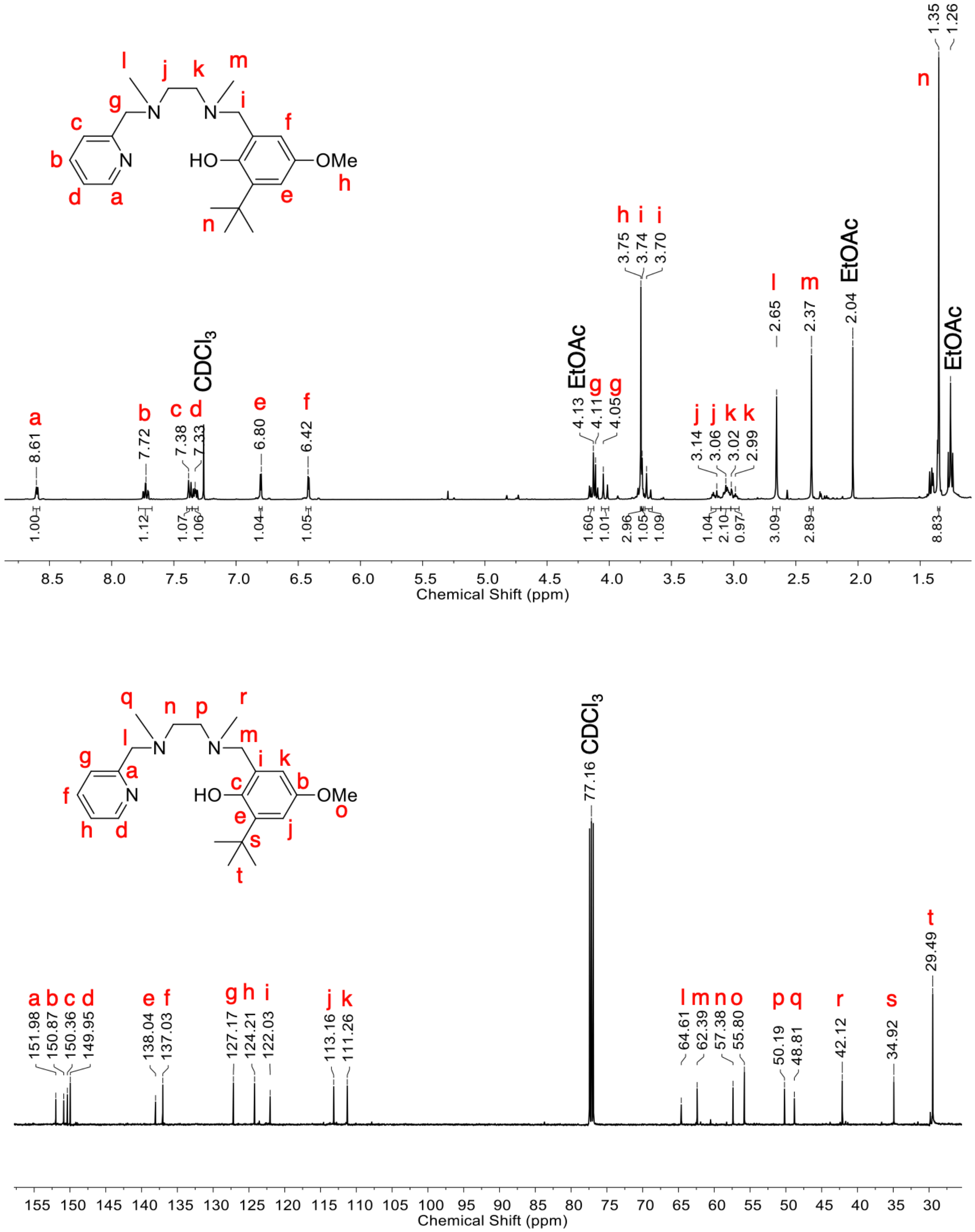

Figure 2.17. ^{1}H (top) and ^{13}C (bottom) NMR spectra of **5c**.

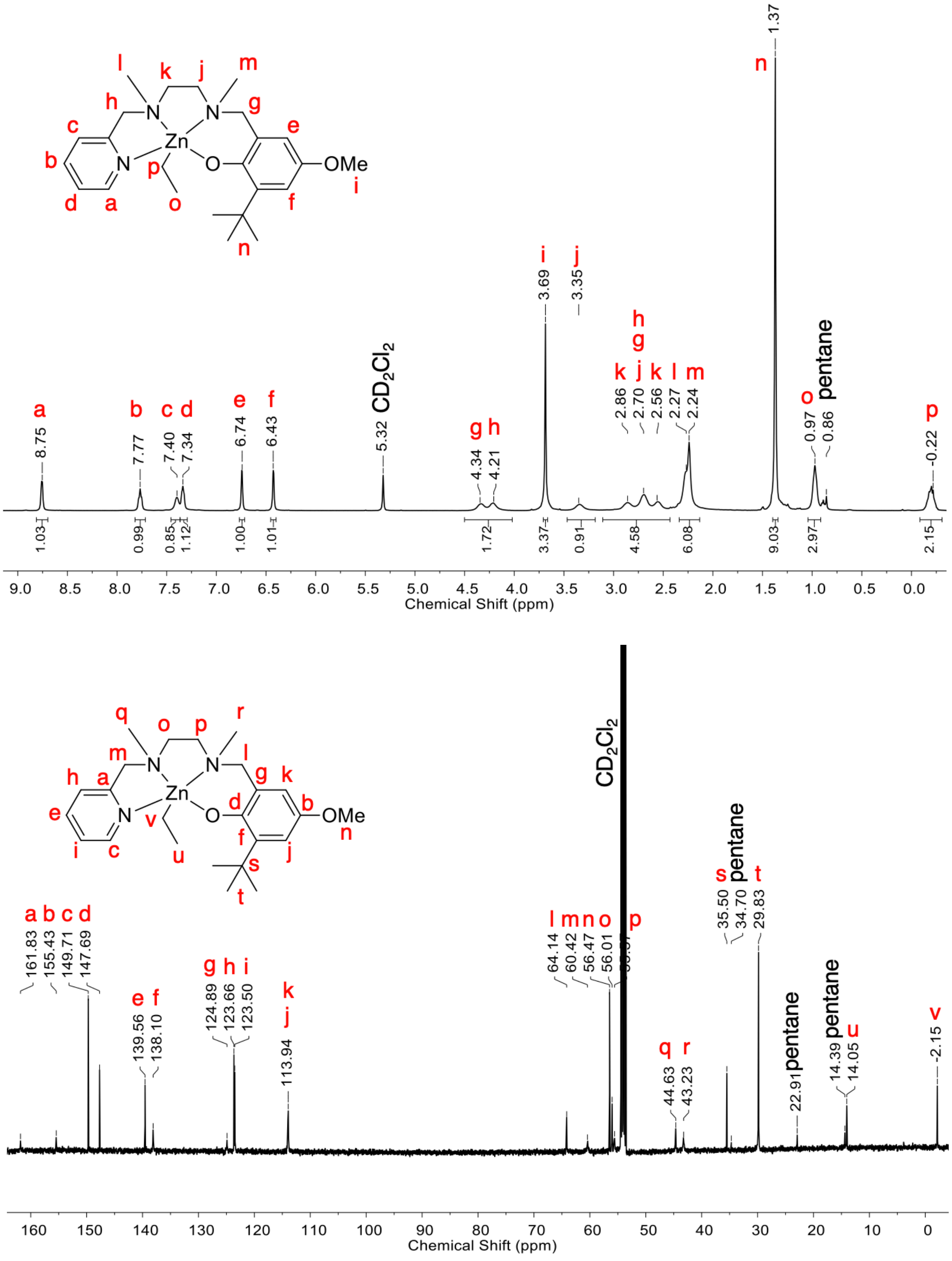

Figure 2.18. ^{1}H (top) and ^{13}C (bottom) NMR spectra of **2.2** (X = OMe).

2.5.3 *Diffusion Ordered Spectroscopy (DOSY)*

DOSY experiments were performed on a Bruker Avance AV-500 in $CDCl_3$ containing TMS as an internal standard and a linear power ramp from 2% to 95% attenuation in 16 steps. The averaged slopes of the $\ln(I/I_0)$ vs. $\gamma^2\delta^2G^2[\Delta-(\delta/3)]x10^{-10}$ (m^2 s) plots determine diffusion coefficients for **2.2** ($X = NO_2$) and **2.2'** ($X = NO_2$). Diffusion constants were then converted to hydrodynamic radii (6.22 Å for **2.2** and 6.98 Å for **2.2'**) via the Stokes-Einstein equation (Eq. 2.1).

2.5.4 *General Procedure for ^{1}H NMR Kinetic Studies*

A sample of 100 µL of 0.02 M L^XZnEt complex, 10 µL of 0.5 M internal standard (bis-*para*-trimethylsilylbenzene), and 480 µL of 1.25 M *rac*-LA (100 equiv.) in dry CD_2Cl_2 was added to an NMR tube inside a nitrogen-filled glove box and capped with a rubber septum. Then 10 µL of a 0.20 M BnOH solution (1 equiv.) in CD_2Cl_2 was taken up into an air-tight syringe and the end pressed into a rubber septum to maintain N_2 atmosphere. An initial NMR of the L^XZnEt complex and *rac*-LA was taken as a baseline for following the polymerization. The sample was removed from the spectrometer, the solution of BnOH was injected into the tube from the air-tight syringe, the tube was shaken to mix the components, and finally returned to the spectrometer to monitor the polymerization. The polymerization rate was evaluated by comparing the integration of the methine peaks of the monomer and the formed polymer to the residual signal of the internal standard in the ^{1}H NMR spectra.

2.5.5 *General Procedure for Exchange Experiments*

A sample of 500 µL of 0.02 M L^XZnEt complex and 50 µL of 0.20 M BnOH solution (1 equiv.) in dry CD_2Cl_2 were added to a 4 mL vial inside of a nitrogen-filled glovebox and stirred for 24 h. Aliquots of the stirring reaction were taken at various time points and were subjected for ^{1}H NMR analysis to monitor the exchange of the BnOH and Et substituent on the Zn center. Complete disappearance of the ethyl peaks on the ^{1}H NMR spectrum indicated full exchange had occurred.

2.5.6 *React-IR Kinetic Studies*

All solutions were prepared in freshly dried CH_2Cl_2 and all experiments were performed in triplicate. Each experiment has a target final concentration of 3.33 mM catalyst and 1 M *rac*-LA (1:300). A stock solution of 66.6 mM catalyst was prepared 24 h in advance by stirring 667 μL 0.099 mM L^XZnEt and 333 μL 0.20 M BnOH. Next, 300 μL CH_2Cl_2 was added to a 20 mL vial and used to record a new solvent spectrum for each experiment. Then 1600 μL 1.25 M *rac*-LA in CH_2Cl_2 was added and the instrument set to start recording a 16 scan spectrum from 2300 cm^{-1} to 650 cm^{-1} every 10 s. Using a gas tight syringe, 100 μL 66.6 mM (salan)L^XZnOBn was added to the reaction vial and the time of addition recorded as $t = 0$. ConcIRT analysis, a global fitting program native to the iC IR instrument software, was performed on each data set from 1900 cm^{-1} to 900 cm^{-1} to determine relative concentration of *rac*-LA and PLA.[103] Analysis using ConcIRT was validated using the standalone Olis GlobalWorks program.[104]

Normalized concentration versus time plots (Figure 2.19) assume [PLA] = 1 M at the end of the experiment and the data is normalized accordingly. Converting the same data to a calibrated concentration using the calibration curve yields a similar concentration versus time plots (Figure 2.20). Both plots were fit to a pseudo-first order rate expression with the COPASI global fitting software.[67] The rate constants determined for the normalized, calibrated, and Olis Globalworks kinetic fits are summarized in Table 2.4.

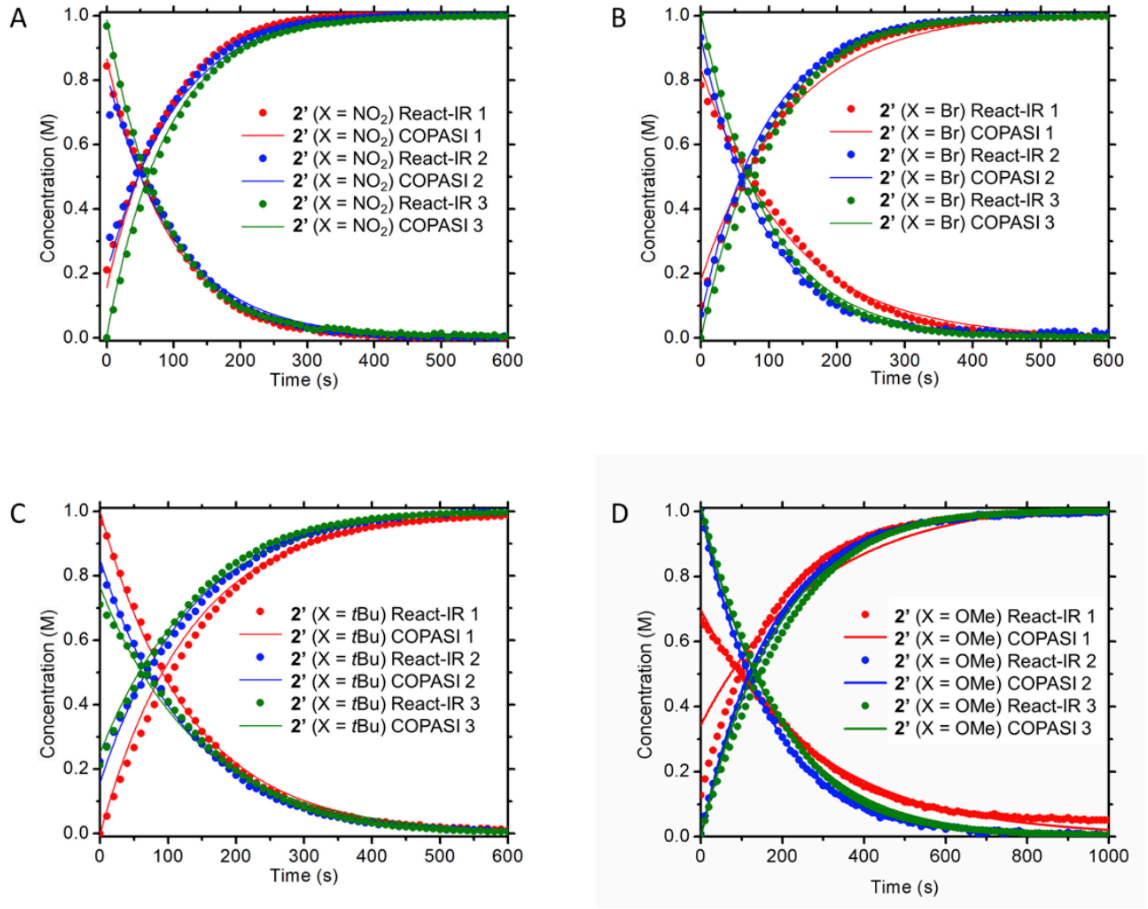

Figure 2.19. Normalized concentration versus time data and COPASI fits for (A) **2.2'** (X = NO$_2$), (B) **2.2'** (X = Br), (C) **2.2'** (X = *t*Bu), and (D) **2.2'** (X = OMe).

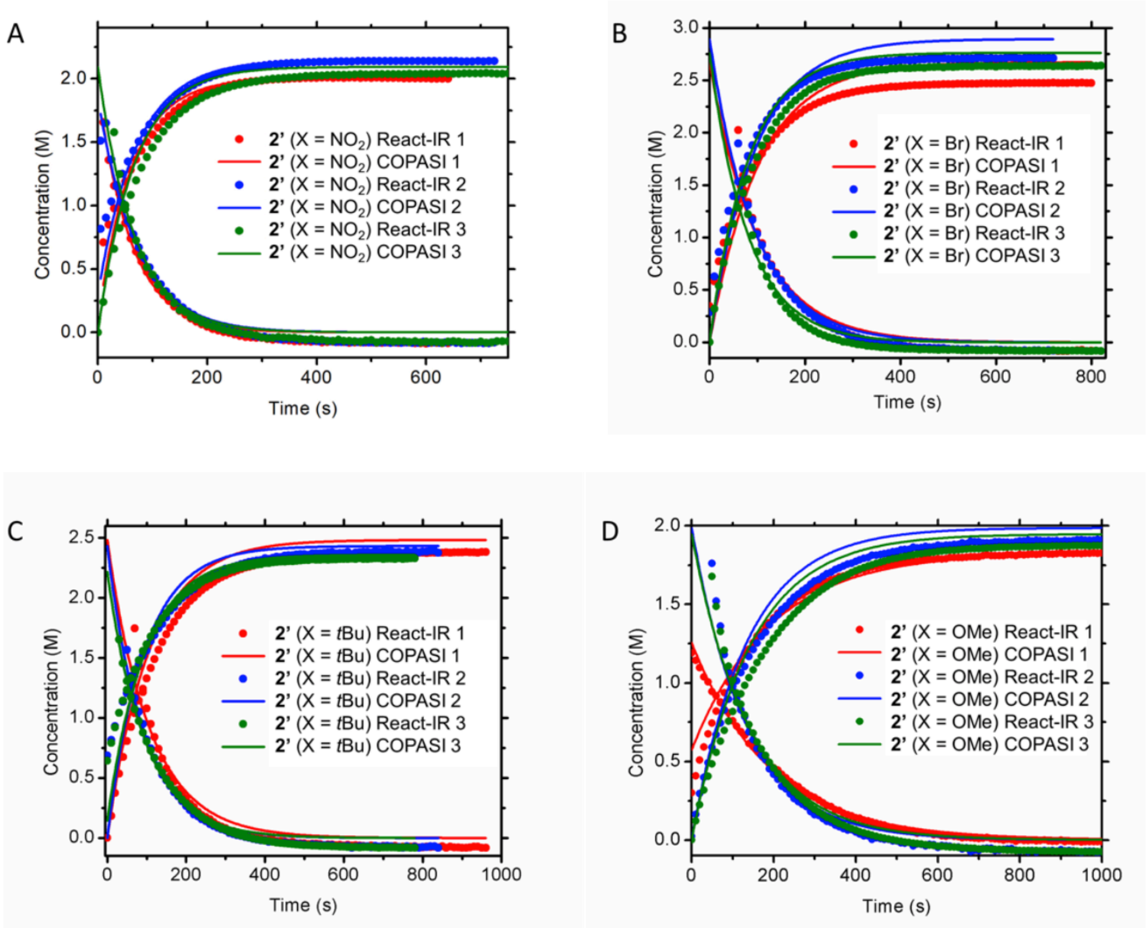

Figure 2.20. Calibrated concentration versus time data and COPASI fits for (A) **2.2'** (X = NO_2), (B) **2.2'** (X = Br), (C) **2.2'** (X = *t*Bu), and (D) **2.2'** (X = OMe).

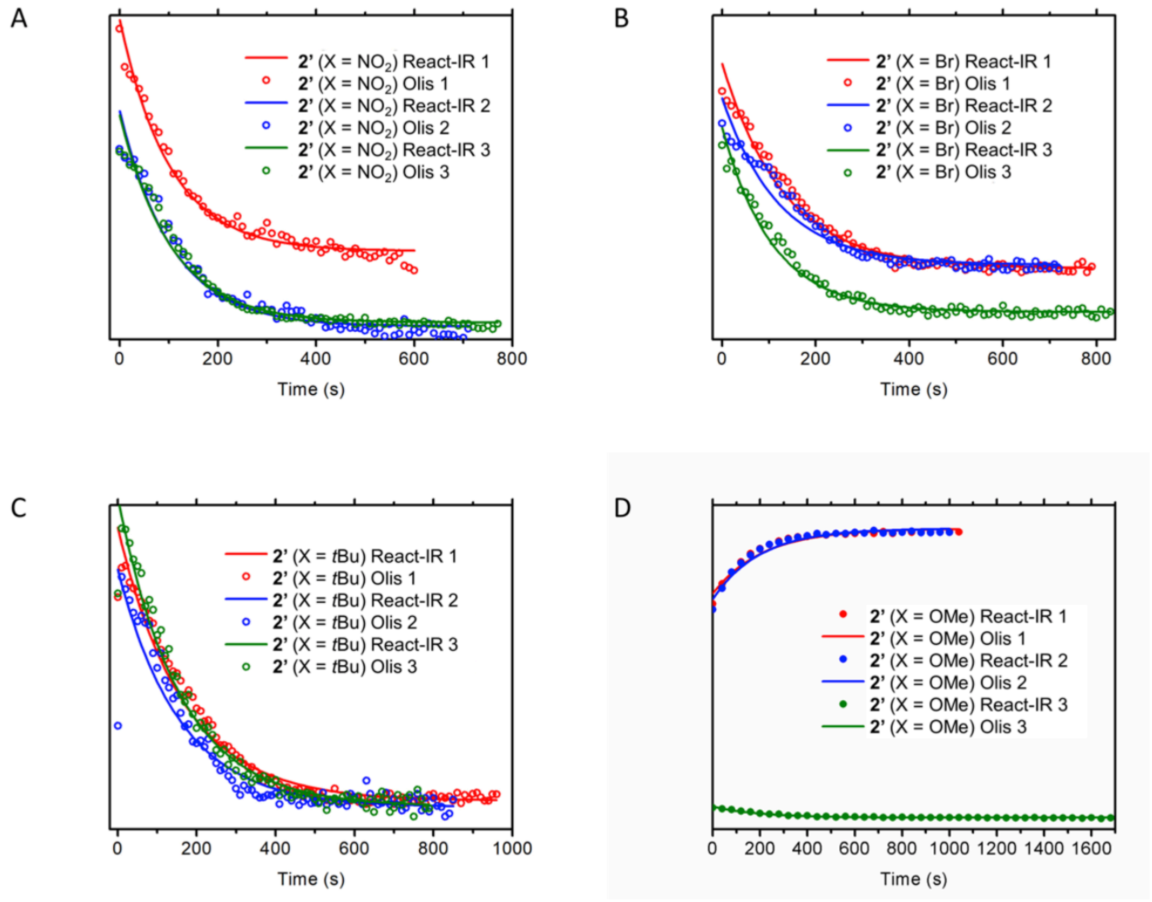

Figure 2.21. Kinetic traces from Olis Globalworks for (A) **2.2'** (X = NO_2), (B) **2.2'** (X = Br), (C) **2.2'** (X = *t*Bu), and (D) **2.2'** (X = OMe).

Table 2.4. Comparison of observed rate constants at 298 K in CH_2Cl_2 for normalized, calibrated, and Olis Globalworks spectral analysis.

Complex	k_{obs} normalized (s^{-1})	k_{obs} calibrated (s^{-1})	k_{obs} Olis (s^{-1})
2.2' (X = NO_2)	0.011(2)	0.014(1)	0.0096(3)
2.2' (X = Br)	0.009(2)	0.010(1)	0.0083(9)
2.2' (X = *t*Bu)	0.0074(4)	0.0102(8)	0.0063(1)
2.2' (X = OMe)	0.004(1)	0.006(1)	0.0048(2)

2.5.7 *Tacticity Measurements*

Tacticity of each polymer was measured by dissolving dried polymer in $CDCl_3$ and submitting the sample for homonuclear decoupled ^{1}H NMR. Using the methine region of the spectrum (5.15–5.25 ppm), the different tetrad concentrations were integrated and Bernoullian statistics (assuming CEM mechanism) were applied to determine the amount of racemic and *meso* character in the polymer.[35] For more accurate integration measurements, deconvolution of the spectra was achieved using MestReNova software.[115]

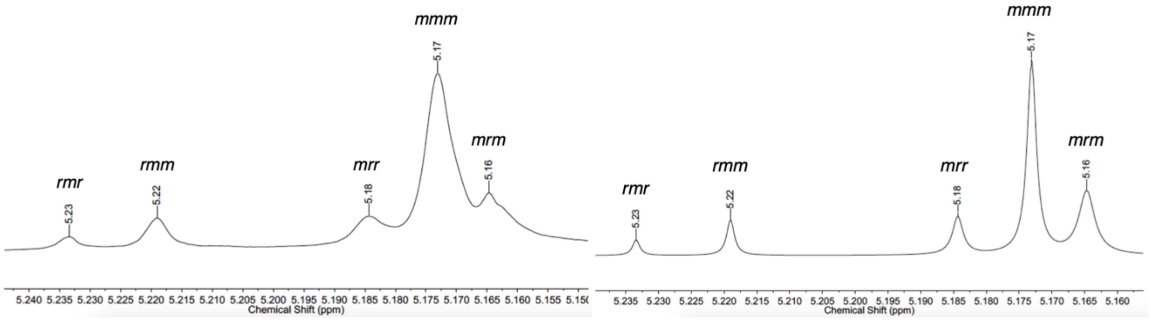

Figure 2.22. Example of the methine region of a homonuclear-decoupled ^{1}H NMR spectrum of PLA polymerized by **2.2’** used for tacticity measurements. Shown here is the spectrum’s normal appearance (left), and the same spectrum, but deconvoluted in MestReNova for measurement simplicity (right).

2.5.8 *Calculation Details* (executed by Aaron B. League, Mukunda Mandal and Christopher J. Cramer)

Structures were optimized at the M06-L level of theory[116,117] in the Gaussian09 software package,[118] using the 6-31+G(d,p) basis set for organic atom types,[119–121] and the SDD basis set and pseudopotentials for Zn and Br atoms.[122] Frequency calculations were performed at the same level of theory to compute relevant partition functions for the prediction of thermochemical quantities. While computationally more efficient local functionals are well known to predict molecular geometries with a high degree of accuracy, to address their tendency to underestimate barrier heights in main-group chemical systems, single-point calculations were then done using the M06-2X functional[123] with the 6-311+G(d,p) basis set for organic atom types and the SDD basis sets and pseudopotentials for Zn and Br atoms. From these data, best-estimate free energies G were computed as $G = E_{\mathrm{M06\text{-}2X}} + (G_{\mathrm{M06\text{-}L}} - E_{\mathrm{M06\text{-}L}})$ where E is the electronic energy.

All calculations were performed including the effects of SMD[124] continuum CH_2Cl_2 solvent, and all calculations employed a density fitting basis set automatically generated by Gaussian to speed evaluation of Coulomb integrals. CM5[125] charges were calculated from the final M06-2X densities. A free-energy adjustment of 1.89 kcal/mol was added to all species to account for a change from 1 atm to 1 M concentration.

An initial M06-L survey of possible transition state structures along a plausible coordination-insertion mechanistic pathway (analogous to the coordination-insertion mechanism proposed for (salen)Al[67]) was conducted using glycolide in place of LA as substrate, and OMe in place of O*i*Pr or phenoxide as an initiator. By eliminating the stereochemistry present in LA compared to glycolide, the number of structures required for a detailed survey was reduced twofold.

2.6 Acknowledgements

Funding for this project was provided by the National Science Foundation Center for Sustainable Polymers at the University of Minnesota, a supported Center for Chemical Innovation (CHE-1413862) and the US-Israel Binational Science Foundation (2012187). The X-ray diffraction experiments were performed using a crystal diffractometer acquired through NSF-MRI Award CHE-1229400. We acknowledge the Minnesota Supercomputing Institute (MSI) at the University of Minnesota for providing resources that contributed to the research results reported within this work.

3. Computational Prediction and Experimental Verification of *ε*-Caprolactone Ring-Opening Polymerization Activity by an Aluminum Complex of an Indolide/Schiff-Base Ligand

Reproduced in part with permission from:

Mandal, M.; Luke, A. M.; Dereli, B.; Elwell, C. E.; Reineke, T. M.; Tolman, W. B.; Cramer, C. J. *ACS Catal.*, **2019**, *9* (2), 885–889.

Copyright 2019 American Chemical Society.

3.1 Overview

Previous work involving collaboration between theory and experiment regarding ROP rates and modulations to Al catalyst structure led to insights into ligand structural effects on polymerization rates.[67,68,70] Through the detailed study of ligand modifications including extension of ligand backbone (2-carbon vs. 3-carbon backbone) and the introduction of sterically encumbering *ortho* substituents (i.e. Ad groups), and their respective structural effects on ROP rate, it was postulated that the closer a structure's resting state geometry was to that of the TSG (required for ring-opening to occur), the faster the overall polymerization rate.[68,70] In an extension of this earlier work, computational screening of a series of Al complexes for their activity in the ROP of CL was performed. Results from this predictive screen led to consideration of a new Al complex with a bis-indolide Schiff-base ligand as an efficient catalyst for CL polymerization. This prediction was tested and verified experimentally through the synthesis and characterization of the complex and evaluation of its ROP reactivity. Results, gained from detailed kinetic study of CL polymerization, showed that theory and experiment matched well (within 1 kcal/mol), verifying the overall validity of said theoretical prediction.

3.2 Introduction

Over the past decade, experiment and theory combined have made significant progress with respect to elucidating the details of ROP mechanisms by metal-alkoxide complexes.[67,68,70,105,111,126,127] The coordination-insertion pathway (Figure 1.5, section 1.2.2, more detailed mechanism shown in Figure 3.1) is usually invoked as a preferred propagation route that proceeds through four elementary steps: 1) coordination of monomer to the penta-coordinated metal-alkoxide catalyst, 2) insertion of the alkoxide into the activated monomer ester via transition state 1 (TS1), which is typically the RDS, 3) rearrangement of the tetrahedral orthoester intermediate with respect to which oxygen atoms interact most closely with the metal center, and, finally, 4) ring-opening ester bond cleavage (via transition state 2, TS2) to generate the polymer chain alkoxide terminus elongated by one unit. The same mechanism is also active for initiation, with energetic details differing somewhat depending on how closely the pre-catalyst –OR group resembles the alkoxide terminus of the growing polymer (from the standpoint of assessing structure-activity relationships, modeling initiation can be more efficient as it avoids the complexities associated with long, flexible growing polymer chains).

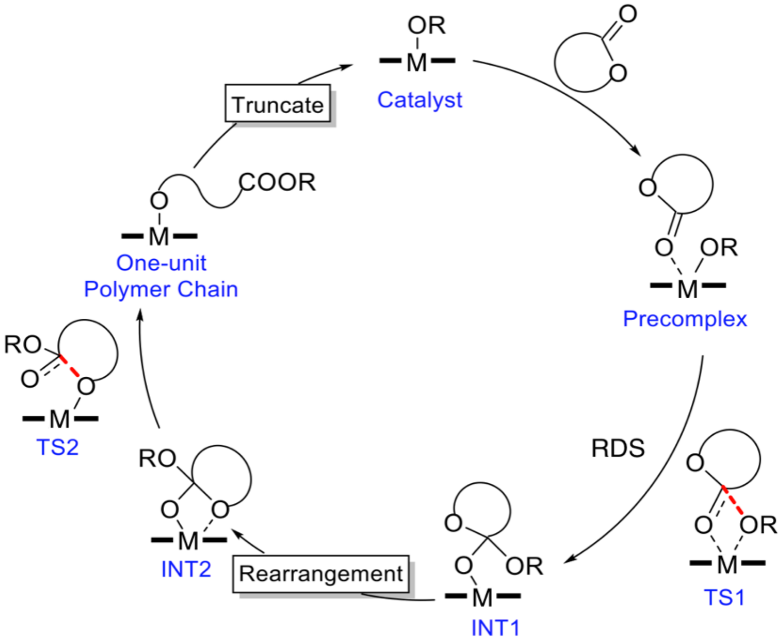

Figure 3.1. Detailed coordination-insertion mechanism for ROP.

Among the plethora of complexes that have been studied for purposes of ROP,[61,128–131] (salen)Al complexes are especially popular because of their high Lewis acidity, low toxicity, and high tunability, allowing systematic exploration of steric/electronic factors on ROP rates, molecular weight control, and selectivities.[132,133] Ligand structure and coordination environment have been identified as two crucial factors that determine the reactivity of a given ROP catalyst. For example, an 11-fold rate increase during *rac*-LA polymerization was observed using a longer backbone tether for an (salen)Al catalyst, and this finding was expanded upon in later work with CL.[51,68] Conversely, increased rigidity in the catalyst backbone—engineered using aryl-fused tethers rather than alkyl tethers—have resulted in decreased rates of LA polymerization.[81] In other related work, an Al complex of dibenzotetramethyltetraazaannulene (TMTAA, complex shown in Figure 3.2) was found to be an especially sluggish catalyst for CL polymerization. This result was attributed to the high rigidity of the TMTAA ligand that made it energetically costly to reach the pivotal octahedral TSG associated with the RDS.[134] Given the significant influence that the ligand framework can have on polymerization rate, the development of efficient computational approaches to screen alternative ligands for activity was targeted to speed experimental testing through the prioritization of synthetic targets.

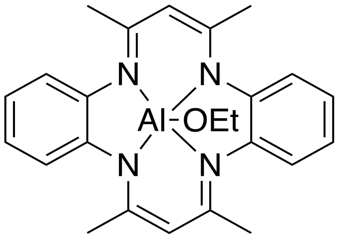

Figure 3.2. TMTAA complex, notably sluggish for CL polymerization (crystal structure of complex revealed $\tau_5 = 0.02$, geometry highly sp).[134]

The FDE hypothesis[68,70,135] can be a useful tool for such screenings. The FDE descriptor rationalizes structure-activity variations for series of catalysts where the geometries of the transition state structures of that of the RDS are all similar, at least with respect to coordination about the active site. For example, the geometries of the RDS transition states structures for polymerization of CL by a series of eight Al catalysts, differing only in the imine tether, were reported to have similar structures, with bond lengths and bond angles about the central Al-atom having deviations from their means of only ~0.01 Å and 3°, respectively.[68] In such instances, the energy required to distort the framework of the pre-catalyst so as to adopt the 'optimal' TSG (defined as the FDE) correlates closely with the overall $\Delta G^‡$ of the reaction (cartoon depiction in Figure 3.3). The FDE can be computed by taking the difference in the electronic energies of two frozen ligand frameworks: one derived by the removal of the alkoxy group of the optimized "resting" pre-catalyst and the other by removing both the alkoxy and CL from the optimized transition state. Still more rapid screenings may in principle be accomplished by computing the energy for the latter structures by first imposing a frozen set of geometric parameters about the metal center for all putative transition state structures and then simply relaxing the remaining geometric degrees of freedom, thereby obviating the need for specific transition state structure *optimizations*, although the utility of this simplified approach will perforce degrade as explored ligand sets increase in diversity.

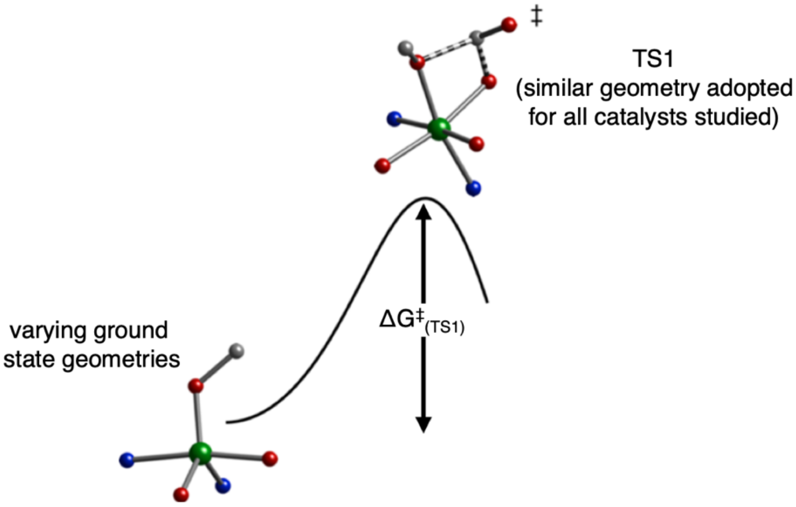

Figure 3.3. Cartoon depicting the relationship between ground state geometry and general TS1 geometry (TSG) via activation free energy. Image reproduced with permission from reference 68, https://pubs.acs.org/doi/abs/10.1021/acscatal.5b02607, further permissions related to the material should be directed to the American Chemical Society.

In this work, the systematic investigation of catalysts screened using the theoretical FDE model led to the identification of a catalyst to test experimentally. This catalyst was synthesized, characterized, and its catalytic activity for CL polymerization was evaluated. High ROP activity was observed, providing key confirmation of the validity of the FDE approach for predicting catalytic activity by AlOR catalysts.

3.3 Results and Discussion

3.3.1 *Density Functional Theory Calculations* (performed by Mukunda Mandal, Büşra Dereli, and Christopher J. Cramer)

This section briefly describes the theoretical modeling involved in this project, with more details available in published work.[136] The ROP of CL is notably rapid for complex **3.1** (Figure 3.4, A) relative to other Al catalysts.[70] The mechanistic details associated with catalysis by **3.1** have been explored via DFT, with $\Delta G^{\ddagger}_{(TS1)}$ and FDE computed to be 7.8 and 12.7 kcal/mol, respectively[70] (note, the original calculations report 10.3 and 12.4 kcal/mol respectively, but this is attributed to the following three factors: 1) CH_2Cl_2 solvation effects instead of those from toluene, 2) inclusion of Grimme's D3-dispersion correction term, and 3) a more favorable orientation of the CL fragment in TS1 identified here). With respect to in silico screening of alternative catalysts, we sought to identify ligands predicted to lead to still lower values of $\Delta G^{\ddagger}_{(TS1)}$ and/or FDE than those computed for **3.1**, ultimately resulting in faster catalysis.

First design efforts focused on modification of the parent system **3.1** through the introduction of additional tethers, of varying length, bridging other atoms of the salen moiety (identified as P_n, Q_n and R_n in Figure 3.4, A, where "n" refers to the number of methylene units in the tether). The goal was to constrain the pre-catalyst to a geometry more closely resembling the corresponding TS1 structure, thereby reducing FDE. However, extensive surveys of frameworks **3.2**–**3.4** for varying values of "n" failed to identify any with FDE or $\Delta G^{\ddagger}_{(TS1)}$ values less than those for **3.1**.

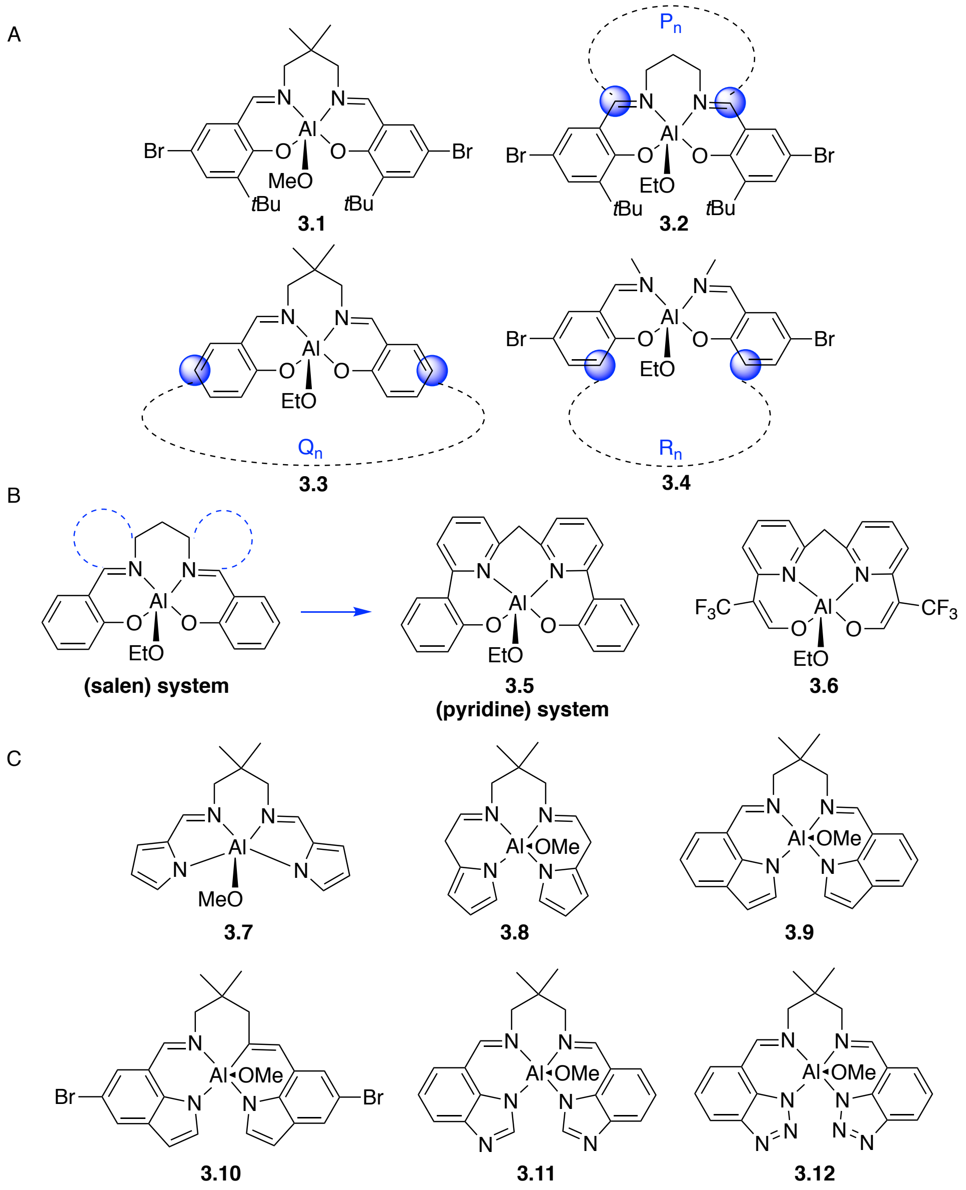

Figure 3.4. (A) Parent salen catalyst and modifications with additional alkyl tethers. (B) Pyridine-based systems as a sidearm modification to salen. (C) Pyrrole/indole-based {N,N,N,N}-complexes.

As favorable constraints on the pre-catalyst geometries were not achieved with additional tethers, incorporation of the imine functionality of the salen ligand into pyridine moieties (**3.5** and **3.6**, Figure 3.4, B) was explored. In this instance, the goal was to tune both the steric and electronic aspects of the catalyst, with the hypothesis being that the pyridine units would modulate the Lewis acidity of the metal center through their π-donor character while simultaneously reducing steric demand associated with the overall tether. Interestingly, both **3.5** and **3.6** are predicted to be potentially active for CL homopolymerization with $\Delta G^{\ddagger}_{(TS1)}$ ~6.5 kcal/mol and FDE ~10.5 kcal/mol, values indeed below those computed for **3.1**. However, it was concluded that the ligands themselves and their assembly about the catalytic center were likely to pose significant synthetic challenges, and on that basis, it was decided instead to explore further modifications in the ligand framework, and in particular to evaluate the replacement of O atom donors with N atom alternatives (**3.7**–**3.12**, Figure 3.4, C). Complex **3.7** with its bis(pyrrolide) Schiff-base ligand was reported previously.[109,137,138] In contrast to the half-salen systems previously reported,[139] where a five-membered-ring chelate of the ligand at Al leads to faster catalysis during CL polymerization than a six-membered one, **3.8** was predicted to be significantly faster than **3.7** for the same reaction (Table 3.1). The larger ligand arm of **3.8** permits it to adopt the octahedral geometry of the RDS TS1 more readily, as reflected by its FDE of 8.5 kcal/mol compared to that of 12.2 kcal/mol for **3.7**.

Changing the pyrrolide functionality to indolide (**3.9**), *para*-bromoindolide (**3.10**), benzimidazolide (**3.11**), and benzotriazolide (**3.12**) was also explored. Table 3.1 further compares key energetic and structural parameters for catalysts **3.1** and **3.7**–**3.12**. The $\Delta G^{\ddagger}_{(TS1)}$ values for **3.8**–**3.12** are all low, implying rapid ROP rates, and a comparison of structures and energetics for **3.1** vs. **3.9** (Figure 3.5) suggests the ligand system of the latter to have significant potential. In addition, when the indolide ligands in **3.9** are modified to make them less electron donating, either by introducing bromo-substituents (**3.10**) or by introducing additional N-atoms in the five-membered ring (**3.11** and **3.12**), the catalyst is predicted to be more Lewis acidic, as judged by a shortening of both r_1, the metal-OR bond distance in the catalyst, and r_2, the metal–carbonyl bond distance in TS1, and there are corresponding improvements in predicted catalytic activity as judged by decreasing values of $\Delta G^{\ddagger}_{(\mathrm{TS1})}$. Interestingly, there is considerably less variation in the predicted FDE, which is consistent with the relatively limited variation in τ_5 predicted for the pre-catalyst structures. Put differently, with τ_5 values already so close to 1.0, additional acceleration must be achieved by tuning of the overall electronic structure toward enhanced Lewis acidity.

Table 3.1. Computed geometry indices (τ_5), activation free energies (kcal/mol), FDEs, (kcal/mol), and key bond lengths (Å) for N_4-donor systems.[a]

Catalyst	$\boldsymbol{\tau_5}$	$\boldsymbol{\Delta G^{\ddagger}_{(\mathrm{TS1})}}$	**FDE**	$\boldsymbol{r_1}$ **(Al-OMe)**	$\boldsymbol{r_2}$ **(Al-O=C)**
3.1	0.71	7.8	12.7	1.765	1.926
3.7	0.42	10.6	12.2	1.756	1.908
3.8	0.75	5.5	8.5	1.762	1.912
3.9	0.80	7.6	11.6	1.772	1.937
3.10	0.79	6.8	11.1	1.771	1.929
3.11	0.80	6.2	11.9	1.764	1.917
3.12	0.84	4.7	12.6	1.755	1.908

[a]Calculations performed at the SMD(CH_2Cl_2)/M06-2X-D3/6-311+G(d,p)//M06-L/6-31+G(d,p) level of theory.

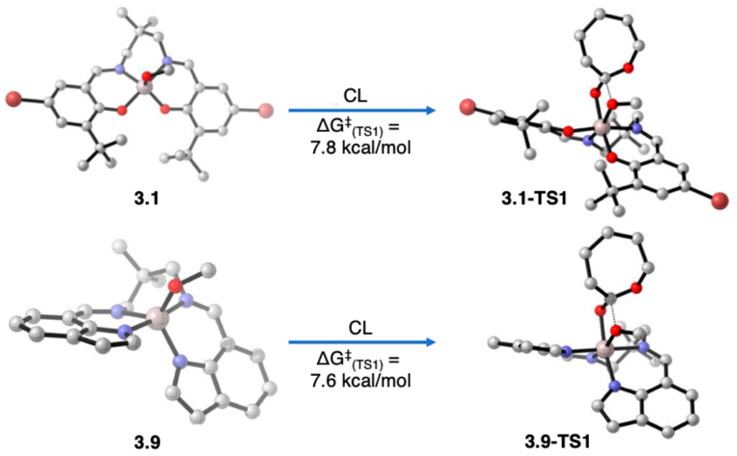

Figure 3.5. Optimized structures for **3.1** and **3.9** and their corresponding RDS transition state structures for CL polymerization.

3.3.2 *Experimental Work*

3.3.2.1 *Synthesis and Characterization of Complex*

Given the computational prediction of good activity for **3.9** coupled with its perceived synthetic accessibility, the synthesis of its benzyloxy analog, **3.14** (Figure 3.6), was targeted. Condensation of 7-indolecarboxaldehyde and 2,2-dimethylpropane-1,3-diamine gave the new ligand precursor, $\mathbf{L^7H_2}$, in high purity and good yield (81%). Characterization by NMR spectroscopy (Figure 3.11, section 3.5.3), HR-ESI-MS, and CHN analysis confirmed its formulation. Notably, the ^{1}H NMR spectrum revealed a shift of aromatic peaks from the carboxaldehyde and the disappearance of both the C*H*O and NH_2 proton resonances from the starting materials concomitant with the appearance of a singlet imine peak at ~8.5 ppm. Metalation with excess diethylaluminum ethoxide (Et_2AlOEt) at 70 °C for 4 d yielded **3.13**, which was isolated as a yellow precipitate in modest yield (23%; a ^{1}H NMR spectrum of the supernatant contained a complex mixture of peaks). The complex was identified by CHN analysis and NMR spectroscopy, with clearly shifted resonances for the ligand hydrogen atoms relative to $\mathbf{L^7H_2}$ and replacement of the N-H signals with shielded peaks for an Et ligand being key indicators for the indicated structural formulation (Figure 3.12, section 3.5.3). Subsequent treatment of a solution of **3.13** in CH_2Cl_2 with BnOH (1 equiv.) gave complex **3.14** as a pale-yellow solid (73%). This complex was characterized by NMR spectroscopy (Figure 3.12, section 3.5.3; the disappearance of the aforementioned ethyl ligand peaks and the appearance of a new, methylene OBn peak at ~ 4.0 ppm were indicative of its formation), CHN analysis, and X-ray crystallography (Figure 3.6).

The X-ray structure of **3.14** revealed a mononuclear, 5-coordinate complex with a distorted tbp geometry ($\tau_5 = 0.87$). The overall geometry is similar to that calculated for methoxy analogue **3.9** (τ_5 value of 0.80). The indolate-Al distances observed (Al-N1 and Al-N4 in Figure 3.6) fall well within the range of other indolide-metal bond distances in the literature (ranging from 1.88–2.20 Å).[140–144] In adopting the tbp structure shown, the chelating ligand in **3.14** is highly twisted, resulting in unique environments for each indolide ring. If this structure were present in solution, the NMR spectrum would be expected to exhibit distinct resonances for each indolide ring and the diastereotopic backbone hydrogen atoms. However, the ^{1}H and ^{13}C NMR spectra (Figure 3.12, section 3.5.3) show only one set of sharp indolide peaks. These findings were inconsistent with a rigid structure in solution akin to that seen in the solid state, and suggested an averaged structure, perhaps due to fluxionality, that would have implications for stereoselective ROP reactions (further investigated and discussed in detail in *Chapter 4*).

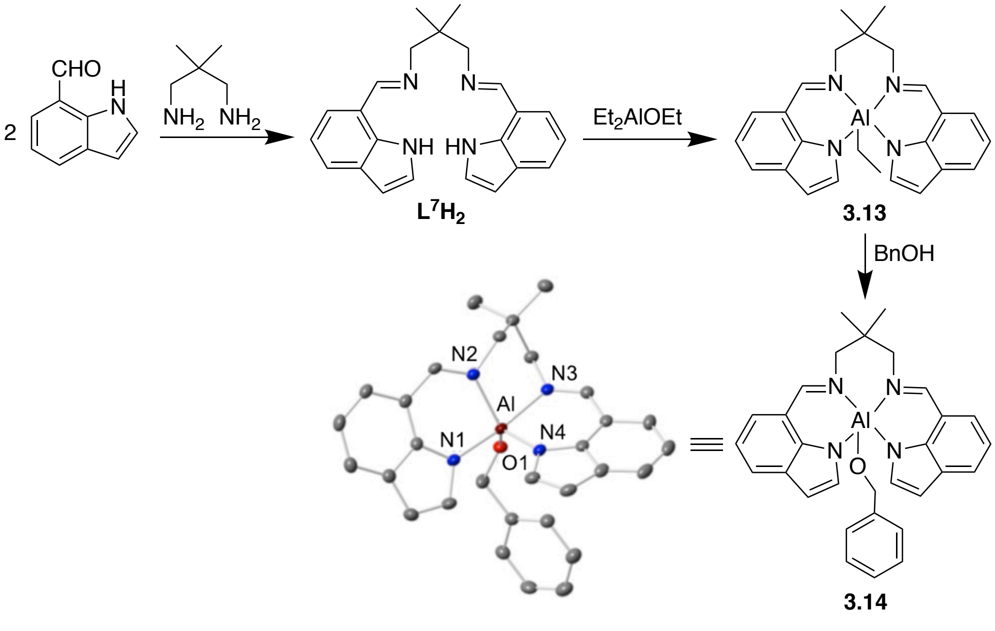

Figure 3.6. Synthesis of ligand precursor (**L^{7}H$_2$**) and complexes **3.13** and **3.14**, with a representation of the X-ray crystal structure of **3.14** shown as 50% thermal ellipsoids (nonhydrogen atoms only). Selected distances (Å) and angles (deg): Al-N1, 1.9388(19); Al-N2, 2.0117(19); Al-N3, 2.074(2); Al-N4, 1.905(2); Al-O1, 1.7484(19); N1-Al-N2, 90.13(9); N1-Al-N3, 173.78(5); N1-Al-N4, 95.63(8); N2-Al-O1, 121.78(8); N2-Al-N4, 114.95(7).

3.3.2.2 *Kinetics of ε-Caprolactone Polymerization*

The kinetics for the polymerization of CL were measured by mixing **3.14**, internal standard (bis-*para*-trimethylsilylbenzene) and monomer (targeting concentrations of 0.007 M, 0.004 M and 2.0 M, respectively, in CD_2Cl_2) and monitoring the loss of monomer and gain in polymer via ^{1}H NMR spectroscopy at 300 K. Quadruplicate data were collected and integration of peaks through use of MestReNova software yielded concentrations of reactant and product. The resulting concentration vs. time data were fit to first-order and saturation (Michaelis-Menten) kinetics equations (Eqs. 1.3 and 1.4, section 1.2.3.1) using COPASI, a global kinetics fitting software package.[66]

The relative merits of both first-order and saturation kinetic fits at slightly varying final concentrations of polymer were unclear (Figures 3.7–3.8). Visually, both fits seemed appropriate for these polymerizations, but K_M and V_{max} values determined from COPASI saturation kinetics fits were wildly inconsistent until higher [CL] were reached (> 1.95 M). At these concentrations, saturation behavior was observed (Figure 3.8), and K_{eq} values determined from these fits were quite small (especially when compared to our previously studied Al systems).[67,68,70] This finding was attributed to an extremely weak binding phenomenon of the monomer to the catalyst before the ring-opening event occurs.

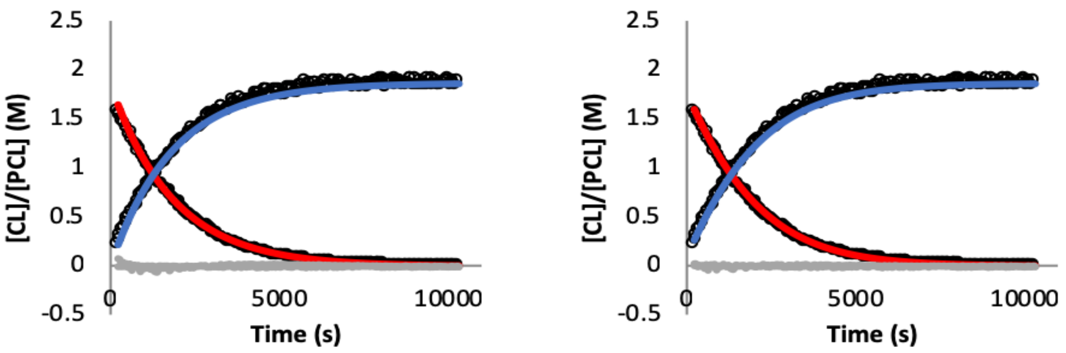

Figure 3.7. Plots of [CL] decay and [PCL] growth over time where final [PCL] reaches 1.88 M. Both first-order (left) and saturation (right) kinetic fits to the data are shown. Weighted error between COPASI fits (blue = PCL growth, red = CL decay) and the data (circles) is shown in grey.

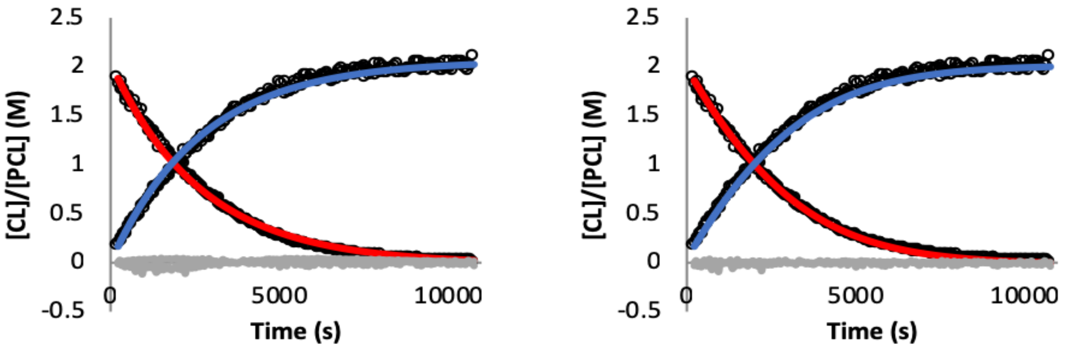

Figure 3.8. Plots of [CL] decay and [PCL] growth over time where final [PCL] reaches 2.05 M. Both first-order (left) and saturation (right) kinetic fits to the data are shown. Weighted error between COPASI fits (blue = PCL growth, red = CL decay) and the data (circles) is shown in grey.

This reasoning correlates well with an independent test of the importance of monomer coordination (implicit in the saturation fits). In this test, we examined ^{1}H NMR spectra of solutions of **3.14** in the presence of variable concentrations (0.005–1.5 M) of *γ*-butyrolactone (BL, not easily ring-opened due to lack of ring strain).[145] Only slight changes in the chemical shifts of the peaks associated with **3.14** were observed (Figure 3.9), and these were consistent with the solvent polarity changes due to the added BL, i.e., no evidence for binding of BL to the complex was observed. It was thus concluded that if CL binding occurs, it must be quite weak, and that the simpler pseudo first-order fits of the kinetic data were preferable for obtaining useful rate constants. A representative plot indicating first-order monomer decay behavior is shown in Figure 3.10.

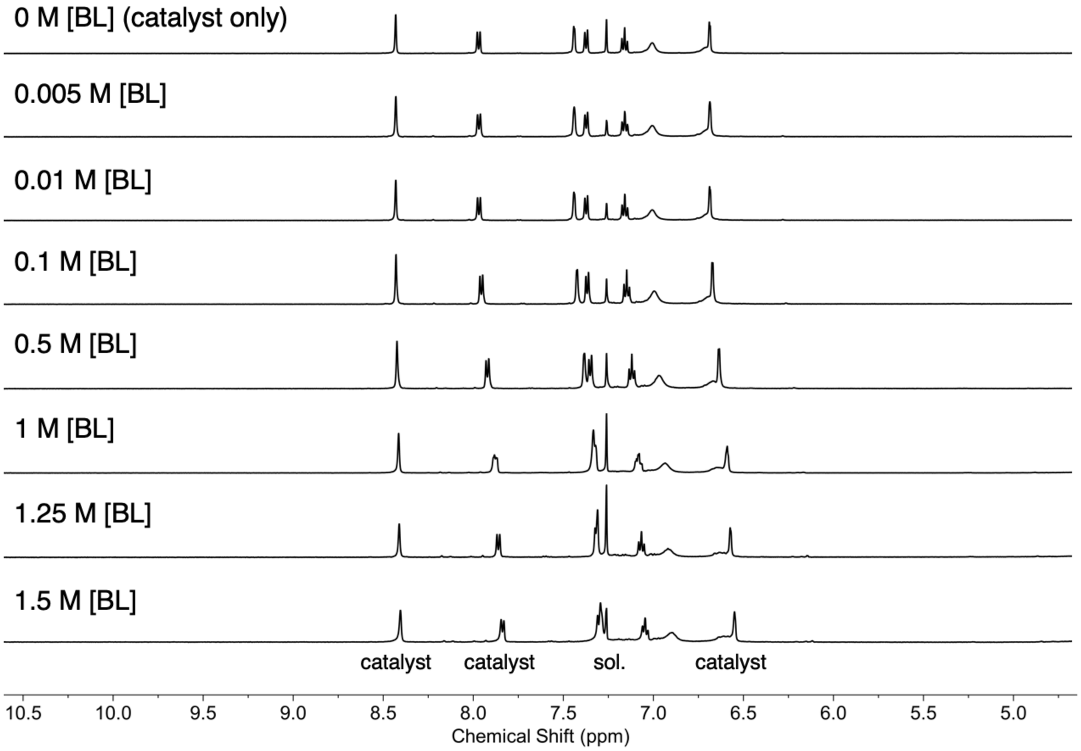

Figure 3.9. Aromatic region overlay of the BL binding studies with **3.14**. Negligible shift in the catalyst peaks as a function of higher [BL] indicates that binding of BL to **3.14** is minimal.

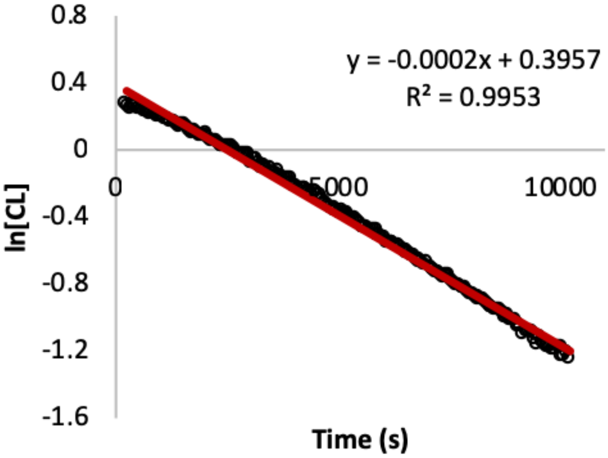

Figure 3.10. First-order decay plot of [CL], where black circles = [CL] data and red line = linear trendline.

The first-order fits yielded an average first-order rate constant (k_{obs}) of 4.1 x 10^{-4} s^{-1}. While theoretical computation would suggest that **3.14** (by analogy to **3.9**) should be about as reactive as **3.1** for ROP of CL, experimentally we observed it to be 5.5-fold slower (times to reach 95% conversion were 20 min for **3.1** and 110 min for **3.14**, under equivalent conditions of $[\text{CL}]_0 = 2$ M, $[\text{cat}]_0 = 7$ mM, 300K). Such a discrepancy—roughly 1 kcal/mol at 298 K—is, however, well within the error one might expect for a DFT-based model, and suggests that FDE can indeed be a practical descriptor for estimating the ROP activity of hypothetical future catalysts, at least with respect to prioritizing (i) more complete computational characterization of reaction paths (e.g., **3.12**, where a relatively low FDE is associated with a $\Delta G^{\ddagger}_{(\text{TS1})}$ value that is 3.1 kcal/mol lower than that for **3.1**) and (ii) promising targets for synthetic realization.

3.4 Concluding Remarks

In summary, new Al-based ROP catalysts in silico by means of DFT calculations were explored. While additional tethers on the salen moiety in the form of P_n, Q_n and R_n series of catalysts did not prove useful in lowering either the calculated FDE, or the $\Delta G^{\ddagger}$ of the RDS TS1, ligand sidearm modification with pyridine donors showed promise by modulating both the overall steric and electronic features of the catalyst. An alternative modification, involving the replacement of all O atom donors with N- counterparts, provided a new class of ROP pre-catalysts having highly distorted tbp geometries—a feature that generally promotes ROP catalysis. We tested this idea experimentally by synthesizing and characterizing complex **3.14** and examining its CL ROP rate. It polymerized CL rapidly, consistent with theoretical predictions. In line with prior CL-ROP studies,[34,51,67] theory suggests that electron withdrawing groups on the five-membered ring of the supporting ligand of **3.9** might lead to even faster catalysts in the form of **3.10**–**3.12**.

This work shows that using the FDE model to screen hypothetical catalysts prior to subsequent more complete computational evaluation—and ultimate experimental realization—continues to hold promise for future catalyst design in suitably related systems.

3.5 Experimental

3.5.1 *Calculation Details* (executed by Mukunda Mandal, Büşra Dereli, and Christopher J. Cramer)

All calculations are performed at the DFT level as implemented in the Gaussian 09 electronic structure program suite.[118] Geometry optimizations are carried out at the M06-L[123] level of theory using the double zeta 6-31+G(d,p)[119] basis set for all atoms, except for bromo-substituted structures where the SDD[146] pseudopotential and its associated basis set has been used. Coulomb integrals are evaluated using an automatically generated density fitting basis set to speed up the relevant calculations. The grid used for numerical integration in DFT was set to "ultrafine". The natures of all stationary points are verified by calculation of quasi-harmonic vibrational frequencies. All vibrational frequencies below 50 cm^{-1} are replaced with values of 50 cm^{-1}. Zero-point vibrational energies and thermal contributions to electronic energy are determined from the computed partition functions at 298.15 K. For better estimate to Gibbs free energies, single point electronic energies are computed using the M06-2X[123] functional with the 6-311+G(d,p)[119] basis set at the M06-L optimized geometries and the resulting electronic energies are summed with thermal free energy contributions computed at the M06-L/6-31+G(d,p) level. For complex **1** and {N,N,N,N}-complexes, Grimme's D3 dispersion correction term[147] has been used for electronic energy calculation at the M06-2X-D3/6-311+G(d,p) level. All reported structures are optimized using the self-consistent reaction field (SCRF) approach with

SMD[148] continuum solvation model with the solvent parameters for toluene or CH_2Cl_2 depending on the reaction (ε(toluene) = 2.374, and $\varepsilon(CH_2Cl_2)$=8.93), unless otherwise stated. Additional information regarding the theoretical details can be found in published work.[136]

3.5.2 *Synthetic Materials, Methods, and General Considerations*

All reactions containing either air- and/or water-sensitive compounds were performed within the inert atmosphere of a nitrogen-filled glovebox or using Schlenk line techniques. All reagents were purchased from commercial sources and were used as received, unless otherwise noted. CL was purified by drying over CaH_2 and subsequent vacuum distillation. All protonated solvents were degassed and a passed through a solvent purification system (Glass Contour, Laguna, CA) prior to use. Deuterated solvents were dried over CaH_2, degassed through freeze-pump-thaw techniques, and distilled before storing them under N_2. Nuclear magnetic resonance (NMR) spectroscopies were performed with a Bruker Avance III (500 MHz) spectrometer equipped with a BBFO SmartProbe. Chemical shifts for ^1H and ^{13}C NMR spectra were references to residual protium in the deuterated solvent (for ^1H NMR) and the deuterated solvent itself (for ^{13}C NMR). Elemental analyses were performed by Robertson Microlit Laboratories in Ledgewood, NJ.

3.5.3 *Synthetic Procedures*

Synthesis of L^7H_2. To an oven-dried round bottom flask equipped with a reflux condenser, 7-indolecarboxaldehyde (2.0 g, 13.78 mmol) was added and dissolved in absolute EtOH (0.63 M) while stirring. To this mixture, 2,2-dimethylpropane-1,3-diamine (0.5 equiv.) was added drop-wise before heating to reflux for 3 d. After the reaction was complete, the reaction mixture was pipetted into a new round bottom flask and was cooled to room temperature before being placed in a −30° C freezer overnight. The resulting pale orange solid was isolated through vacuum filtration and dried via Schlenk line for 6–8 h. ^{1}H NMR analysis indicated this material was extremely pure and required no further purification before subsequent synthetic steps. Yield: 1.98 g, 81%. ^{1}H NMR (500 MHz, CD_2Cl_2) δ 10.75 (s, 2H, N*H*), 8.53 (s, 2H, C*H*=N), 7.77 (d, *J* = 7.63 Hz, 2H, Ar*H*), 7.34 (d, *J* = 7.63 Hz, 2H, Ar*H*), 7.31 (m, 2H, HNC*H*=CH), 7.19 (t, *J* = 7.63 Hz, 2H, Ar*H*), 6.60 (m, 2H, HNCH=C*H*), 3.69 (s, 4H, $NCH_2C(CH_3)_2CH_2N$), 1.19 (s, 6H, $NCH_2C(CH_3)_2CH_2N$); ^{13}C NMR (125 MHz, CD_2Cl_2) δ 163.39, 134.63, 128.87, 125.75, 125.61, 123.88, 120.08, 119.72, 102.62, 71.59, 37.20, 25.15. HRMS (ESI/Q-TOF) *m/z*: $[M+H]^+$ Calcd. for $C_{23}H_{24}N_4$, 357.2074; found, 357.2083. Anal. Calcd for $C_{23}H_{24}N_4$: C, 77.50; H, 6.79; N, 15.72. Found: C, 77.46; H, 6.79; N, 15.70.

Synthesis of 3.13. To an oven-dried screw cap bomb flask equipped with a stir bar, ligand (0.37 g, 1.04 mmol) and Et_2AlOEt (excess) were dissolved in toluene while in a nitrogen-filled glovebox. The sealed flask was pumped out of the box, heated to 70° C and stirred for 4 d. After cooling to room temperature, the bomb flask was pumped back into the glovebox. The resulting solids were collected via vacuum filtration and were washed with pentane. The product was then recrystallized from toluene layered with pentane in a –40° C freezer overnight. The purified product was isolated as a bright yellow solid and was stored under N_2 until subsequent use. Yield: 0.10 g, 23%. ^{1}H NMR (500 MHz, CD_2Cl_2) δ 8.47 (s, 2H, C*H*=N), 7.89 (d, *J* = 7.75 Hz, 2H, Ar*H*), 7.35 (d, *J* = 7.75 Hz, 2H, Ar*H*), 7.28 (d, *J* = 2.58 Hz, 2H, NC*H*=CH), 7.12 (t, *J* = 7.75 Hz, 2H, Ar*H*), 6.61 (d, *J* = 2.58 Hz, 2H, NCH=C*H*), 3.68 (d, *J* = 12.29 Hz, 2H, $NCH_2C(CH_3)_2CH_2N$), 3.52 (d, *J* = 12.29 Hz, 2H, $NCH_2C(CH_3)_2CH_2N$), 1.23 (s, 3H, $NCH_2C(CH_3)_2CH_2N$), 1.04 (s, 3H, $NCH_2C(CH_3)_2CH_2N$), 0.50 (t, *J* = 7.94 Hz, 3H, CH_2CH_3), –0.18 (q, *J* = 7.94 Hz, 2H, CH_2CH_3); ^{13}C NMR (125 MHz, CD_2Cl_2) δ 169.72, 142.58, 138.62, 132.47, 127.69, 126.79, 118.13, 116.77, 103.37, 68.91, 36.72, 25.24, 25.12, 10.71. Despite using a broad sweep width (up to −200 ppm) and using variable temperature (VT) NMR techniques, no signal for the methylene of the ethyl substituent bound to the Al center could be identified. Anal. Calcd for $C_{25}H_{27}AlN_4$: C, 73.15; H, 6.63; N, 13.65. Found: C, 74.16; H, 6.27; N, 13.80.

Synthesis of 3.14. To an oven-dried vial equipped with a small stir bar, **1** (0.037 g, 0.09 mmol) was added and dissolved in a minimal amount of CH_2Cl_2. Using a 1 M stock solution in CH_2Cl_2, a stoichiometric amount of BnOH was added to the vial. The reaction was stirred overnight, and the solvent was removed *in vacuo*, yielding a light-yellow solid. The solid was stirred in pentane before being isolated through vacuum filtration. Purification was completed by recrystallizing the material in toluene layered with pentane in a −40° C freezer overnight. The material was subsequently stored under N_2. Yield: 0.02 g, 73%. ^{1}H NMR (500 MHz, CD_2Cl_2) δ 8.51 (s, 2H, C*H*=N), 7.95 (d, *J* = 7.68 Hz, 2H, Ar*H*), 7.44 (d, *J* = 7.68 Hz, 2H, Ar*H*), 7.38 (d, *J* = 2.69 Hz, 2H, NC*H*=CH), 7.17 (t, *J* = 7.68 Hz, 2H, Ar*H*), 7.02 (m, 3H, OCH_2Ar*H*), 6.79 (app. bs, 2H, OCH_2Ar*H*), 6.67 (d, *J* = 2.69 Hz, 2H, NCH=C*H*), 4.01 (app. bs, 2H, OCH_2Ar), 3.77 (d, *J* = 11.28 Hz, 2H, $NCH_2C(CH_3)_2CH_2N$), 3.50 (d, *J* = 11.28 Hz, 2H, $NCH_2C(CH_3)_2CH_2N$), 1.05 (s, 3H, $NCH_2C(CH_3)_2CH_2N$), 1.02 (s, 3H, $NCH_2C(CH_3)_2CH_2N$); ^{13}C NMR (125 MHz, CD_2Cl_2) δ 170.02, 142.43, 138.72, 132.42, 128.20, 127.97, 127.20, 127.05, 126.31, 118.39, 116.29, 103.82, 68.85, 65.78, 36.30, 25.69, 24.96. Anal. Calcd for $C_{30}H_{29}AlN_4O$: C, 73.75; H, 5.98; N, 11.47. Found: C, 70.25; H, 5.97; N, 11.35.

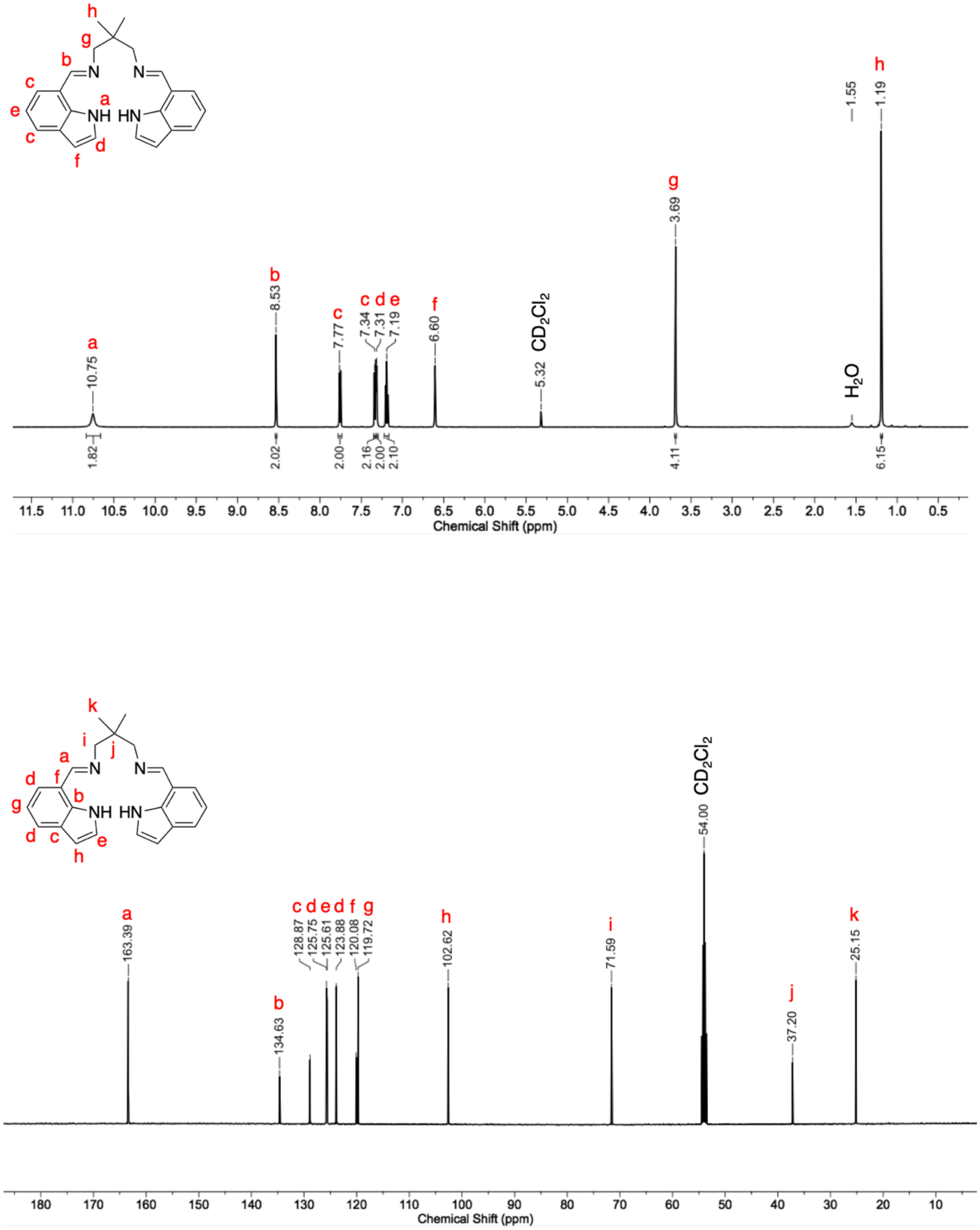

Figure 3.11. ^1H (top) and ^{13}C (bottom) NMR spectra for **L^7H_2**.

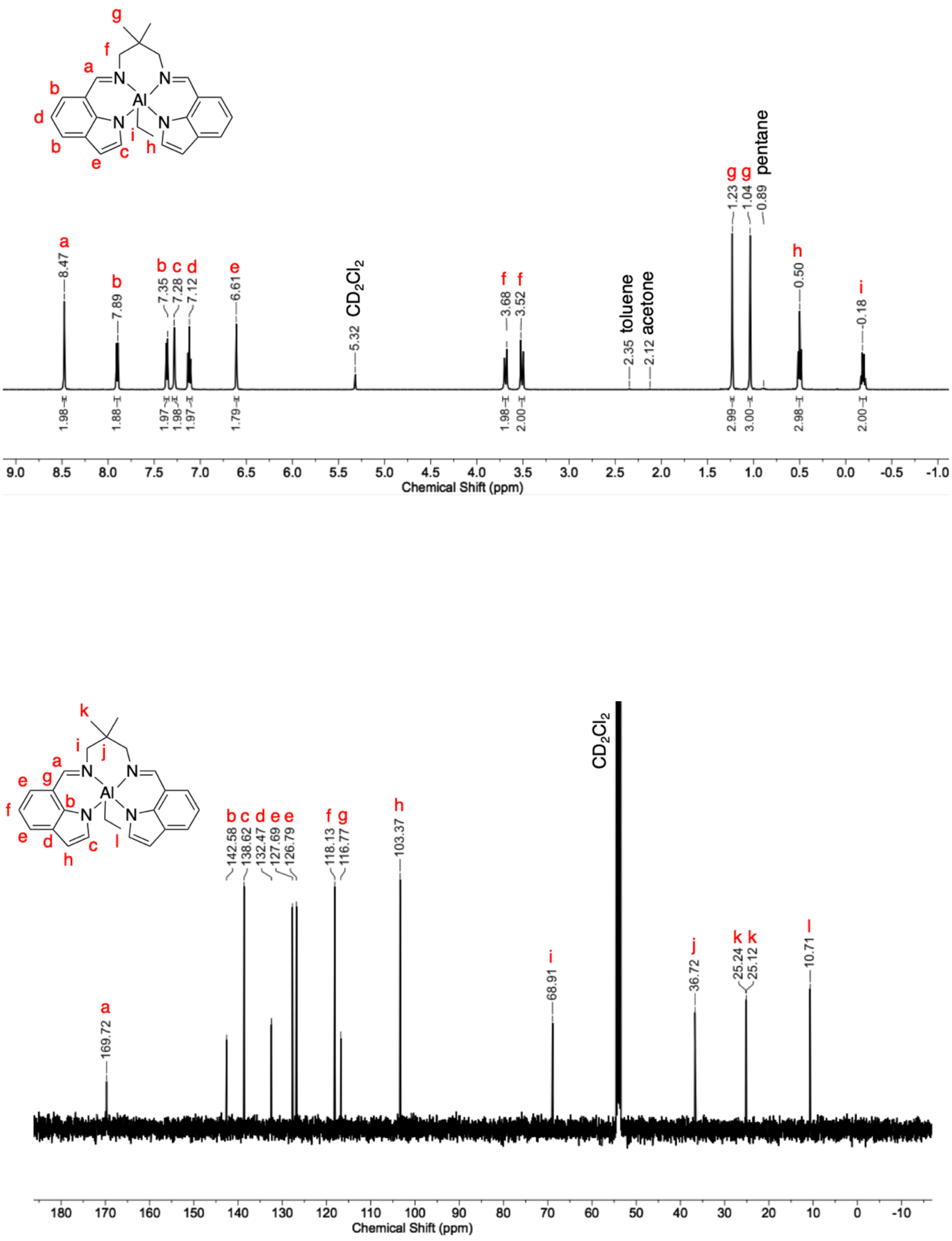

Figure 3.12. ^{1}H (top) and ^{13}C (bottom) NMR spectra for **3.13**.

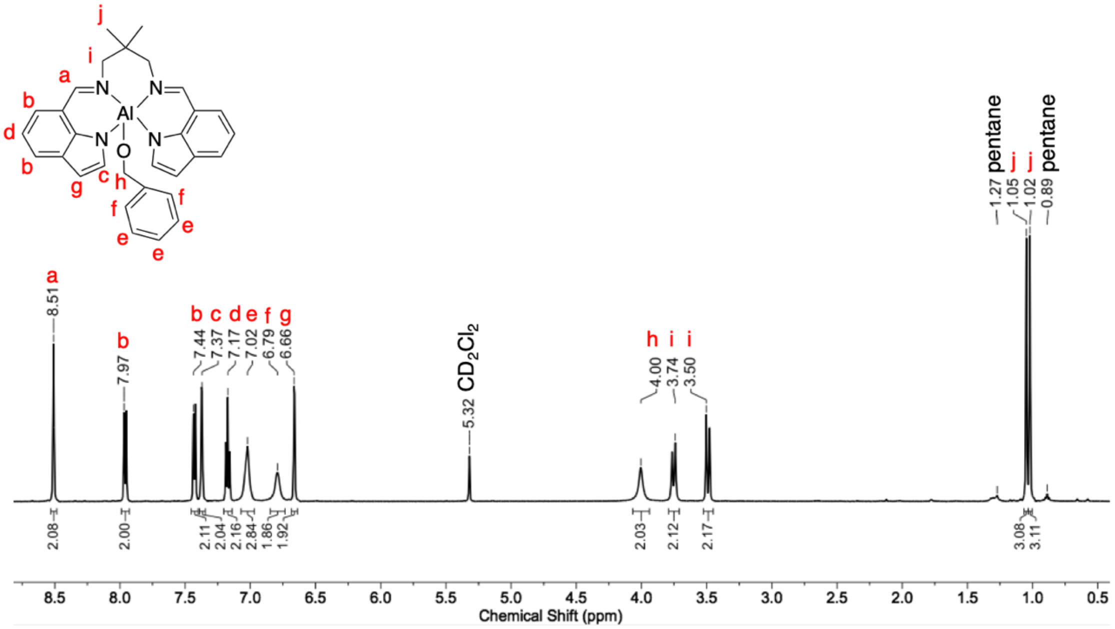

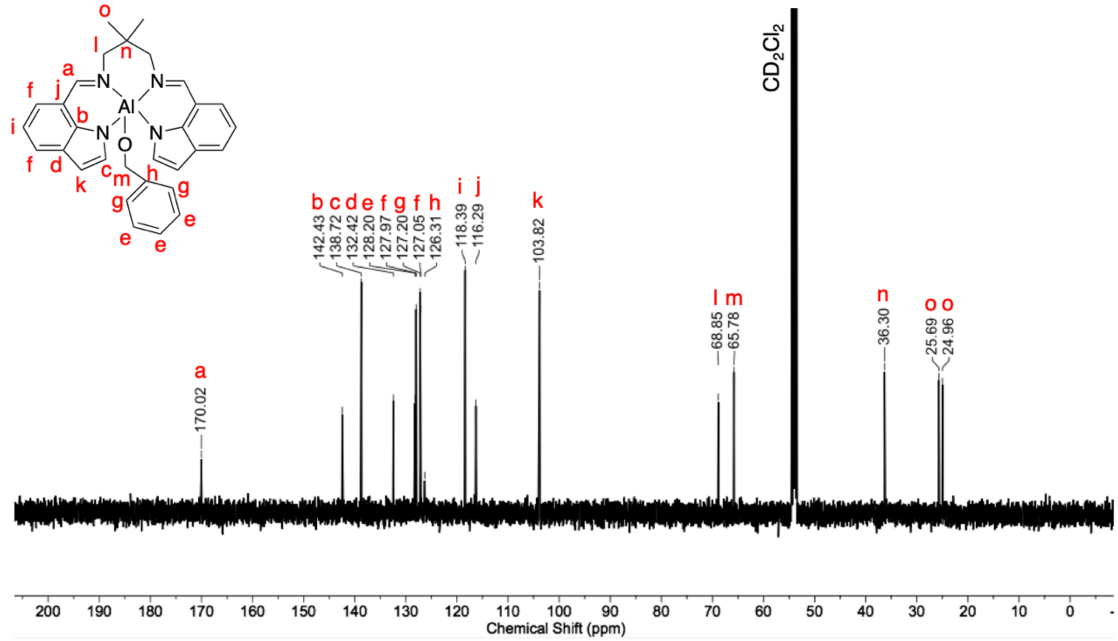

Figure 3.13. ^{1}H (top) and ^{13}C (bottom) NMR spectra for **3.14**.

3.5.4 *Kinetic Measurements and Analysis*

Polymerization kinetics were performed by adding 450 μL of a stock solution of catalyst in CD_2Cl_2 (9.7 mM) and 5 μL of a stock solution of internal standard (bis-*para*-trimethylsilylbenzene) in CD_2Cl_2 (0.5 M) to a new NMR tube inside a nitrogen-filled glovebox. The NMR tube was capped with a rubber septum and wrapped with electrical tape to maintain an N_2 environment inside. A gas-tight syringe charged with 170 μL of a stock solution of CL in CD_2Cl_2 (7.35 M) was also capped with a septum to prevent air contamination. The target concentrations for the polymerization reaction were 0.007 M catalyst, 0.004 M internal standard and 2.0 M CL. Both the NMR tube and the syringe were pumped outside of the box and brought to the NMR spectrometer (500 MHz Bruker Avance III). Once at the instrument, monomer was injected into the NMR tube, the tube was shaken vigorously and was immediately injected into the spectrometer (probe temperature = 25 ºC). The time between monomer injection and spectral array was measured in seconds and the spectral array was started as soon as the NMR tube had reached good shims. An array of spectra was taken every 48 s (four scans) with a relaxation delay of 10 s, gain of 10, and acquisition time of 2 s. Auto-shim was used to ensure proper shimming through the entirety of the reaction. The reaction was monitored until there was complete disappearance of monomer peaks on the spectrum. The polymerization reaction was done in quadruplicate and the obtained NMR data was analyzed through MestReNova software by integration. The integrated peak and concentration of the internal standard allowed for concentrations of all species to be calculated as a function of time. Then, the reaction time was calculated in seconds by using the known time duration of each spectrum and the amount of time between injecting the NMR tube into the spectrometer and beginning the ^1H NMR spectrum acquisition. The concentration vs. time data was entered into COPASI software and was fit to a first-order equation, Eq. 1.3, section 1.2.3.1, to obtain a k_{obs} value for each polymerization. The reaction rates were then plotted as a function of [CL].

3.5.5 *Binding Studies with γ-butyrolactone*

The binding studies between **3.14** and BL were completed as follows. In a glovebox, 0.005 M catalyst and a set concentration of BL (ranging from 0 M to 1.5 M) were added to eight new NMR tubes. The tubes were shaken, capped, and taped with electrical tape before being pumped out of the box and being brought down to the NMR instrument. Each tube was analyzed via ^{1}H NMR spectroscopy and the resulting spectra were compared (Fig. 3.7). Lack of significant shift of the catalyst peaks with varying concentration of BL indicated that the monomer was not binding to the catalyst, and no K_{eq} could be calculated.

3.6 Acknowledgements

Funding for this project was provided by the National Science Foundation Center for Sustainable Polymers, a supported Center for Chemical Innovation (CHE-1413862). The X-ray diffraction experiment was performed using a crystal diffractometer acquired through NSF MRI Award CHE-1229400. The NMR experiments were performed on Bruker Avance III 500 MHz spectrometers acquired through NIH Award S10OD011952. Dr. Letitia Yao is thanked for help with NMR experiments.

4. Mechanism of Initiation Stereocontrol in Polymerization of *rac*-Lactide by Aluminum Complexes Supported by Indolide-Imine Ligands

Reproduced in part with permission from:

Luke, A. M.†; Peterson, A.†; Chiniforoush, S.; Mandal, M.; Popowski, Y.; Sajjad, H.; Bouchey, C. J.; Shopov, D. Y.; Graziano, B. J.; Yao, L. J.; Cramer, C. J.; Reineke, T. M.; Tolman, W. B. *Macromolecules*, **2020**, *53* (5), 1809–1818. †Authors contributed equally.

Copyright 2020 American Chemical Society.

4.1 Overview

In this work, the solid state and fluxional behaviors in solution of two indolide/Al complexes (namely, **L^2AlOBn** and **L^7AlOBn**) supported by an analog of salen incorporating indolide arms connected via their 2- and 7-positions were defined by experiment and theory. The complexes catalyze the stereoselective conversion of *rac*-LA to isotactically enriched PLA. A key aspect of the stereocontrol was examined through study of polymerization initiation via NMR spectroscopy, X-ray crystallography of the 1:1 catalyst:monomer ring-opened products, and theory. The results include the first unambiguous structural definition of stereocontrol in ring-opening of LA by a metal-alkoxide complex and the finding that definition of the stereochemistry of initiation by the studied system is governed thermodynamically rather than kinetically.

4.2 Introduction

An important goal of contemporary research is to develop catalysts capable of polymerizing bio-derived monomers with high selectivity, good molecular weight control, fast and/or convenient rates, and sufficient robustness to operate under potentially useful and/or industrially relevant conditions.[7,21,22,149] The stereoselective ROP of *rac*-LA to yield PLA has been particularly well-studied[131] because of the utility of PLA in a wide range of applications, and because of the importance PLA tacticity plays in determining its material properties.[150,151] As stated, among the breadth of catalysts examined for this purpose, (salen)AlOR complexes (Figure 4.1) have garnered considerable attention due to their high molecular weight control, rates convenient for NMR spectroscopic monitoring, and ease of synthesis of ligand derivatives, with several having engendered high stereoselectivity in polymerizations of *rac*-LA.[34,37,154–159]

While previous work involving such catalysts has provided considerable insight, detailed molecular-level mechanistic understanding is limited, and further work is needed to address such issues as the impact of supporting ligand structural features on polymerization behavior, the specific molecular basis for observed stereocontrol using both chiral and achiral supporting ligands, and the precise structures of key intermediates. Such understanding is of potential utility for future catalyst design.

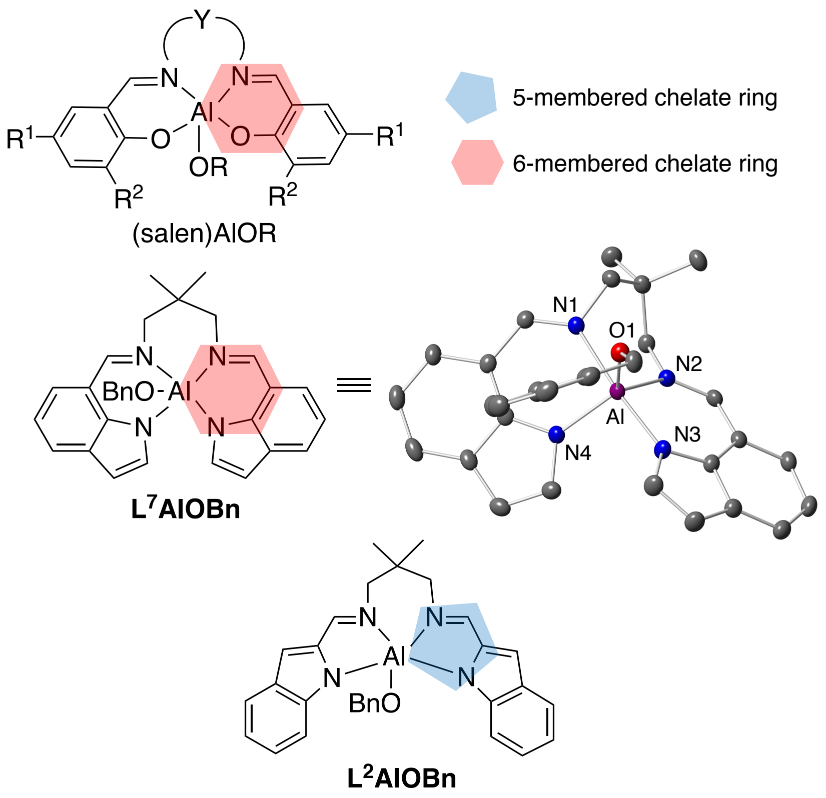

Figure 4.1. Complexes used as ROP catalysts. X-ray crystal structure reported in reference 167 (Λ isomer shown).

Recently, predictions by theory of cyclic ester polymerization efficiency for a series of Al catalysts, including the complex **L^{7}AlOBn** (formerly named **3.14**, *Chapter 3*) supported by a novel analog of salen incorporating indolide arms connected at their 7-position (Figure 4.1) was reported[136] (see *Chapter 3* for details). Subsequent synthesis of **L^{7}AlOBn** and studies of the kinetics of ROP of CL by the complex confirmed the prediction, validating the theoretical approach towards catalyst design. In that work, the X-ray crystal structure of the complex revealed a chiral structure with the ligand twisted such that the indolide rings are inequivalent. NMR spectroscopy showed the rings to be equivalent, however, suggesting operation of a fluxional process in solution. In view of these structural attributes and analogies to efficacious (salen)AlOR systems (for example, (salen)^{N}AlOR, with Y =

$CH_2CMe_2CH_2$, R^1 = H, R^2 = TBS),[34] we hypothesized that **L^{7}AlOBn** might exert stereocontrol in ROP of *rac*-LA.

Herein, the evaluation of the fluxionality of **L^{7}AlOBn** in solution by variable temperature (VT) NMR spectroscopy, theory, and studies of the ROP of *rac*-LA by the complex is described. Also, its structural features and reactivity to an analogous complex **L^{2}AlOBn** in which the indolide rings are connected at the 2- rather than the 7-position to yield 5- instead of 6-membered chelate rings (Figure 4.1) are compared.[137] Most of the work involving **L^{2}AlOBn** was completed by collaborator Appie Peterson, and while some of the key results learned from studying this complex are described herein, a more wholistic look into the catalyst, its characterization and its ability to polymerize *rac*-LA are included in published work.[47]

It is important to note that as this work was being completed, the synthesis and use of L^{2}AlO*i*Pr in stereoselective polymerizations of LA, as well as the identification of a ring-opened LA complex, were reported, but the rationale for selectivity in ROP was not studied.[160] In this work however, through synergistic theoretical and experimental approaches, the effects of the supporting ligand differences on the ROP behavior of **L^{2}AlOBn** and **L^{7}AlOBn** were evaluated, with a specific emphasis on understanding the basis of the observed stereocontrol in the first ring-opening step (initiation) of *rac*-LA. Among our findings are precise structural determinations by X-ray crystallography of the initial products of ring-opening of *rac*-LA by metal-alkoxide complexes, revealing the stereochemistry of initiation. In addition, said initiation was evaluated by both two-dimensional NMR spectroscopy and theory, leading to new insights into the basis for stereoselectivity and a key finding of thermodynamic rather than kinetic governance of stereocontrol. These studies, placed in perspective through comparisons to (salen)AlOR systems and, more broadly, to many other catalysts,[34,43,45,51,80,153–161] provide deep mechanistic understanding of ROP reactions of importance for sustainable polymer synthesis.

4.3 Results and Discussion

4.3.1 *Synthesis and Characterization of Complexes*

The complex **L^7AlOBn** was prepared as described previously[136] and the synthesis of **L^2AlOBn** was performed similarly (additional details provided in published work).[47] Both **L^2AlOBn** and **L^7AlOBn** were characterized by CHN analysis and NMR spectroscopy, as well as X-ray crystallography (details of **L^7AlOBn** synthesis and characterization are included in *Chapter 3*). The structure of **L^2AlOBn** features distorted tbp geometry, with a τ_5 value of 0.62 (theory: 0.68) similar to that reported for L^2AlO*i*Pr (0.65).[160] By comparison, the values for **L^7AlOBn** and **^{N}AlOBn**[34] are 0.87 and 0.83, respectively, indicating geometries closer to ideal tbp for these complexes. Each of the complexes crystallizes as a mixture of enantiomers; for the complexes of $(L^2)^{2-}$ and $(L^7)^{2-}$, the ligand in each stereoisomer is twisted so that the indolide rings are inequivalent, with the enantiomers differentiated by the indolide ring orientation (labeled as Δ or Λ as indicated in Figure 4.2).

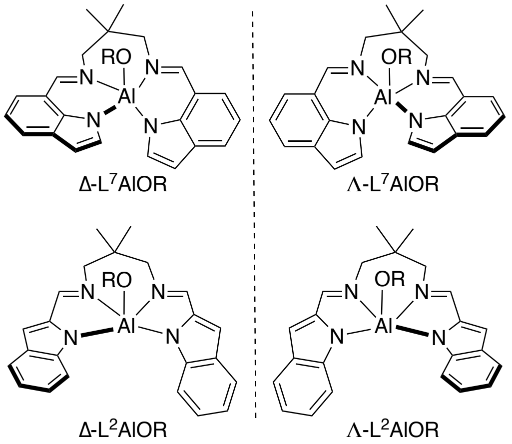

Δ-L^{7}AlOR

Λ-L^{7}AlOR

Δ-L^{2}AlOR

Λ-L^{2}AlOR

Figure 4.2. Enantiomers of complexes L^{7}AlOR and L^{2}AlOR (R = Bn), with labeling of chirality indicated.

The inequivalence of the indolide rings in the X-ray structures of **L^{2}AlOBn** and **L^{7}AlOBn** is not reflected in their ^{1}H NMR spectra at 300 K, as only one set of peaks for the indolide and imine hydrogen atoms is observed (example **L^{7}AlOBn**, Figure 4.3). This observation suggests a fluxional process that interconverts the indolide ring environments and is sufficiently rapid on the NMR time scale to result in averaging of the associated peaks. This hypothesis was confirmed through VT NMR experiments for both complexes (that of **L^{7}AlOBn** featured in Figure 4.3, entire spectrum in Figure 4.19, section 4.5.6). Illustrative peaks for the hydrogen atoms on the imine and the 6-position of the indolide rings for L^7 and 7-position for L^2 undergo reversible decoalescence to yield a peak pattern indicative of inequivalent indolide rings upon lowering the temperature. Spectral fitting and Eyring analyses (Figures 4.21–4.22 and Table 4.2, section 4.5.6) yielded $\Delta G^{\ddagger}_{298K}$ = 10.2 kcal/mol and 10.7 kcal/mol for the processes for **L^{7}AlOBn** and **L^{2}AlOBn**, respectively. As similar fluxionality had been proposed for (salen)AlOR complexes[34] (Figure 4.1); **^{N}AlOBn** was prepared according to the literature procedure[34] and through VT NMR studies determined $\Delta G^{\ddagger}_{298K}$, which was similar (9.0 kcal/mol).

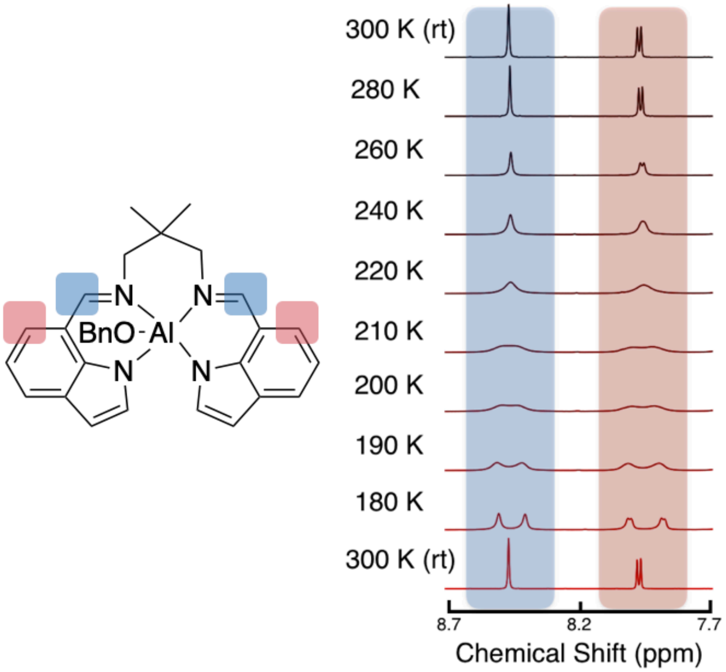

Figure 4.3. Selected VT NMR (^{1}H) data for **L^{7}AlOBn** with proposed assignments. The bottom spectra were collected after returning to room temperature to show reversibility. Full spectra are shown in Figure 4.19, section 4.5.6.

Hypothesizing that the fluxionality observed in solution was derived from interconversion of the Δ and Λ enantiomers of the complexes (Figure 4.2), DFT calculations to interrogate the process were performed. After a thorough conformational search to find all the low-lying conformers of **L^{2}AlOBn** and **L^{7}AlOBn**, the barrier for chirality inversion for the complexes was then found through optimizing the transition state structures. The barriers found for the complexes were similar (**L^{7}AlOBn** = 9.9 kcal/mol; **L^{2}AlOBn** = 11.6 kcal/mol) and agreed closely with those found experimentally (10.2 and 10.7 kcal/mol, respectively). For **L^{7}AlOBn**, the lowest energy conformer has a twist-boat-like conformation in the six-membered metallacycle formed by the Al atom and the ligand backbone, whereas in the transition state, the metallacycle has a more symmetric chair-like conformation. As a result, the fluxional process happens in two steps, involving conformational change of the metallacycle followed by movement of the rings into the more symmetric transition state (Figure 4.4). For **L^{2}AlOBn**, the metallacycle is already in a chair-like conformation, so the chirality flipping happens in one step. Finally, we note parenthetically that the catalyst fluxionality for these systems resembles that proposed for Ti complexes that catalyze syndiospecific propene polymerization.[162,163]

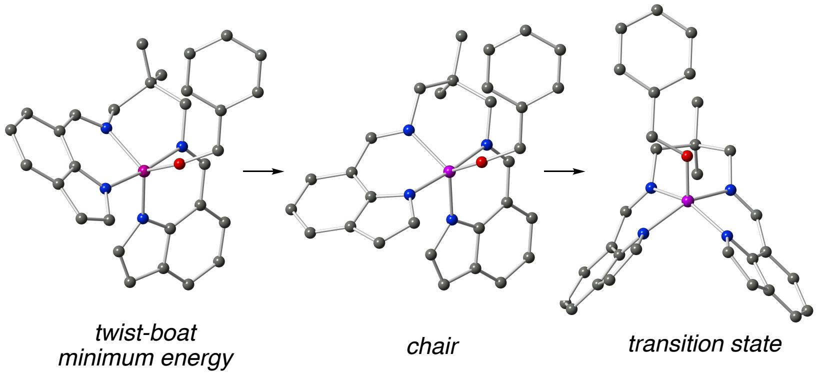

Figure 4.4. Calculated structures for the fluxional process that interconverts Δ and Λ enantiomers of **L^{7}AlOBn**, depicting the lowest energy structure for the Δ enantiomer, the next highest energy (+2.3 kcal/mol) structure for the chair conformation of the metallacycle, and the "symmetric" transition state structure.

4.3.2 *Polymerization Behavior*

The catalytic polymerization of *rac*-LA by **L^{7}AlOBn** and **L^{2}AlOBn** under a variety of conditions, ranging from 35 °C in CD_2Cl_2 (300:1 monomer:catalyst ratio, except in the case of toluene) to neat reactions in the melt (135–180 °C) was examined. As indicated in Table 4.1, the reactions proceeded at rates that depended on the conditions used to yield PLA characterized by low $Đ$ values (measured by SEC using light scattering detection) and P_m values (measured via analysis of homonuclear decoupled ^{1}H NMR data, example in Figure 4.23, section 4.5.7). These latter values varied from 0.53 (low isotacticity, entries 9 and 14) to 0.80 (high isotacticity, entries 1 and 2), depending on the supporting ligand and the conditions. DSC data revealed T_m features in only three cases (entries 1–3, Table 4.1, example plots shown in Figure 4.24, section 4.5.8), indicating attainment of isotactic segment lengths sufficient for crystallization only in these instances. Previously reported data for **^{N}AlOBn**[34] are shown for comparison (entries 15, 17, 19, Table 4.1), along with data for the same complex that we prepared and tested independently (entries 16, 18, 20, Table 4.1) that are in good agreement. In general, the level of stereocontrol exhibited by **^{N}AlOBn** was higher than for **L^7AlOBn** and **L^2AlOBn**. The stereoselectivity exhibited by the complex of $(L^7)^{2-}$ is slightly higher than that supported by $(L^2)^{2-}$, which exhibits faster rates than the former. As such, for both complexes, comparison of the polymerization kinetics of L-LA vs. *rac*-LA showed a higher rate for the single enantiomer (see Figure 4.14, section 4.5.4).

Table 4.1. Data for polymerizations of *rac*-LA by the indicated complexes.

Entry[a]	**Temp. (°C)**	**LA:cat**	**Time**	**Conv.**[b]	M_n **(kDa)**[c]	**Đ**[c]	P_m[d]	T_m **(°C)**[e]
L^7 1	35 (CD_2Cl_2)	300	14 d	99%	85	1.06	0.80	163
L^7 2	55 (THF-d_8)	300	4 d	99%	36	1.03	0.80	155
L^7 3	70 (tol-d_8)	100	3 d	98%	24	1.20	0.74	150
L^7 4	135	300	30 min	96%	40	1.11	0.64	*f*
L^7 5	150	300	25 min	78%	85	1.22	0.63	*f*
L^7 6	165	300	20 min	91%	29	1.16	0.66	*f*
L^7 7	180	300	15 min	93%	54	1.44	0.68	*f*
L^2 8	35 (CD_2Cl_2)	300	6 d	95%	35	1.08	0.67	*f*
L^2 9	55 (THF-d_8)	300	2 d	99%	42	1.17	0.53	*f*
L^2 10	70 (tol-d_8)	100	3 d	98%	24	1.31	0.67	*f*
L^2 11	135	300	30 min	93%	34	1.74	0.58	*f*
L^2 12	150	300	25 min	94%	60	1.85	0.62	*f*
L^2 13	165	300	20 min	79%	115	1.31	0.55	*f*
L^2 14	180	300	15 min	99%	64	1.23	0.53	*f*
^{N} 15[g]	70 (tol-d_8)	100	14 h	96%	22[h]	1.07[h]	0.98	209
^{N} 16				*96%*	*25*[h]	*1.07*[h]	*0.92*	*207*
^{N} 17[g]	130	300	30 min	73%	44[h]	1.08[h]	0.92	189
^{N} 18				*79%*	*53*	*1.15*	*0.89*	*187*
^{N} 19[g]	180	300	20 min	91%	60[h]	1.13[h]	0.84	176
^{N} 20				*90%*	*59*	*1.34*	*0.85*	*179*

[a] L^7 = **L^{7}AlOBn**, L^2 = **L^{2}AlOBn**, ^{N} = **^{N}AlOBn**. [b] Determined by ^{1}H NMR spectroscopy. [c] Except as noted, these values were determined by SEC using light scattering detection with THF eluent. Theoretical values are 44 kDa for 300 equiv. of LA and 15 kDa for 100 equiv. LA. [d] Determined by homonuclear decoupled ^{1}H NMR spectroscopy. [e] Determined by DSC. [f] No feature corresponding to a T_m value was observed. [g] Previously reported values (reference 34) with values we independently determined below in italics. [h] Values determined by SEC using a refractive index detector and polystyrene standards with $CHCl_3$ eluent.

4.3.3 *Experimental Insights into Stereocontrol in Initiation*

In order to begin to understand the basis for stereocontrol for LA polymerization by **L^{7}AlOBn**, stoichiometric reactions of *rac*-, L(*S,S*)-, and D(*R,R*)-LA with the complexes, as well as with ^{N}**AlOBn** for comparison were examined. In the experiments, a solution of LA (1 equiv.) in CD_2Cl_2 or $CDCl_3$ was added to a solution of the complex in the same solvent (6.5 mM) at room temperature and a ^{1}H NMR spectrum was immediately measured. The spectra showed complete consumption of starting materials and the appearance of predominantly one species with new peaks that we assign to the single ring-opened product L^{7}Al(oLAOBn) (where oLAOBn refers to the ring-opened LA terminated by -OBn; Figure 4.5) or ^{N}Al(oLAOBn) (Figure 4.16, section 4.5.5), as reported previously.[34] Importantly, the spectra for the products of the reactions with *rac*-, L(*S,S*)-, and D(*R,R*)-LA are nearly identical (Figures 4.6 and 4.17, section 4.5.5).

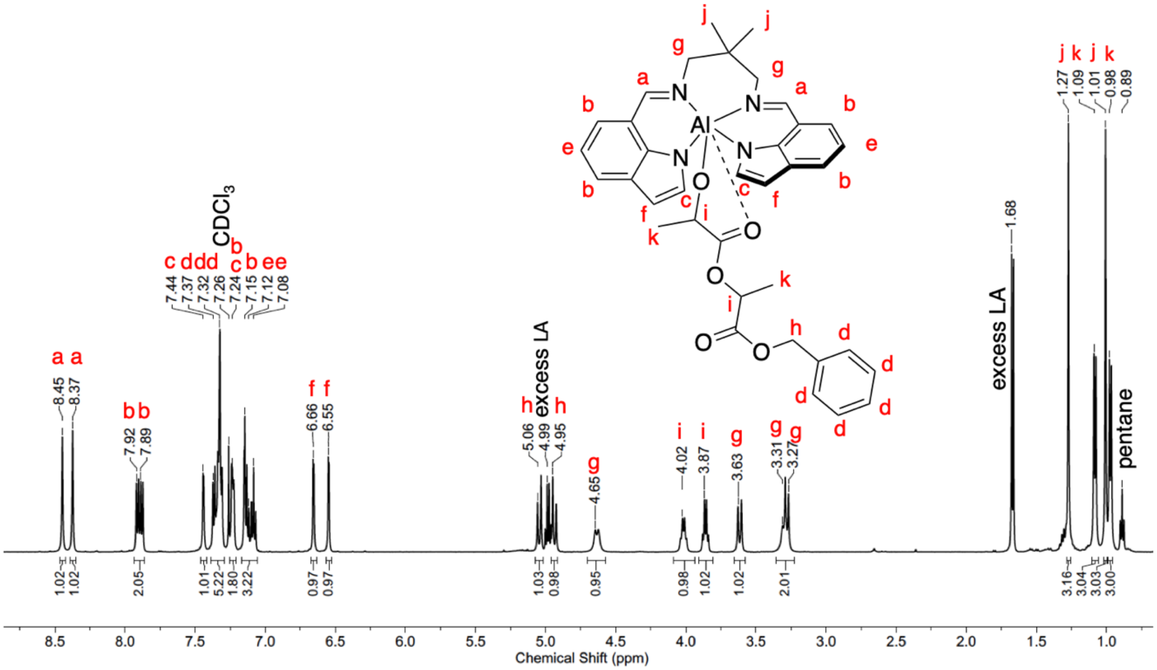

Figure 4.5. ^{1}H NMR spectrum of 1:1 *rac*-LA:**L^{7}AlOBn**.

The peak patterns are consistent with selective formation of either a 1:1 mixture of two symmetric complexes (i.e., indolide or phenolate rings are equivalent for each, which would only be possible if peaks due to diastereomeric species were averaged as a result of fluxionality) or a single asymmetric complex (with inequivalent rings). Thus, for example, the spectra of L^{7}Al(oLAOBn) exhibit two peaks (8.37 and 8.45 ppm) integrating equally for the imine protons.

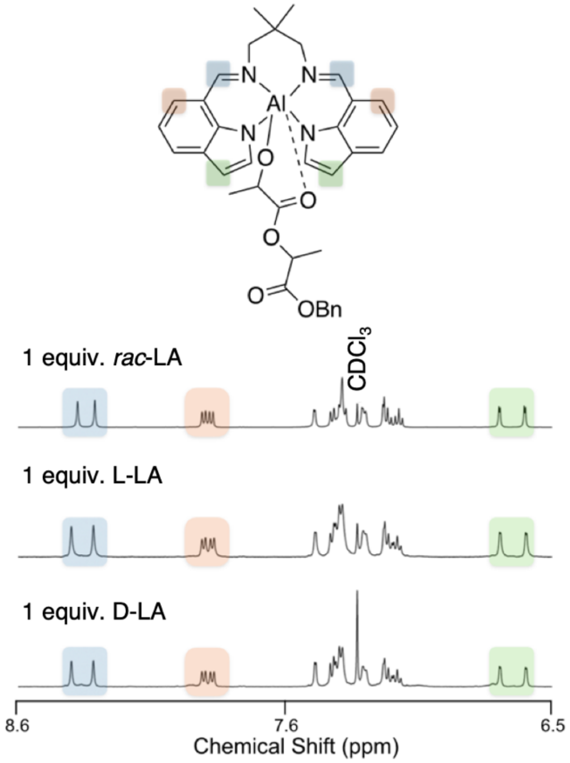

Figure 4.6. Selected portion of the ^{1}H NMR spectra of the products of the reactions of (top) *rac*-LA, (middle) L(*S,S*)-LA, or (bottom) D(*R,R*)-LA with **L^{7}AlOBn**, with the indicated assignments.

To interpret the results from NMR spectroscopy, we present all the possible structures for the products of ring-opening of D(*R,R*)- and L(*S,S*)-LA by the two interconverting stereoisomers of **L^{7}AlOBn** in Scheme 4.1. Thus, each stereoisomer Δ- or Λ-**L^{7}AlOBn** can react with either L(*S,S*)-LA or D(*R,R*)-LA. The result is four possible stereoisomers, classified as two diastereomeric pairs of enantiomers: Δ-L(*S,S*)/Λ-D(*R,R*) and Δ-D(*R,R*)/Λ-L(*S,S*). These are drawn with the opened LA chain binding in bidentate fashion via alkoxide and carbonyl O atoms, which is what was observed via X-ray crystallography (*via infra*). Each pair of enantiomers (i.e., each diastereomeric set) would be expected to give rise to a spectrum featuring inequivalent indolide rings and one set of peaks associated with the opened LA chain. The observed spectrum for the reaction with *rac*-LA (e.g., the pairs of peaks of equal intensity shown in Figure 4.6) is consistent with highly stereoselective formation of *one* of the diastereomeric sets (i.e., one pair of enantiomers). The observation of the same spectrum in reactions of pure L(*S,S*)- or D(*R,R*)-LA is explained by selective formation of one diastereomer (i.e., for the reaction with L(*S,S*)-LA, either Δ-L(*S,S*) or Λ-L(*S,S*)). The NMR data are not sufficient to distinguish which set of enantiomers (for the reaction with *rac*-LA) or which particular diastereomer (for the reactions with pure L(*S,S*)- or D(*R,R*)-LA) is formed. The alternative explanation that the peaks observed are due to a rapidly interconverting mixture of *both* diastereomers would predict line broadening or decoalescence of these peaks upon lowering the temperature, but this was not observed (to –185 K, Figure 4.20, section 4.5.6). While the imine peaks in the spectrum were not perturbed upon lowering the temperature, significant changes in the peaks arising from the ring-opened LA chain were observed. This is speculated to be due to changes in chain conformations, but we do not offer further unambiguous insights, in part due to the complexity of the chain structures. It is also noted that the alternative explanation for the two imine peaks (averaging of peaks due to both diastereomers being present) is inconsistent with the EXSY data that is discussed later in this section. Finally, we note that similar considerations apply to the ^{N}Al system.

Scheme 4.1. Possible products L^{7}Al(oLAOBn) resulting from the reaction of the interconverting stereoisomers **L^{7}AlOBn** (in box) with L(*S,S*)- and D(*R,R*)-LA, labeled according to the configuration at Al (Δ vs. Λ) and LA (D(*R,R*) vs. L(*S,S*)). The isomers labeled "X-ray" are the ones identified by X-ray crystallography.

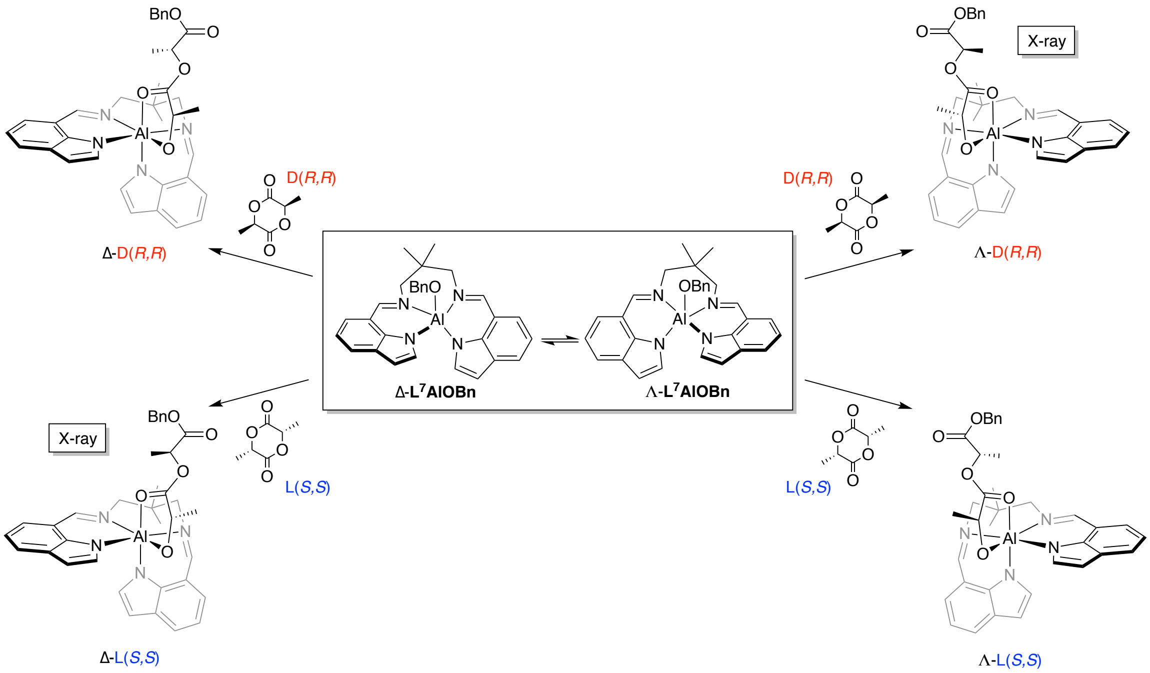

By layering pentane on CD$_2$Cl$_2$ solutions of the product L^{7}Al(oLAOBn) (formed upon stoichiometric reaction of **L^{7}AlOBn** with *rac*-LA) and storing at –30 °C, crystals suitable for X-ray diffraction were obtained (Figure 4.7, the crystal structure of L^{2}Al(oLAOBn) is featured in published work).[168] In both cases, the ring-opened products crystallized as a pair of enantiomers comprising a *single* diastereomer, consistent with our interpretation of the ^{1}H NMR spectra of the product solutions. These enantiomers were identified as the complexes labeled Δ-L(*S,S*) and Λ-D(*R,R*) in Scheme 4.1, with only the former enantiomer for each case shown in Figure 4.7. In the structure, the Al-O1 (alkoxide) distance (1.807(3) Å) is shorter than all other metal-ligand bonds (range 2.094(7)-1.932(3) Å). The Al geometries are octahedral, with the ring-opened LA bound in bidentate fashion featuring Al-O2 distances of 2.094(7) Å and 2.1784(17) Å, respectively. This X-ray structure, along with that of L^{2}Al(oLAOBn),[47] represents a rare example of a high-quality structural determination for ring-opened LA bound to a metal complex.[164,165] Such species had been previously identified by spectroscopy[80,157,161,166] and modeled in structures of methyl lactate complexes (one collected from a stoichiometric reaction with $^{\mathbf{N}}$**AlOBn** and methyl (*S*) lactate, yielding a similar hexacoordinate complex with Al-O (carbonyl) and Al-O (alkoxide) bond distances of 2.165 and 1.840 Å, respectively,[34] and the other being that of a (BDI)Zn complex, synthesized via *rac*-methyl lactate, featuring slightly longer bond distances with Zn-O (carbonyl) and Zn-O (alkoxide) of 2.189 and 1.879 Å, respectively.[35]

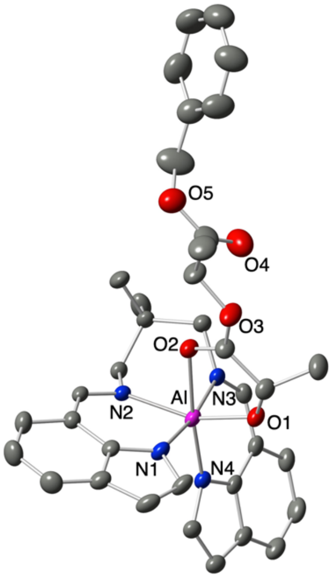

Figure 4.7. Representation of the X-ray crystal structure of the ring-opened product, L^{7}Al(oLAOBn), resulting from the reaction of **L^{7}AlOBn** with 1 equiv. *rac*-LA. Only a single enantiomer is shown (Δ-L(*S,S*); the other Λ-D(*R,R*) enantiomer is also present in the unit cell), with all atoms presented as 50% ellipsoids and hydrogen atoms omitted for clarity. Selected bond distances (Å) and angles (deg): Al1-O1, 1.807(3); Al1-N1, 1.9475(18); Al1-N2, 2.0647(16); Al1-N3, 2.0779(18); Al1-N4, 1.9344(17); N3-Al-N1, 171.24(7); N3-Al1-O1, 90.80(8); N3-Al1-O2, 89.33(13); N3-Al1-N2, 82.69(6); N3-Al1-N4, 89.49(7); N2-Al1-N4, 103.71(7); O2-Al1-O1, 79.47(11); N2-Al1-O2, 81.07(9); N4-Al1-O1, 95.56(9); N4-Al1-O2, 174.88(12); N1-Al1-N4, 94.99(7); N1-Al1-N2, 88.93(7); N1-Al1-O2, 86.84(14); N1-Al1-O1, 96.24(9).

Re-dissolution of the crystals used for the X-ray structure determinations yielded ^{1}H NMR spectra identical to those obtained for the initial product solutions. These results are consistent with the NMR spectral features arising from the Δ-L(*S,S*) and Λ-D(*R,R*) enantiomers (the single diastereomer) observed by X-ray crystallography. Nonetheless, it is also possible that the diastereomer observed by NMR spectroscopy participates in an equilibrium with a small (essentially unobservable) amount of the other diastereomer (*vide infra*), and that this minor diastereomer preferentially crystallizes (and reverts to the major diastereomer upon redissolution). While we view this alternative possibility as unlikely (preferential crystallization of an equilibrating minor diastereomer for *both* $(L^2)^{2-}$ and $(L^7)^{2-}$ systems), it cannot be ruled out by the available experimental data. The above considerations raise the question: Is the initiation reaction selectivity based on kinetic or thermodynamic control? That is, does the initiation stereoselectivity result from differences in the barriers for ring-opening (as postulated previously on the basis of theory for other catalysts)[167] or from differences in the stabilities of the products that are rapidly equilibrating? Such equilibration might involve rapid intermolecular exchange of alkoxide ligands (e.g., between Δ-L(*S,S*) and Δ-D(*R,R*) isomers), de-coordination of the carbonyl group and racemization at Al as observed for the fluxionality of LAlOBn (e.g., between Δ-L(*S,S*) and Λ-L(*S,S*) isomers), or both (Figure 4.8).

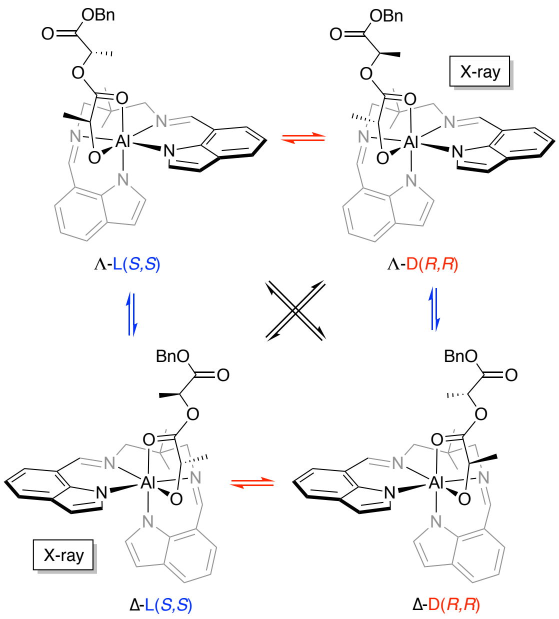

Figure 4.8. Illustration of possible interconversions of stereoisomers L^7Al(oLAOBn). The red arrows indicate processes involving intermolecular exchange of LA enantiomers, blue arrows correspond to racemization at Al (e.g., via carbonyl de-coordination, isomerization, and re-coordination), and black arrows correspond to both.

To test for these possibilities, we performed a set of experiments using NMR Exchange Spectroscopy (EXSY).[168] The experiments involved acquisition of data on solutions of (a) L^7Al(oLAOBn) prepared from reactions of the respective benzyloxide complexes with *rac*-LA, (b) L^7Al(oLAOBn) prepared from reaction of **L^7AlOBn** with L(*S*,*S*)-LA, (c) a 1:1 mixture of L^7Al(oLAOBn) and L^2Al(oLAOBn) prepared by mixing solutions resulting from reaction of the respective benzyloxide complexes with *rac*-LA, and (d) a 1:1 mixture of L^7Al(oLAOBn) and **^{N}AlOBn** prepared by mixing solutions resulting from reaction of the respective benzyloxide complexes with *rac*-LA. The detailed methods and interpretations of all studies are described in section 4.5.9, yet key results are shared herein.

From (a), we interpreted the observed EXSY peaks (blue off-diagonal peaks, whereas red = NOESY signals) to indicate exchange between the major diastereomer L^7Al(oLAOBn) with a minor one. Thus, the methine proton resonances corresponding to that of the alkoxide ligand in the major diastereomer (**a**) exchange with those attributed to the minor one (**b)** (relationships designated by purple circles in the spectrum and purple arrows in the scheme, Figure 4.9). Similarly, the methylene proton resonances of the benzyl group were observed to exchange (**c** and **e**), serving as clear evidence of exchange between the ring-opened alkoxide chains. To confirm the assignment of **b** as that of a methine resonance from an alkoxide ligand in the minor diastereomer, a COSY NMR experiment was run on the same sample, and correlation between **b** and a small doublet in the alkyl region (characterized to be a LA methyl resonance on the same ligand) was observed (Figure 4.25, section 4.5.9).

Figure 4.9 also shows exchange between the backbone protons of the major complex (**d**, green circles in the spectrum and green arrows in the scheme). This exchange was hypothesized to be a result of the backbone protons changing position due to interconversion of enantiomers, which could occur by alkoxide exchange, racemization at Al, or both.

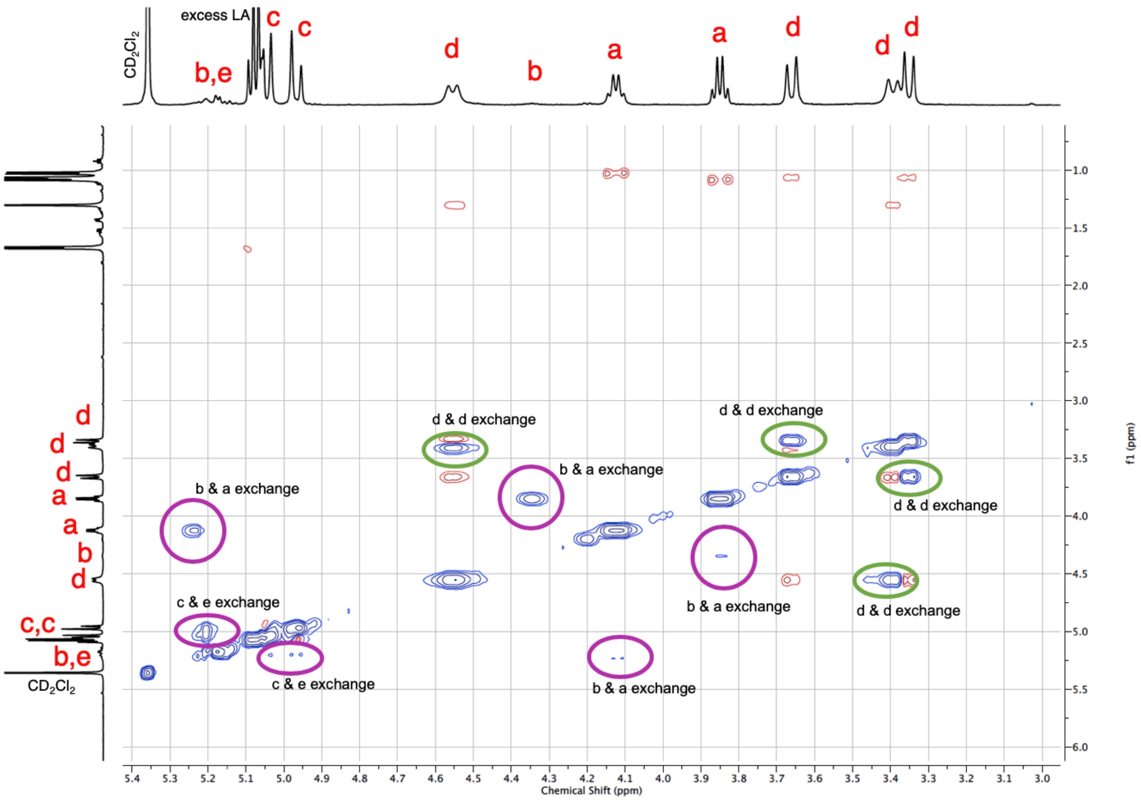

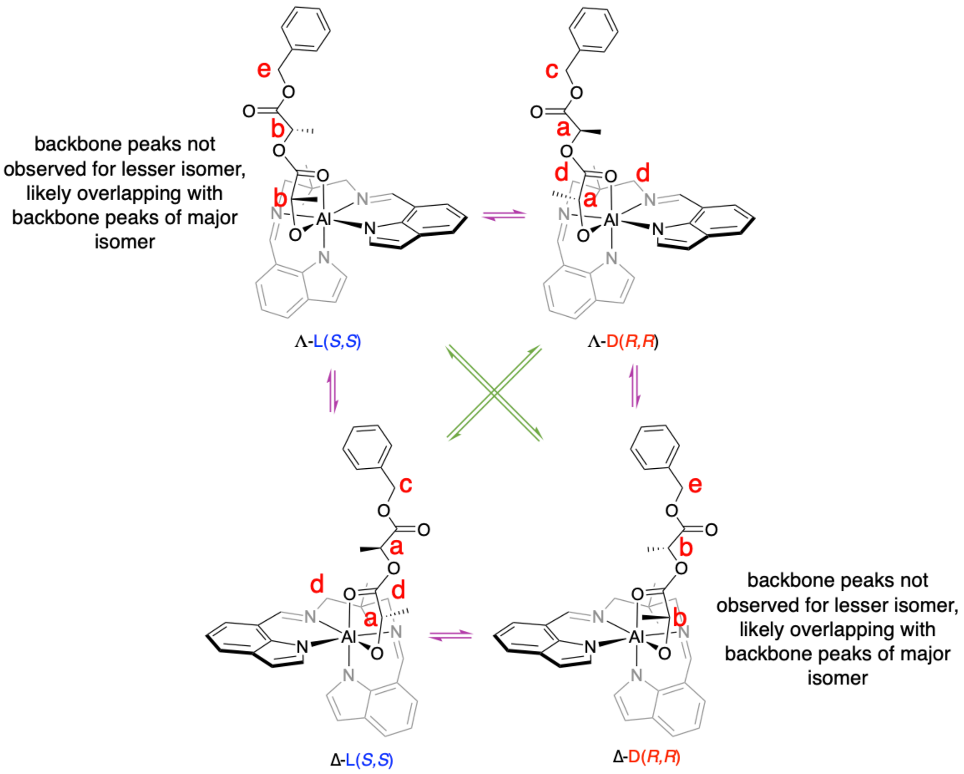

Figure 4.9. NOESY/EXSY NMR spectrum of the product of reaction of *rac*-LA with $\mathbf{L^7AlOBn}$ (i.e., $L^7Al(oLAOBn)$) (top) and corresponding equilibrium scheme hypothesized to explain the results (bottom). Both diastereomeric (purple) and enantiomeric exchange (green) are observed. While we assign the major isomer in the spectrum as Δ-L(*S,S*) (and consequently, its enantiomer as Λ-D(*R,R*)) due to the results of X-ray crystallography, we note the possibility that these assignments may be reversed if the minor isomer is that which was identified by crystallography.

By integration, the ratio (K_{eq}) of the equilibrating major:minor isomers for $L^7Al(oLAOBn)$ is ~9:1, corresponding to $\Delta G°_{298} = -1.3$ kcal/mol. Using EXSYcalc,[169] rate constants of 4.1 s^{-1} and 0.44 s^{-1} were obtained, which correspond to $K_{eq} \sim 9$, in good agreement with the integration ratio. Similar results for $L^2Al(oLAOBn)$, (K_{eq} by integration ~9.5, K_{eq} via EXSYcalc ~8.8) were observed.[47]

To test the assignment of the exchange peaks in Figure 4.9 for protons **d**, NOESY/EXSY NMR data were collected for the product of reaction of L-LA with $\mathbf{L^7AlOBn}$ (experiment b). Results from (b) indicated the same alkoxide peaks for exchange between diastereomers as observed in the data for the product of reaction of *rac*-LA (purple circles in the spectrum and purple arrows in the scheme, Figure 4.26, section 4.5.9), consistent with racemization at Al. However, no peaks were observed for exchange between the backbone protons. These data are consistent with the hypothesis that such exchange peaks in Figure 4.9 derive from exchange between enantiomers, which are not present in the experiment with L-LA. We recognize that diastereotopic backbone peaks are not observed for the minor isomer in Figures 4.9 or 4.26 (section 4.5.9), which is hypothesized to be due to overlapping chemical shifts, such that any exchange peaks between the major and minor isomers backbone signals lie in the diagonal of the spectra.

To test for intermolecular exchange of alkoxide ligands between two different Al centers, two "crossover" NOESY/EXSY experiments were performed. In one, (c), equimolar amounts of the products of reaction of *rac*-LA with **L^7AlOBn** and with **L^2AlOBn** (i.e., L^7Al(oLAOBn) + L^2Al(oLAOBn) were mixed (see the ^{1}H NMR data in Figure 4.27, section 4.5.9) and NOESY/EXSY data collected (Figure 4.10). Importantly, exchange between the two complexes was observed (black circles and arrows), confirming intermolecular alkoxide exchange. In addition, exchange was observed for the alkoxide peaks for both L^7Al(oLAOBn) and its minor isomer, and L^2Al(oLAOBn) and its minor isomer (denoted by purple and pink relationships, respectively). Enantiomer exchange of backbone peaks was observed for both L^7Al(oLAOBn) (green circles and arrows) and L^2Al(oLAOBn) (orange circles and arrows), as well. Taken together, the data are consistent with intermolecular alkoxide exchange and racemization at Al.

In a second "crossover" experiment, (d), L^7(oLAOBn) and ^{N}Al(oLAOBn) were mixed; ^{1}H NMR data are shown in Figure 4.28, section 4.5.9 and NOESY/EXSY data are shown in Figure 4.29. The latter showed exchange between *both* the major and minor isomers of L^7(oLAOBn) and ^{N}Al(oLAOBn) (teal and black circles and arrows, respectively), consistent with intermolecular alkoxide exchange. Exchange between the major and minor isomers of L^7(oLAOBn) is also apparent (purple circles and arrows).

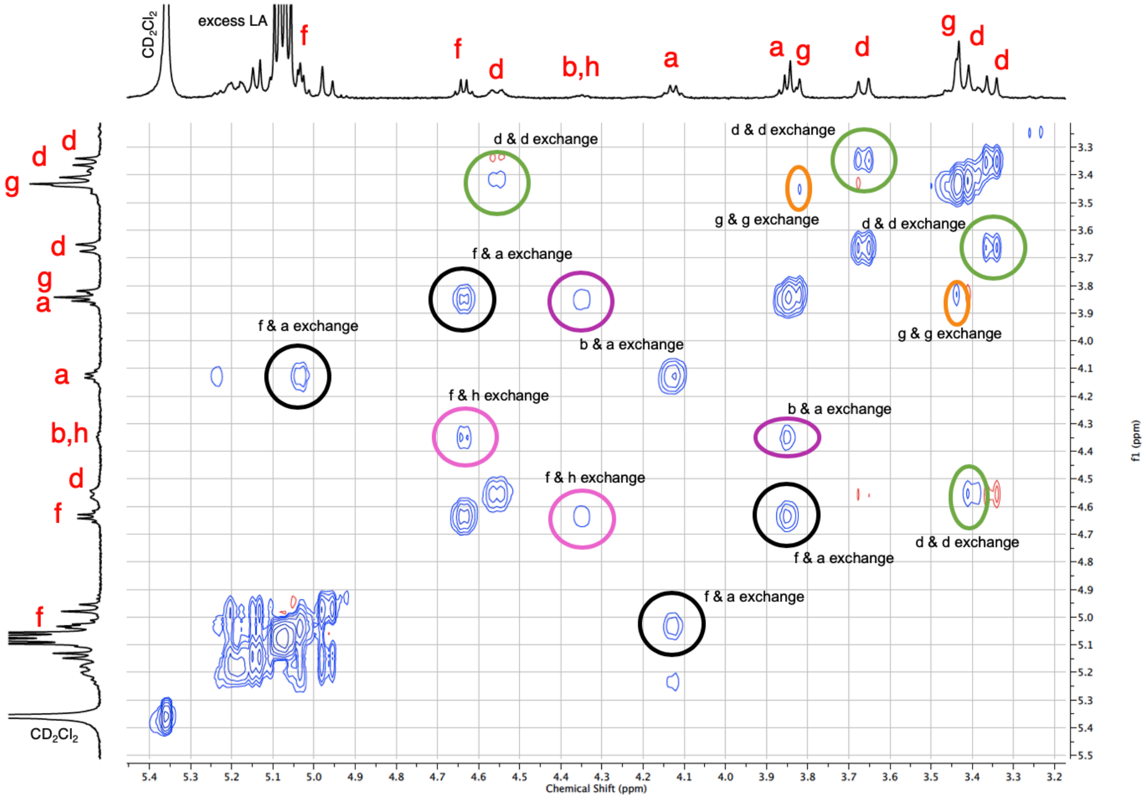

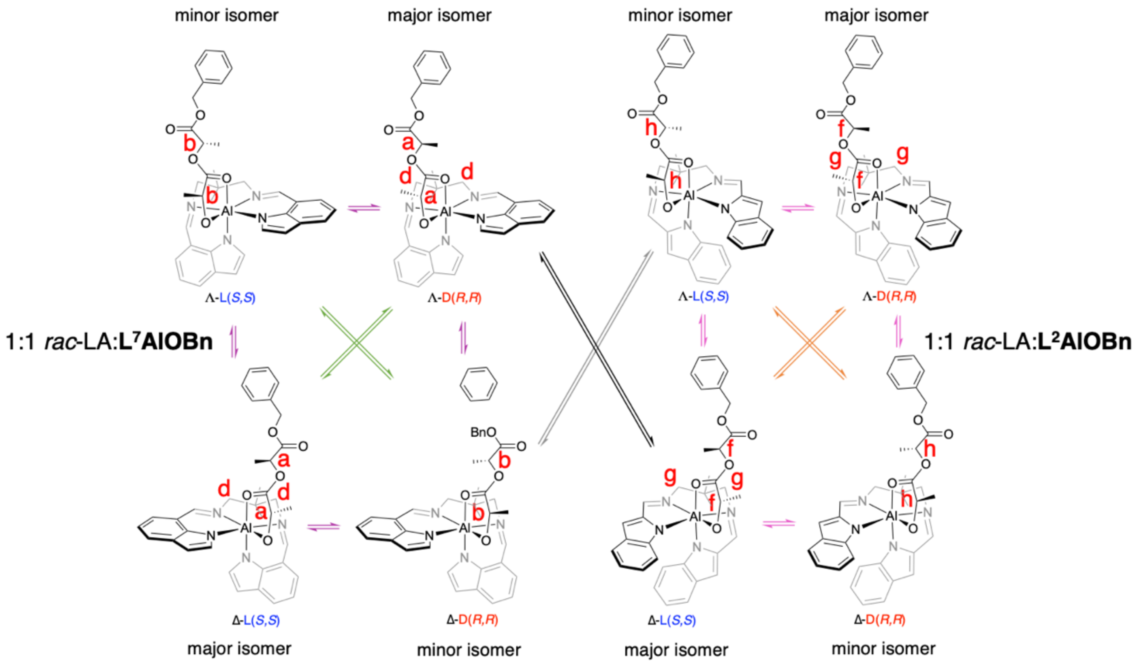

Figure 4.10. NOESY/EXSY spectrum of mixture of equimolar amounts of L^{7}Al(oLAOBn) and L^{2}Al(oLAOBn) (top) and equilibrium scheme hypothesized to rationalize the results (bottom). Exchange of alkoxide ligands between Al centers is denoted in black, diastereomeric exchanges are denoted in purple and pink, and backbone enantiomer exchanges are denoted in green and orange. The exchange between minor isomers of both the 1:1 *rac*-LA:**L^{7}AlOBn** and 1:1 *rac*-LA:**L^{2}AlOBn** is shown in grey, but is not observed in the NOESY/EXSY spectrum (postulated to be due to peak overlap).

Taken together, the EXSY data are consistent with rapid equilibria in solution between all species (illustrated in Figure 4.8 for the case of L^{7}Al(oLAOBn)), favoring one diastereoisomeric pair (K_{eq} = 9), via all possible pathways (intermolecular alkoxide exchange and racemization at Al). Importantly, the data support thermodynamic control of stereoselectivity in the initiation, such that the product ratio is controlled by the relative stability of the products that rapidly equilibrate.

Similar stoichiometric experiments between of **L^{7}AlOBn** and *meso*-LA were performed, to see if the same initiation selectivity was observed with a molecule with differing stereochemistry (i.e., one *(R)* and one *(S)* stereocenter). As with 1 equiv. of *rac*-LA, the reaction of **L^{7}AlOBn** and 1 equiv. of *meso*-LA could lead to four different species, (two sets of diastereomeric enantiomers, see Scheme 4.2).

Scheme 4.2. Possible products resulting from the reaction of the interconverting stereoisomers **L^{7}AlOBn** (in box) with *meso*-LA, labeled according to the configuration at Al (Δ vs. Λ) and LA ((*R*) vs. (*S*)).

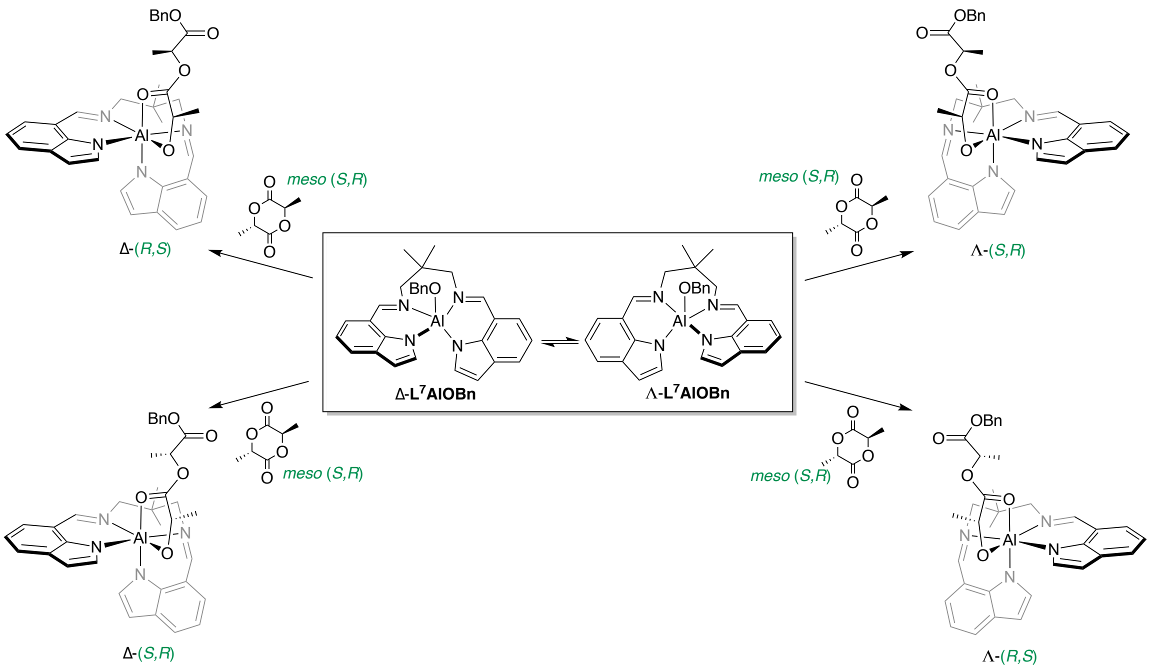

As such, ^{1}H NMR data from the 1:1 reaction between **L^{7}AlOBn** and *meso*-LA led to a similar NMR spectrum compared to that of the analogous 1:1 reaction completed with *rac*-LA (i.e., a doubling of peaks of equal intensity, indicating asymmetric enantiomers were present, with no significant indication of diastereomeric peaks, Figure 4.18, section 4.5.5). Even more, similarly to the EXSY NMR experiments with L^7(oLAOBn) synthesized by 1:1 reactions with *rac*-LA, EXSY experiments with *meso*-LA showed exchange peaks between a small diastereomeric species and that of the larger enantiomeric species (Figure 4.11). Exchange between backbone protons (denoted by green circles and arrows in spectrum and scheme, respectively) was also observed and is assumed to be a result of interconversion of enantiomers, akin to what was observed with L^7(oLAOBn) via *rac*-LA.

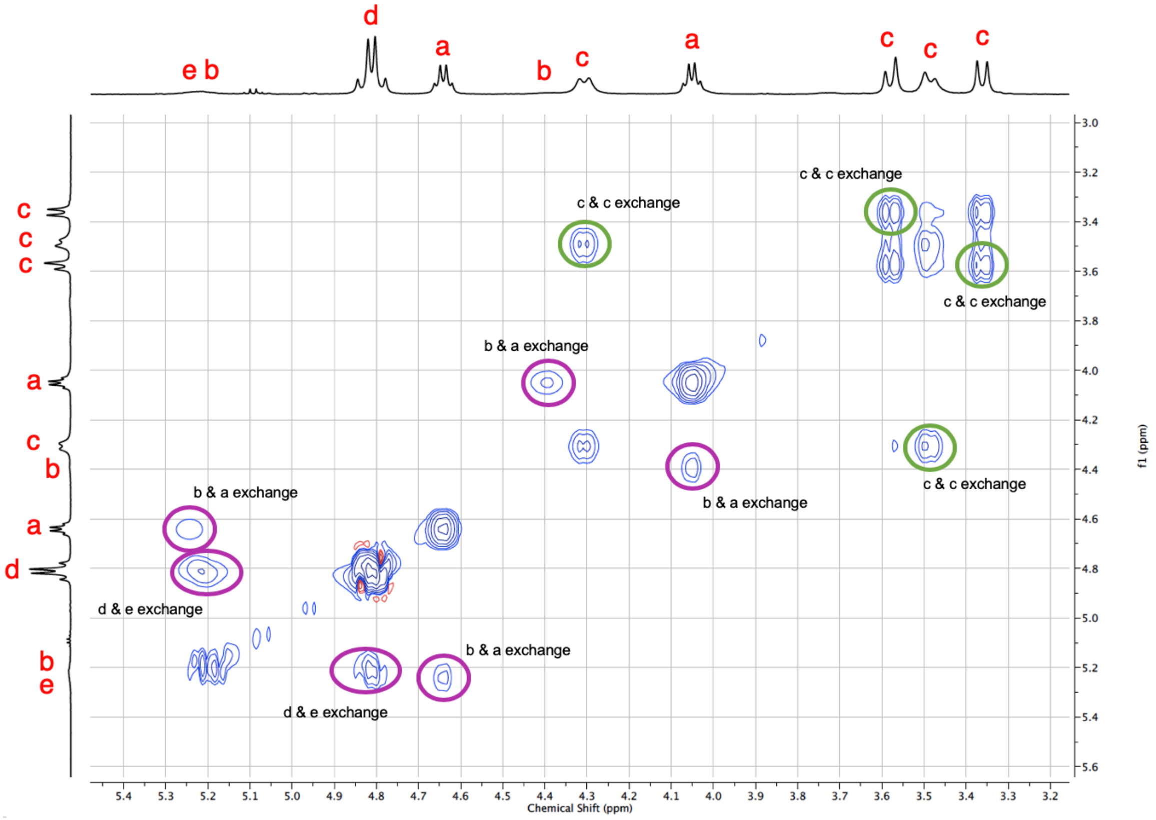

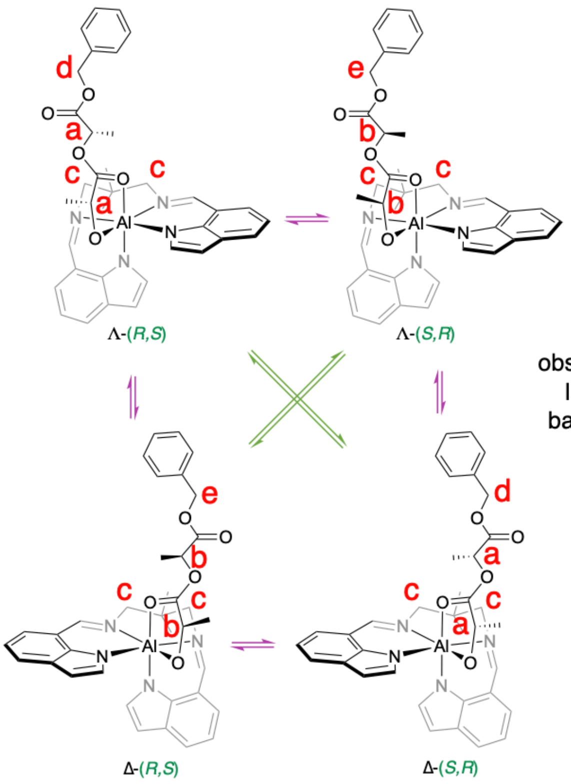

backbone peaks not observed for lesser isomer, likely overlapping with backbone peaks of major isomer

Figure 4.11. NOESY/EXSY NMR spectrum of the product of reaction of *meso*-LA with **L^{7}AlOBn** (top), and corresponding equilibrium scheme hypothesized to explain the results (bottom). Both diastereomeric (purple) and enantiomeric exchange (green) are observed. While we arbitrarily assigned the major isomer in the spectrum as Δ-(*S,R*) (and consequently, its enantiomer as Λ-(*R,S*)) due to lack of X-ray crystallographic data, we note the likelihood of these assignments being reversed.

Therefore, results from these stoichiometric experiments indicate that the **L^{7}AlOBn** maintains a high level of initiation selectivity when reacted with *meso*-LA, indicating that only one stereocenter of a LA molecule helps determine initial selectivity. Yet, as with *rac*-LA, the alkoxide ligands of such reactions are labile. It should be noted that analogous results were observed for that of **^{N}AlOBn** and *meso*-LA, too.

4.3.4 ***Theory Calculations*** (performed by Sina Chiniforoush, Mukunda Mandal and Christopher J. Cramer)

This section focuses on the critical theoretical conclusions from this work, while more detail is available in the published manuscript and supporting files.[47] To better understand factors contributing to stereocontrol in the initiation process that we were able to characterize experimentally, the free energy profiles for the initiation steps associated with both L^{2}AlOR and L^{7}AlOR were computationally determined for both L(*S,S*)- and D(*R,R*)-LA (see section 4.5.10 for details). Both L^{7}AlOMe and L^{7}AlOBn were examined in order to assess the significance of variation of the alkoxide. Since the results were similar, only the methoxy initiator was considered for all other catalysts in order to reduce computational cost.

For initiation, three structural descriptors define all possible pathways. These are (i) the LA coordination mode, (ii) the chirality of the LA monomer, and (iii) the prochirality of the LA carbonyl group subject to nucleophilic attack. The calculated pathway for all systems is illustrated for one particular catalyst enantiomer (Δ-L^{2}AlOMe), one substrate enantiomer (D(*R,R*)-LA), and one particular approach trajectory (prochirality; see below) in Figure 4.12. The process involves LA binding and attack of the alkoxy group at the LA carbonyl via TS1 to yield intermediate 1 (INT1). After rearrangement to INT2 (which involves shifting which ether oxygen of the tetrahedral intermediate is bound to the metal), ring-opening via TS2 yields the product comprising one incorporated LA unit. While we find no minima where LA coordinates to aluminum prior to nucleophilic attack — instead, only van der Waals complexes with long Al–O distances exist on the potential energy surface — coordination *is* present in TS1 structures for nucleophilic attack, and there are two possibilities for the relative position of the LA monomer: trans either to the N atom of an indole or to the N atom of a backbone imine (each alternative then dictates the position of the alkoxy group). The LA itself may be D(*R,R*) or L(*S,S*), and finally the *re* or *si* prochirality of the face of the LA carbonyl group exposed to the alkoxy ligand sets the rotational degree of freedom for the monomer. Given these differentiating structural factors, there are eight pathways that must be considered in order to comprehensively assess all possible initiation paths for a given catalyst enantiomer (Figure 4.13).

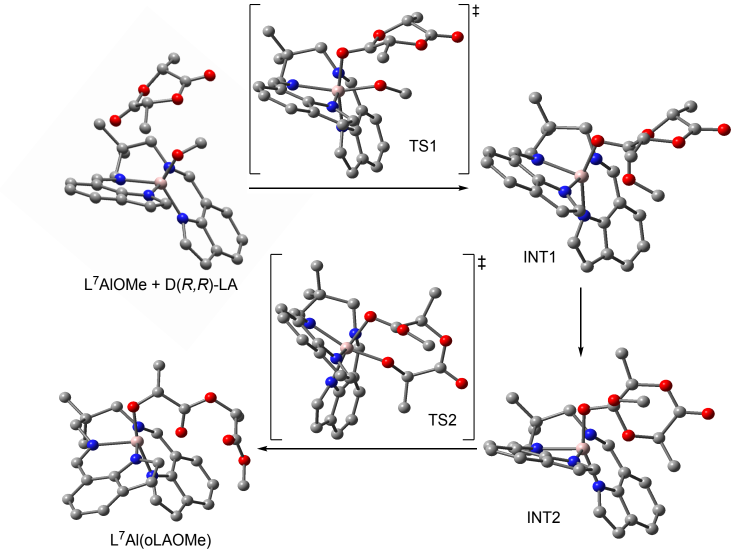

Figure 4.12. Illustration of the calculated initiation pathway for a selected catalyst (Δ-L^{7}AlOMe), substrate (D(*R,R*)-LA), and approach trajectory. H atoms are not shown for clarity. Key: pink = Al, red = O, blue = N, gray = C.

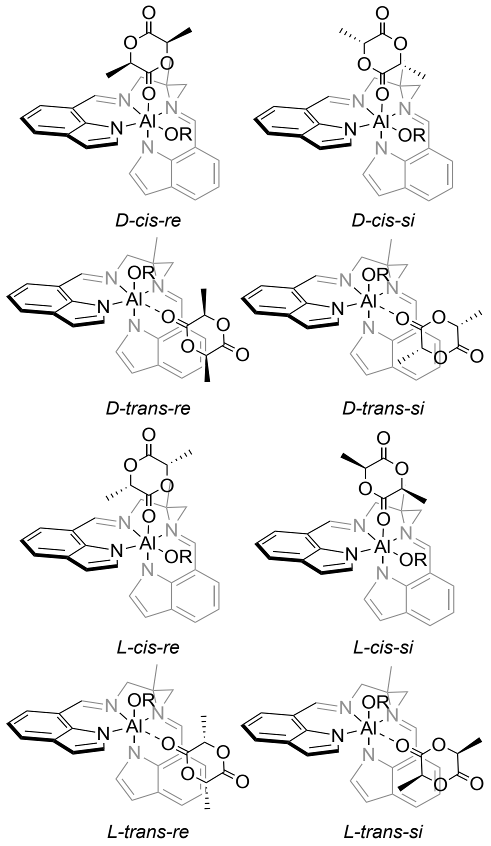

Figure 4.13. Starting structures along the eight alternative pathways for initiation of D(*R,R*)- and L(*S,S*)-LA for Δ-L^7AlOMe. The cis and trans descriptors indicate the positions of the imine groups of the complex with respect to the LA, specifically, in the trans pathway, the LA C=O is trans to *one* imine group while in the cis pathway it is cis to *both* imine groups.

The results of energetic calculations for all reaction pathways involving Δ-L^7AlOMe, -L^7AlOBn, -L^2AlOMe, and ^{N}AlOMe are included in published work.[47] Comparing the results from these calculations, it is apparent that for both methoxy and benzyloxy as an initiator, reaction of the Δ isomer of the complexes with D(*R,R*)-LA is calculated to be kinetically favored for all complexes. There are differences in whether the *cis-re* or *trans-re* pathways are preferred, depending on the nature of the ligands. Importantly, these findings for the kinetic preferences are in disagreement with the stereochemistry observed in the X-ray crystal structures of L^2Al(oLAOBn) and L^7Al(oLAOBn) (the latter featured in Figure 4.7). In contrast, the Δ-L(*S,S*) isomer observed by X-ray crystallography is calculated to be thermodynamically more favorable for both L^7AlOMe and, to a lesser extent, L^2AlOMe. While the computed energy differences are small, suggesting that product mixtures might be expected under thermodynamic conditions, the agreement with the $\Delta G^\circ_{298} = -1.3$ kcal/mol for the postulated equilibria between the diastereomers determined from integration of NMR spectra is reasonable considering the inherent accuracy of the calculations (ca. ±1 kcal/mol). Thus, the computations corroborate the conclusions drawn experimentally, that the stereoselectivity observed is determined by the relative thermodynamic stability of the products, and that the preferred stereoisomer is that which was characterized structurally by X-ray crystallography. Again, however, because the calculated energy differences between the products are small, we cannot unambiguously rule out the possibility that the minor isomer is the one that crystallizes.

Putting these findings in context, previous DFT investigations of the origins of stereoselectivity in LA polymerizations by metal-alkoxide catalysts have focused on differences in kinetic barriers for ring-opening of LA stereoisomers.[44,105,167,170,171] Both kinetic and thermodynamic preferences were identified by theory for the addition of a second monomer to the initially formed ring-opened species in syndiotactic polymerization of *rac*-*β*-butyrolactone by yttrium catalysts supported by salan-type ligands.[172] Small energetic differences arising from subtle secondary interactions (typically with the growing chain end in propagation steps) were identified in the previous DFT studies.[173] While general rules for predicting stereoselectivity are lacking, the finding herein that thermodynamic control of stereoselectivity in ROP initiation suggests that similar ideas should be considered in evaluating stereocontrol in propagation reactions.

4.4 Concluding Remarks

We have synthesized and characterized the solution and solid-state structures of the complexes **L^{2}AlOBn** and **L**7**AlOBn**, including the delineation of the nature of the fluxional process that interconverts the enantiomeric forms of the complexes through VT NMR spectroscopy and computations. The complexes polymerize *rac*-LA stereoselectively. As a first step towards developing a molecular-level understanding of the mechanistic basis for the observed stereoselectivity, we studied the initiation reaction. Treatment of the complexes with 1 equiv. of *rac*-LA yielded the ring-opened products L^{2}Al(oLAOBn) and L^{7}Al(oLAOBn) and on the basis of NMR spectroscopy, the major product for each reaction was identified as a single diastereomer (pair of enantiomers). Crystals isolated from the product solutions were characterized by X-ray diffraction, revealing unambiguously for the first time the detailed molecular structure and stereochemistry of a product of initiation of cyclic ester polymerization by a metal-alkoxide complex. Studies of the product solutions by EXSY showed that the products exist as stereoisomers that rapidly interconvert via both intermolecular alkoxide exchange and racemization at the Al center. Examination of the initiation reactions by theory delineated the mechanistic details, in particular the reaction energetics as a function of stereochemistry. We conclude, with appropriate caveats because of the small energetic differences found by theory, that the stereoselectivity observed in the initiation reaction is likely not the result of kinetic preferences (which predict preferential formation of the stereoisomer *not* observed by X-ray crystallography). Instead, thermodynamic control of selectivity is supported by the experimental NMR data indicative of equilibration of diastereomers in solution and by the prediction by theory that the stereoisomer observed by X-ray crystallography is the most stable (keeping in mind the possibility, albeit in our view unlikely, that the crystals isolated could be the minor isomer).

In addition to providing specific information on particular systems, the mechanistic results reported herein significantly augment our general understanding of stereocontrol of ROP initiation by metal-alkoxide complexes and suggest the importance of thermodynamic control in determining the favored product stereoisomer. We speculate that similar considerations apply to understanding subsequent monomer enchainment, the stereochemistry of which may similarly rely on product stability rather than kinetic barriers typically emphasized in theoretical studies.

4.5 Experimental

4.5.1 *General Considerations*

All reactions containing either air- and/or water-sensitive compounds were performed within the inert atmosphere of a nitrogen-filled glovebox or using Schlenk line techniques. All reagents were purchased from commercial sources and were used as received, unless otherwise noted. *rac*-LA was purified by recrystallization (3x) from toluene and subsequent vacuum drying. All protonated solvents were degassed and passed through a solvent purification system (Glass Contour, Laguna, CA) prior to use. Deuterated solvents were dried over CaH_2, degassed through freeze-pump-thaw techniques, and distilled before being stored under N_2. Nuclear magnetic resonance (NMR) spectroscopy experiments were performed with a Bruker Avance III (500 MHz) spectrometer equipped with a BBFO SmartProbe, Varian Unity Inova (500 MHz), or Varian Unity Plus 300 MHz equipped with an AutoSW PFG 4NUC/30-122 MHz temperature probe. Chemical shifts for ^{1}H and ^{13}C NMR spectra were referenced to residual protium in the deuterated solvent (for ^{1}H NMR) and the deuterated solvent itself (for ^{13}C NMR). NOESY/EXSY NMR experiments were accomplished with a mixing time of 0.8 s. Molecular weights (M_n and M_w) and polydispersities ($Đ$) of the PLA samples were determined in THF at 25 °C with a flow rate of 1 mL/min. on an Agilent 1260 Infinity HPLC with Waters Styragel (HR6, HR4, and HR1) columns connected to a Wyatt DAWN Heleos II light scattering detector and a Wyatt OPTILAB T-rEX refractive index detector. Molecular weight (M_n and M_w) and polydispersity ($Đ$) of the PLA sample for entry 16 in Table 4.1 (section 4.3.2) was determined using an Agilent 1100 series SEC with an HP1047A refractive index detector using a $CHCl_3$ mobile phase at 35 °C through 3 Varian PLgel Mixed C Columns with a flow rate of 1 mL/min. DSC experiments were conducted via a TA Instruments Discovery DSC, using samples hermetically sealed in aluminum pans, at a heating rate of 10 °C/min. Reported T_m values are from the second heating ramp. Elemental analyses were performed by Robertson Microlit Laboratories in Ledgewood, NJ and Galbraith Laboratories Inc. in Knoxville, TN. X-ray diffraction measurements were collected with Mo Kα source and with either a Bruker D8 VENTURE diffractometer equipped with a Photon II CPAD using normal parabolic mirrors as monochromators, a Bruker D8 VENTURE diffractometer equipped with a Photon III CMOS using normal parabolic mirrors as monochromators, or a Bruker X8 diffractometer equipped with a Kappa Apex II CCD using a graphite monochromator. Structure solutions were performed with SHELXT[174] or SHELXS[175] using OLEX2[176] or ShelXle[177] as graphical interfaces. The structures were refined against F^2 on all data by full matrix least squares with SHELXL.[175]

4.5.2 *Synthetic Procedures*

Synthesis of L^7AlOBn. This complex was synthesized as previously described.[136]

Synthesis of ^{N}AlOBn. This complex was synthesized as previously described.[34,178]

4.5.3 *Polymerization Experiments and Analysis*

Polymerizations were performed in deuterated solvents (CD_2Cl_2, THF-d_8, and tol-d_8) at various temperatures (35, 55, and 70 °C, respectively). Example polymerization procedures were completed as follows. Stock solutions of catalyst (1 mL, 9.7 mM) and *rac*-LA (1 mL, 1.5 M for CD_2Cl_2 and THF-d_8, 0.1 M for tol-d_8) were prepared. A J-Young NMR tube was sequentially charged with catalyst stock solution (240 µL, 2.3 µmol for CD_2Cl_2 and THF-d_8; 72 µL, 0.70 µmol for tol-d_8, 1 equiv.), monomer stock solution (460 µL, 0.70 mmol for CD_2Cl_2 and THF-d_8, 300 equiv.; 630 µL, 70 µmol for tol-d_8, 100 equiv.), for a final concentrations of 3.3 mM catalyst and 1.0 M monomer (CD_2Cl_2 and THF-d_8) or 0.001 M catalyst and 0.1 M monomer (tol-d_8). Once the polymerizations reached >95% conversion (CD_2Cl_2 and THF-d_8), they were quenched via air exposure. An aliquot of the polymerization was removed and subjected to ^{1}H NMR analysis in order to determine the monomer conversion. The rest of the reaction mixture was precipitated into cold MeOH and the resulting PLA was dried under vacuum for ~12 h. The polymerizations in toluene-d_8 stalled at 80% and 88% (for **L^{7}AlOBn** and **L^{2}AlOBn**, respectively), and were therefore quenched before >95% conversion, but otherwise worked up identically to the polymerizations in CD_2Cl_2 and THF-d_8.

Melt polymerization studies were performed by weighing out catalyst (0.0059 g, 0.012 mmol, 1 equiv.) into an oven-dried screw-cap bomb flask charged with a stir bar and monomer (0.52 g, 3.6 mmol, 300 equiv.) in a nitrogen-filled glovebox. The bomb flask was capped, removed from the glovebox, and then heated and stirred at the desired temperature for a given amount of time. The polymerizations were quenched by opening up the flask to air. An aliquot from the reaction mixture was immediately taken in order to determine monomer conversion (^{1}H NMR spectroscopy). The rest of the reaction mixture was then dissolved in CH_2Cl_2 before being poured into cold MeOH to precipitate the polymer. After decanting off the remaining MeOH, the resulting polymer was washed with MeOH (3 x 10 mL) and dried under vacuum for ~12 h.

All polymer samples were dried by vacuum oven for an additional 12 h before analysis by $^1H\{^{13}C\}$ spectroscopies (P_m), SEC analysis (M_n, $Đ$) and DSC analysis (T_m).

4.5.4 *Rac- and L-Lactide Kinetic Comparisons*

A kinetic comparison of the polymerization of both *rac*- and L-LA by **L^7AlOBn** was performed. As expected for polymerizations of *rac*-LA that proceed with isotactic selectivity, in the cases with both catalysts, the homopolymerization of L-LA was faster than that of *rac*-LA.

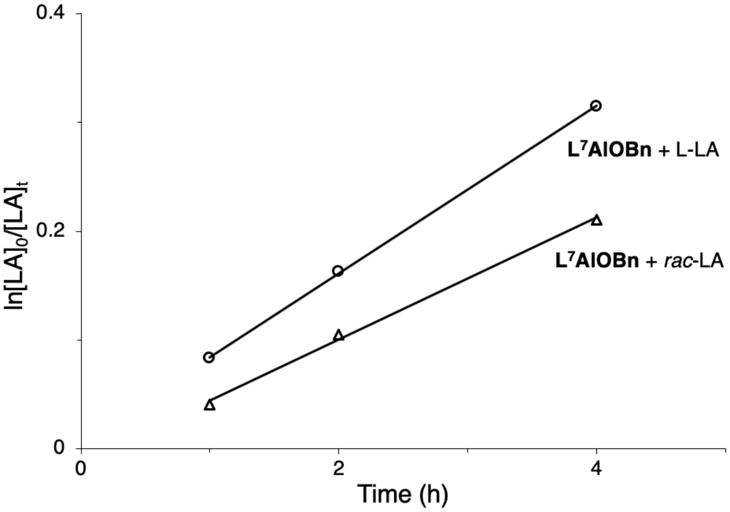

Figure 4.14. Kinetic comparison of L-LA and *rac*-LA polymerizations by **L^7AlOBn** over 4 h. Polymerization conditions: toluene, 70 °C, $[\text{L-LA}]_0 = [\textit{rac}\text{-LA}]_0 = 0.1$ M; $[\text{LA}]_0 : [\text{cat}]_0 = 100$.

4.5.5 *Stoichiometric Experiments*

For NMR experiments, reactions of *rac*-, L-, and D-LA with complexes (1:1) were performed by making a 0.0065 M stock solution (1 mL) of catalyst in $CDCl_3$ and a 0.078 M stock solution (500 μL) of the designated LA monomer in $CDCl_3$. In a glovebox, 600 μL (3.9 μmol) of catalyst stock solution and 50 μL (3.9 μmol) of monomer stock solution (along with 50 μL pure $CDCl_3$) were added to a J-young NMR tube, targeting a final concentration of 0.0055 M for both catalyst and monomer and a final NMR volume of 700 μL. The J-young tube was then removed from the glovebox, shaken, and immediately analyzed by NMR spectroscopy.

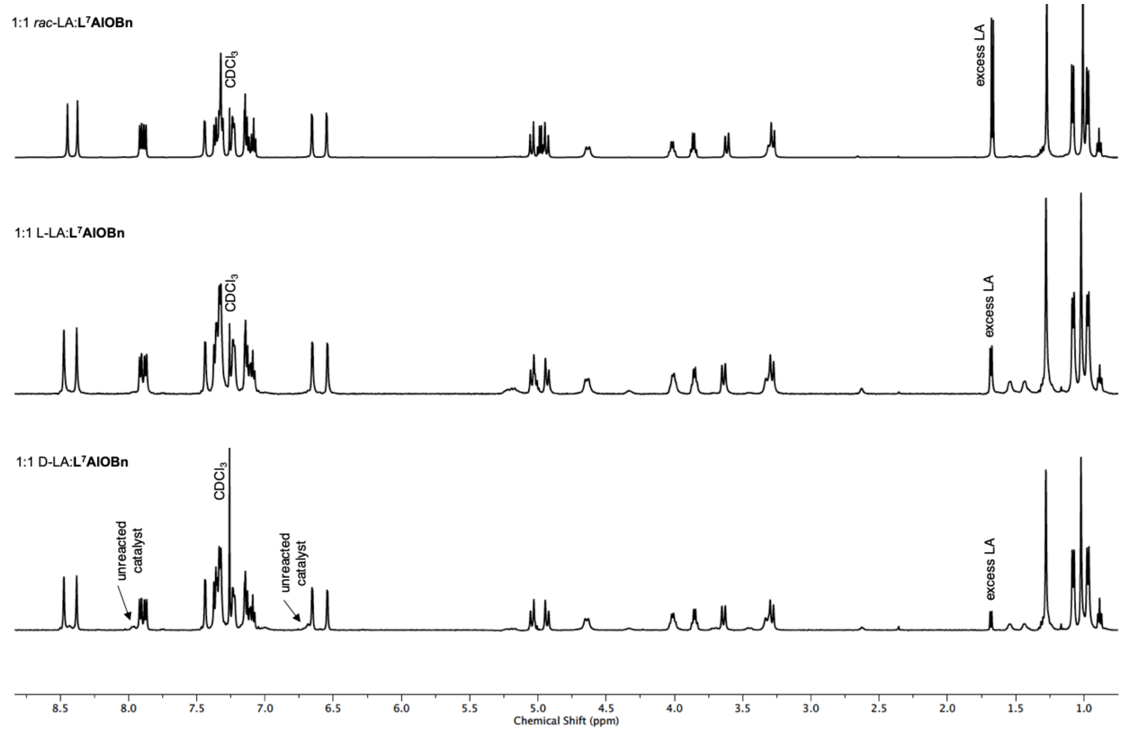

Figure 4.15. Overlay of ^1H NMR spectra of the products of the reactions of $\mathbf{L^7AlOBn}$ with 1 equiv. *rac*-, D-, and L-LA.

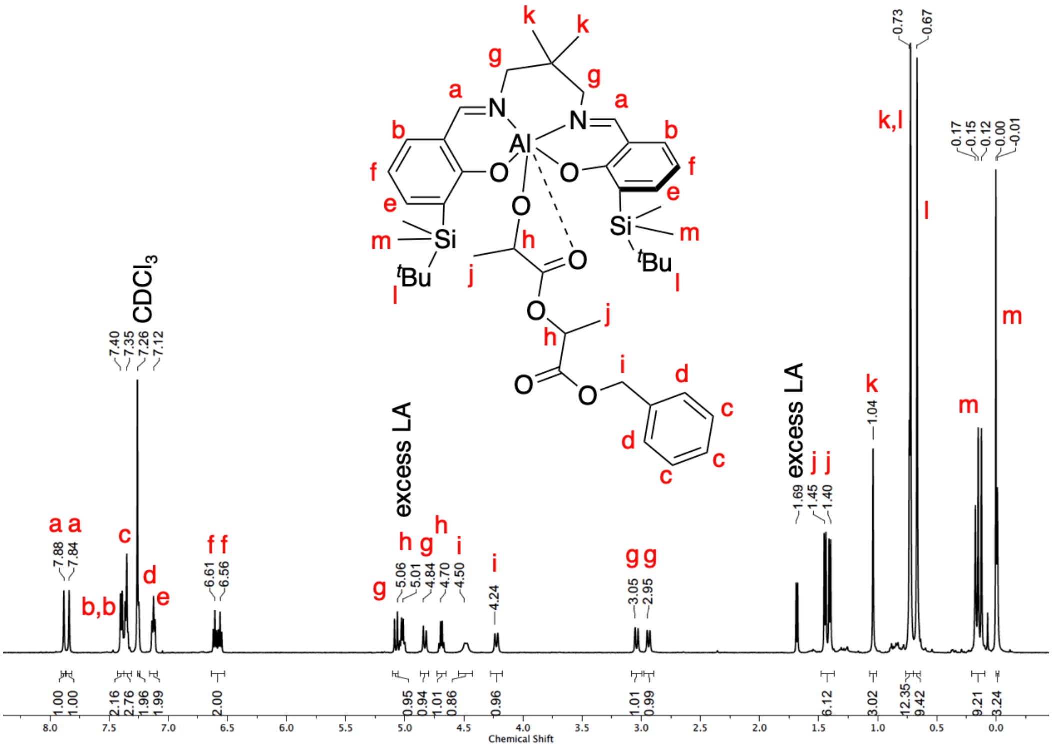

Figure 4.16. ^{1}H NMR spectrum of 1:1 *rac*-LA:$^{\mathbf{N}}$**AlOBn**.

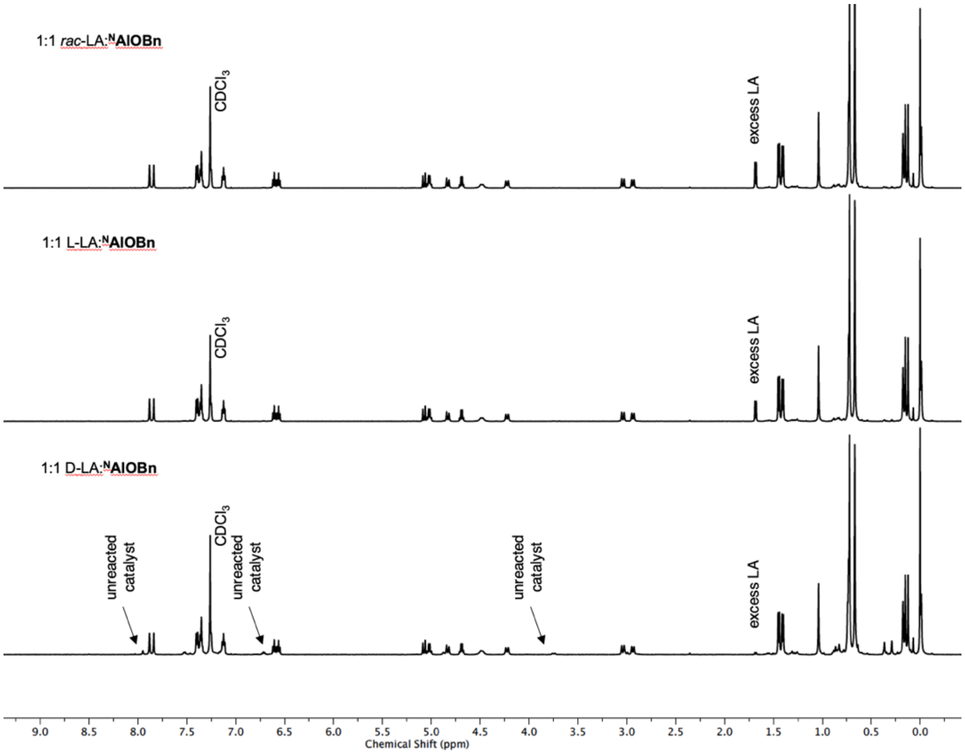

Figure 4.17. Overlay of ^{1}H NMR spectra of the products of the reactions of $^{\mathbf{N}}$**AlOBn** with 1 equiv. *rac*-, D-, and L-LA.

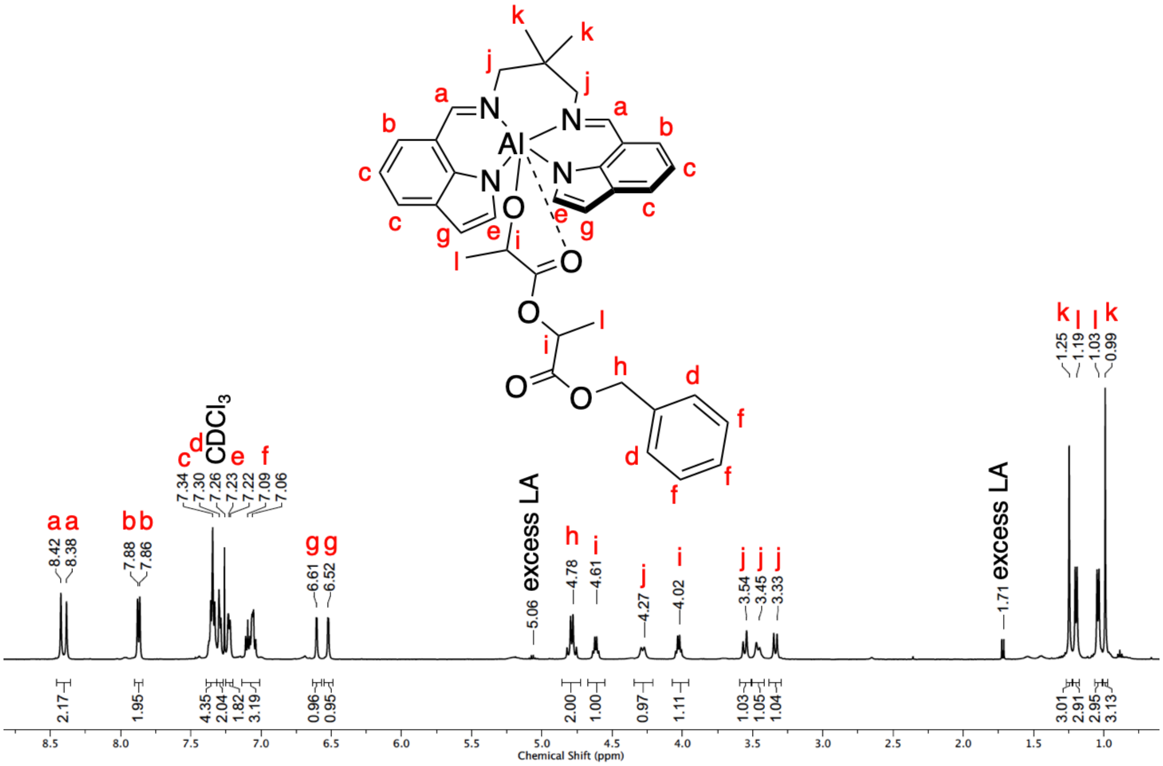

Figure 4.18. ^{1}H NMR spectrum of 1:1 *meso*-LA:**L^{7}AlOBn**.

4.5.5.1 *Stoichiometric Crystallization Conditions*

In a nitrogen filled glovebox, 500 µL of a solution of catalyst (0.020 M, 10 µmol) in CD_2Cl_2 was combined with a solution of *rac*-LA (0.15 M, 67 µL, 10 µmol) in CD_2Cl_2 in a J-Young NMR tube. The NMR tube was pumped out of the glovebox, shaken, and immediately analyzed by NMR spectroscopy. Afterward, the tube was brought back into the glovebox and the solution transferred to a 4 mL scintillation vial which was subsequently layered with pentane and stored at −30 °C. The solution yielded pale yellow crystals suitable for diffraction after 3 d. The 1:1 structures were found to crystallize in the centrosymmetric space group P-1, indicating that the crystals are racemates of both enantiomers.

4.5.6 *Variable Temperature ^{1}H NMR Spectroscopy Experiments*

VT ^{1}H NMR studies on **L^{7}AlOBn** its corresponding 1:1 ring-opened units of *rac*-LA, were performed in CD_2Cl_2, in the range of 180–300 K with temperatures determined by using a MeOH temperature calibrant. Figure 4.16 reveal that at lower temperatures, the fluxionality of the complex is slowed so that distinguishable proton resonances are observed. Using dynamic NMR interpretation (fitting model), the rate constant for fluxionality at each temperature close to the coalescence temperature was determined using WinDNMR[179] (Fig. 4.18) and the subsequent Eyring plots (Fig. 4.19) yielded activation parameters (for all complexes studied). Figure 4.17 examine the variable temperature profile of 1 equiv. of complex **(L^{7}AlOBn)** and a single ring-opened unit of *rac*-LA. Lack of broadening of peaks corresponding to the complexes' proton resonances indicates that once ring-opened, the complexes are no longer fluxional, and any peak broadening of monomer peaks is a result of monomer fluxionality.

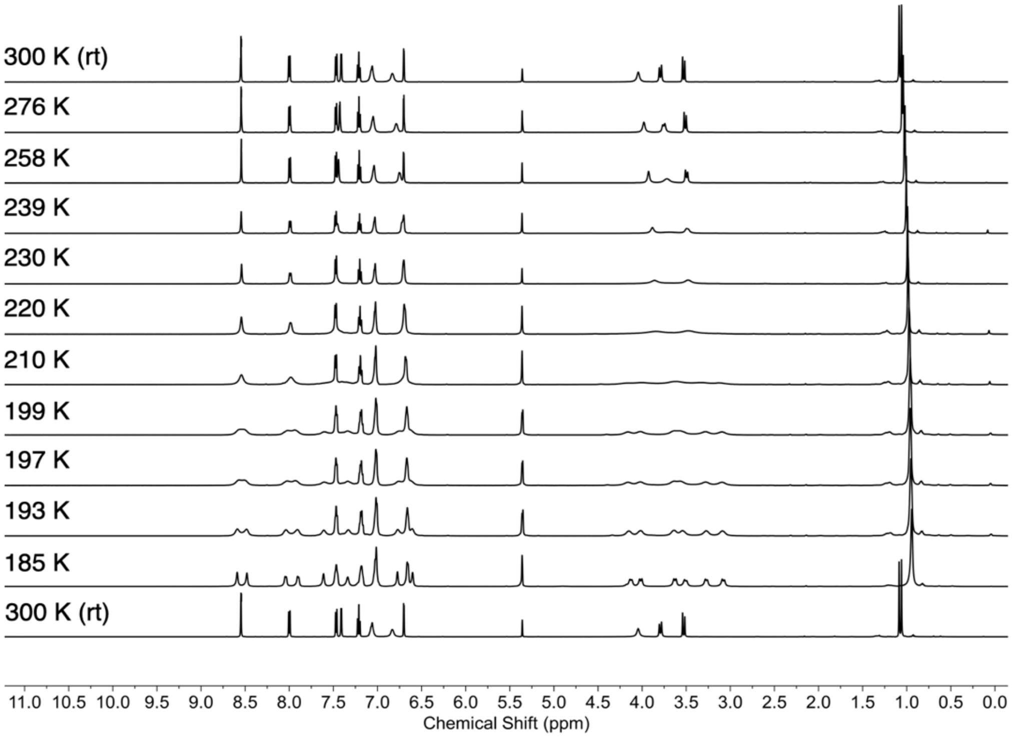

Figure 4.19. VT ^{1}H NMR overlay of **L^{7}AlOBn**. The fluxionality of the complex is inhibited at lower temperatures, as indicated by the individual peaks (first appearing at ~199 K).

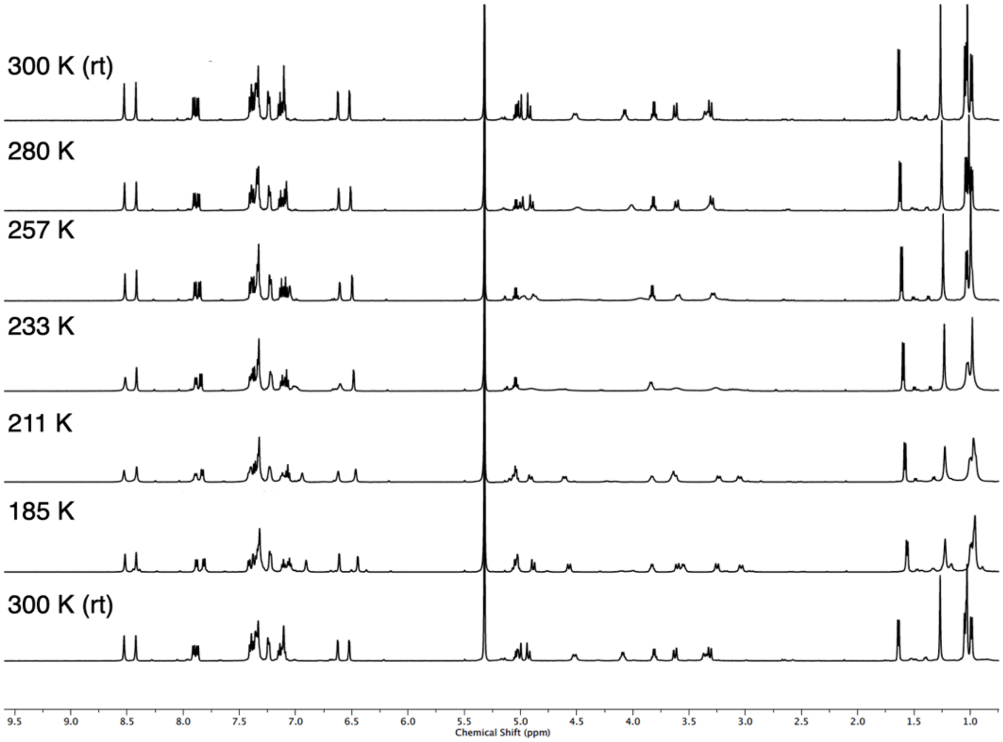

Figure 4.20. VT ^{1}H NMR overlay of 1:1 *rac*-LA:**L^{7}AlOBn**.

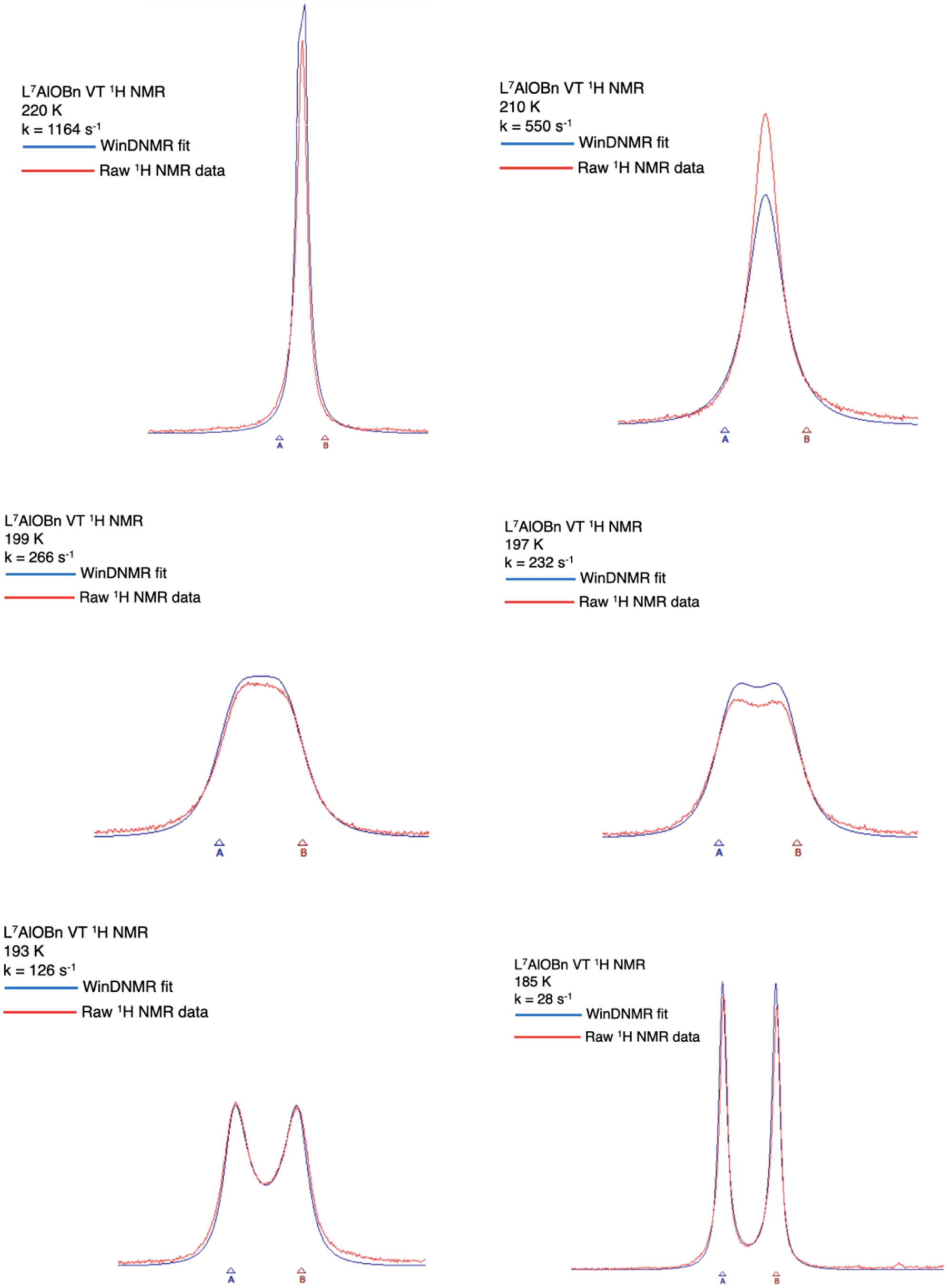

Figure 4.21. Overlay of raw ^{1}H NMR data from VT studies with **L^{7}AlOBn** and corresponding WinDNMR fits. The featured peak is the imine proton resonance of the complex (~8.6 ppm, see Figure 4.19). Rate constants for each temperature measured for Eyring analysis are shown. Analyses for **L^{2}AlOBn** and **^{N}AlOBn** were done analogously, using the imine proton resonance of their respective complexes, as well.

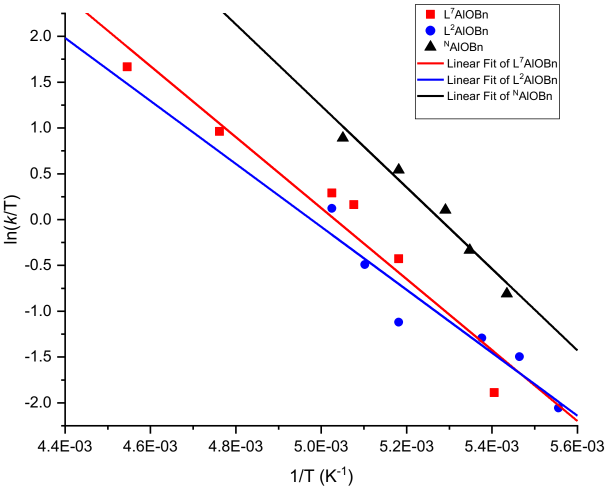

Figure 4.22. Eyring plots for fluxionality studies of **L^7AlOBn**, **L^2AlOBn** and **^{N}AlOBn** with respective linear fits of $R^2 = 0.94$, 0.90, and 0.97. Rate constants were determined by WinDNMR analysis of VT ^{1}H NMR spectra.

Table 4.2. Activation parameters for the fluxional interconversion between enantiomers, determined from Eyring plot analysis. Associated errors are estimated from WinDNMR fits.

Complex	$\Delta G^{\ddagger}$ (kcal/mol)	$\Delta H^{\ddagger}$ (kcal/mol)	$\Delta S^{\ddagger}$ (cal/K·mol)
L^7AlOBn	10.2(3)	7.7(2)	−8.5(2)
L^2AlOBn	10.7(7)	6.8(3)	−13.2(5)
^{N}AlOBn	9.0(6)	8.8(3)	−0.54(10)

4.5.7 *Tacticity Measurements*

Tacticity of each polymer was measured by dissolving dried polymer in $CDCl_3$ and submitting the sample for homonuclear decoupled ^{1}H NMR. Using the methine region of the spectrum (5.15–5.25 ppm), the different tetrad concentrations were integrated and Bernoullian statistics (assuming CEM, based on values obtained from DSC measurements, Table 4.1, section 4.3.2) were applied to determine the amount of racemic and *meso* character in the polymer.[35] For more accurate integration measurements, deconvolution of the spectra was achieved using MestReNova software.[115] An example of such analysis is depicted in Figure 4.23.

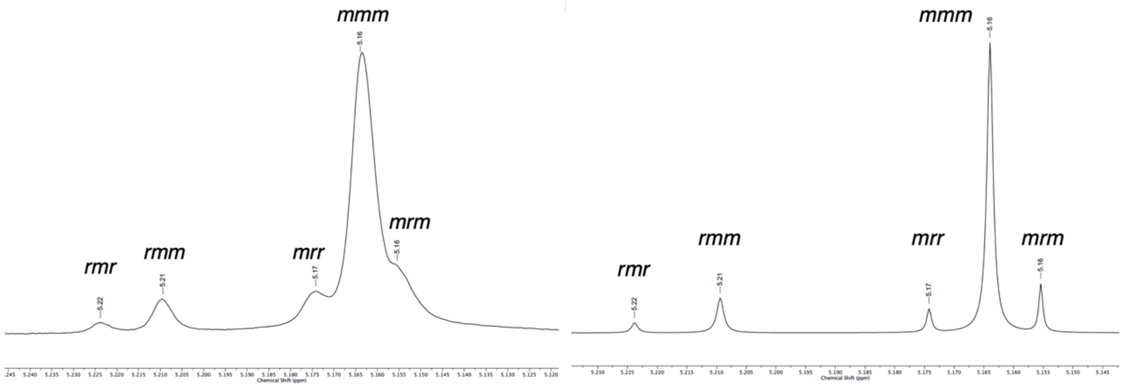

Figure 4.23. Example raw data (methine region, **L^{7}AlOBn**, 35 °C, CD_2Cl_2) from the homonuclear decoupled ^{1}H NMR spectra of PLA (left) and its deconvoluted form (right) with $P_m = 0.80$.

4.5.8 *Differential Scanning Calorimetry Measurements*

A few example DSC thermograms from various polymerizations with a heating ramp of 10 °C/min are shown. Corresponding T_m values were determined from the second heating ramp. Samples were annealed overnight at 120 °C before DSC measurements were taken.

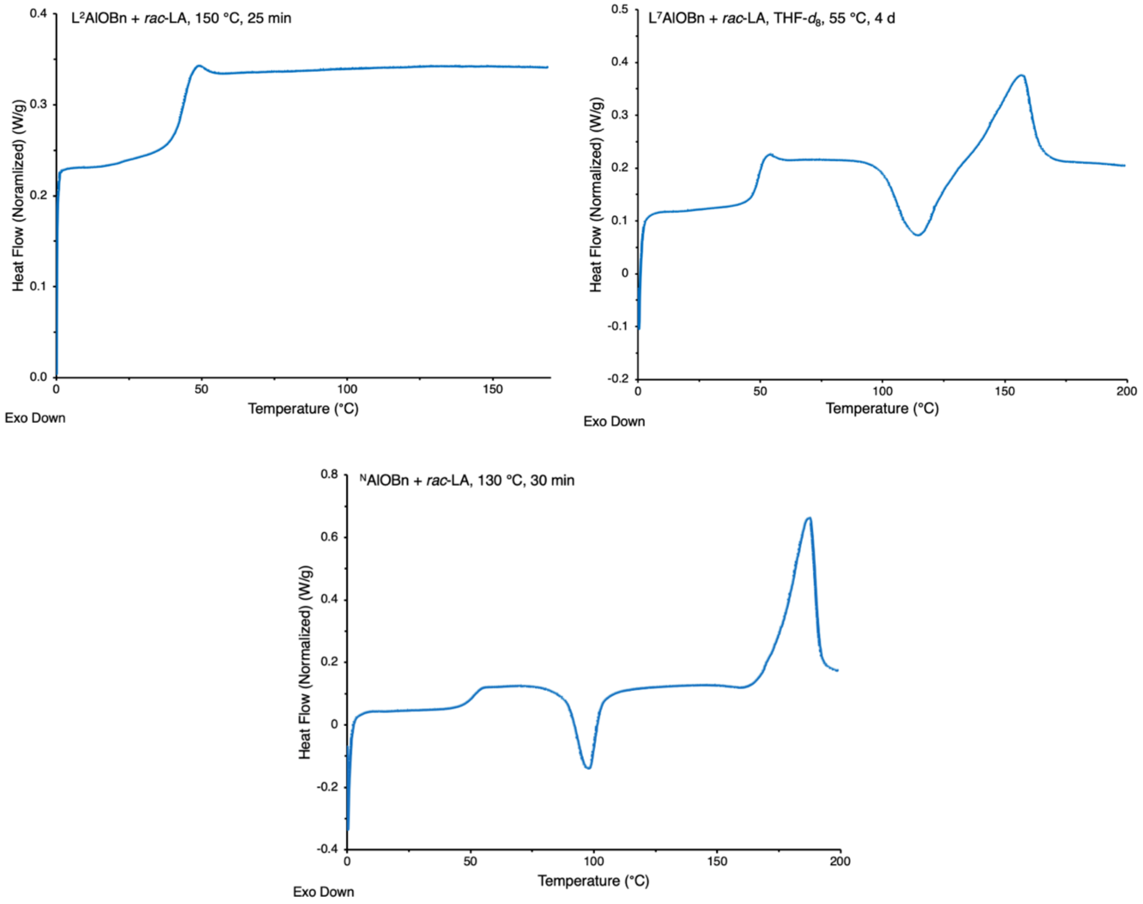

Figure 4.24. (Top left) DSC thermogram of **L^2AlOBn** + *rac*-LA, 150 °C, 25 min. No feature corresponding with T_m was observed. (Top right) DSC thermogram of **L^7AlOBn** + *rac*-LA, THF-d_8, 55 °C, 4 d (T_m = 155 °C), and (bottom) DSC thermogram of **^{N}AlOBn** + *rac*-LA, 130 °C, 30 min (T_m = 187 °C).

4.5.9 *NOESY/EXSY NMR Spectroscopy Experiments*

NOESY/EXSY NMR experiments were conducted by first synthesizing and isolating the respective 1:1 LA:AlOBn complexes (either **L^7AlOBn**, **L^2AlOBn** or **^{N}AlOBn**, labeled with LA), then making 0.005 M stock solutions of the complexes in CD_2Cl_2 (1500 µL). After checking them individually for purity, 350 µL of each complex being examined (or 700 µL in the case of only examining 1:1 *rac*-LA:**L^7AlOBn**, 1:1 L-LA:**L^7AlOBn**, and 1:1 *rac*-LA:**L^2AlOBn**) were added to a J-Young NMR tube (total volume = 700 µL) and immediately analyzed via ^{1}H, COSY, and NOESY/EXSY NMR (mixing time = 0.8 s). EXSYcalc[169] were performed in order to obtain a rate constant for ligand exchange in the cases of 1:1 *rac*-LA:**L^{7}AlOBn** and 1:1 *rac*-LA:**L^{2}AlOBn**. To do this, two NOESY/EXSY experiments were run on each sample, one with a mixing time of 0.8 s and the other with the lowest limit, 0.0025 s, as a reference.

Analysis of the data shown in Figure 4.8 using EXSYcalc led to the finding that the forward rate constant of equilibrium, k_1, for going to the major isomer was 4.1 s^{-1} and the reverse, k_{-1}, = 0.44 s^{-1} (favoring the major isomer by ~90%). Integration of the ^{1}H NMR spectrum revealed a similar ratio of isomers (~90% major, ~10% minor). Similar NOESY/EXSY data were acquired for the product of reaction of *rac*-LA with **L^{2}AlOBn** was obtained (data not shown), and EXSYcalc revealed the forward rate constant of equilibrium, k_1, for going to the major isomer to be 2.2 s^{-1} and the reverse, k_{-1}, to be 0.25 s^{-1} (favoring the major isomer by ~90%). Integration of the ^{1}H NMR spectrum revealed a similar ratio of isomers (~95% major, ~5% minor).

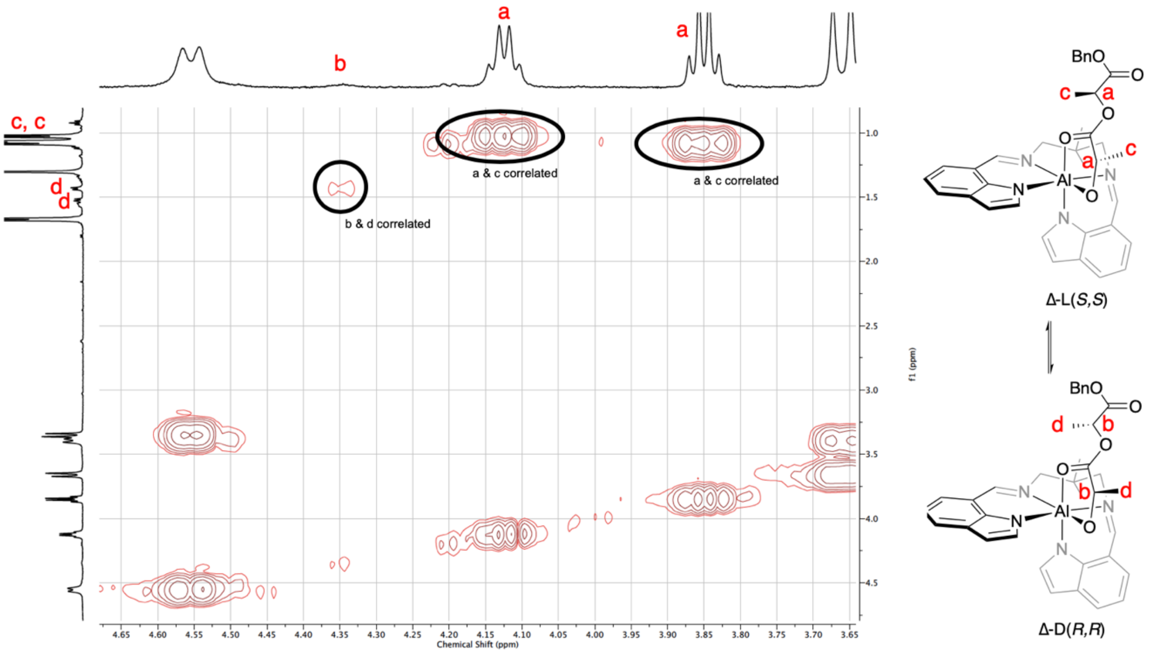

Figure 4.25. COSY spectrum of L^{7}Al(oLAOBn). The circled resonances show correlation between the alkoxide ligand methines of both the lesser and more populated isomers (**b** and **a**, respectively) and their corresponding doublets (methyl substituents of the LA units, **d** and **c**, respectively).

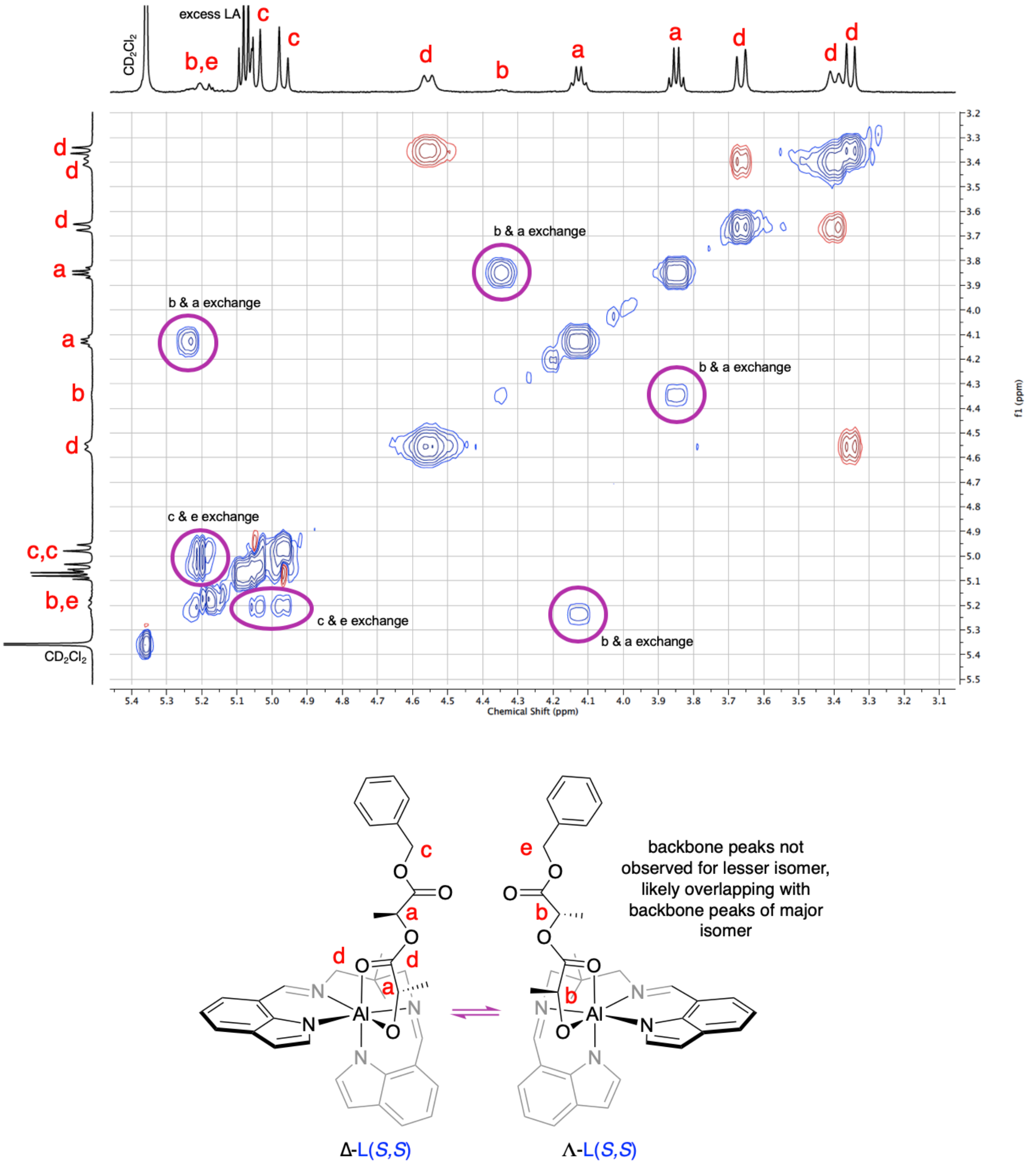

Figure 4.26. NOESY/EXSY spectrum of the product of reaction of L-LA with **L^{7}AlOBn** (top) and the equilibrium scheme proposed to rationalize the results (bottom). The peaks of interest for diastereomeric exchange are circled in purple. Only NOESY peaks (red) are observed between backbone protons (labeled as **d**).

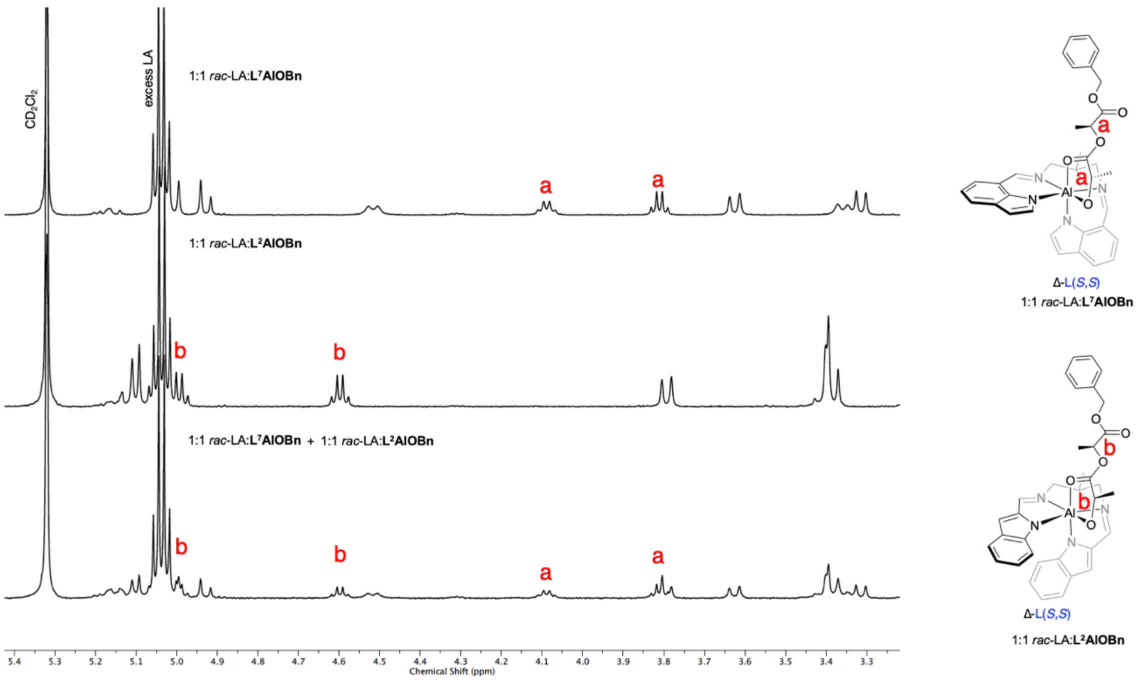

Figure 4.27. Overlay of ^{1}H NMR spectra for the products of reactions with *rac*-LA with **L^{7}AlOBn** (top) and **L^{2}AlOBn** (middle), and a mixture of the two (bottom).

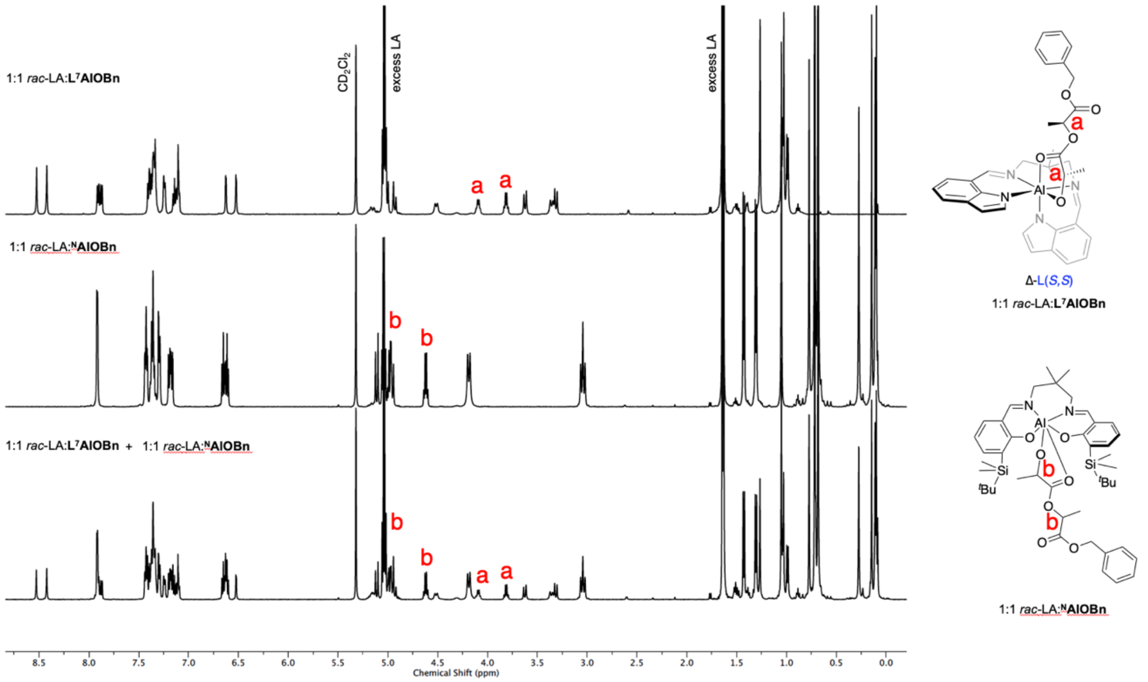

Figure 4.28. Overlay of ^{1}H NMR spectra for the products of reactions with *rac*-LA with **L^{7}AlOBn** (top) and **^{N}AlOBn** (middle), and a mixture of the two (bottom).

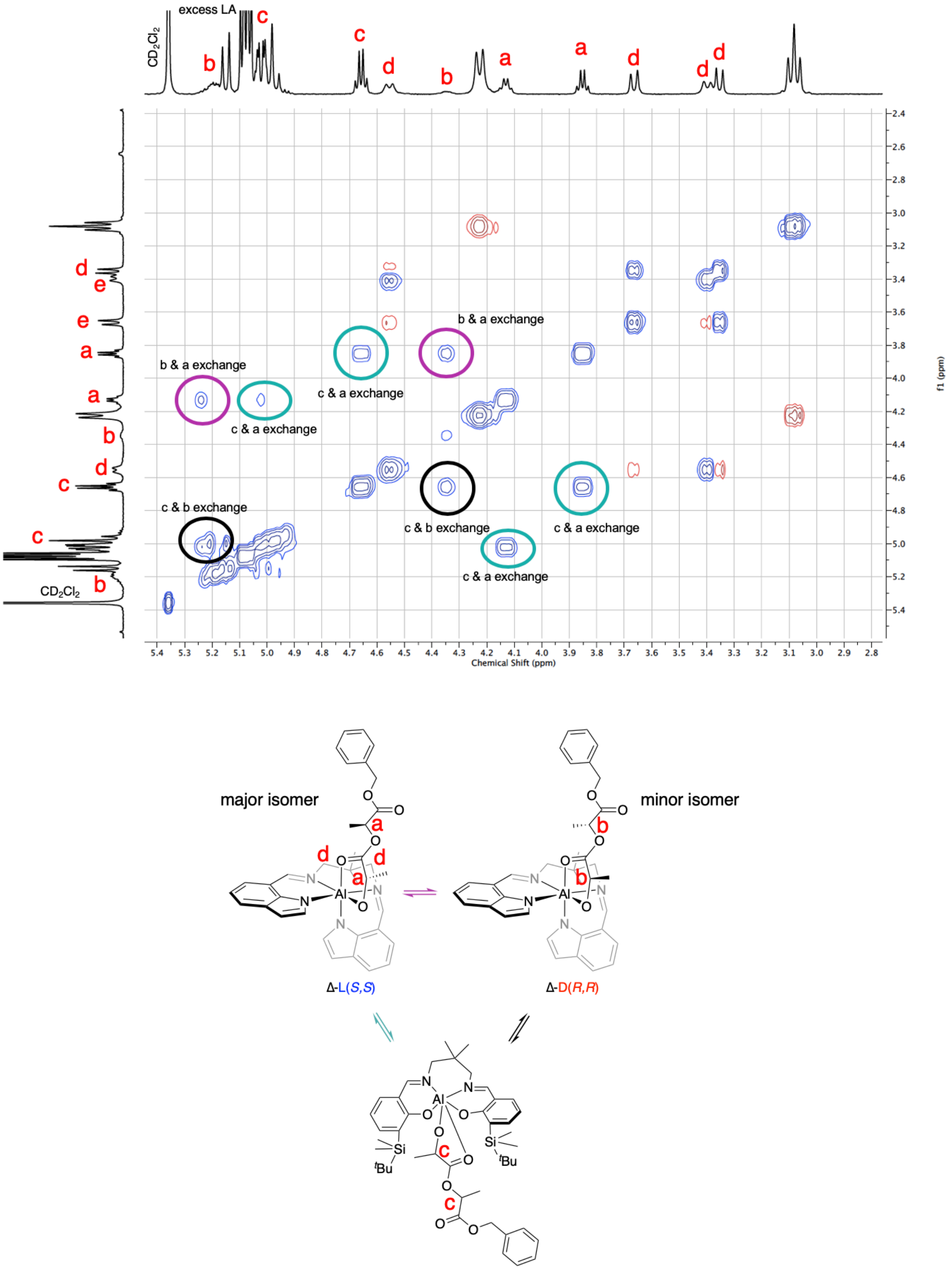

Figure 4.29. NOESY/EXSY spectrum of mixture of equimolar amounts of L^{7}Al(oLAOBn) and ^{N}Al(oLAOBn) (top), and equilibrium scheme hypothesized to rationalize the results (bottom).

4.5.10 *Calculation Details* (executed by Sina Chiniforoush, Mukunda Mandal and Christopher J. Cramer)

Monte Carlo searches for low-energy conformations of the benzyloxy-substituted pre-catalysts themselves (and the ring-opened methoxy products) were undertaken using the OPLS3 force field.[180] All identified minima were then re-optimized at the BP86[181] DFT level using the 6-31G(d)[119] basis set, and then again at the M06-L[116] DFT level using the 6-31+G(d,p)[119] basis set and the SMD implicit solvation model[124] (with methyl butanoate chosen as solvent to simulate a LA melt). Harmonic vibrational frequencies were computed at this level to verify the nature of all stationary points, and for use in molecular vibrational partition functions using the quasi-harmonic-oscillator approximation[182] (where all frequencies below 50 cm^{-1} are replaced by values of 50 cm^{-1}). Finally, single point DFT calculations at the SMD/M06-2X[123]/6-311+G(d,p) level of theory were carried out for all optimized structures to obtain improved electronic energies to which thermal contributions to free energy were added from the M06-L/6-31+G(d,p) step. For stationary points along the initiation process, the steric crowding implicit in the octahedral coordination about Al, and the choice of a single catalyst enantiomorph, eliminated the need for a Monte Carlo search, and relevant geometries were identified manually and computed at the same composite SMD/M06-2X/6-311+G(d,p)//M06-L/6-31+G(d,p) level already described above. The energetic results were also verified using other DFT methods. All DFT calculations were performed with the Gaussian 16[183] suite of electronic structure programs. Other details regarding the computational details of this project can be found in published work.[47]

4.6 Acknowledgments

This work was supported by the NSF Center for Sustainable Polymers, an NSF Center for Chemical Innovation, CHE-1901635. X-ray diffraction data were collected using diffractometers acquired through NSF-MRI Award, CHE-1229400.

5. Investigation and Comparison of *rac*-Lactide Polymerization Initiation by Fluxional and Non-fluxional Aluminum Catalysts

5.1 Overview

A fluxional indolide Al complex (**L^{7Ed}AlOBn**, featuring a 2-carbon backbone) and a non-fluxional, enantiopure, indolide Al complex (**L^{7Cy}AlOBn**, bearing an (*R*,*R*) cyclohexyl backbone) were compared with respect to enantioselective *rac*-LA initiation and subsequent polymerization. While both catalysts exhibited similar reactivity in initiation studies (an equilibrium between unreacted and ring-opened monomer was reached in both cases), only **L^{7Ed}AlOBn** demonstrated high levels of stereoselective initiation. Despite structural differences, both catalysts exhibited similar *rac*-LA polymerization activity, yielding well-controlled polymers ($Đ$ ~ 1.2 under melt conditions) with moderate isotacticities (P_m values reaching 0.80 and 0.82 for **L^{7Ed}AlOBn** and **L^{7Cy}AlOBn**, respectively).

5.2 Introduction

As noted in *Chapters 3* and *4*, salen-type ligands with various metal ions have been long used to study ROP, mostly due to their relatively easy syntheses and high tunability.[63,85] These features have made investigation of structural parameters of the catalyst as a function of the polymerization behavior relatively straightforward. Much work has focused on (salen)Al catalysts due to their moderate ROP activity, allowing for facile kinetic studies.[67,68,70] Nevertheless, advances in stereoselective and robust polymerization of racemic monomers (such as *rac*-LA) via these types of catalysts are still highly coveted, as relatively few literature examples have shown high levels of stereoselectivity for polymerizations performed at low temperatures in various solvents[74,157,184–188] or under industrially relevant bulk conditions (> 130 °C).[34,47,52,156] We aim to develop such catalysts while also studying the mechanism by which they operate, so that the fundamental aspects of these polymerizations can be understood in order to provide insight for rational catalyst design.

Previous work involving the study of stereoselective polymerization initiation of *rac*-LA by a fluxional Al catalyst[47] (**L^{7}AlOBn**, detailed work included in *Chapter 4*) is an example of such efforts. The interconverting complex rapidly fluctuated between its delta and lambda enantiomers, yet each form was selective toward only one enantiomer of *rac*-LA in initiation, as shown through NMR spectroscopy and X-ray crystallography. The initiation selectivity exhibited by **L^{7}AlOBn** was high (upwards of 90% by NMR spectroscopy). In terms of polymerization stereoselectivity, PLA isotacticity measurements reached P_m = 0.80 at 35 °C in solution, but were lower upon heating in bulk conditions (P_m = 0.64 and 0.68 at 135 and 180 °C, respectively).[47]

On the basis of this work, we hypothesized that a non-fluxional, enantiopure Al indolide-type catalyst may exhibit even better polymerization selectivity with *rac*-LA than **L^{7}AlOBn**. We proposed that synthesizing a single enantiomer of an analog catalyst (**L^{7Cy}AlOBn**, Figure 5.1), where the backbone was rigidly held in its enantiopure (*R*,*R*) form, may preferentially ring-open a single enantiomer over the other, ultimately providing polymer samples with high T_m values as a result of stereocomplexing.[189,190]

We also targeted **L^{7Ed}AlOBn** (Figure 5.1). This catalyst differs from **L^{7}AlOBn** in that it bears a shorter, 2-carbon backbone and lacks a gem-dimethyl substituent in the backbone, but would represent a potentially flexible, achiral variant of the rigid complex **L^{7Cy}AlOBn**. Thus, we sought to see if 1) its fluxional nature impacted stereoselective polymerization initiation, and/or 2) its shorter, less flexible backbone relative to that in **L^{7}AlOBn** would lead to changes in overall polymerization rate.

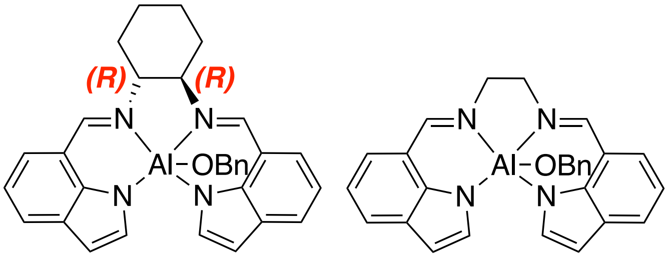

L^{7Cy}AlOBn **L^{7Ed}AlOBn**

Figure 5.1. Targeted complexes **L^{7Cy}AlOBn** (left) and **L^{7Ed}AlOBn** (right).

5.3 Results and Discussion

5.3.1 *Synthesis and Characterization of Complexes*

5.3.1.1 *Synthesis*

The synthesis of both **L^{7Cy}AlOBn** and **L^{7Ed}AlOBn** were achieved in an analogous fashion to that of **L^{7}AlOBn**[47] (Figure 5.2). Condensation of 7-indolecarboxaldehyde and the corresponding diamine (*trans*-1,2-cyclohexanediamine in the case of L^{7Cy}, and ethylene diamine in the case of L^{7Ed}) yielded ligands, **L^{7Cy}H$_2$** (1.02 g, 80%) and **L^{7Ed}H$_2$** (0.438 g, 41%) in high purity, with no purification steps required. Next, metalation with diethylaluminium ethoxide in toluene (or a 5:1 mixture of toluene:THF for **L^{7Cy}H$_2$**, for solubility reasons) led to precipitation of the pure corresponding alkyl complexes, **L^{7Cy}AlEt** (0.036 g, 50%) and **L^{7Ed}AlEt** (0.097 g, 44%). ^{1}H NMR spectroscopy of **L^{7Cy}AlEt** revealed a full set of resonances consistent with a non-fluxional complex in a geometry that renders each indolide inequivalent (Figure 5.10, section 5.5.2). Complex **L^{7Ed}AlEt** however, showed a single set of resonances in its ^{1}H NMR spectrum at room temperature indicative of either a perfectly symmetric complex or a highly fluxional one. Further details of the NMR analysis are provided in section 5.5.2.

Stoichiometric exchange with 1 equiv. of BnOH led to the desired alkoxide complexes, **L^{7Cy}AlOBn** (0.058 g, 72%) and **L^{7Ed}AlOBn**, (0.028 g, 52%). Most notably, the highly shielded Et peaks of the starting AlEt complexes disappeared from the ^{1}H NMR spectra and new peaks for the OBn methylenes appeared at 4.55 (CD_2Cl_2) and 4.49 ($CDCl_3$) ppm for **L^{7Cy}AlOBn** and **L^{7Ed}AlOBn**, respectively (Figures 5.11 and 5.14). Similar to what was observed for the Al-alkyl precursors, ^{1}H and ^{13}C NMR spectroscopy revealed a full set of resonances indicative of inequivalent indolide rings for **L^{7Cy}AlOBn**, and a single set of peaks for **L^{7Ed}AlOBn**. The complexes were also characterized by elemental analysis and X-ray crystallography in the case of **L^{7Ed}AlOBn**.

The crystal structure of **L^{7Ed}AlOBn** revealed a mononuclear pentacoordinate species (Figure 5.2), with a τ_5 value of 0.78, indicating a distorted tbp geometry. The Al-OBn bond (1.75 Å) is quite comparable to that of analogous AlOR species studied within the context of this work,[47,67,68,70,136] and the indolate-Al bond distances (ranging from 1.91–2.04 Å) fall well within the normal range of similar complexes in literature.[140–144,160] Unsurprisingly, the structure bears strong similarities to bond distances in **L^{7}AlOBn**'s structure (indolate-

Al bond distances ranging from 1.91–2.07 Å,[136] see additional detail in *Chapter 3*, section 3.3.2.1).

Moreover, the crystal structure of **L^{7Ed}AlOBn** revealed a lack of symmetry within the complex; this result comprised with its room temperature NMR spectra (which bore a single set of peaks) led us to the hypothesis that the complex was fluxional in nature. This idea was further explored via VT NMR spectroscopy (section 5.3.1.2).

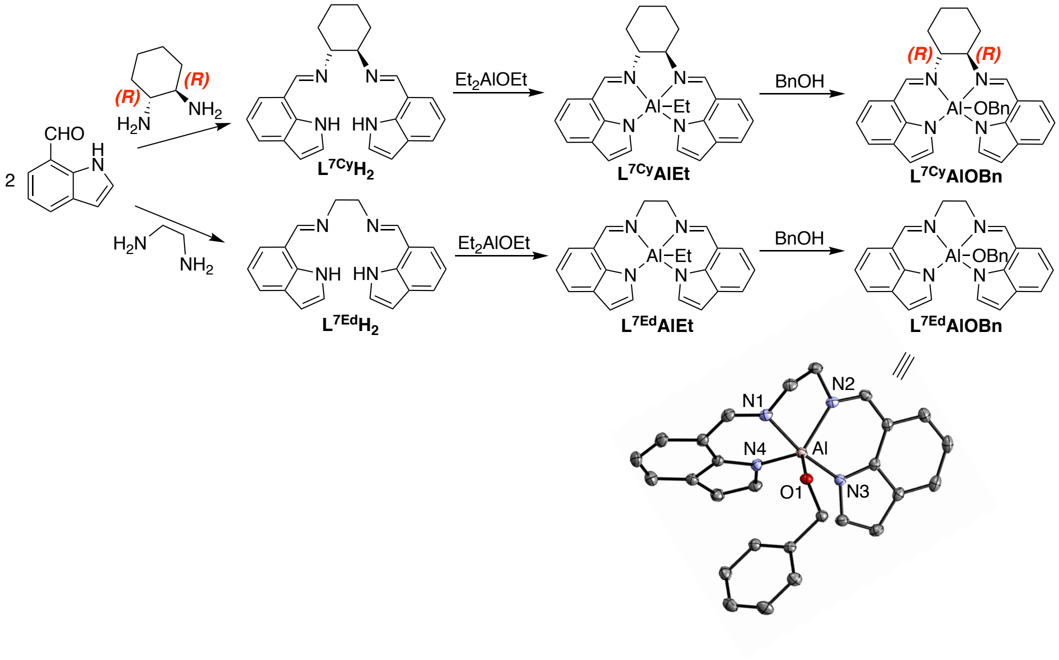

Figure 5.2. Synthesis of **L^{7Cy}AlOBn** and **L^{7Ed}AlOBn** and representation of the X-ray crystal structure of **L^{7Ed}AlOBn**. All atoms are presented as 50% ellipsoids and hydrogen atoms are omitted for clarity. Selected bond distances (Å) and angles (deg): Al-N1, 2.0422(11); Al-N2, 2.0035(11); Al-N3, 1.9242(11); Al-N4, 1.9076(11); Al-O1, 1.7492(9); N1-Al-N2, 79.33(4); N1-Al-N3, 169.72(5); N1-Al-N4, 87.76(4); N1-Al-O1, 85.96(4); N2-Al-O1, 116.63(4); N3-Al-O1, 100.69(4); N4-Al-O1, 117.43(4); N2-Al-N3, 90.64(4); N2-Al-N4, 123.04(5); N3-Al-N4, 95.96(5).

5.3.1.2 *Variable Temperature ^{1}H NMR Spectroscopy Studies*

The single set of equivalent resonances in the NMR data of **L^{7Ed}AlOBn** contrasted with its X-ray crystal structure, which revealed the indolide moieties to be inequivalent. Rapid fluxionality of the complex, in which the structure interconverts between its delta and lambda enantiomers would account for this discrepancy. To evaluate this hypothesis, VT

NMR spectroscopy was employed using experiments analogous to those performed with **L^{7}AlOBn** and ^{N}AlOBn, which revealed had discrepancies between NMR and X-ray data (*Chapter 4*, section 4.3.1).

Results from these VT NMR experiments showed a general broadening of peaks upon reaching low temperatures (Figure 5.3, full spectrum in Figure 5.15, section 5.5.2). Due to solvent freezing point restrictions and NMR probe temperature limits, temperatures below 185 K were not achieved. While the findings are consistent with fluxionality being slowed upon cooling, neither coalescence (peak broadening to the point of flattening), nor complete peak distinction was observed so the activation energy of fluxionality could not be calculated for **L^{7Ed}AlOBn**.

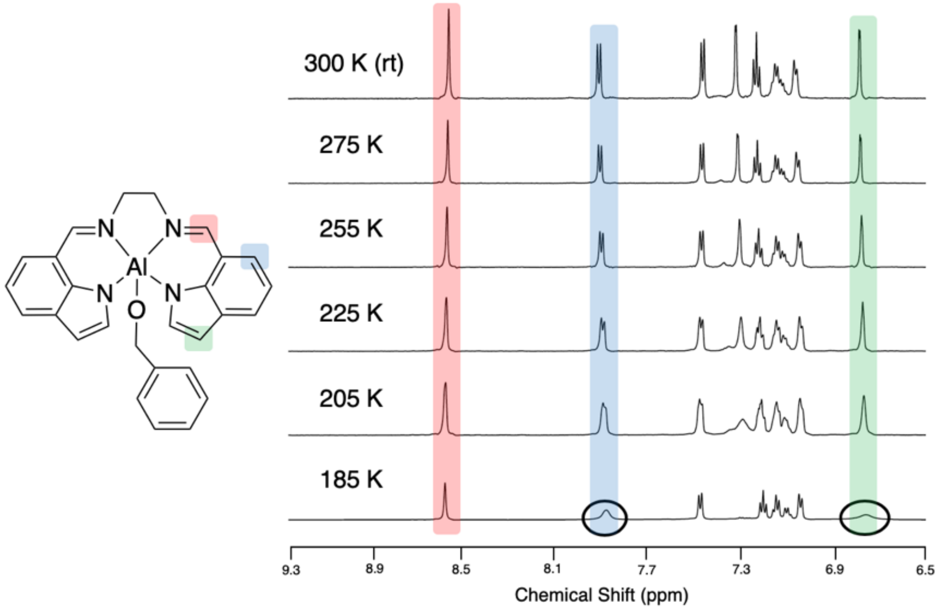

Figure 5.3. Overlaid VT NMR spectra of **L^{7Ed}AlOBn**. Black circles indicate the start of peak coalescence.

5.3.2 *Polymerization Behavior*

To better understand how **L^{7Cy}AlOBn** and **L^{7Ed}AlOBn** behaved as catalysts, polymerization experiments with *rac*-LA were performed (Table 5.1). While overall polymerization rates were relatively slow in solution ($p > 95\%$ after several days), excellent polymerization control was exhibited by both catalysts (even in the melt, entries 5–6 and 8–9, Table 5.1) Both **L^{7Cy}AlOBn** and **L^{7Ed}AlOBn** exhibited similar stereoselectivities (P_ms = 0.82 and 0.80 at 55 °C, for **L^{7Cy}AlOBn** and **L^{7Ed}AlOBn**, respectively). These moderate isotacticities led to polymer T_m values of 158 °C (entries 4 and 7, Table 5.1), which we attribute to crystallinity within the polymer chains. Overall, these results match well with those obtained with structural analog **L^{7}AlOBn**[47] (entries 1–3, Table 5.1), showing that the structural differences among the catalysts had minimal effect on overall polymerization capability.

Table 5.1. *rac*-LA polymerization data by **L^{7}AlOBn**, **L^{7Cy}AlOBn** and **L^{7Ed}AlOBn**.

Entry[a]	Temp. (°C)	LA:cat	Time	Conv.[b]	M_n (kDa)[c]	$Đ$[c]	P_m[d]	T_m (°C)[e]
L^7 1	55 (THF-d_8)	300	4 d	99%	36	1.03	0.80	155
L^7 2	135	300	30 min	96%	40	1.11	0.64	*f*
L^7 3	180	300	15 min	93%	54	1.44	0.68	*f*
L^{7Cy} 4	55 (THF-d_8)	300	6 d	99%	36	1.03	0.82	158
L^{7Cy} 5	135	300	30 min	96%	53	1.23	0.73	*f*
L^{7Cy} 6	180	300	15 min	94%	69	1.22	0.65	*f*
L^{7Ed} 7	55 (THF-d_8)	300	4 d	99%	49	1.06	0.80	158
L^{7Ed} 8	135	300	30 min	85%	74	1.20	0.70	*f*
L^{7Ed} 9	180	300	15 min	94%	77	1.24	0.69	*f*

[a]L^7 = **L^{7}AlOBn**, L^{7Cy} = **L^{7Cy}AlOBn**, L^{7Ed} = **L^{7Ed}AlOBn**. [b]Determined by ^{1}H NMR spectroscopy. [c]Values were determined by SEC using light scattering detection with THF eluent. Theoretical values are 44 kDa for 300 equiv. of LA. [d]Determined by homonuclear decoupled ^{1}H NMR spectroscopy. [e]Determined by DSC. [f]No feature corresponding to a T_m value was observed.

5.3.3 *Stoichiometric Experiments with rac-Lactide*

5.3.3.1 *L^{7Cy}AlOBn Stoichiometric Experiments*

The relatively high levels of stereoselectivity exhibited by both **L^{7Cy}AlOBn** and **L^{7Ed}AlOBn** in polymerizations of *rac*-LA raised the question of whether these catalysts would exhibit high enantioselectivity in initiation as well. To address this question, stoichiometric (1:1) experiments between catalyst and monomer were performed and monitored via NMR spectroscopy. When subjected to 1 equiv. of *rac*-LA, **L^{7Cy}AlOBn** ring-opened both enantiomers of the monomer (see Figure 5.4, full spectrum in Figure 5.16), but in contrast to analogous stoichiometric experiments with **L^{7}AlOBn**, not all catalyst was consumed immediately. To see how long it would take before all the catalyst was consumed and the fully ring-opened products were formed (denoted as L^{7Cy}Al(oL-LAOBn) and L^{7Cy}Al(oD-LAOBn) depending on the enantiomer of *rac*-LA), a long kinetic study was implemented, in which 1:1 **L^{7Cy}AlOBn**:*rac*-LA was monitored for several days. Even after 6 days, unreacted catalyst was still present. In fact, minimal change was observed after 70 min, and integration values indicate that a maximum of ring-opening was reached after 4 hours (only 15% of unreacted catalyst remained). These results suggest that the system had reached an equilibrium after ~70 min.

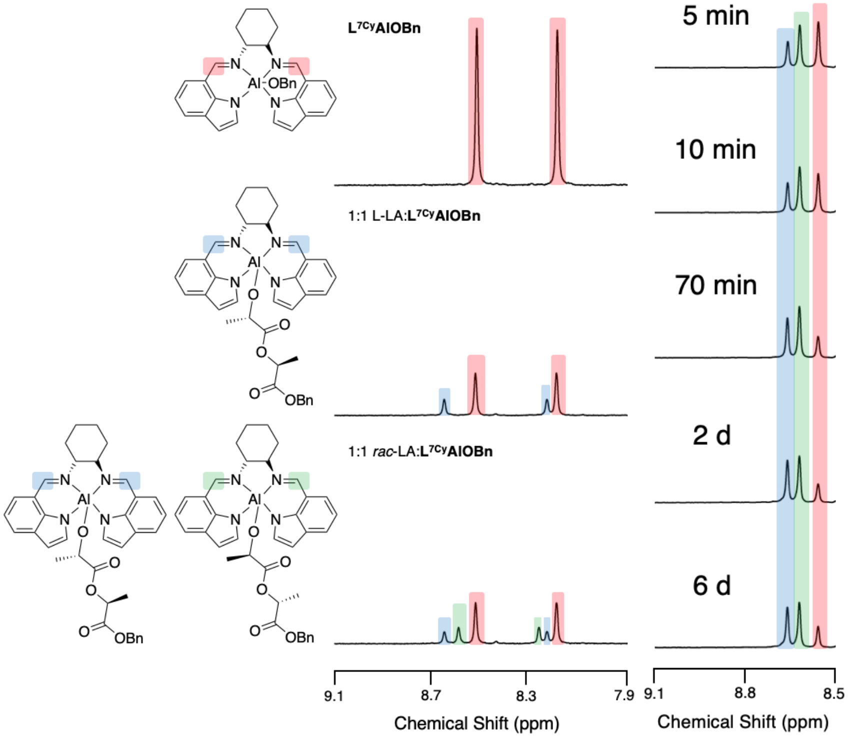

Figure 5.4. Portions of ^{1}H NMR spectra for stoichiometric studies of **L^{7Cy}AlOBn** and LA (left). Overlaid ^{1}H NMR spectra of 1:1 *rac*-LA:**L^{7Cy}AlOBn** after indicated amounts of time (right). In both figures, red = unreacted **L^{7Cy}AlOBn** catalyst, blue = L^{7Cy}Al(oL-LAOBn) and green = L^{7Cy}Al(oD-LAOBn).

To gain further insight into these results, and to see whether or not a kinetic preference was observed when only one enantiomer of monomer was subjected to catalyst, kinetics of single enantiomer ring-opening by **L^{7Cy}AlOBn** were performed. In these studies, stoichiometric amounts of catalyst and a single enantiomer of LA were added to a J-young NMR tube and respective concentrations of both unreacted monomer and L^{7Cy}Al(oLAOBn) complex were monitored via ^{1}H NMR kinetic array over several hours. Data from these parallel experiments indicated that **L^{7Cy}AlOBn** exhibits a significant preference toward D-LA (ring-opened approximately 2.5 x faster than L-LA). Even more, the equilibrium between unreacted monomer and respective L^{7Cy}Al(oLAOBn) complexes was reached after 90 and 225 min, for D- and L-LA, respectively, suggesting that for both enantiomers, the overall equilibrium monomer concentration is low.

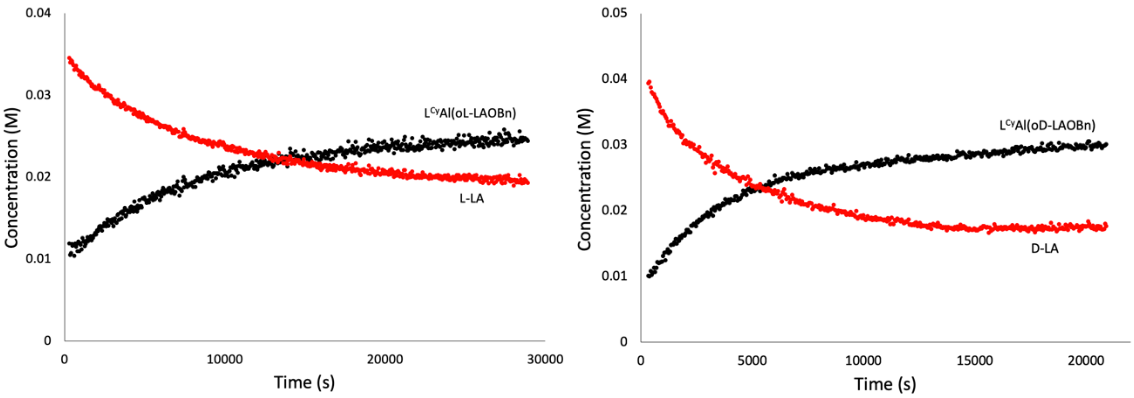

Figure 5.5. Kinetic plots of 1:1 L-LA:**L^{7Cy}AlOBn** (left) and 1:1 D-LA:**L^{7Cy}AlOBn** (right), where ring-opened species growth is indicated in black and monomer decay is shown in red.

5.3.3.2 *L^{7Ed}AlOBn Stoichiometric Experiments*

Analogous stoichiometric reactions between monomer and **L^{7Ed}AlOBn** were also performed. Reaction with 1 equiv. of *rac*-LA resulted in a ^{1}H NMR spectrum that no longer exhibited a single set of peaks; rather, a spectrum consistent with that of a non-fluxional molecule with inequivalent indolide rings was observed (Figures 5.6 and 5.17). This change was indicative of either the formation of indistinguishable, enantiomeric, non-fluxional complexes with unique resonances for each proton, *or* the formation of fluxional, diastereomeric complexes distinguishable by NMR. The same type of spectral change was observed with stoichiometric monomer and catalyst reactions of **L^{7}AlOBn** (see *Chapter 4* for additional detail). In that case, VT NMR was instrumental in deciphering between the two aforementioned possibilities postulated from the observed spectral change. As such, VT NMR was used on the L^{7Ed}Al(oLAOBn) complex. The resulting VT NMR spectra of the 1:1 **L^{7Ed}AlOBn**:*rac*-LA reaction mixture revealed a general broadening of alkoxide moiety peaks, but relatively minimal change for the ligand resonances was observed (Figure 5.19, section 5.5.4). A lack of coalescence for ligand resonances solidified the notion that the L^{7Ed}Al(oLAOBn) complex did not exhibit the same fluxionality observed for its precursor, **L^{7Ed}AlOBn**, but was "locked" into position instead.

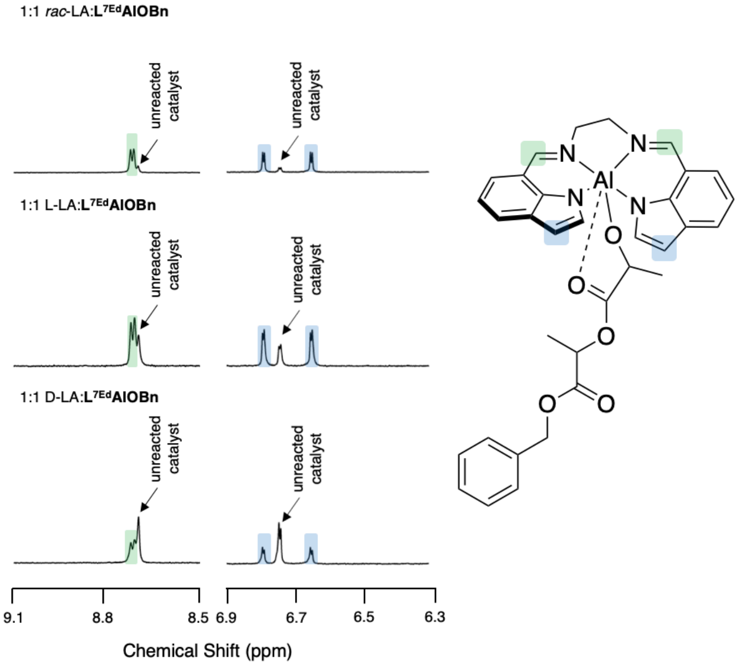

Figure 5.6. Selected portions of the ^{1}H NMR spectra of the products of the reactions of (top) *rac*-LA, (middle) L-LA, or (bottom) D-LA with **L^{7Ed}AlOBn**, with the indicated assignments shown in blue and green. The spectra shown were observed 10 min after the stoichiometric reaction was begun.

Overlaid ^{1}H NMR spectra of the product mixture formed upon reaction of **L^{7Ed}AlOBn** and 1 equiv. of either L-LA, D-LA or *rac*-LA are identical (Figure 5.6). The same spectra would be expected for indistinguishable enantiomeric species, thus serving as additional proof that enantiomers are formed upon ring-opening. Thus, like **L^{7}AlOBn**, **L^{7Ed}AlOBn** shows a high level of enantioselectivity in initiation. Further confirmation of this conclusion and identification of possible equilibria will require NOESY/EXSY NMR spectroscopy studies. Also, without an X-ray crystallographic structure of the product complex, we cannot determine which enantiomer of *rac*-LA is selectively opened by which enantiomer of catalyst (possibilities outlined in Scheme 5.1).

Scheme 5.1. Possible L^{7Ed}Al(oLAOBn) products, (2 sets of enantiomers, 2 sets of diastereomers) resulting from the reaction of the interconverting enantiomers of **L^{7Ed}AlOBn** with 1 equiv. of either L- or D-LA.

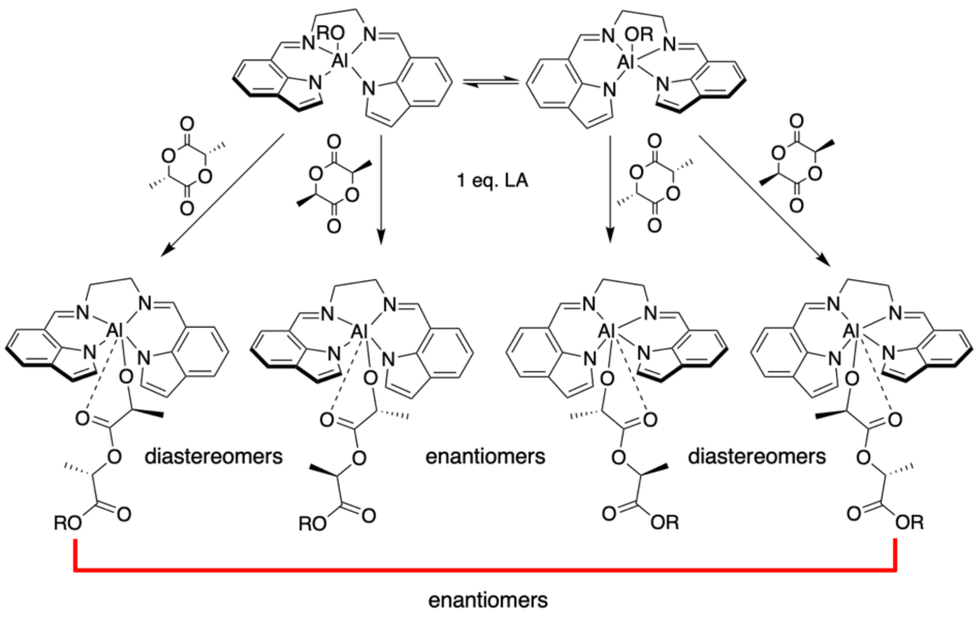

Importantly, ^{1}H NMR studies of these stoichiometric reactions indicate that **L^{7Ed}AlOBn** has different ring-opening rates with each form of LA; the spectra in Figure 5.6 were all observed 10 minutes after the stoichiometric reaction was begun, and catalyst consumption is varied among all three reactions. While ring-opening rate was not measured, (largely due to the short timeframe in between reaction start and NMR analysis), it is noted that opposite to **L^{7Cy}AlOBn**, **L^{7Ed}AlOBn** shows a preference for ring-opening L-LA over D-LA when subjected to both enantiomers. Stoichiometric reaction with *rac*-LA yielded the fastest ring-opening rate overall (nearly all catalyst is consumed upon immediate introduction to the monomer, despite all reactions having the same concentration). However, just as with **L^{7Cy}AlOBn**, an equilibrium between ring-opened monomer and unreacted monomer was reached in minutes in the case of all forms of LA. Despite experiments in which additional equivalents of monomer was subjected to catalyst, or the reactions are heated to 50 °C for extended periods of time (3 d), **L^{7Ed}AlOBn** is not fully consumed, indicating its low equilibrium monomer concentration.

Due to the fluxionality of **L^{7Ed}AlOBn**, and under the assumption that a fluxional complex would react similarly to enantiomers, the discrepancy between rate in ring-opening each form of LA was unexpected. We postulated that residual monomer impurity could be a cause for different **L^{7Ed}AlOBn** reactivities, as even trace amounts of monomer impurity could affect the integrity of the catalyst. To further explore this idea, equimolar amounts of purchased (and subsequently recrystallized) *rac*-LA and a "homemade" *rac*-LA (taken from mixing stoichiometric amounts of L-LA and D-LA, both of which were purchased and recrystallized separately) were subjected to **L^{7Ed}AlOBn**. However, both ^{1}H NMR spectra of these reactions were identical (Figure 5.7, full spectrum in Figure 5.18, section 5.5.4), proving that monomer impurity was not a valid reason for the different reactivities observed. Rather the catalyst, despite its fluxionality, exhibits different ring-opening rates based on the type of monomer subjected to it.

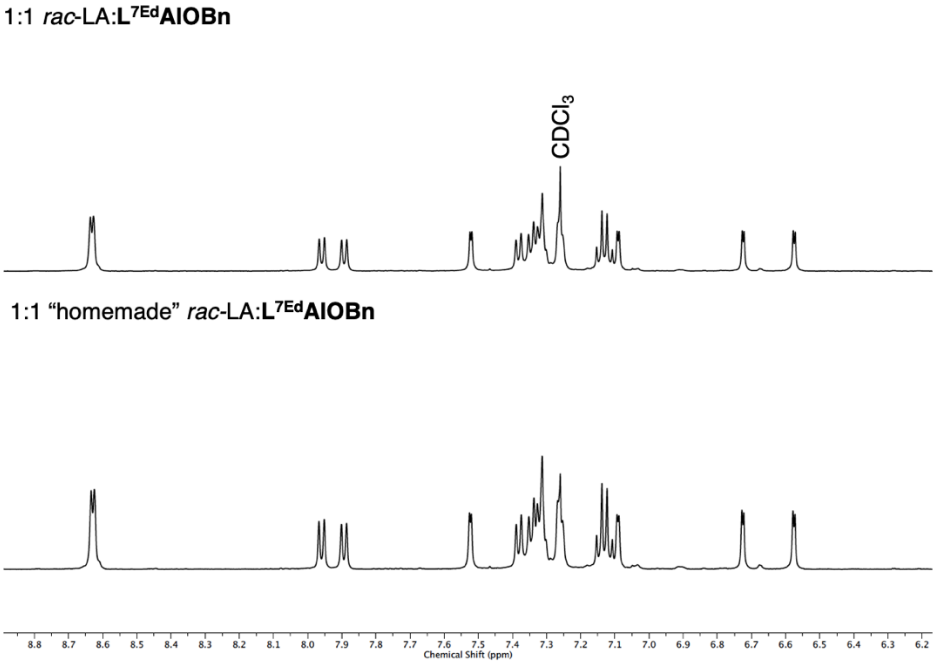

Figure 5.7. Overlay of a portion of the ^{1}H NMR spectra of the products of the reactions of **L^{7Ed}AlOBn** with 1 equiv. *rac*-LA (purchased and recrystallized), and 1 equiv. *rac*-LA (50:50 mixture of D- and L-LA, both purchased and recrystallized separately).

5.3.4 *Exchange Experiments with L^{7Cy}AlOBn*

To better understand the ring-opening equilibrium observed via **L^{7Cy}AlOBn**, and to help determine whether initiation was under thermodynamic or kinetic control, NOESY/EXSY NMR spectroscopy was employed.[47,169] Any exchange observed between peaks of each respective diastereomer (L^{7Cy}Al(oL-LAOBn) or L^{7Cy}Al(oD-LAOBn)) would indicate equilibration, signifying thermodynamic control. However, EXSY experimentation revealed that there was no exchange between alkoxide oLAOBn methine groups of the diastereomers (Figure 5.8). Lack of exchange signals argues against a rapid equilibration of alkoxide ligands of the respective diastereomers and is inconsistent with thermodynamic control. This result is in stark contrast to that of **L^{7}AlOBn**, whose enantiomeric and diastereomeric species were observed to rapidly equilibrate via EXSY NMR.

However, in a puzzling finding, the backbone protons of **L^{7Cy}AlOBn** showed strong exchange correlation, which is improbable due to their locked position in this rigid (nonfluxional) complex. We speculate that these exchange peaks could be a result of a second insertion product (i.e., $L^{7Cy}Al$(oLA-LAOBn), an outcome from adding extra monomer to the reaction in order to push the equilibrium toward consumed catalyst. We postulate that this second insertion product contains resonances hidden underneath those of the backbone protons and is participating in some sort of rapid ligand exchange. This reasoning is speculative, however, as the identity of most of the smaller peaks in the spectrum that exhibit strong exchange correlations are not well-characterized; additional characterization studies of these minor species are ongoing so that they can better identified. As well, it is recognized that any ligand exchanges associated with the complex may be occurring at different rates, and the standard EXSY mixing time of 0.8 s may not be sufficient to capture each level of ligand exchange.

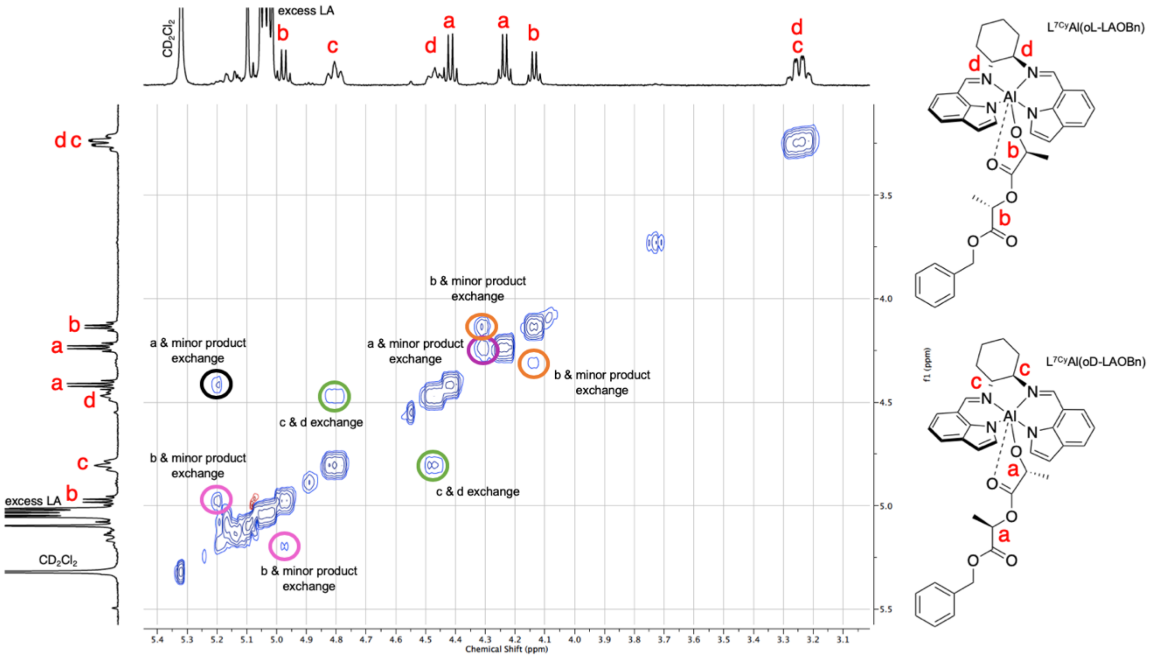

Figure 5.8. NOESY/EXSY NMR spectrum of the product of reaction of *rac*-LA with **L^{7Cy}AlOBn** (i.e., L^{7Cy}Al(oLAOBn)) and corresponding structures of products within the analyzed sample. Exchange correlations between backbone resonances are indicated in green, while exchanges between major methine resonances and unidentified minor products are shown in black, pink, purple and orange; each color represents a unique type of exchange.

Therefore, while the results from these EXSY experiments involving L^{7Cy}Al(oLAOBn) are inconclusive, we plan on continuing studies that are 1) more exact in stoichiometry (to try and rid the spectra of any second insertion peaks), and 2) variant in mixing time, so that different exchange processes may be better identified. As well, EXSY experiments with L^{7Ed}Al(oLAOBn) will also be performed, primarily to identify whether or not thermodynamic control leads to an equilibration of the main enantiomeric products and any lesser diastereomeric species.

5.4 Concluding Remarks

Comparison and analysis of two new, indolide-type Al catalysts, varying only in their backbone structure, was made with regard to stereoselective *rac*-LA initiation and polymerization. The first, **L^{7Ed}AlOBn**, a fluxional catalyst bearing an ethylene diamine backbone, showed excellent enantioselectivity via ^{1}H NMR spectroscopy studies of *rac*-LA initiation, yet showed different reactivity toward each enantiomer in terms of ring-opening rate. On the contrary, an asymmetric and enantiopure catalyst, **L^{7Cy}AlOBn**, bearing an (*R*,*R*) cyclohexyl backbone, did not exhibit stereoselectivity in stoichiometric *rac*-LA initiation, but single-enantiomer kinetic studies indicated its slight preference for D-LA. NOESY/EXSY NMR studies to prove thermodynamic control in this case were inconclusive and work to further elucidate the results are ongoing.

Both catalysts exhibited moderate stereoselectivity in polymerization of *rac*-LA (achieving P_ms of 0.82 and 0.80 for **L^{7Cy}AlOBn** and **L^{7Ed}AlOBn**, respectively), similar to that of what was achieved by **L^{7}AlOBn**.[47] While these structural variations in the indolide-frameworks produced interesting results with regard to polymerization initiation, neither modification had a significant effect on overall *rac*-LA polymerization compared to that of what had been studied previously.[47]

5.5 Experimental

5.5.1 *General Considerations*

All reactions containing either air- and/or water-sensitive compounds were performed within the inert atmosphere of a nitrogen-filled glovebox or using Schlenk line techniques. All reagents were purchased from commercial sources and were used as received, unless otherwise noted. *rac*-, D- and L-LA was purified by recrystallization (3x) from toluene and subsequent vacuum drying. All solvents were dried over CaH_2 or sodium benzophenone, degassed through freeze-pump-thaw techniques, and distilled before being stored under N_2. Nuclear magnetic resonance (NMR) spectroscopy experiments were performed with a Bruker Avance III (500 MHz) spectrometer equipped with a BBFO SmartProbe. Chemical shifts for ^{1}H and ^{13}C NMR spectra were referenced to residual protium in the deuterated solvent (for ^{1}H NMR) and the deuterated solvent itself (for ^{13}C NMR). NOESY/EXSY NMR experiments were accomplished with a mixing time of 0.8 s. Molecular weights (M_n and M_w) and dispersities (M_w/M_n) of the PLA samples were determined in THF at 25 °C with a flow rate of 1 mL per min on an Agilent 1260 Infinity HPLC with Waters Styragel (HR6, HR4, and HR1) columns connected to a Wyatt DAWN Heleos II light scattering detector and a Wyatt OPTILAB T-rEX refractive index detector. Differential scanning calorimetry experiments were conducted via a TA Instruments Discovery DSC, using samples hermetically sealed in aluminum pans, at a heating rate of 10 °C/min. Reported T_m values are from the second heating ramp. Elemental analyses were performed by Robertson Microlit Laboratories in Ledgewood, NJ. X-ray diffraction measurements were collected with Mo Kα source and with either a Bruker D8 VENTURE diffractometer equipped with a Photon II CPAD using normal parabolic mirrors as monochromators, a Bruker D8 VENTURE diffractometer equipped with a Photon III CMOS using normal parabolic mirrors as monochromators.

5.5.2 *Synthetic Procedures*

Synthesis of $\mathbf{L^{7Cy}H_2}$. Synthesis and characterization of this molecule has been previously reported.[191] However, a slightly different synthetic approach that what has been reported was taken while synthesizing $\mathbf{L^{7Cy}H_2}$. To an oven-dried round bottom flask equipped with a reflux condenser and charged with a stir bar, 7-indolecarboxaldehyde (1.00 g, 6.89 mmol) was added and dissolved in absolute ethanol (0.63 M) while stirring. To this mixture, *trans*-1,2-cyclohexanediamine (0.393 g, 0.5 equiv.) was added before heating to reflux (80 °C) for 3 d. After 3 d, the reaction mixture and its precipitate were filtered via vacuum filtration and the solid was washed with cold ethanol (3 x 10 mL). The resulting off-white solid was dried via Schlenk line for 6–8 h before being pumped into an N_2

glovebox. ^{1}H NMR analysis indicated this material was pure and required no further purification before subsequent synthetic steps. Yield: 1.02 g, 80%. Characterization matches what has been recently published for this ligand.[191]

Synthesis of L^{7Cy}AlEt. To an oven-dried screw cap bomb flask equipped with a stir bar, ligand (0.064 g, 0.175 mmol) and Et_2AlOEt (excess) were dissolved in a 50:50 mixture of toluene and THF (2 mL, each) while in an N_2 glovebox. The sealed flask was pumped out of the box, heated to 75° C and stirred for 3 d. After cooling to room temperature, the bomb flask was pumped back into the glovebox and the solvent removed *in vacuo*. The resulting oil was triturated with pentane to yield a bright yellow solid. The solid was then collected via vacuum filtration and washed with pentane (3 x 5 mL) to reveal pure product. The product was isolated as a bright-yellow solid and was stored under N_2 until subsequent use. Yield: 0.036 g, 50%. ^{1}H NMR (500 MHz, CD_2Cl_2) δ 8.76 (s, 1H, C*H*=N), 8.43 (s, 1H, C*H*=N), 8.01 (d, *J* = 7.75 Hz, 1H, Ar*H*), 7.78 (d, *J* = 7.75 Hz, 1H, Ar*H*), 7.67 (d, *J* = 2.71 Hz, 1H, NC*H*=CH), 7.38 (m, 2H, Ar*H*), 7.11 (m, 2H, Ar*H*), 6.77 (d, *J* = 2.71 Hz, 1H, NCH=C*H*), 6.36 (d, *J* = 2.93 Hz, 1H, NCH=C*H*), 6.26 (d, *J* = 2.93 Hz, 1H, NC*H*=CH), 4.08 (m, 1H, NC*H*CH_2), 3.23 (m, 1H, NC*H*CH_2), 2.50 (m, 2H, $NCH_2CH_2CH_2CH_2N$), 2.15 (m, 1H, $NCH_2CH_2CH_2CH_2N$), 2.05 (m, 1H, $NCH_2CH_2CH_2CH_2N$), 1.72–1.56 (m, 4H, $NCH_2CH_2CH_2CH_2N$), 0.77 (t, *J* = 8.07 Hz, 3H, $AlCH_2CH_3$), 0.16–0.06 (m, 2H, $AlCH_2CH_3$); ^{13}C NMR (125 MHz, CD_2Cl_2) δ 171.44, 159.42, 142.12, 138.60, 138.18, 133.15, 132.14, 128.66, 127.79, 126.58, 126.08, 118.35, 118.24, 117.96, 116.06, 103.29, 103.29, 103.06, 68.09, 63.18, 33.36, 27.78, 25.29, 24.73, 10.89. Despite using a broad sweep width (up to −200 ppm) and using VT NMR techniques, no signal for the methylene of the ethyl substituent bound to the Al center could be identified. Anal. Calcd for $C_{26}H_{27}AlN_4$: C, 73.91; H, 6.44; N, 13.26. Found: C, 72.99; H, 6.34; N, 12.70.

Synthesis of L^{7Cy}AlOBn. To an oven-dried vial equipped with a small stir bar, **L^{7Cy}AlEt** (0.068 g, 0.160 mmol) was added and dissolved in a minimal amount of $CHCl_3$. Using a 1 M stock solution in $CHCl_3$, a stoichiometric amount of BnOH was added to the vial. The reaction was stirred overnight, and the solvent was then removed *in vacuo*, yielding a bright-yellow solid. The solid was stirred in pentane before being isolated through vacuum filtration. Purification was completed by recrystallizing the material in toluene layered with pentane in a −40° C freezer overnight. The material was subsequently stored under N_2. Yield: 0.058 g, 72%. ^{1}H NMR (500 MHz, CD_2Cl_2) δ 8.74 (s, 1H, C*H*=N), 8.48 (s, 1H, C*H*=N), 8.06 (d, *J* = 7.67 Hz, 1H, Ar*H*), 7.84 (d, *J* = 7.81 Hz, 1H, Ar*H*), 7.72 (d, *J* = 2.49 Hz, 1H, NC*H*=CH), 7.43 (app t, *J* = 7.70 Hz, 2H, Ar*H*), 7.17 (m, 5H, Ar*H*), 7.03 (m, 2H, Ar*H*), 6.81 (d, *J* = 2.49 Hz, 1H, NCH=C*H*), 6.43 (app s, 2H, NC*H*=CH, NCH=C*H*), 4.55 (app s, 2H, OCH_2Ph), 4.11 (m, 1H, NC*H*CH_2), 3.17 (m, 1H, NC*H*CH_2), 2.46 (m, 1H, NCH_2CH_2CH_2CH_2N), 2.38 (m, 1H, NCH_2CH_2CH_2CH_2N), 2.05 (m, 1H, NCH_2CH_2CH_2CH_2N), 1.97 (m, 1H, NCH_2CH_2CH_2CH_2N), 1.58 (m, 1H, NCH_2CH_2CH_2CH_2N), 1.44 (m, 3H, NCH_2CH_2CH_2CH_2N); ^{13}C NMR (125 MHz, CD_2Cl_2) δ 170.92, 160.46, 146.11, 142.31, 142.00, 138.66, 138.57, 133.08, 132.09, 128.88, 128.37, 128.03, 127.17, 126.79, 126.56, 126.45, 118.65, 118.65, 118.14, 118.14, 117.59, 115.81, 103.81, 103.57, 67.73, 65.92, 63.31, 23.40, 27.82, 25.08, 24.41. Despite multiple attempts to collect CHN elemental analysis for this complex, results consistently yielded slightly lower percentages for carbon and nitrogen atoms than what was calculated. This is likely due to incomplete combustion during the experiment, as the high purity of the complex was confirmed via NMR spectroscopy.

Synthesis of $L^{Ed}H_2$. To an oven-dried round bottom flask equipped with a reflux condenser and charged with a stir bar, 7-indolecarboxaldehyde (1.00 g, 6.89 mmol) was added and dissolved in absolute ethanol (0.63 M) while stirring. To this mixture, ethylenediamine (0.207 g, 0.5 equiv.) was added before heating to reflux (80 °C) for 3 d. After 3 d, the reaction mixture was transferred to a new round bottom flask before being placed in a −20 °C freezer overnight. The resulting precipitate were filtered via vacuum filtration and the solid was washed with cold ethanol (3 x 10 mL) before being isolated. The resulting taupe solid was dried via Schlenk line for 6–8 h before being pumped into an N_2 glovebox. ^{1}H NMR analysis indicated this material was pure and required no further purification before subsequent synthetic steps. Yield: 0.438 g, 41%. ^{1}H NMR (500 MHz, $CDCl_3$) δ 10.73 (s, 2H, N*H*) 8.57 (s, 2H, C*H*=N), 7.77 (d, J = 7.69 Hz, 2H, Ar*H*), 7.30 (d, J = 7.69 Hz, 2H, Ar*H*), 7.17 (m, 4H, NC*H*=CH, Ar*H*), 6.58 (app s, 2H, NCH=C*H*), 4.08 (app s, 4H, NCH_2CH_2N); ^{13}C NMR (125 MHz, $CDCl_3$) δ 163.43, 134.16, 128.45, 125.39, 125.09, 123.78, 119.41, 119.28, 102.28, 62.38. CHN elemental analysis was not attempted for this molecule.

Synthesis of L^{7Ed}AlEt. To an oven-dried screw cap bomb flask equipped with a stir bar, ligand (0.189 g, 0.600 mmol) and Et_2AlOEt ethoxide (excess) were dissolved in toluene (~2 mL) while in an N_2 glovebox. The sealed flask was pumped out of the box, heated to 70 °C and stirred for 3 d. After cooling to room temperature, the bomb flask was pumped back into the glovebox and put in the glovebox freezer overnight. The resulting solid was collected via vacuum filtration as a light yellow solid and was stored under N_2 until subsequent use. Yield: 0.097 g, 44%. ^{1}H NMR (500 MHz, $CDCl_3$) δ 8.55 (s, 2H, C*H*=N), 7.93 (d, J = 7.70 Hz, 2H, Ar*H*), 7.31 (d, J = 7.70 Hz, 2H, Ar*H*), 7.24 (d, J = 2.97 Hz, 2H, NC*H*=CH), 7.10 (t, J = 7.70 Hz, 2H, Ar*H*), 6.64 (d, J = 2.97 Hz, 2H, NCH=C*H*), 4.30 (m, 2H, NCH_2CH_2N), 3.78 (m, 2H, NCH_2CH_2N), 0.72 (t, J = 8.07 Hz, 3H, $AlCH_2CH_3$), 0.02 (q, J = 8.07 Hz, 2H, $AlCH_2CH_3$); ^{13}C NMR (125 MHz, $CDCl_3$) δ 168.18, 142.12, 138.53, 132.26, 127.75, 126.47, 117.81, 116.48, 103.06, 54.60, 10.50. Despite using a broad sweep width (up to −200 ppm) and using variable temperature NMR techniques, no signal for the methylene of the ethyl substituent bound to the Al center could be identified. Anal. Calcd for $C_{22}H_{21}AlN_4$: C, 71.72; H, 5.75; N, 15.21. Found: C, 71.62; H, 5.67; N, 14.74.

Synthesis of $\mathbf{L^{7Ed}AlOBn}$. To an oven-dried vial equipped with a small stir bar, $\mathbf{L^{7Ed}AlEt}$ (0.046 g, 0.124 mmol) was added and dissolved in a minimal amount of $CHCl_3$. Using a 1 M stock solution in $CHCl_3$, a stoichiometric amount of BnOH was added to the vial. The reaction was stirred overnight and the solvent was then removed *in vacuo*, yielding a muted yellow solid. The solid was stirred in pentane before being isolated through vacuum filtration. Purification was completed by recrystallizing the material in toluene layered with pentane in a −40° C freezer overnight. The material was subsequently stored under N_2. Yield: 0.028 g, 52%. ^{1}H NMR (500 MHz, $CDCl_3$) δ 8.49 (s, 2H, C*H*=N), 7.97 (d, *J* = 6.63 Hz, 2H, Ar*H*), 7.34 (d, *J* = 2.99 Hz, 2H, NC*H*=CH), 7.31 (d, *J* = 7.63 Hz, 2H, Ar*H*), 7.13 (t, *J* = 7.63 Hz, 2H, Ar*H*), 7.04 (app s, 3H, Ar*H*), 6.92 (app s, 2H, Ar*H*), 6.69 (d, *J* = 2.99 Hz, 2H, NCH=C*H*), 4.49 (app s, 2H, OCH_2Ph) 4.19 (m, 2H, NCH_2CH_2N), 3.65 (m, 2H, NCH_2CH_2N); ^{13}C NMR (125 MHz, $CDCl_3$) δ 168.48, 142.15, 138.61, 132.27, 127.90, 127.80, 126.85, 126.72, 125.98, 118.05, 116.02, 103.74, 65.54, 54.88. Anal. Calcd for $C_{27}H_{23}AlN_4O$: C, 72.63; H, 5.19; N, 12.55. Found: C, 71.44; H, 4.98; N, 12.05.

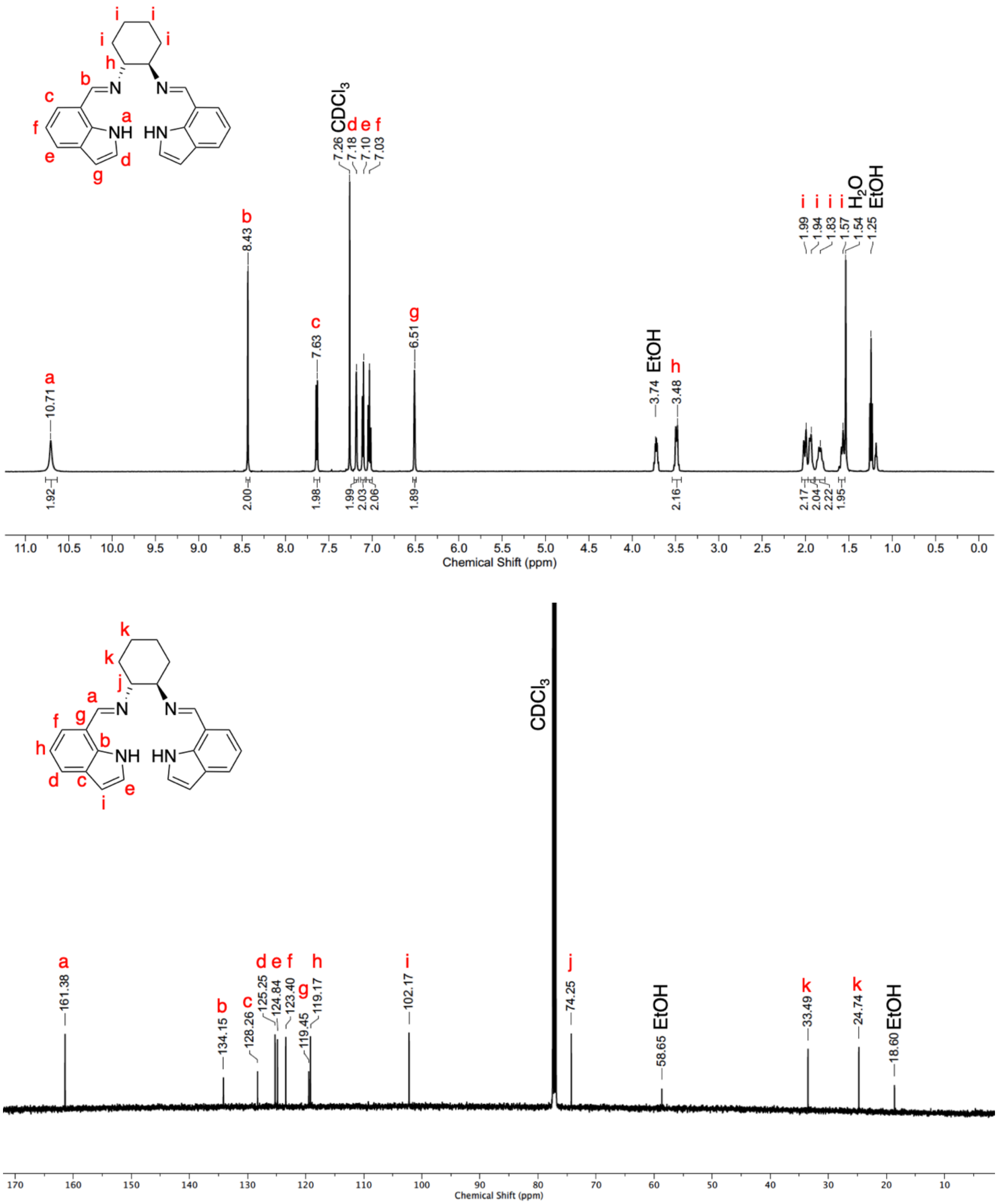

Figure 5.9. ^{1}H (top) and ^{13}C (bottom) NMR spectra of $\mathbf{L^{7Cy}H_2}$.

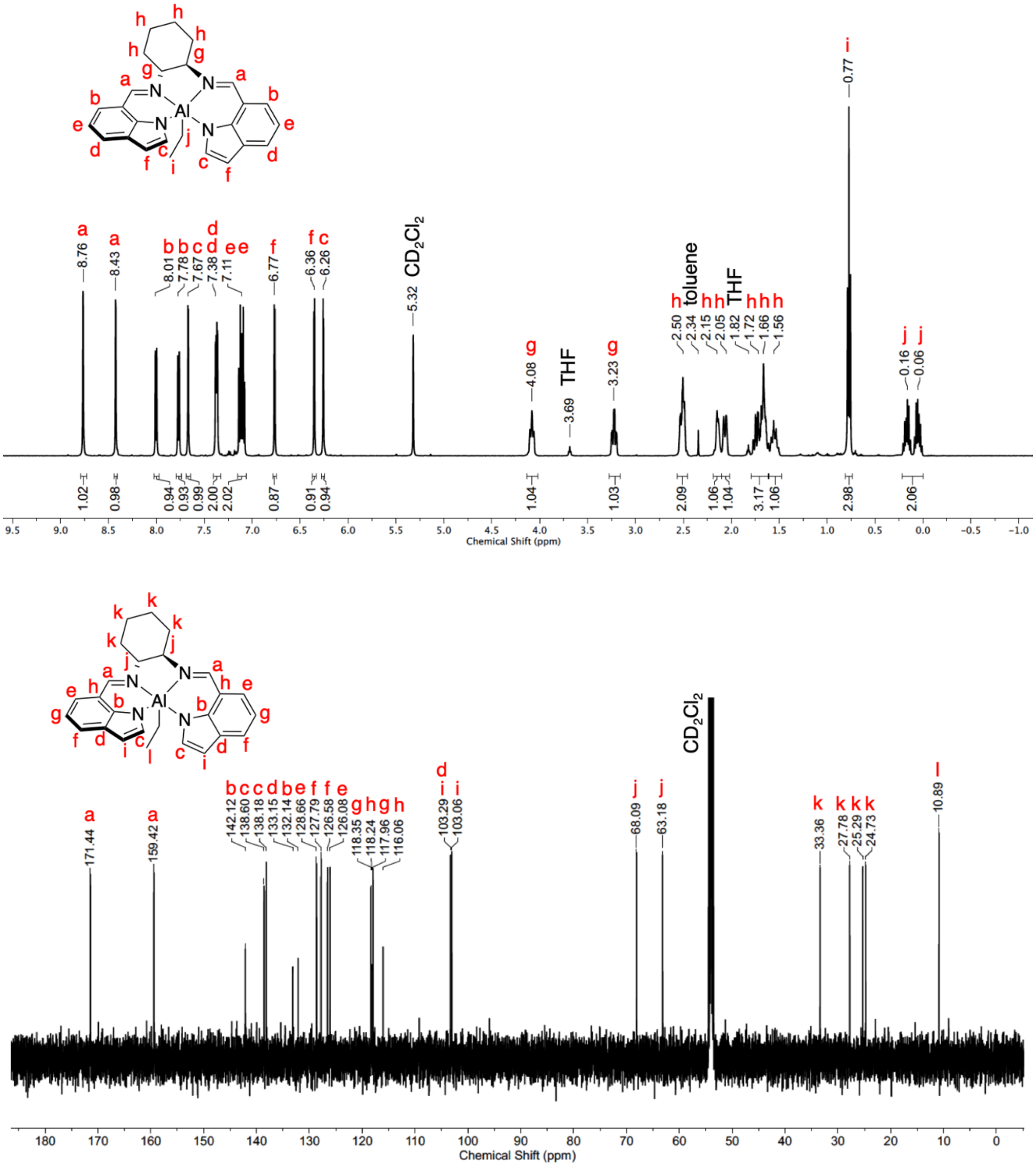

Figure 5.10. ^{1}H (top) and ^{13}C (bottom) NMR spectra of **L^{7Cy}AlEt**.

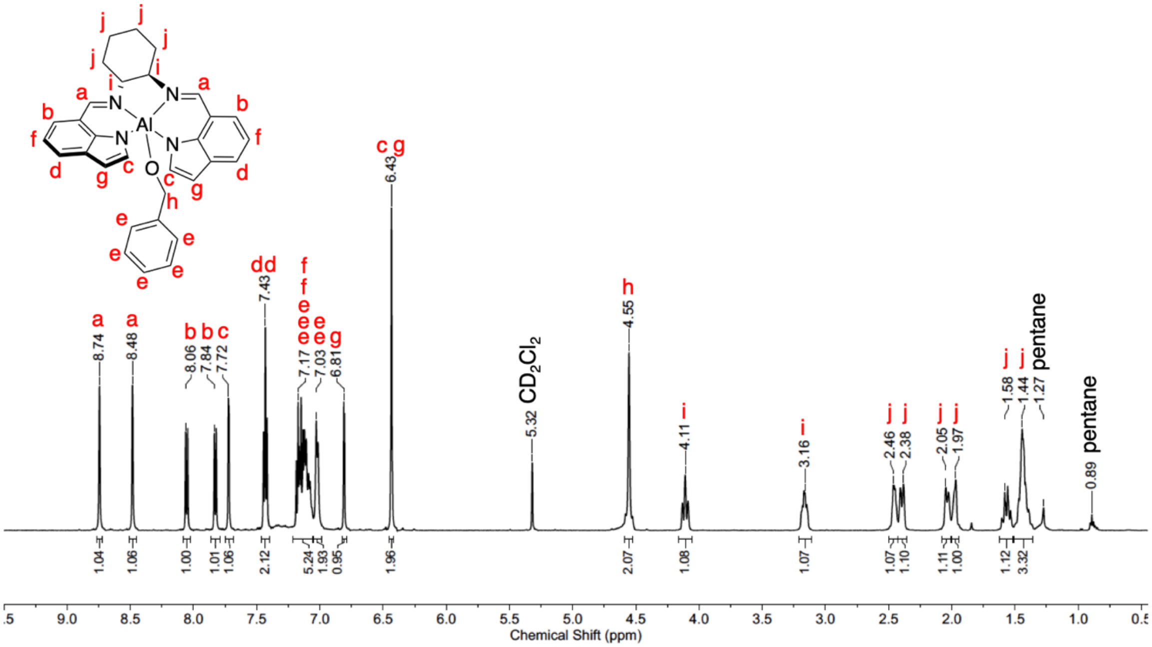

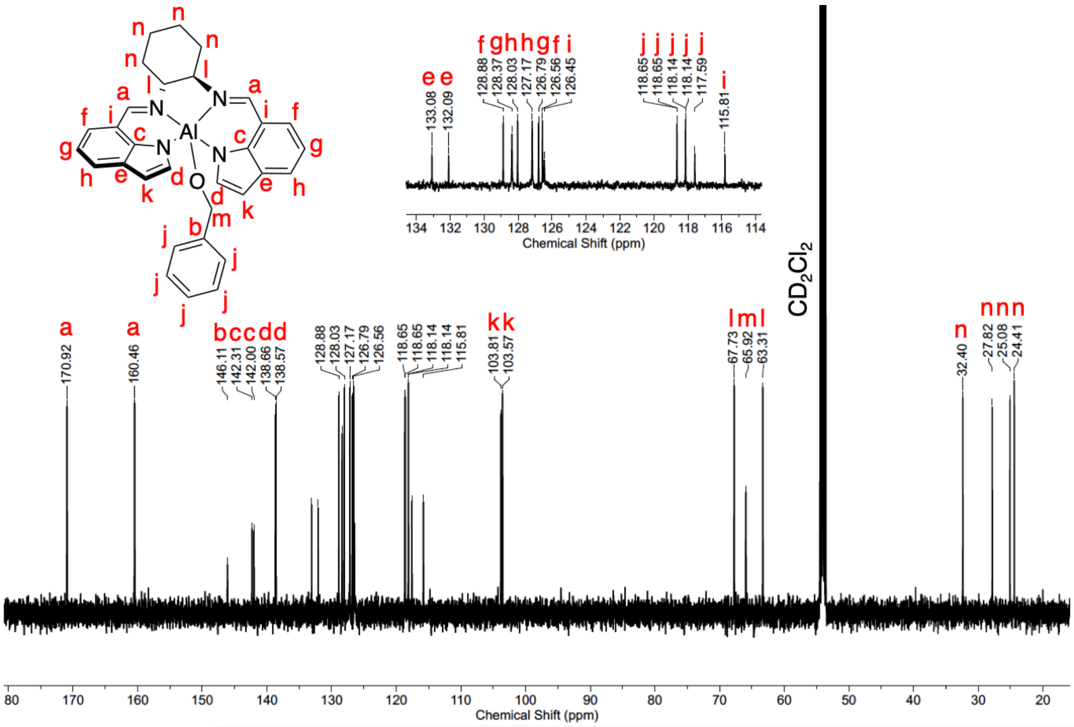

Figure 5.11. ^{1}H (top) and ^{13}C (bottom) NMR spectra of **L^{7Cy}AlOBn**.

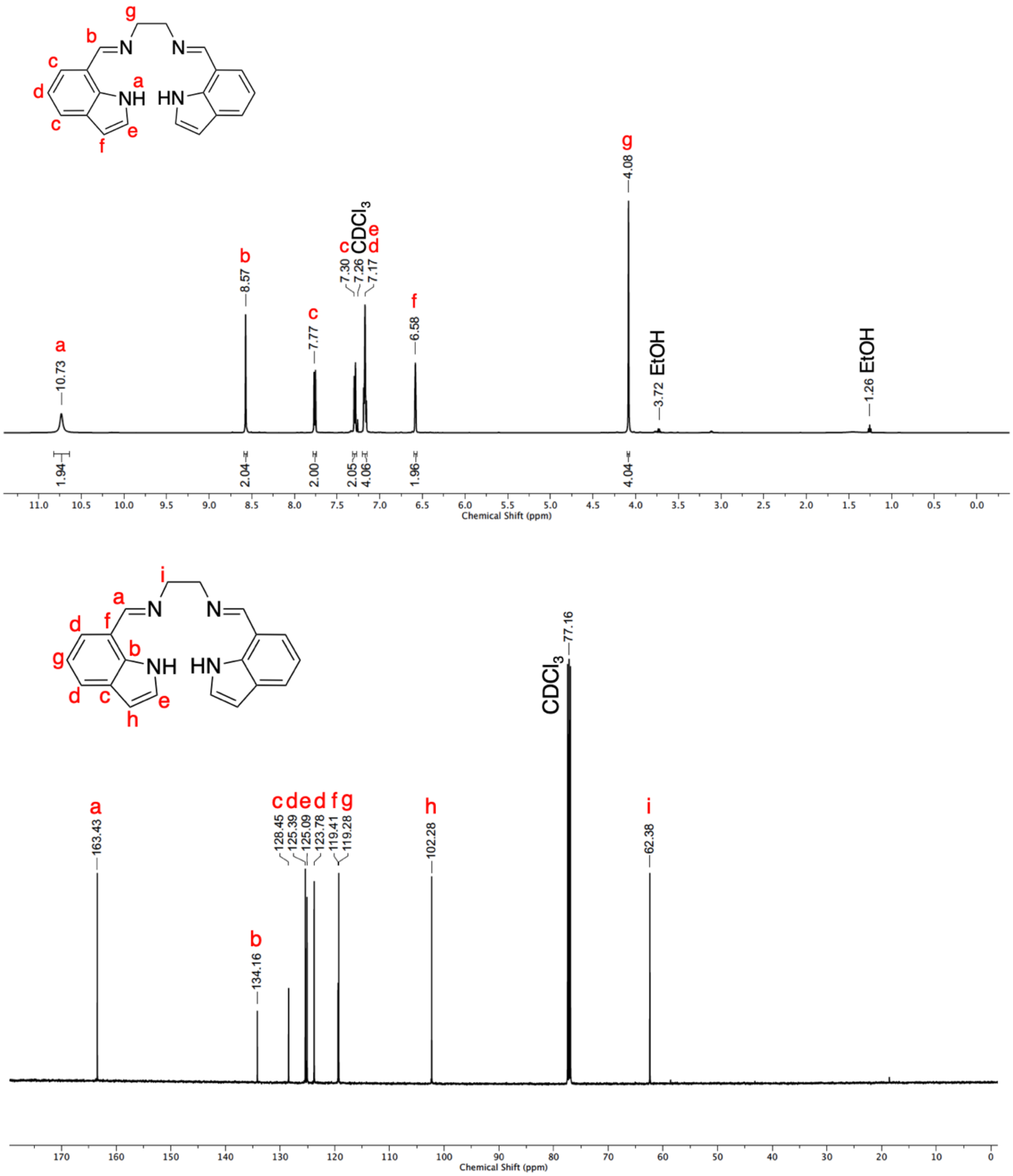

Figure 5.12. ^{1}H (top) and ^{13}C (bottom) NMR spectra of $\mathbf{L^{7Ed}H_2}$.

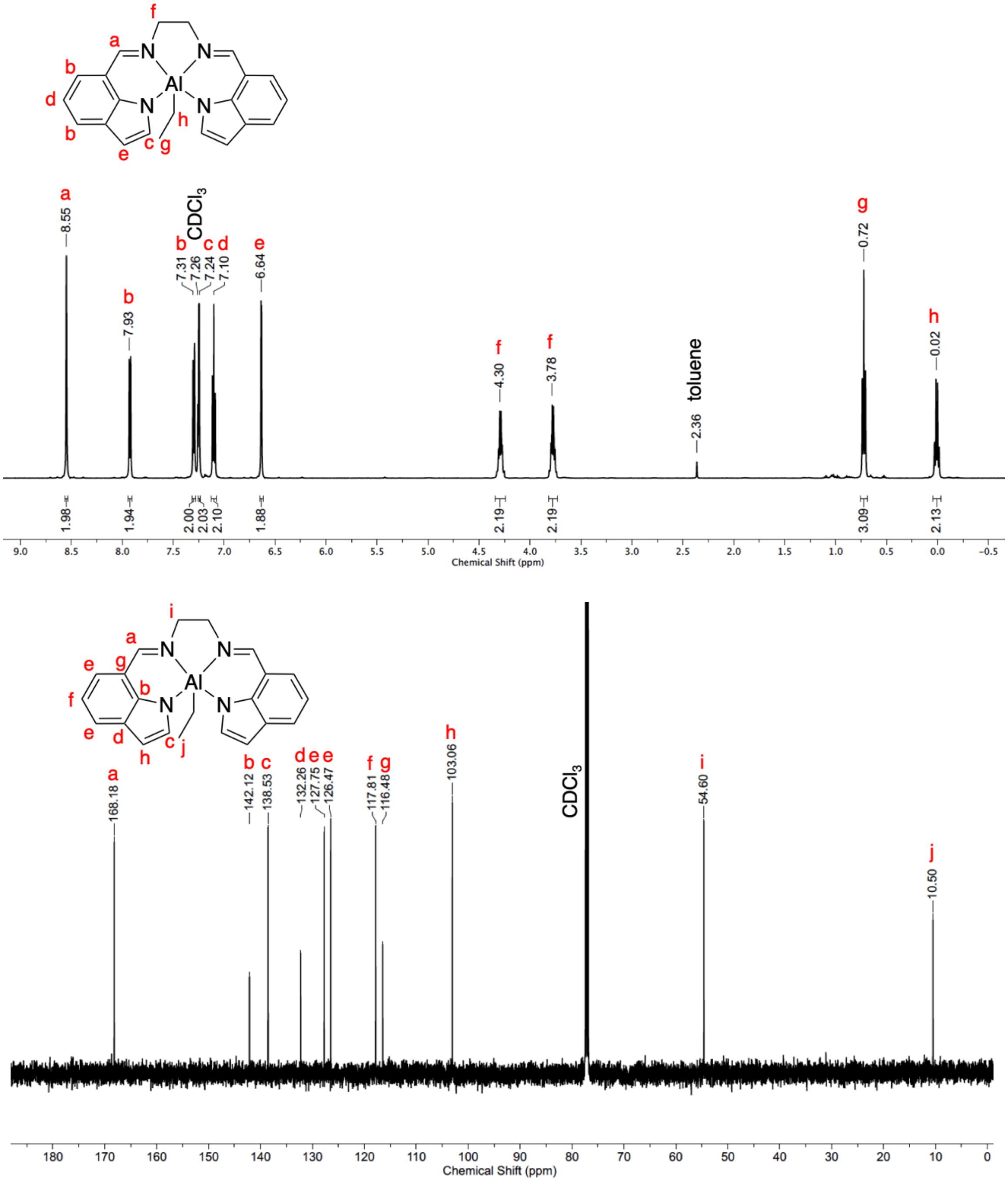

Figure 5.13. ^{1}H (top) and ^{13}C (bottom) NMR spectra of **L^{7Ed}AlEt**.

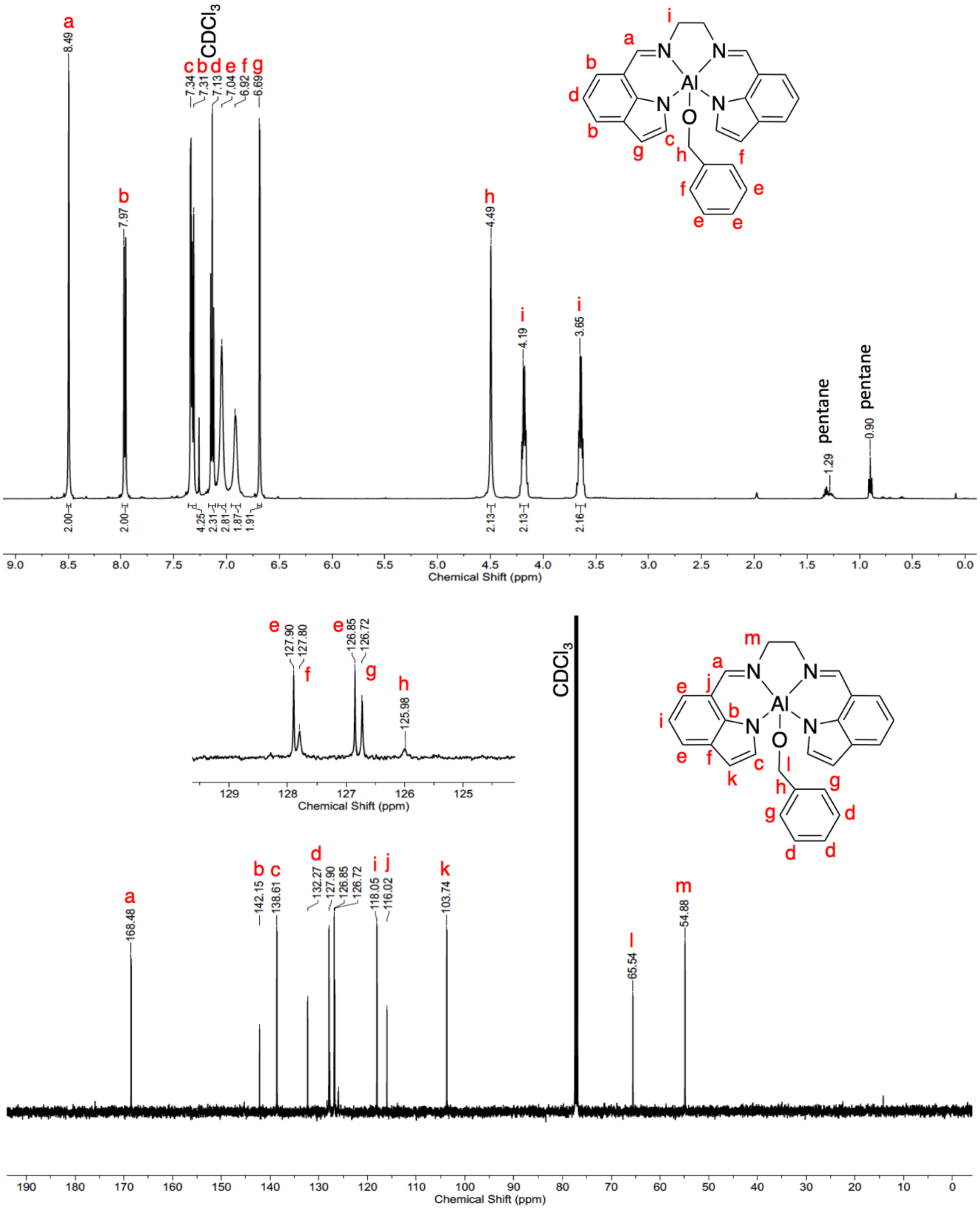

Figure 5.14. ^{1}H (top) and ^{13}C (bottom) NMR spectra of **L^{7Ed}AlOBn**.

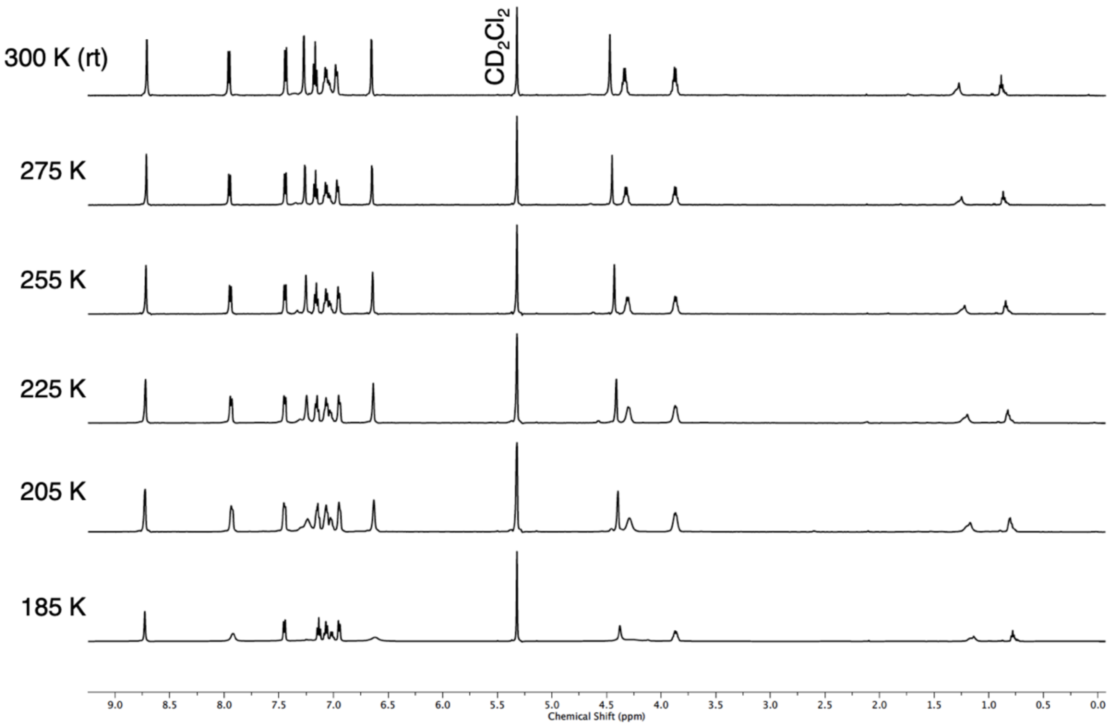

Figure 5.15. VT ^{1}H NMR overlay of **L^{7Ed}AlOBn**. The fluxionality of the complex is inhibited at lower temperatures, as indicated by the wide broadening of peaks (first appearing at ~185 K).

5.5.3 *Polymerization Experiments and Analysis*

Polymerizations in solution were performed in deuterated solvent (THF-d_8) at 55 °C. Polymerization procedures (solution) were completed by first making stock solutions of catalyst (1 mL, 9.7 mM, THF-d_8) and *rac*-LA (1 mL, 1.5 M, THF-d_8,), then sequentially adding them to a J-Young NMR tube (240 µL catalyst stock, 465 µL monomer stock) for final concentrations of 3.3 mM catalyst and 1.0 M monomer in a total volume of 705 µL. Once the polymerizations reached >95% conversion, they were quenched via air exposure. An aliquot of the polymerization was removed and subjected to ^{1}H NMR analysis in order to determine the monomer conversion. The remainder of the reaction mixture was dissolved in CH$_2$Cl$_2$ before being precipitated into cold MeOH. The resulting PLA was then dried under vacuum for ~12 h before being submitted for additional analysis.

Melt polymerization studies were performed by weighing out catalyst (0.003 g, 0.006 mmol, 1 equiv.) into an oven-dried screw-cap bomb flask charged with a stir bar and monomer (0.260 g, 1.80 mmol, 300 equiv.) in a nitrogen filled glovebox. The bomb flask was capped, removed from the glovebox, and then heated and stirred at the desired temperature for a given amount of time. The polymerizations were quenched and worked up in the same manner as the polymerizations performed in solution.

5.5.4 *Stoichiometric Experiments*

Stoichiometric monomer:catalyst NMR experiments were performed by first making a 0.0065 M stock solution (1 mL) of catalyst in $CDCl_3$ and a 0.078 M stock solution (500 µL) of the designated LA monomer in $CDCl_3$ while in a nitrogen-filled glovebox. Then, 600 µL (3.9 µmol) of catalyst stock solution and 50 µL (3.9 µmol) of monomer stock solution (along with 50 µL pure $CDCl_3$) were added to a J-young NMR tube, targeting a final concentration of 0.0055 M for both catalyst and monomer and a final NMR volume of 700 µL. The J-young tube was then removed from the glovebox, shaken, and immediately analyzed by NMR spectroscopy.

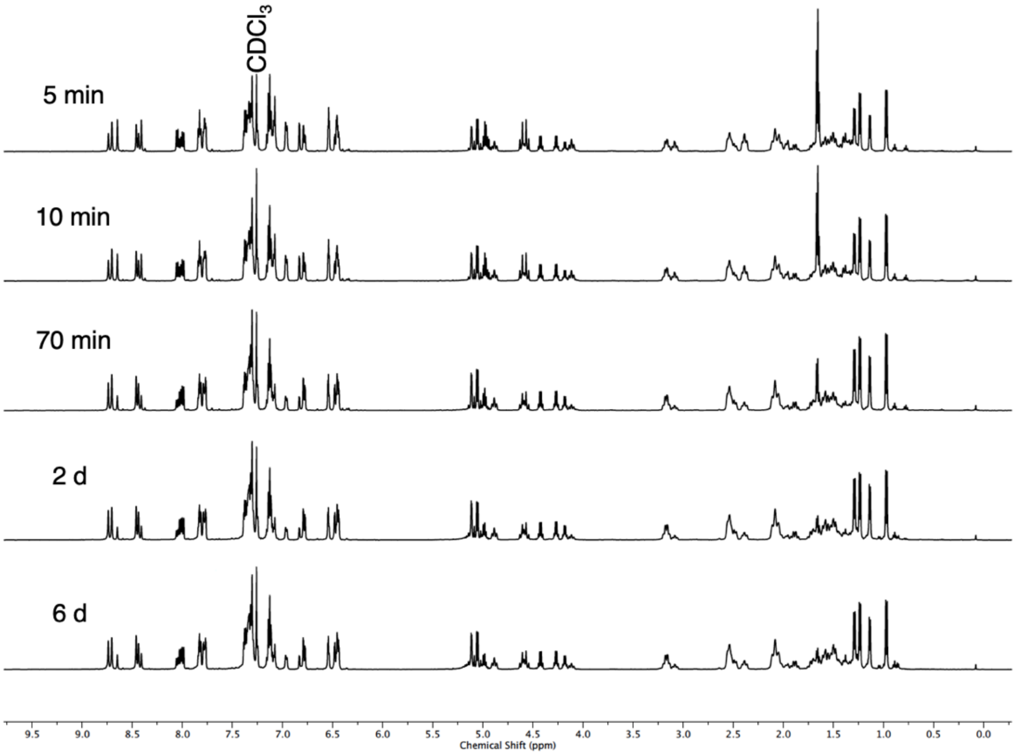

Figure 5.16. Overlay of ^{1}H NMR spectra of the products of the reaction of **L^{7Cy}AlOBn** with 1 equiv. *rac*-LA after specified amounts of time.

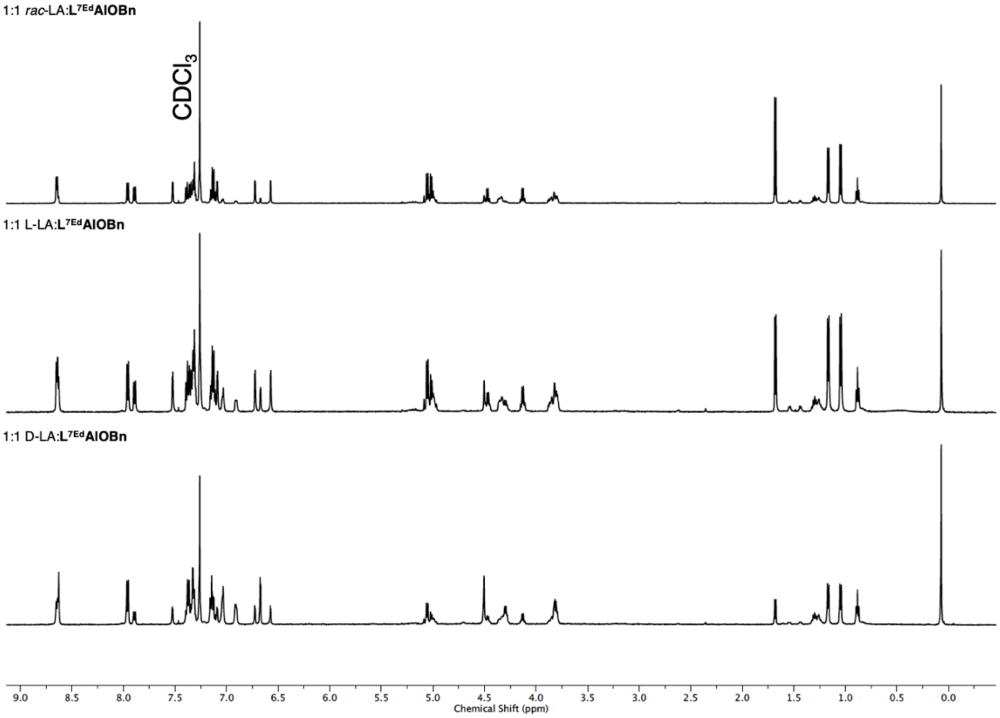

Figure 5.17. Overlay of ^{1}H NMR spectra of the products of the reactions of **L^{7Ed}AlOBn** with 1 equiv. *rac*-, L-, and D-LA (after 3 h).

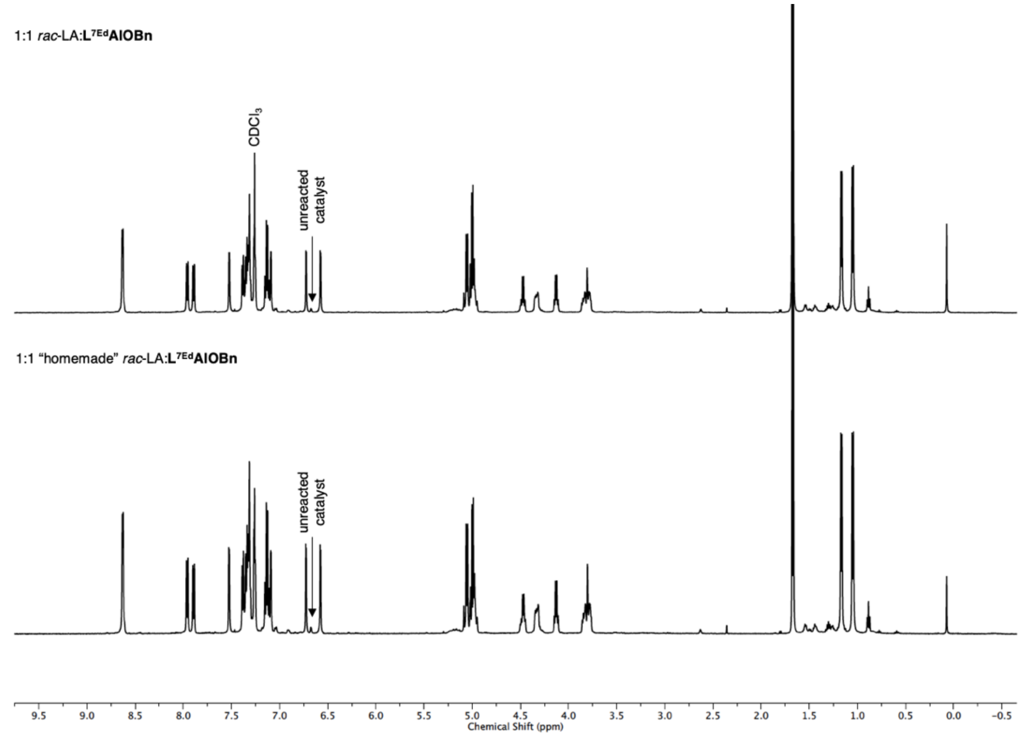

Figure 5.18. Overlay of ^{1}H NMR spectra of the products of the reactions of **L^{7Ed}AlOBn** with 1 equiv. *rac*-LA (purchased and recrystallized), and 1 equiv. *rac*-LA (50:50 mixture of D- and L-LA, both purchased and recrystallized separately).

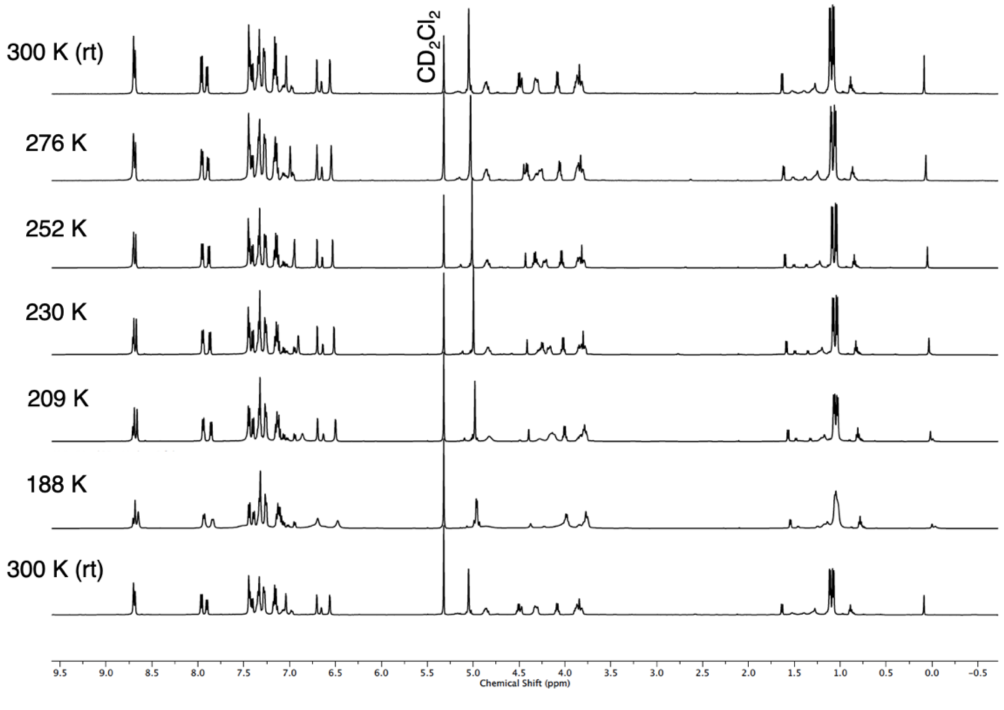

Figure 5.19. VT ^{1}H NMR overlay of 1:1 *rac*-LA:**L^{7Ed}AlOBn**.

5.5.5 *NOESY/EXSY NMR Spectroscopy Experiments*

NOESY/EXSY NMR spectroscopy experiments were conducted by first adding 0.003 g (0.006 mmol) **L^{7Cy}AlOBn** catalyst and 0.002 g (0.014 mmol) respective LA monomer to a scintillation vial (excess monomer was used in order to push the equilibrium toward ring-opened LA). Shortly thereafter, 700 µL of CD_2Cl_2 was added to the vial, and the mixture was allowed to sit for 10 min. The solution was then pipetted into a J-Young NMR tube before being analyzed it via ^{1}H, COSY, and NOESY/EXSY NMR spectroscopy (mixing time = 0.8 s).

To better identify the diastereomers of L^{7Cy}Al(o*rac*-LAOBn) in EXSY experiments, ^{1}H NMR spectra of L^{7Cy}Al(o*rac*-LAOBn) and L^{7Cy}Al(oD-LAOBn) were overlaid (Figure 5.20) and corresponding peak assignments were made.

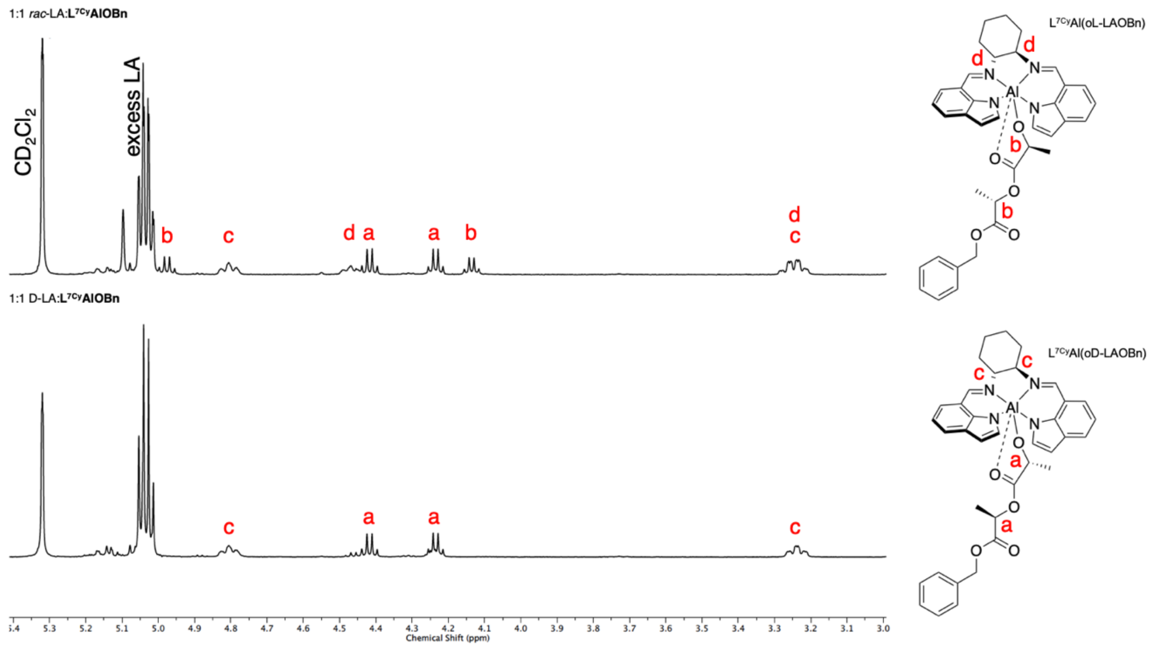

Figure 5.20. Overlay of ^{1}H NMR spectra of the products of reactions of **L^{7Cy}AlOBn** with *rac*-LA (top) and D-LA (bottom) and corresponding assignments (right).

5.5.6 *Tacticity and Differential Scanning Calorimetry Measurements*

Tacticity of each polymer was measured by dissolving dried polymer in $CDCl_3$ and submitting the sample for homonuclear decoupled ^{1}H NMR. Using the methine region of the spectrum (5.15–5.25 ppm), the various tetrad concentrations were integrated and Bernoullian statistics (assuming CEM, largely based on values obtained from DSC measurements, Table 5.1, section 5.3.4) were applied to determine the amount of racemic and *meso* character in the polymer.[35] For more accurate integration measurements, deconvolution of the spectra was achieved using MestReNova software.[115] An example of such analysis is depicted in Figure 5.21.

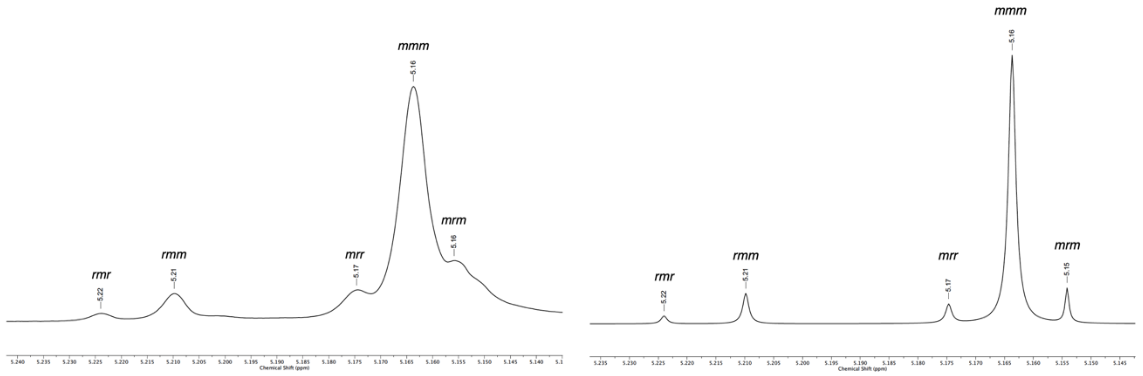

Figure 5.21. Example raw data (methine region, **L^{7Cy}AlOBn**, 55 °C, THF-d_8) from the homonuclear decoupled ^{1}H NMR spectra of PLA (left) and its deconvoluted form (top right) with $P_m = 0.82$.

Example DSC thermograms with a heating ramp of 10 °C/min are shown (Figure 5.22). Corresponding T_m values were determined from the second heating ramp. Samples were annealed overnight at 120 °C before DSC measurements were taken.

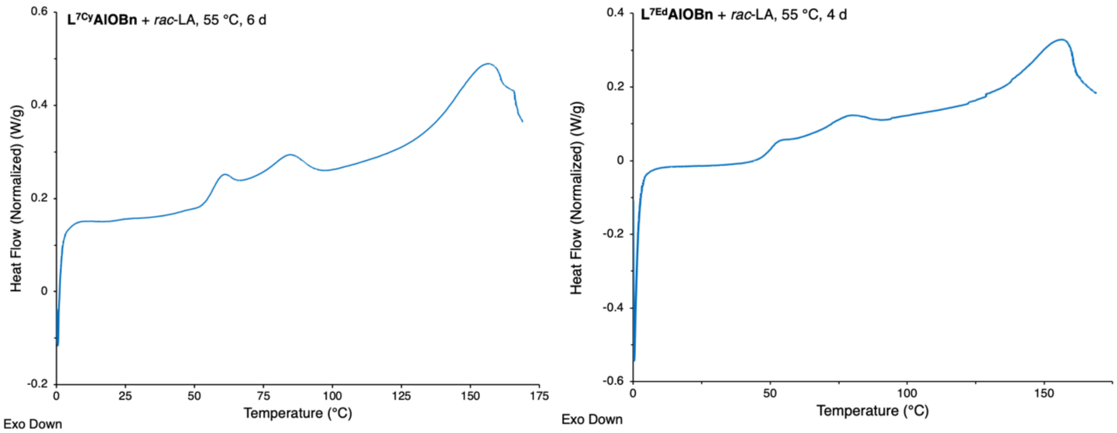

Figure 5.22. (Left) DSC thermogram of $\mathbf{L^{7Cy}AlOBn}$ + *rac*-LA, THF-d_8, 55 °C, 6 d (T_m = 158 °C). (Right) DSC thermogram of $\mathbf{L^{7Ed}AlOBn}$ + *rac*-LA, THF-d_8, 55 °C, 4 d (T_m = 158 °C).

5.6 Acknowledgements

This work was supported by the NSF Center for Sustainable Polymers, an NSF Center for Chemical Innovation, CHE-1901635. X-ray diffraction data were collected using diffractometers acquired through NSF-MRI Award, CHE-1229400. Hussnain Sajjad is thanked for running DSC experiments with regard to this project. Brendan J. Graziano is thanked for collecting and solving the $\mathbf{L^{7Ed}AlOBn}$ X-ray crystal structure.

6. Synthesis and Characterization of Unexplored Ring-Opening Polymerization Catalysts: Various Metal Ions and Ligand Structures

6.1 Overview and Introduction

In addition to work focused on a more complete understanding of ROP through the use of various catalysts (described in *Chapters 2–5*), several other ROP complexes were studied. The results of these works are comparatively incomplete, but worthy of presentation because of lessons learned from their study, along with their potential for further research. This chapter will examine the synthesis and preliminary characterization of various metal complexes featuring a variety of metal ions (Al, Zn, Ti) and ligand structures (salen-type, indolide-type, and those featuring highly flexible backbones). Synthetic challenges, preliminary polymerization results, and potential future directions for the use of these catalysts are included.

6.2 Exploration of Indolide-Type Frameworks

As alluded to in *Chapters 3* and *4*, the indolide-type framework remains relatively unexplored in terms of ROP catalysis.[47,160] Just as had been done with aforementioned salen-type frameworks, we aimed to answer the question of how altering the ligand framework of these complexes would affect the ROP mechanism. These alterations primarily focused on the addition of steric bulk to the 2-position of the indolide ring ($\mathbf{L^{7Me}H_2}$, Figure 6.1) as well as increasing the flexibility of these complexes by introducing additional carbons to the backbone (i.e., 4- and 5-member carbon backbones, $\mathbf{L^{7C4}H_2}$ and $\mathbf{L^{7C5}H_2}$, Figure 6.1). This section will explore such modular changes in synthetic detail and will describe challenges faced in efforts to isolate and use the subsequent Al complexes for ROP.

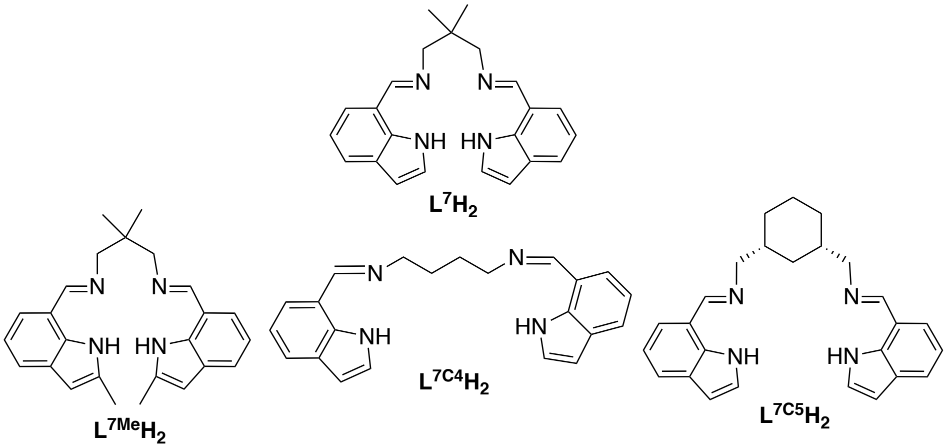

Figure 6.1. Various ligand frameworks featuring the parent $\mathbf{L^{7}H_2}$ ligand (top), added steric encumberment ($\mathbf{L^{7Me}H_2}$, bottom left) and extended backbone linkers ($\mathbf{L^{7C4}H_2}$ and $\mathbf{L^{7C5}H_2}$, bottom middle and bottom right, respectively).

6.2.1 *Added Steric Bulk*

We hypothesized that the introduction of a substituent at the 2-position would force the indole rings of the ligand framework to splay from each other, causing a change in the overall geometry of the molecule compared to that of the parent complex, $\mathbf{L^{7}AlOBn}$ (see

Chapters 3 and *4* and ligand **L^7H_2** in Figure 6.1, for reference). We sought to explore this potential geometrical change in relation to ROP efficacy.

6.2.1.1 *Synthesis and Characterization*

The synthesis of **$L^{7Me}H_2$** was accomplished through a condensation reaction between 2-methylindole-7-carboxaldehyde and a half equiv. of 2,2-dimethylpropane-1,3-diamine, via a procedure analogous to one used for ligands synthesized previously (Figure 6.2).[47,136] The resulting precipitate, a waxy solid (54%), required no further purification before being used for subsequent steps. Characterization by NMR spectroscopy revealed that the aldehyde resonance from the starting material had disappeared, and one belonging to an imine resonance took its place, indicative of ligand formation (Figure 6.7, section 6.6.2). Metalation with Et_2AlOEt at elevated temperatures for several days led to the formation of a complex (Figure 6.2). Coordination was postulated based on the change in reaction color over time (from colorless to bright yellow after 3 d), but NMR spectroscopy revealed that the donor amine protons on the ligand were still present, suggesting that while likely coordinated, complete Al metalation had not occurred. Metalation with excess $Al(Et)_3$ under similar conditions however, led to the disappearance of the amine protons and significant shifts in the framework peaks, suggesting complete metalation (Figure 6.2).

Nonetheless, the resulting product could not be isolated due to its high solubility in nonpolar solvents. Despite attempts at recrystallization and trituration via nonpolar solvents such as pentane, hexanes, and hexamethyldisiloxane (HMDSO), we were unable to isolate the complex as a pure compound. We also attempted a one-pot reaction starting with metalation of **$L^{7Me}H_2$** with 1 equiv. of $Al(Et)_3$, followed by stoichiometric addition of BnOH (Figure 6.2). However, no product was successfully isolated from this approach.

Our interests thus turned away from this approach to understanding ligand backbone alterations and their relation to ROP capability.

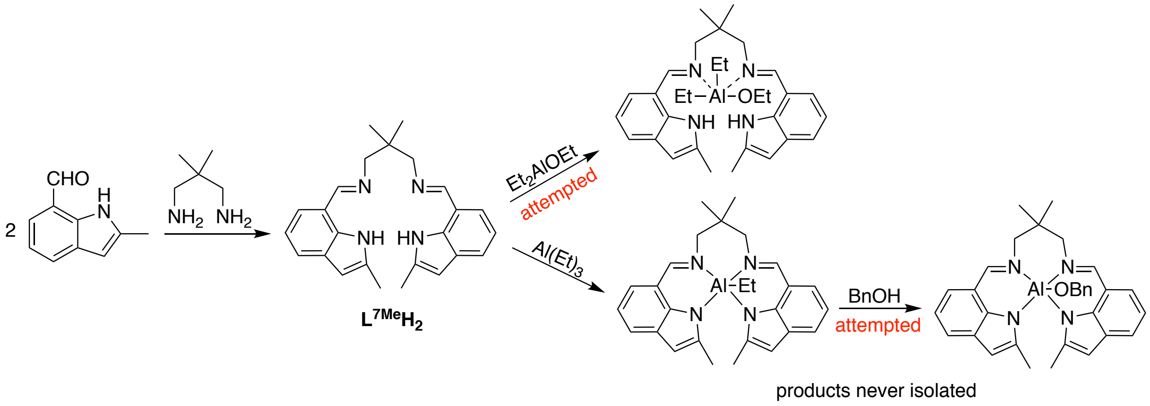

Figure 6.2. Synthesis of **$L^{7Me}H_2$**, and subsequent synthetic attempts to prepare L^{7Me} complexes.

6.2.2 *Increased Flexibility in the Ligand Backbone* (in collaboration with CSP REU student Morgan Young, computational studies performed by Mukunda Mandal and Christopher J. Cramer)

Previous collaboration with the Cramer group led to a predictive model (see details in *Chapters 1* and *3*) which used DFT calculations to estimate catalyst activation barriers for ROP based on catalyst geometry and ability to conform to the TSG. While designing potential catalysts *in silico*, our computational collaborators suggested an indolide-type ligand bearing a 4-carbon backbone linker (**$L^{7C4}H_2$**, Figure 6.3), the Al complex of which was calculated to have a $\Delta G^{\ddagger}_{TSG}$ of 6.2 kcal/mol (1.4 kcal/mol less than **L^7AlOBn**, a fast ROP catalyst predicted by the same FDE model and experimentally tested in *Chapter 3*). To this end, we sought to synthesize **$L^{7C4}H_2$** and subsequently metalate it to generate new AlOR species and test their efficacies for ROP.

6.2.2.1 *Synthesis and Characterization of Complexes*

The synthesis of **$L^{7C4}H_2$** was completed through a simple condensation reaction between 7-indolecarboxaldehyde and putrescine. The product precipitated from the reaction mixture after hours of stirring at reflux as a bright yellow solid (88%). The ligand was characterized using NMR spectroscopy and the disappearance and appearance of the aldehyde and imine resonances, respectively, indicated ligand formation (Figure 6.8, section 6.6.2).

We aimed to synthesize a mononuclear catalyst with this ligand, as dinuclear species with multiple initiators can complicate mechanistic studies.[44,54] Despite increased flexibility in the ligand, we believed the synthesis of mononuclear complexes possible, largely due to a previous report of mononuclear (salen)AlOR complex featuring a 4-carbon backbone.[192] Metalations of **$L^{7C4}H_2$** with $Al(Et)_3$, Et_2AlOEt, and $Al(O\textit{i}Pr)_3$ under various conditions (including slow addition of metal species and low reaction temperatures) were attempted. Preliminary characterization via NMR spectroscopy suggested that each synthetic approach resulted in dinuclear complexes (Figure 6.3). NMR spectroscopy data of **$L^{7C4}(AlEt_2)_2$** showed a single set of proton resonances (Figure 6.9, section 6.6.2), indicating either symmetry throughout the molecule, or highly fluxional behavior (neither was confirmed). Complexes **$L^{7C4}(AlEtOEt)_2$** and **$L^{7C4}(Al(O\textit{i}Pr)_2)_2$** however, revealed unique proton resonances for each proton on the molecule (Figures 6.10 and 6.11, section 6.6.2). With the former, it was hypothesized that the synthesis of the species led to the formation of a 50:50 mixture of distinguishable diastereomers (each proton resonance belonged to that of a single diastereomer). Unique proton resonances for the latter however, is hypothesized to be a result of the complex lacking symmetry, thus resulting in a doubling of proton resonances in the NMR spectrum compared to that of a symmetric molecule. While these spectral assignments are corroborated with NMR data, it is noted that full characterization of the complexes via methods including elemental analysis and HR-ESI-MS is still required.

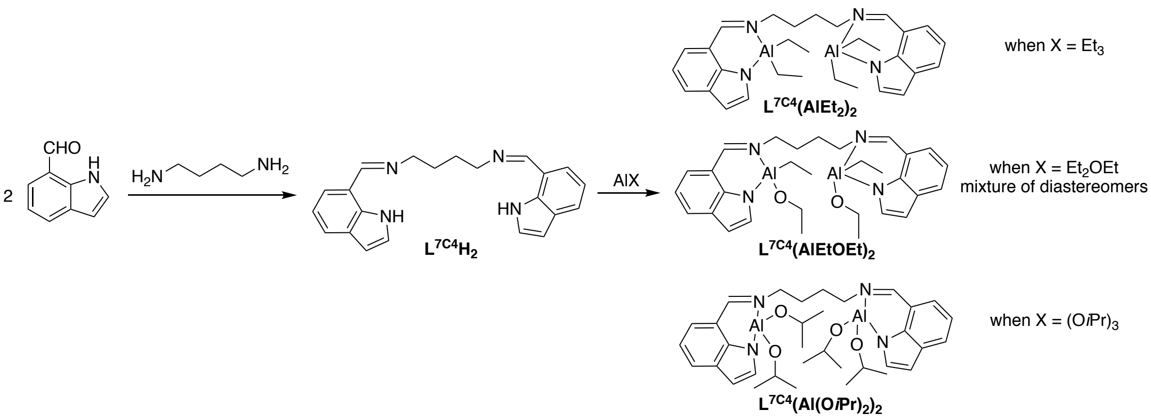

Figure 6.3. Generic scheme of synthesis and subsequent metalation reactions of **$L^{7C4}H_2$** via various Al sources.

6.2.2.2 *Polymerization Behavior*

Despite dinuclearity, preliminary ROP studies between **$L^{7C4}(AlEtOEt)_2$** and **$L^{7C4}(Al(OiPr)_2)_2$** and *rac*-LA were explored. As indicated in Table 6.1, a few conditions were attempted. Reactions with both catalysts were sluggish at slightly elevated temperatures (60 °C, in $CDCl_3$), taking days to reach high conversions, but **$L^{7C4}(AlEtOEt)_2$** yielded high conversions in the melt after 30 min, while providing a high molecular weight polymer with good control ($Đ$ = 1.24). Even so, the complex showed no preference for stereoselectivity within the polymerization, as atactic polymer was produced.

Table 6.1. Data for polymerizations of *rac*-LA by the indicated complexes.

Catalyst[a]	**Temp. (°C)**	**LA:cat**	**Time**	**Conv.**[b]	**M_n (kDa)**[c]	**$Đ$**[c]	**P_m**[d]	**T_m (°C)**
AlEtOEt	60 ($CDCl_3$)	300	5 d	81%	*X*[e]	*X*[e]	*X*[e]	*X*[e]
AlEtOEt	135	300	30 min	61%	54	1.24	0.53	*X*[e]
Al(O*i*Pr)$_2$	60 ($CDCl_3$)	300	4 d	96%	*X*[e]	*X*[e]	*X*[e]	*X*[e]

[a] AlEtOEt = $L^{7C4}(AlEtOEt)_2$ and Al(O*i*Pr)$_2$ = $L^{7C4}(Al(OiPr)_2)_2$. [b] Determined by ^{1}H NMR spectroscopy. [c] Determined by SEC using light scattering detection with THF eluent. Theoretical values are 44 kDa for 300 equiv. of LA. [d] Determined by homonuclear decoupled ^{1}H NMR spectroscopy. [e] Parameter not measured.

6.2.3 *Balancing Flexibility and Proximity of Ligand Donor Atoms* (in collaboration with CSP REU student Morgan Young)

Because **$L^{7C4}H_2$** metalations only resulted in dinuclear species, we sought a new ligand design, one with increased flexibility in the backbone compared to that of the parent **L^7H_2**, but one that forced the imine N atoms closer to each other, hopefully resulting in a mononuclear complex. As such, the synthesis of **$L^{7C5}H_2$**, bearing a 5-carbon backbone as part of a more rigid cyclohexyl ring was attempted (Figure 6.4).

6.2.3.1 *Synthesis and Characterization*

$L^{7C5}H_2$ was synthesized via a condensation reaction between 7-indolecarboxaldehyde and *cis*-1,3-bis(aminomethyl)cyclohexane (Figure 6.4) via bomb flask (due to moisture sensitivity of the diamine). An off-white precipitate was observed after heating for 3 d and was collected via vacuum filtration (23%). ^{1}H NMR analysis indicated its full formation through disappearance of the starting material's aldehyde resonance and formation of the imine resonance, along with significant shifts in the backbone resonances (Figure 6.12, section 6.6.2). While NMR data suggests the successful synthesis of **$L^{7C5}H_2$**, we note that additional and more wholistic characterization data is needed to confirm this notion.

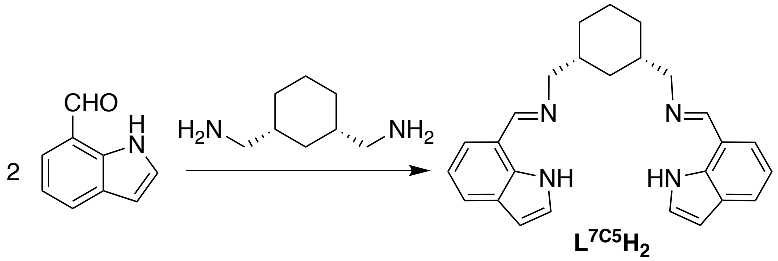

Figure 6.4. Synthesis of **$L^{7C5}H_2$**.

Metalation with **$L^{7C5}H_2$** proved to be difficult, as multiple attempts with various Al sources (specifically Al(Et)$_3$, Et$_2$AlOEt, and Al(O*i*Pr)$_3$) and reaction conditions led to incomplete metalation (evidence of NH peaks still present, despite adding excess metal, even at elevated temperatures for extended periods of time). Therefore, no discrete complex synthesized with this ligand was isolated.

6.3 Pursuit of an Indolide-Zn Complex

Along with ligand variations of **L^7H_2**, we began to explore complexes of different metal ions and focused first on the Zn complex **L^7Zn** (Figure 6.5). We hypothesized that the addition of 1 equiv. of alcohol to this could complex could result in a ZnOR species (Figure 6.5), that might be highly active.

6.3.1 *Synthesis and Characterization of Complex*

Synthesis of **L^7Zn** was accomplished via metalation with **L^7H_2** and excess $ZnEt_2$ (Figure 6.5). Immediately upon metal addition, a yellow precipitate formed (79%). NMR spectroscopy revealed full metalation (denoted by the disappearance of NH peaks, see Figure 6.13, section 6.6.2). The complex is quite stable, as indicated by no change in its properties after days in air, or the addition of substoichiometric amounts of H_2O or a stoichiometric amount of BnOH, even after an extended period of time (3 d). Even at higher temperatures in a higher-boiling solvent (130 °C, toluene), no reaction with the alcohol was observed (Figure 6.5).

Nonetheless, a preliminary polymerization experiment was performed, with the assumption that the **L^7Zn** molecule could serve as a Lewis acid in an activated monomer mechanism, by which the carbonyl of the monomer coordinates to the Zn center before being nucleophilically attacked by the exogenous alcohol (in this case, 1 equiv. BnOH). Reaction with 300 equiv. of *rac*-LA at 135 °C for 4 h led to 24% conversion to PLA, a sluggish level of reactivity.

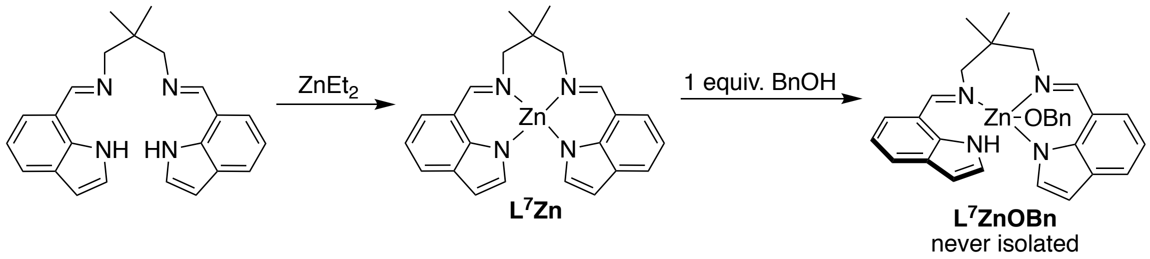

Figure 6.5. Synthesis of **L^{7}Zn** and proposed **L^{7}ZnOBn** species.

6.4 Exploration of (salen)Ti-alkoxide Complexes

Among Al and Zn catalysts, titanium-alkoxide (TiOR) complexes have also been studied in terms of ROP capability.[56,193–195] However, understanding of catalyst structural effects on ROP reactivity for such systems is rudimentary.[195] Additionally, inconsistent trends in comparisons of Ti and Al catalysts as a function of electronics and ROP rate[193] inspired the idea of studying electronic effect as a function of metal ion alone (i.e., keeping consistent ligand frameworks). Thus, we decided to implement electronic changes to Ti complexes using the electronically varied salen ligands previously described in *Chapter 1* (used for Al complex synthesis and subsequent CL polymerization). Once synthesized, we aimed to compare Ti and Al-based ROP of CL via the same ligand frameworks.

6.4.1 *Synthesis and Characterization of Complexes*

The synthesis of the proligands was achieved as described previously.[67,68] Metalation with Ti(O*i*Pr)$_4$ resulted in complexes **(salen)L^{NO_2}Ti** and **(salen)L^{OMe}Ti** in 26% and 43% yields, respectively (Figure 6.6). Characterized by ^{1}H NMR spectroscopy, the complexes were revealed to be mononuclear, and full metalation was denoted by the complete disappearance of the phenolic OH peaks, as well as significant shifts in the ligand framework proton resonances (Figures 6.14–6.15). Again, while the NMR spectroscopy data substantiates the spectral assignments made, additional characterization of these complexes is still needed.

Unfortunately, the complexes were extremely sluggish catalysts for CL polymerization. For example, **(salen)L^{NO_2}Ti**, at room temperature, showed no monomer conversion after 3 d. Upon heating to 100 °C, the catalyst started to decompose (observed via NMR spectroscopy), proving its inability to be useful as a melt catalyst for monomers with elevated melting points.

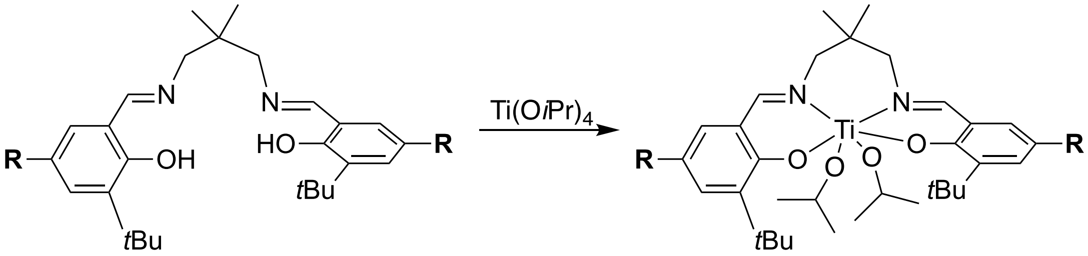

Figure 6.6. Synthesis of electronically varied (salen)Ti complexes, where **R** = NO_2 and OMe.

6.5 Concluding Remarks

Several potential ROP catalysts bearing structurally varied ligand frameworks and metal ions were explored in this work. Isolation of several proposed complexes proved difficult, while complexes bearing extremely flexible backbones formed undesired dinuclear complexes upon metalation. While examples of (indolide)Zn and (salen)Ti$(OR)_2$ catalysts were also explored as potential ROP catalysts, their sluggish reactivities rendered them unsuitable for future study.

6.6 Experimental

6.6.1 *Synthetic Materials, Methods and General Considerations*

All reactions containing either air- and/or water-sensitive compounds were performed within the inert atmosphere of a nitrogen-filled glovebox or using Schlenk line techniques. All reagents were purchased from commercial sources and were used as received, unless otherwise noted. CL was purified by drying over CaH_2 and subsequent vacuum distillation. LA was purified by recrystallization (3x) from toluene and subsequent vacuum drying. All protonated solvents were degassed and a passed through a solvent purification system (Glass Contour, Laguna, CA) prior to use. Deuterated solvents were dried over CaH_2, degassed through freeze-pump-thaw techniques, and distilled before storing them under N_2. Nuclear magnetic resonance (NMR) spectroscopies were performed with a Bruker Avance III (500 MHz) spectrometer equipped with a BBFO SmartProbe. Chemical shifts for ^1H and ^{13}C NMR spectra were references to residual protium in the deuterated solvent (for ^1H NMR) and the deuterated solvent itself (for ^{13}C NMR).

6.6.2 *Synthetic Procedures*

The following complexes were characterized through NMR spectroscopy, but due to the relatively unexplored nature of these complexes, most were not characterized beyond that. At the very least, detailed ^1H NMR information for each molecule is included (while all designations were corroborated with COSY NMR spectroscopy).

Synthesis of $L^{7Me}H_2$. To an oven-dried round bottom flask equipped with a reflux condenser and charged with a stir bar, 2-methylindole-7-carboxaldehyde (0.100 g, 0.628 mmol) was added and dissolved in absolute ethanol (0.63 M) while stirring. To this mixture, 2,2-dimethylpropane-1,3-diamine (0.032 g, 0.5 equiv.) was added before heating to reflux (80 °C) for 3 d. After 3 d, the reaction mixture was transferred to a new round bottom flask before being placed in a −20 °C freezer overnight. The resulting precipitate, a waxy solid, was filtered via vacuum filtration and the solid was washed with cold ethanol (3 x 10 mL). The remaining solid was dried via Schlenk line for 6-8 h before being pumped into an N_2 glovebox. ^1H NMR analysis indicated this material was pure and required no further purification before subsequent synthetic steps. Yield: 0.065 g, 54%. ^1H NMR (500 MHz, $CDCl_3$): δ 10.51 (s, 2H, N*H*), 8.48 (s, 2H, C*H*=N), 7.62 (d, J = 7.81 Hz, 2H, Ar*H*), 7.20 (d, J = 7.81 Hz, 2H, Ar*H*), 7.12 (t, J = 7.81 Hz, 2H, Ar*H*), 6.26 (app s, 2H, CH_3C=C*H*), 3.64 (s, 4H, NCH_2,C(CH_3)$_2$CH_2N), 2.45 (s, 6H, CH_3C=CH), 1.16 (s, 6H, NCH$_2$,C(CH_3)$_2$CH$_2$N).

Synthesis of $L^{7C4}H_2$. To an oven-dried round bottom flask equipped with a reflux condenser and charged with a stir bar, 7-indolecarboxaldehyde (1.00 g, 6.28 mmol) was added and dissolved in absolute ethanol (0.63 M) while stirring. To this mixture, putrescine (0.364 g, 0.5 equiv.) was added before heating to reflux (80 °C) for 4 d. After 4 d, a yellow precipitate formed, was collected via vacuum filtration and washed with cold EtOH (3 x 10 mL). The yellow solid was dried via Schlenk line for 6–8 h before being pumped into an N_2 glovebox. ^{1}H NMR analysis indicated this material was pure and required no further purification before subsequent synthetic steps. Yield: 1.04 g, 88%. ^{1}H NMR (500 MHz, $CDCl_3$): δ 10.78 (s, 2H, N*H*), 8.53 (s, 2H, C*H*=N), 7.77 (d, *J* = 8.33 Hz, 2H, Ar*H*), 7.31 (m, 4H, ArH, NC*H*=CH), 7.20 (t, *J* = 8.33 Hz, 2H, Ar*H*), 6.62 (app t, *J* = 2.49 Hz, 2H, NCH=C*H*), 3.78 (m, 4H, NCH_2CH$_2$CH$_2$CH_2N), 1.93 (m, 4H, NCH$_2$CH_2CH_2CH$_2$N); ^{13}C NMR (125 MHz, $CDCl_3$) δ 162.34, 134.17, 128.40, 125.21, 124.55, 123.54, 119.50, 119.27, 102.26, 61.68, 29.34.

Synthesis of $L^{7C4}(AlEt_2)_2$. To an oven-dried scintillation vial equipped with a stir bar, $L^{C4}H_2$ (0.050 g, 0.146 mmol) was added in an N_2 glovebox. A minimal amount of toluene (~0.5 mL) was added and stirred until the ligand had dissolved. Drop-wise, excess $Al(Et)_3$ (~0.4 mL, 1 M in hexanes) was added to the stirring mixture and stirred at room temperature for 3 d. After 3 d, the mixture was put in a −40 °C freezer overnight and a yellow precipitate formed. The excess solvent was decanted and the remaining yellow solid was triturated with excess pentane to form a yellow powder. The powder was isolated via vacuum filtration and washed with pentane (3 x 5 mL), without need for further purification afterward. The solid was stored under N_2 until subsequent use. Yield: 0.075 g, 57%. ^{1}H NMR (500 MHz, $CDCl_3$): δ 8.42 (s, 2H, C*H*=N), 7.95 (d, *J* = 7.07 Hz, 2H, Ar*H*), 7.45 (d, *J* = 2.22 Hz, 2H, NC*H*=CH), 7.30 (d, *J* = 7.07 Hz, 2H, Ar*H*), 7.09 (t, *J* = 7.07 Hz, 2H, Ar*H*), 6.70 (d, *J* = 2.22 Hz, 2H, NCH=C*H*), 3.77 (m, 4H, $NCH_2CH_2CH_2CH_2N$), 1.95 (m, 4H, $NCH_2CH_2CH_2CH_2N$), 0.95 (t, *J* = 8.12 Hz, 12H, $AlCH_2CH_3$), 0.01 (m, 8H, $AlCH_2CH_3$).

Synthesis of $L^{7C4}Al(Et_2OEt)_2$. To an oven-dried tubular bomb flask equipped with a stir bar, **$L^{C4}H_2$** (0.098 g, 0.292 mmol) was added in an N_2 glovebox. A minimal amount of toluene (~2 mL) was added and stirred until the ligand had dissolved. Drop-wise, excess Et_2AlOEt (~0.3 mL, 25 wt % in toluene) was added to the stirring mixture. The flask was capped and pumped out of the glovebox and stirred at 110 °C for 3 d. After 3 d, the bomb flask was pumped back into the box and the solvent was removed *in vacuo*. The remaining oil was triturated with pentane (10 mL) and a yellow powder formed. The powder was isolated via vacuum filtration. The solid was stored under N_2 until subsequent use. Yield: 0.034 g, 21%. ^{1}H NMR (500 MHz, $CDCl_3$): δ 8.67 (s, 2H, C*H*=N), 8.34 (s, 2H, C*H*=N), 7.94 (d, *J* = 7.57 Hz, 2H, Ar*H*), 7.79 (d, *J* = 7.57 Hz, 2H, Ar*H*), 7.53 (d, *J* = 2.37 Hz, 2H, NC*H*=CH), 7.29 (d, *J* = 7.51 Hz, 2H, Ar*H*), 7.18 (d, *J* = 7.51 Hz, 2H, Ar*H*), 7.07 (2t, *J* = 7.57, 7.51 Hz, 4H, Ar*H*), 6.68 (d, *J* = 2.72 Hz, 2H, NC*H*=CH), 6.28 (d, *J* = 2.72 Hz, 2H, NCH=C*H*), 6.07 (d, *J* = 2.37 Hz, 2H, NCH=C*H*), 4.89 (m, 2H, $NCH_2CH_2CH_2CH_2N$), 3.68 (m, 4H, $NCH_2CH_2CH_2CH_2N$), 3.38 (m, 4H, $NCH_2CH_2CH_2CH_2N$, OCH_2CH_3), 2.78 (m, 6H, OCH_2CH_3), 2.19 (m, 4H, $NCH_2CH_2CH_2CH_2N$), 1.74 (m, 4H, $NCH_2CH_2CH_2CH_2N$), 1.05 (m, 12H, OCH_2CH_3, $AlCH_2CH_3$), 0.95 (t, *J* = 8.12 Hz, $AlCH_2CH_3$), 0.84 (t, *J* = 7.20 Hz, OCH_2CH_3), −0.13– −0.26 (m, 8H, $AlCH_2CH_3$); ^{13}C NMR (125 MHz, $CDCl_3$) δ 170.46, 170.37, 141.37, 141.36, 138.58, 137.97, 131.79, 131.76, 127.18, 127.11, 126.38, 125.88, 117.27, 117.13, 116.92, 116.09, 101.84, 101.45, 62.19, 62.11, 58.25, 57.95, 31.66, 29.32, 18.16, 18.09, 9.54, 9.39. Despite using a broad sweep width (up to −200 ppm), no signal for the methylene of the ethyl substituent bound to the Al center could be identified.

Synthesis of $\mathbf{L^{7C4}(Al(O\mathit{i}Pr)_2)_2}$. To an oven-dried tubular bomb flask equipped with a stir bar, $\mathrm{L^{C4}H_2}$ (0.175 g, 0.511 mmol) was added in an $\mathrm{N_2}$ glovebox. A minimal amount of toluene (~3 mL) was added and stirred until the ligand had dissolved. Then, slowly, $\mathrm{Al(O\mathit{i}Pr)_3}$ was added (excess, 0.261 g) and the mixture was stirred. The flask was capped and pumped out of the glovebox and stirred at 110 °C for 3 d. After 3 d, the bomb flask was pumped back into the box and the solvent was removed *in vacuo*. The remaining oil was triturated with pentane (10 mL) and a yellow powder formed. The powder was isolated via vacuum filtration and was stored under $\mathrm{N_2}$ until subsequent use. Yield: 0.037 g, 11%. ^{1}H NMR (500 MHz, $\mathrm{CDCl_3}$): δ 8.66 (s, 2H, C*H*=N), 8.25 (s, 2H, C*H*=N), 7.96 (d, *J* = 2.71 Hz, 2H, NC*H*=CH), 7.92 (d, *J* = 7.61 Hz, 2H, Ar*H*), 7.74 (d, *J* = 7.61 Hz, 2H, Ar*H*), 7.18 (m, 2H, Ar*H*), 7.13 (m, 2H, Ar*H*), 7.02 (2t, *J* = 7.61, 7.42 Hz, 4H, Ar*H*), 6.66 (d, *J* = 2.13 Hz, 2H, NC*H*=CH), 6.19 (d, *J* = 2.71 Hz, 2H, NCH=C*H*), 5.85 (d, *J* = 2.13 Hz, 2H, NC*H*=CH), 5.30 (m, 2H, $\mathrm{NC}\mathit{H}_2\mathrm{CH_2CH_2C}\mathit{H}_2\mathrm{N}$), 4.19 (2sep, *J* = 6.02, 5.80 Hz, 4H, $\mathrm{OC}\mathit{H}\mathrm{(CH_3)_2}$), 3.88 (sep, *J* = 6.00 Hz, 2H, $\mathrm{OC}\mathit{H}\mathrm{(CH_3)_2}$), 3.68 (m, 4H, $\mathrm{NC}\mathit{H}_2\mathrm{CH_2CH_2C}\mathit{H}_2\mathrm{N}$), 3.38 (m, 2H, $\mathrm{NC}\mathit{H}_2\mathrm{CH_2CH_2C}\mathit{H}_2\mathrm{N}$), 3.08 (sep, *J* = 6.29 Hz, 2H, $\mathrm{OC}\mathit{H}\mathrm{(CH_3)_2}$), 2.17 (m, 4H, $\mathrm{NCH_2C}\mathit{H}_2\mathrm{C}\mathit{H}_2\mathrm{CH_2N}$), 1.79 (m, 4H, $\mathrm{NCH_2C}\mathit{H}_2\mathrm{C}\mathit{H}_2\mathrm{CH_2N}$), 1.27 (d, *J* = 6.02 Hz, 6H, $\mathrm{OCH(C}\mathit{H}_3\mathrm{)_2}$), 1.13 (m, 9H, $\mathrm{OCH(C}\mathit{H}_3\mathrm{)_2}$), 1.11 (d, *J* = 5.80 Hz, 6H, $\mathrm{OCH(C}\mathit{H}_3\mathrm{)_2}$), 1.04 (d, *J* = 6.00 Hz, 6H, $\mathrm{OCH(C}\mathit{H}_3\mathrm{)_2}$), 0.81 (d, *J* = 6.29 Hz, 6H, $\mathrm{OCH(C}\mathit{H}_3\mathrm{)_2}$), 0.10 (d, *J* = 6.20 Hz, 6H, $\mathrm{OCH(C}\mathit{H}_3\mathrm{)_2}$).

Synthesis of $\mathbf{L^{7C5}H_2}$. To an oven-dried tubular bomb flask charged with a stir bar, 7-indolecarboxaldehyde (0.425 g, 2.93 mmol) was added and dissolved in EtOH (0.63 M) while stirring in an $\mathrm{N_2}$ glovebox. To this mixture, *cis*-1,3-bis(aminomethyl)cyclohexane

(1.76 g, 0.5 equiv.) was added before the flask was pumped out of the box and heated at 80 °C for 3 d. After 3 d, the flask was pumped back into the glovebox and was placed in a –40 °C freezer overnight to induce precipitation. An off-white precipitate was collected via vacuum filtration and was washed with pentane (3 x 10 mL). ^{1}H NMR analysis indicated this material was pure and required no further purification before subsequent synthetic steps. Yield: 0.267 g, 23%. ^{1}H NMR (500 MHz, $CDCl_3$): δ 10.69 (s, 2H, N*H*), 8.45 (s, 2H, C*H*=N), 7.72 (d, *J* = 8.40 Hz, 2H, Ar*H*), 7.28 (d, *J* = 8.40 Hz, 2H, Ar*H*), 7.16 (m, 4H, Ar*H*, NC*H*=CH), 6.56 (m, 2H, NCH=C*H*), 3.57 (m, 4H, NCH_2CH), 2.00 (m, 1H, Cy*H*), 1.87 (m, 5H, Cy*H*), 1.35 (m, 1H, Cy*H*), 1.03 (m, 2H, Cy*H*), 0.89 (m, 1H, Cy*H*).

Synthesis of L^7Zn. To an oven-dried scintillation vial equipped with a stir bar, L^7H_2 (referenced in *Chapters 3* and *4*, 0.100 g, 0.281 mmol) was added in an N_2 glovebox. A minimal amount of toluene (~1 mL) was added and stirred until the ligand had dissolved. Drop-wise, excess $ZnEt_2$ (~0.2 mL, 1 M in hexanes) was added to the stirring mixture and stirred at room temperature. A yellow precipitate immediately formed, and the excess solvent was decanted. The bright yellow powder was collected via vacuum filtration and washed with pentane (3x 5 mL), without need for further purification. The solid was stored under N_2 until subsequent use. Yield: 0.221 g, 79%. ^{1}H NMR (500 MHz, CD_2Cl_2) δ 8.61 (s, 2H, C*H*=N), 7.92 (d, *J* = 7.62 Hz, 2H, Ar*H*), 7.39 (d, *J* = 7.62 Hz, 2H, Ar*H*), 7.30 (d, *J* = 2.63 Hz, 2H, NC*H*=CH), 7.12 (t, *J* = 7.62 Hz, 2H, Ar*H*), 6.63 (d, *J* = 2.63 Hz, 2H, NCH=C*H*), 3.93 (d, *J* = 11.68 Hz, 2H, $NCH_2,C(CH_3)_2$), 3.28 (d, *J* = 11.68 Hz, 2H, $NCH_2,C(CH_3)_2$), 1.10 (s, 6H, $NCH_2,C(CH_3)_2$).

Synthesis of (salen)L^{NO_2}Ti. To an oven-dried screw cap bomb flask equipped with a stir bar, (salen)$L^{NO_2}H_2$ (referenced in *Chapter 1*, 0.100 g, 0.195 mmol) and titanium isopropoxide (excess) were dissolved in toluene (~1 mL) while in an N_2 glovebox. The sealed flask was stirred at room temperature for 24 h and the solvent was then removed *in vacuo*. The resulting solid was a fine, yellow powder and was collected via vacuum filtration via pentane wash (3 x 5 mL) with no need for further purification. The solid was stored under $\mathrm{N_2}$ until subsequent use. Yield: 0.033 g, 26%. ^{1}H NMR (500 MHz, $\mathrm{CDCl_3}$) δ 8.31 (d, J = 2.94 Hz, 1H, Ar*H*), 8.21 (d, J = 2.83 Hz, 1H, Ar*H*), 8.19 (d, J = 2.83 Hz, 1H, Ar*H*), 8.12 (d, J = 2.94 Hz, 1H, Ar*H*), 8.07 (s, 1H, C*H*=N), 8.03 (s, 1H, C*H*=N), 4.97 (sep, J = 6.32 Hz, 1H, $(\mathrm{CH_3})_2\mathrm{C}H\mathrm{O}$), 4.73 (d, J = 10.22 Hz, 1H, $\mathrm{N C}H_2\mathrm{,C(CH_3)_2}$), 4.43 (sep, J = 6.09 Hz, 1H, $(\mathrm{CH_3})_2\mathrm{C}H\mathrm{O}$), 4.02 (d, J = 11.99 Hz, 1H, $\mathrm{N C}H_2\mathrm{,C(CH_3)_2}$), 3.26 (2d, J = 10.22, 11.99 Hz, 2H, $\mathrm{C}H_2\mathrm{,C(CH_3)_2}$), 1.45 (s, 9H, $(\mathrm{C}H_3)_3\mathrm{C}$), 1.26 (d, J = 6.32 Hz, 1H, $(\mathrm{C}H_3)_2\mathrm{CHO}$), 1.20 (d, J = 6.32 Hz, 3H, $(\mathrm{C}H_3)_2\mathrm{CHO}$), 1.14 (s, 3H, $\mathrm{NCH_2,C(C}H_3)_2$), 0.98 (s, 9H, $(\mathrm{C}H_3)_3\mathrm{C}$), 0.85 (2d, J = 6.09, 6.09 Hz, 6H, $(\mathrm{C}H_3)_2\mathrm{CHO}$), 0.69 (s, 3H, $\mathrm{NCH_2,C(C}H_3)_2$).

Synthesis of (salen)L$^{\mathrm{OMe}}$Ti. To an oven-dried screw cap bomb flask equipped with a stir bar, (salen)L$^{\mathrm{OMe}}$H$_2$ (referenced in *Chapter 1*, 0.100 g, 0.207 mmol) and titanium isopropoxide (excess) were dissolved in toluene (~2 mL) while in an $\mathrm{N_2}$ glovebox. The sealed flask was stirred at room temperature for 24 h and the solvent was then removed *in vacuo*. The resulting solid was a fine, yellow powder and was collected via vacuum filtration via pentane wash (3 x 5 mL) with no need for further purification. The solid was stored under $\mathrm{N_2}$ until subsequent use. Yield: 0.055 g, 43%. ^{1}H NMR (500 MHz, $\mathrm{CD_2Cl_2}$) δ 7.98 (s, 1H, C*H*=N), 7.92 (s, 1H, C*H*=N), 7.03 (d, J = 2.41 Hz, 1H, Ar*H*), 6.90 (d, J = 2.41 Hz, 1H, Ar*H*), 6.66 (d, J = 1.83 Hz, 1H, Ar*H*), 6.59 (d, J = 1.83 Hz, 1H, Ar*H*), 4.87 (sep, J = 5.92 Hz, 1H, $(\mathrm{CH_3})_2\mathrm{C}H\mathrm{O}$), 4.77 (d, J = 10.02 Hz, 1H, $\mathrm{N C}H_2\mathrm{,C(CH_3)_2}$), 4.39 (sep, J = 5.92 Hz, 1H, $(\mathrm{CH_3})_2\mathrm{C}H\mathrm{O}$), 3.90 (d, J = 12.00 Hz, 1H, $\mathrm{N C}H_2\mathrm{,C(CH_3)_2}$), 3.75 (s, 3H, $\mathrm{OC}H_3$), 3.71 (s, 3H, $\mathrm{OC}H_3$), 3.19–3.11 (m, 2H, $\mathrm{N C}H_2\mathrm{,C(CH_3)_2}$), 1.42 (bs, 9H, $(\mathrm{C}H_3)_3\mathrm{C}$), 1.19 (d, *J* = 5.92 Hz, 3H, $(CH_3)_2CHO$), 1.14 (d, *J* = 6.32 Hz, 3H, $(CH_3)_2CHO$), 1.08 (bs, 3H, NCH_2,$C(CH_3)_2$), 1.01 (bs, 9H, $(CH_3)_3C$), 0.85 (d, *J* = 5.92 Hz, 3H, $(CH_3)_2CHO$), 0.78 (d, *J* = 5.92 Hz, 3H, $(CH_3)_2CHO$), 0.66 (bs, 3H, NCH_2,$C(CH_3)_2$).

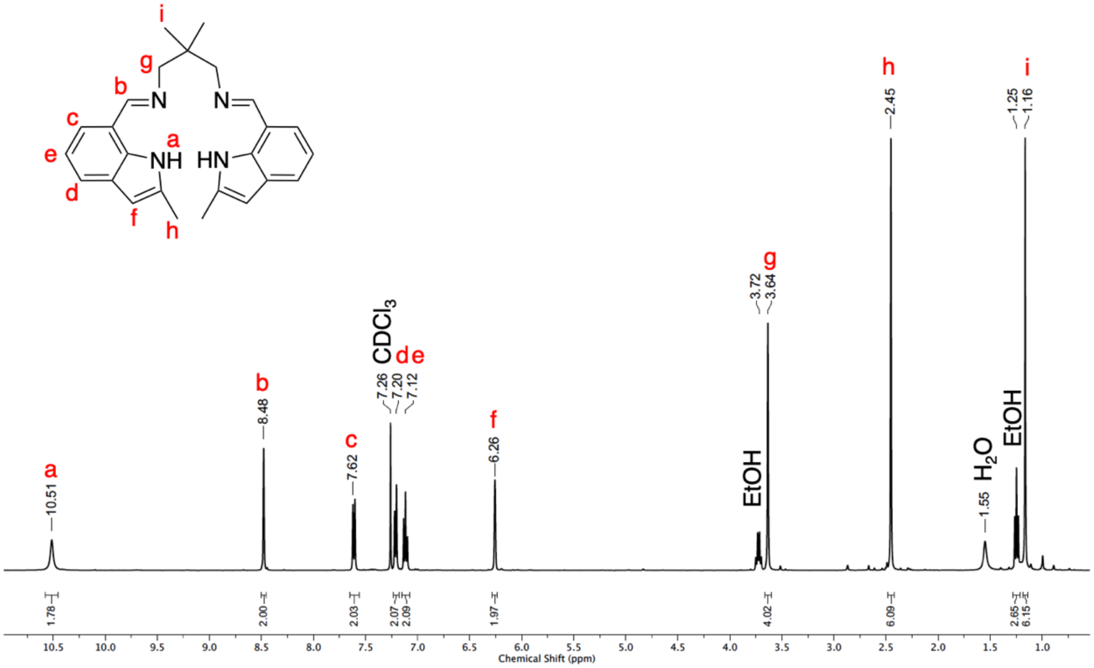

Figure 6.7. ^{1}H NMR spectrum of $\mathbf{L^{7Me}H_2}$.

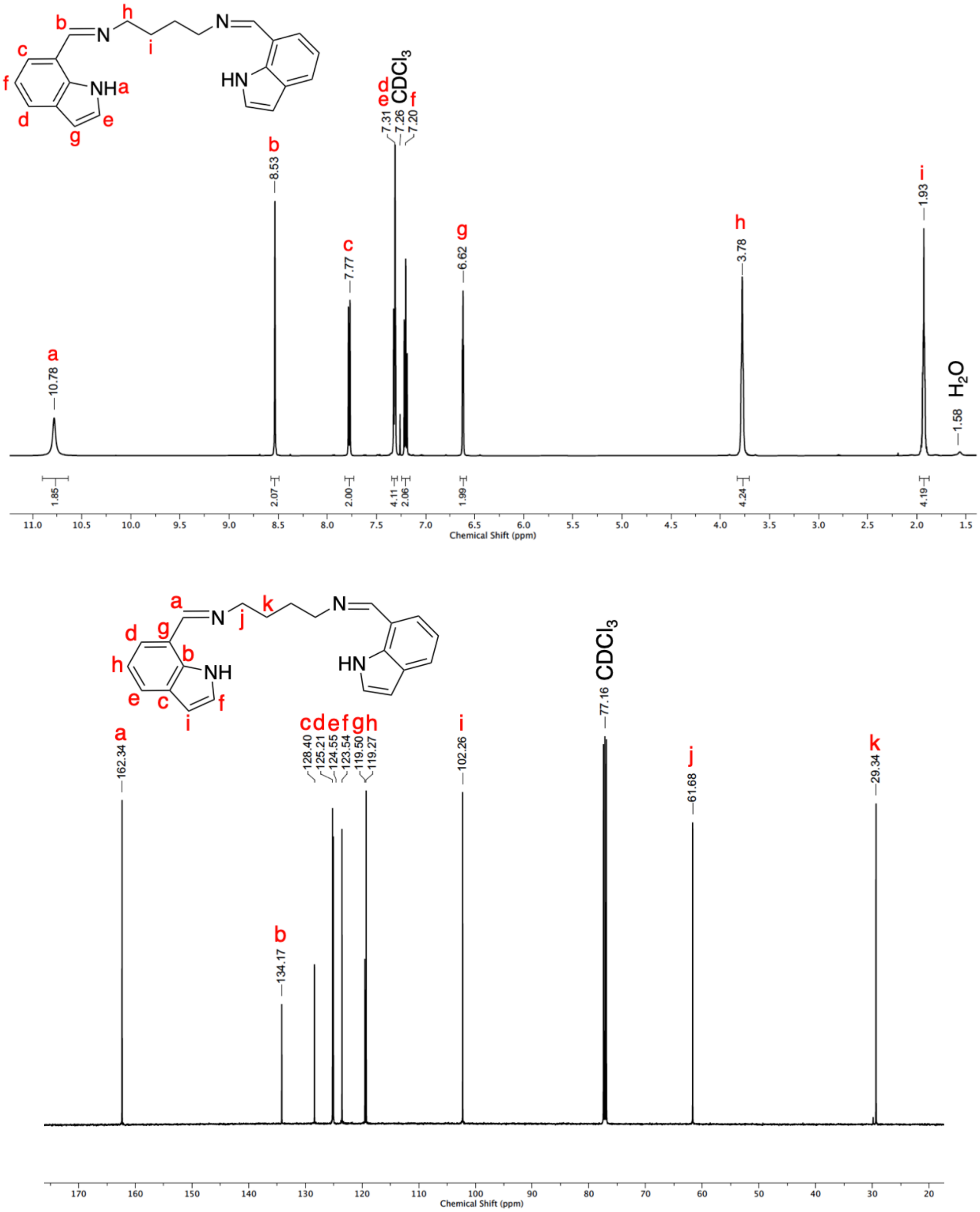

Figure 6.8. ^{1}H (top) and ^{13}C (bottom) NMR spectra of **L^{7C4}H$_2$**.

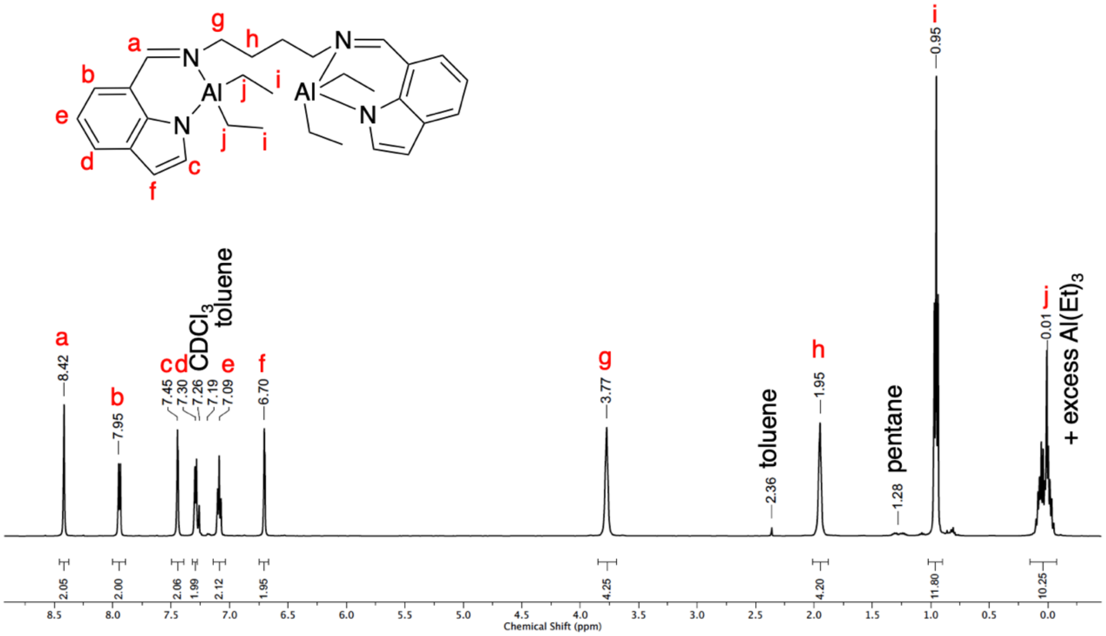

Figure 6.9. ^{1}H NMR spectrum of **L^{7C4}(AlEt$_2$)$_2$**.

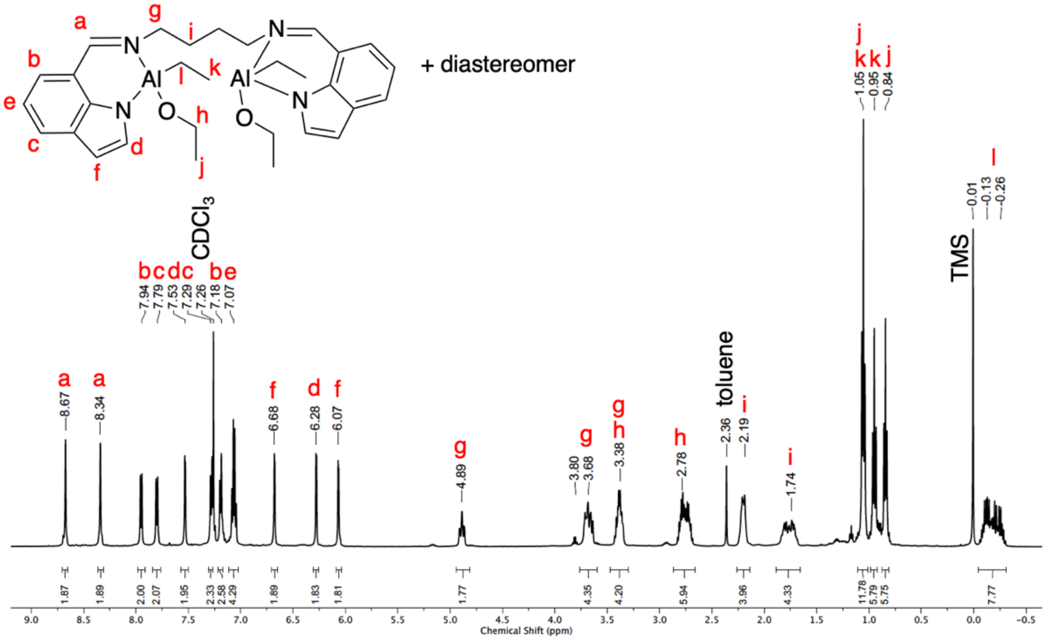

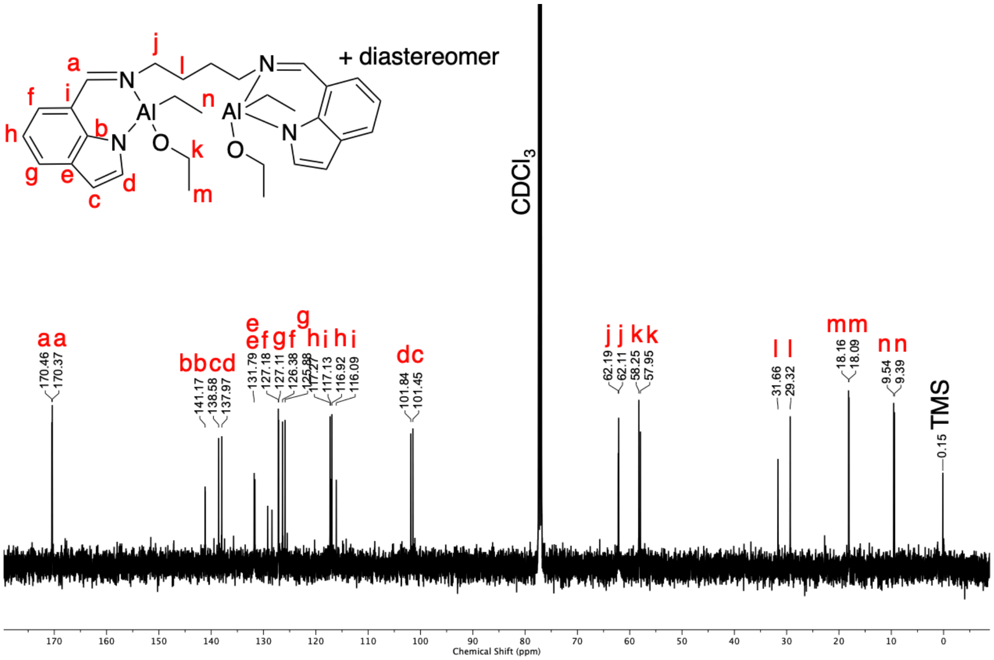

Figure 6.10. ^{1}H (top) and ^{13}C (bottom) NMR spectra of **L^{7C4}(AlEtOEt)$_2$**.

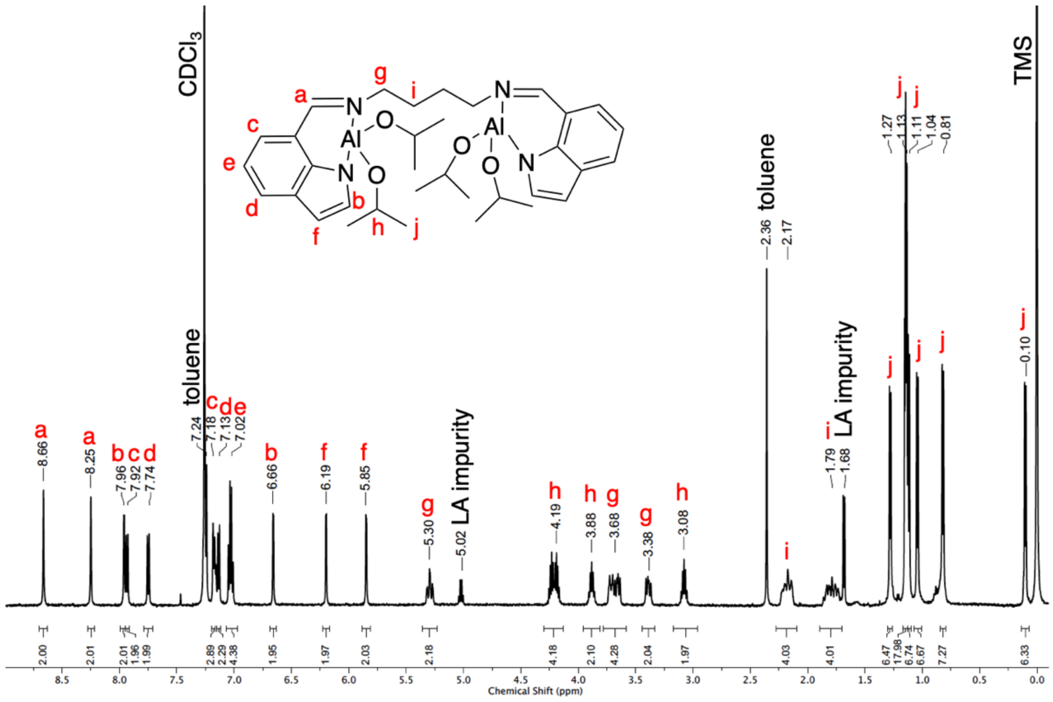

Figure 6.11. ^{1}H NMR spectrum of **L^{7C4}(Al(O*i*Pr)$_2$)$_2$**.

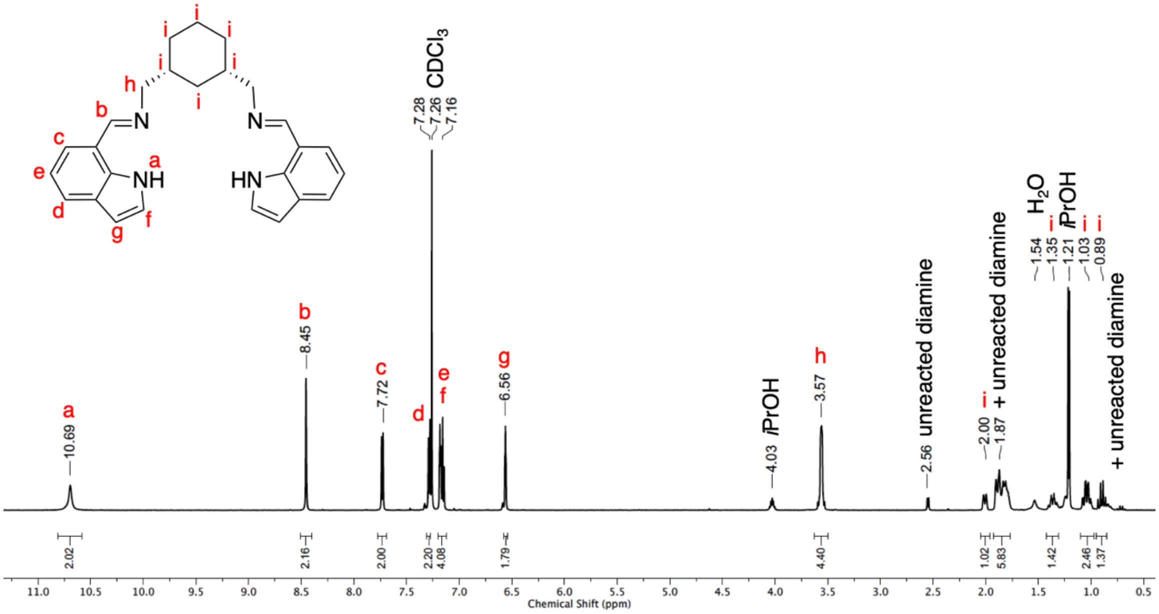

Figure 6.12. ^{1}H NMR spectrum of $\mathbf{L^{7C5}H_2}$.

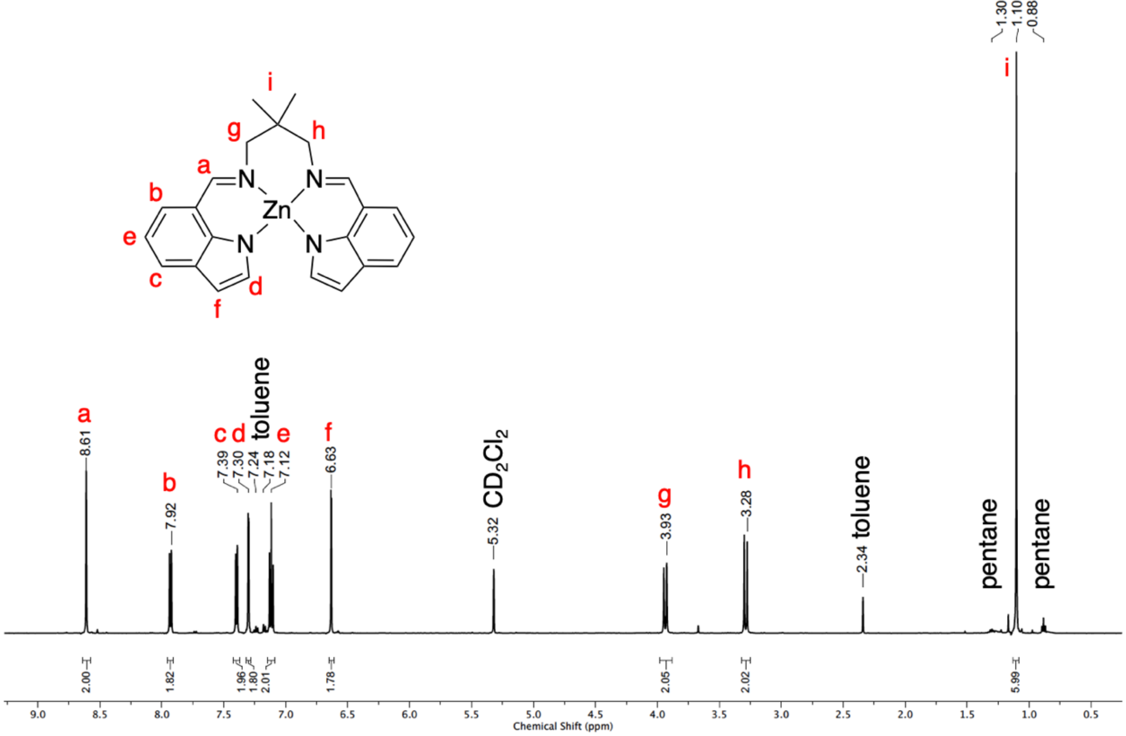

Figure 6.13. ^{1}H NMR spectrum of $\mathbf{L^7Zn}$.

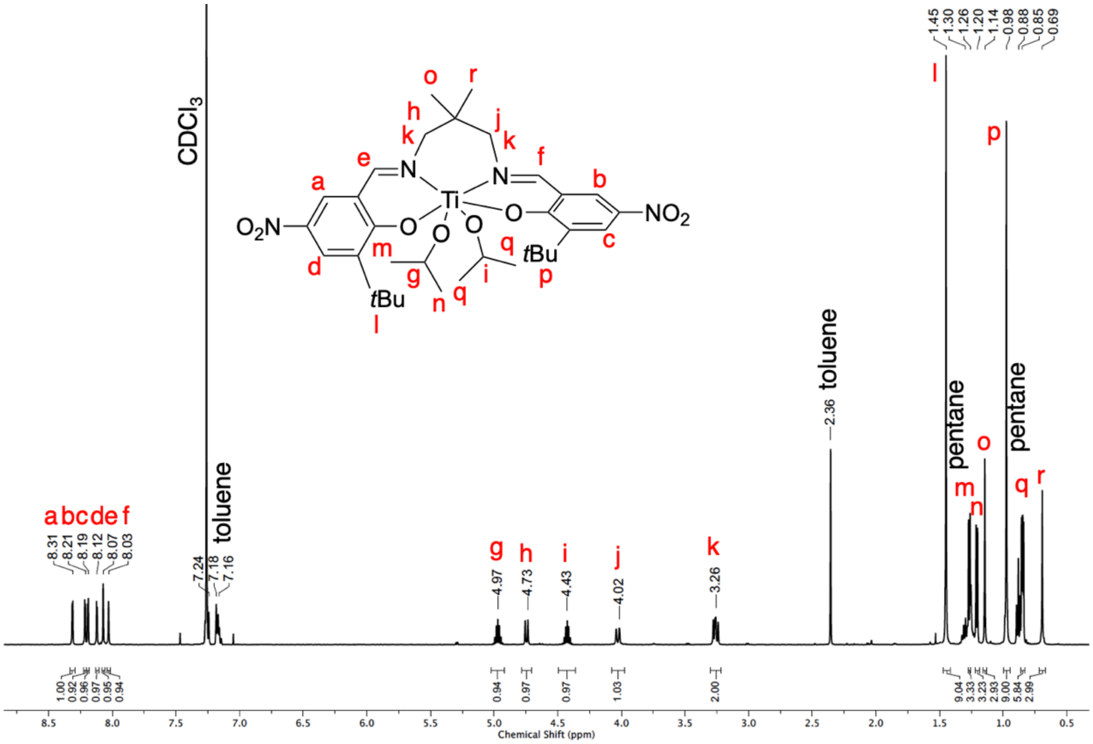

Figure 6.14. ^{1}H NMR spectrum of **(salen)L^{NO_2}Ti**.

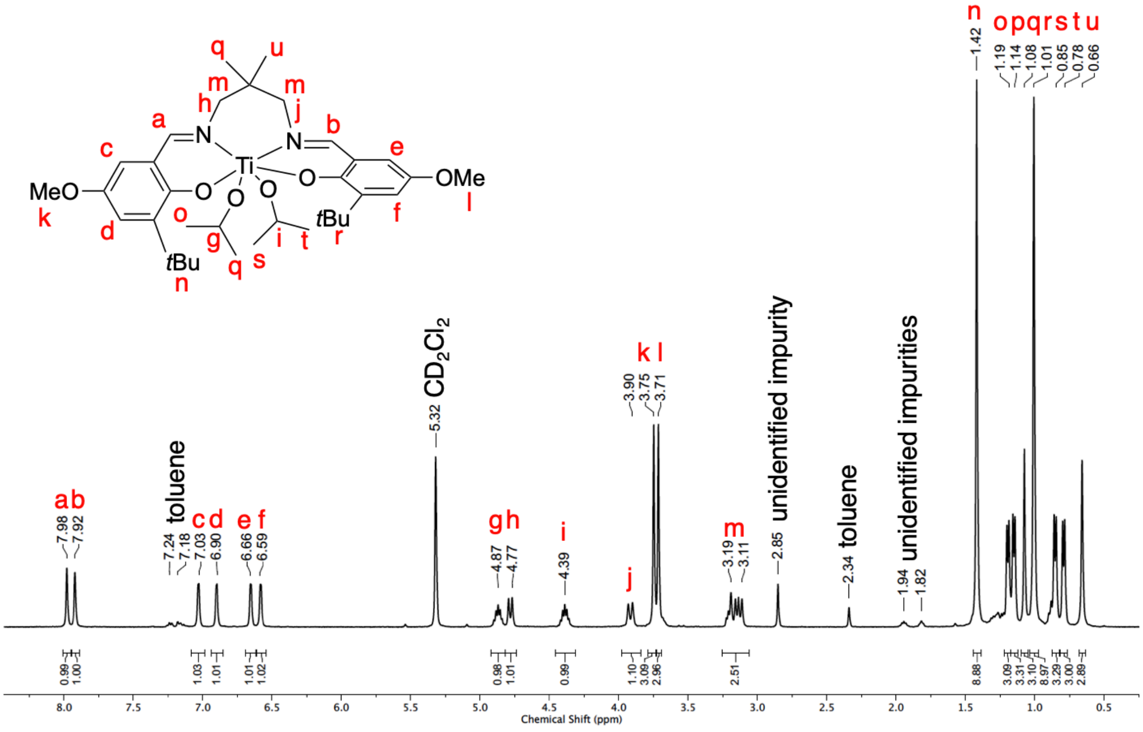

Figure 6.15. ^{1}H NMR spectrum of **(salen)L^{OMe}Ti**.

6.6.3 *Polymerization Experiments and Analysis*

6.6.3.1 *Lactide Polymerizations*

Polymerizations that were performed in a deuterated solvent ($CDCl_3$ at 60 °C) were completed as follows. Stock solutions of catalyst (1 mL, 9.7 mM) and *rac*-LA (1 mL, 1.5 M) were prepared. A J-Young NMR tube was sequentially charged with catalyst stock solution (240 μL, 2.3 μmol), and monomer stock solution (460 μL, 0.70 mmol), for final concentrations of 3.3 mM catalyst and 1.0 M monomer. Monomer conversion was monitored via ^1H NMR analysis. Polymerizations were quenched by opening them up to air, then dissolving the reaction mixture in CH_2Cl_2 before being precipitated into cold MeOH. The resulting PLA was dried under vacuum for ~12 h before being submitted for analysis.

Melt polymerization studies were performed by weighing out catalyst (1 equiv.) into an oven-dried screw-cap bomb flask charged with a stir bar and monomer (300 equiv.) in a nitrogen filled glovebox. The bomb flask was capped, removed from the glovebox, and then heated and stirred at the desired temperature for a given amount of time. The polymerizations were quenched by opening up the flask to air. An aliquot from the reaction mixture was immediately taken in order to determine monomer conversion (via ^1H NMR spectroscopy). The rest of the reaction mixture was then dissolved in CH_2Cl_2 before being poured into cold MeOH to precipitate the polymer. After decanting off the remaining MeOH, the resulting polymer was washed with cold MeOH (3 x 10 mL) and dried under vacuum for ~12 h before being submitted for analysis.

6.6.3.2 *ε-Caprolactone Polymerizations*

Polymerizations were performed by adding 450 μL of a stock solution of catalyst in CD_2Cl_2 (9.7 mM) and 170 μL of a stock solution of CL in CD_2Cl_2 (7.35 M) to a J-young

NMR tube inside a nitrogen-filled glovebox (target concentrations were 0.007 M catalyst and 2.0 M CL). The NMR tube was pumped out of the box, and monomer conversion over time was monitored via ^{1}H NMR spectroscopy.

6.7 Acknowledgements

This work was supported by the NSF Center for Sustainable Polymers, an NSF Center for Chemical Innovation, CHE-1901635. Morgan Young is thanked for her synthetic help with regard to the L^{7C4}/L^{7C5} ligands and resulting complexes.

Bibliography

(1) Coates, G. W.; Getzler, Y. D. Y. L. Chemical Recycling to Monomer for an Ideal, Circular Polymer Economy. *Nat. Rev. Mater*. **2020**.

(2) Zalasiewicz, J. A. N.; Williams, M.; Steffen, W.; Crutzen, P. The New World of the Anthropocene. *Environ. Sci*. **2010**, *44* (7), 2228–2231.

(3) Geyer, R.; Jambeck, J. R.; Law, K. L. Production, Use, and Fate of All Plastics Ever Made. *Sci. Adv.* **2017**, *3* (7), e1700782.

(4) World Economic Forum, E. M. F. and M. & C. *The New Plastics Economy: Rethinking the Future of Plastics*; 2016.

(5) Huysman, S.; Debaveye, S.; Schaubroeck, T.; Meester, S. De; Ardente, F.; Mathieux, F.; Dewulf, J. The Recyclability Benefit Rate of Closed-Loop and Open-Loop Systems: A Case Study on Plastic Recycling in Flanders. *Resour. Conserv. Recycl.* **2015**, *101*, 53–60.

(6) Adamus, G.; Musiol, M.; Sikorska, W.; Kowalczuk, M. Packaging Materials From Compostable Plastics – Technological and Social Aspects. *Adv. Plast. Technol. APT '13. Proc. 10th Int. Conf. held Sosnow. Poland, 8–10, Oct. 2013*.

(7) Schneiderman, D. K.; Hillmyer, M. A. 50th Anniversary Perspective: There Is a Great Future in Sustainable Polymers. *Macromolecules* **2017**, *50* (10), 3733–3749.

(8) McKenna, R.; Nielsen, D. R. Styrene Biosynthesis from Glucose by Engineered E. Coli. *Metab. Eng.* **2011**, *13* (5), 544–554.

(9) Jang, Y. S.; Kim, B.; Shin, J. H.; Choi, Y. J.; Choi, S.; Song, C. W.; Lee, J.; Park, H. G.; Lee, S. Y. Bio-Based Production of C2-C6 Platform Chemicals. *Biotechnol Bioeng*. **2012**, *109* (10), 2437–2459.

(10) Miranda, M. O.; Pietrangelo, A.; Hillmyer, M. A.; Tolman, W. B. Catalytic

Decarbonylation of Biomass-Derived Carboxylic Acids as Efficient Route to Commodity Monomers. *Green Chem.* **2012**, *14* (2), 490–494.

(11) Jem, K. J.; Tan, B. The Development and Challenges of Poly (Lactic Acid) and Poly (Glycolic Acid). *Adv. Ind. Eng. Polym. Res.* **2020**, *3* (2), 60–70.

(12) O'Keefe, B. J.; Hillmyer, M. A.; Tolman, W. B. Polymerization of Lactide and Related Cyclic Esters by Discrete Metal Complexes. *J. Chem. Soc. Dalt. Trans.* **2001**, *15*, 2215–2224.

(13) Kamber, N. E.; Jeong, W.; Waymouth, R. M.; Pratt, R. C.; Lohmeijer, B. G. G.; Hedrick, J. L. Organocatalytic Ring-Opening Polymerization. *Chem. Rev*. **2007**, *107* (12), 5813–5840.

(14) Buntara, T.; Noel, S.; Phua, P. H.; Melián-Cabrera, I.; De Vries, J. G.; Heeres, H. J. Caprolactam from Renewable Resources: Catalytic Conversion of 5-Hydroxymethylfurfural into Caprolactone. *Angew. Chemie - Int. Ed.* **2011**, *50* (31), 7083–7087.

(15) Kasperczyk, J. E. Microstructure Analysis of Poly(Lactic Acid) Obtained by Lithium Tert-Butoxide as Initiator. *Macromolecules* **1995**, *28* (11), 3937–3939.

(16) Kricheldorf, H.; Kreiser-Saunders, I. Polylactones, 19. Anionic Polymerization of L-lactide in Solution. *Die Makromol. Chemie* **1990**, *191* (5), 1057–1066.

(17) Kricheldorf, H.; Dunsing, R. Polylactones, 8. Mechanism of the Cationic Polymerization of L,L-dilactide. *Die Makromol. Chemie* **1986**, *187* (7), 1611–1625.

(18) Bourissou, D.; Martin-Vaca, B.; Dumitrescu, A.; Graullier, M.; Lacombe, F. Controlled Cationic Polymerization of Lactide. *Macromolecules* **2005**, *38* (24), 9993–9998.

(19) Nederberg, F.; Connor, E. F.; Möller, M.; Glauser, T.; Hedrick, J. L. New Paradigms

for Organic Catalysts: The First Organocatalytic Living Polymerization. *Angew. Chemie - Int. Ed.* **2001**, *40* (14), 2712–2715.

(20) Dove, A. P.; Pratt, R. C.; Lohmeijer, B. G. G.; Culkin, D. A.; Hagberg, E. C.; Nyce, G. W.; Waymouth, R. M.; Hedrick, J. L. N-Heterocyclic Carbenes: Effective Organic Catalysts for Living Polymerization. *Polymer (Guildf).* **2006**, *47* (11), 4018–4025.

(21) Wu, J.; Yu, T. L.; Chen, C. T.; Lin, C. C. Recent Developments in Main Group Metal Complexes Catalyzed/Initiated Polymerization of Lactides and Related Cyclic Esters. *Coord. Chem. Rev*. **2006**, *250* (5–6), 602–626.

(22) Dechy-Cabaret, O.; Martin-Vaca, B.; Bourissou, D. Controlled Ring-Opening Polymerization of Lactide and Glycolide. *Chem. Rev.* **2004**, *104* (12), 6147–6176.

(23) Castro-Aguirre, E.; Iñiguez-Franco, F.; Samsudin, H.; Fang, X.; Auras, R. Poly(Lactic Acid)—Mass Production, Processing, Industrial Applications, and End of Life. *Adv. Drug Deliv. Rev*. **2016**, *107*, 333–366.

(24) Anderson, K. S.; Schreck, K. M.; Hillmyer, M. A. Toughening Polylactide. *Polym. Rev.* **2008**, *48* (1), 85–108.

(25) Jing, F.; Hillmyer, M. A. A Bifunctional Monomer Derived from Lactide for Toughening Polylactide. *J. Am. Chem. Soc.* **2008**, *130* (42), 13826–13827.

(26) Fang, H.; Jiang, F.; Wu, Q.; Ding, Y.; Wang, Z. Supertough Polylactide Materials Prepared through in Situ Reactive Blending with PEG-Based Diacrylate Monomer. *ACS Appl. Mater. Interfaces* **2014**, *6* (16), 13552–13563.

(27) Feng, L.; Bian, X.; Chen, Z.; Li, G.; Chen, X. Mechanical, Aging, Optical and Rheological Properties of Toughening Polylactide by Melt Blending with Poly(Ethylene Glycol) Based Copolymers. *Polym. Degrad. Stab.* **2013**, *98* (9),

1591–1600.

(28) Young, R. J.; Chung, C. I. Introduction to Polymers. *J. Eng. Mater. Technol.* **1982**, *104* (4), 297.

(29) Baugh, L. S.; Canich, J. A. M. *Stereoselective Polymerization with Single-Site Catalysts*; CRC Press: 2007.

(30) Rosen, T.; Popowski, Y.; Goldberg, I.; Kol, M. Zinc Complexes of Sequential Tetradentate Monoanionic Ligands in the Isoselective Polymerization of *Rac*-Lactide. *Chem. - A Eur. J.* **2016**, *22* (33), 11533–11536.

(31) Shaver, M. P.; Cameron, D. J. A. Tacticity Control in the Synthesis of Poly(Lactic Acid) Polymer Stars with Dipentaerythritol Cores. *Biomacromolecules* **2010**, *11* (12), 3673–3679.

(32) Cheng, M.; Attygalle, A. B.; Lobkovsky, E. B.; Coates, G. W. Single-Site Catalysts for Ring-Opening Polymerization: Synthesis of Heterotactic Poly(Lactic Acid) from *Rac*-Lactide. *J. Am. Chem. Soc*. **1999**, *121* (49), 11583–11584.

(33) Anderson, K. S.; Hillmyer, M. A. Melt Preparation and Nucleation Efficiency of Polylactide Stereocomplex Crystallites. *Polymer (Guildf).* **2006**, *47* (6), 2030–2035.

(34) Nomura, N.; Ishii, R.; Yamamoto, Y.; Kondo, T. Stereoselective Ring-Opening Polymerization of a Racemic Lactide by Using Achiral Salen- and Homosalen-Aluminum Complexes. *Chem. - A Eur. J.* **2007**, *13* (16), 4433–4451.

(35) Chamberlain, B. M.; Cheng, M.; Moore, D. R.; Ovitt, T. M.; Lobkovsky, E. B.; Coates, G. W. Polymerization of Lactide with Zinc and Magnesium *β*-Diiminate Complexes: Stereocontrol and Mechanism. *J. Am. Chem. Soc.* **2001**, *123* (14), 3229–3238.

(36) Hiemenz, P. C.; Lodge, T. P. *Polymer Chemistry,* 2nd ed.; CRC Press: Boca Raton,

Fl, 2007.

(37) Nomura, N.; Ishii, R.; Akakura, M.; Aoi, K. Stereoselective Ring-Opening Polymerization of Racemic Lactide Using Aluminum-Achiral Ligand Complexes: Exploration of a Chain-End Control Mechanism. *J. Am. Chem. Soc.* **2002**, *124* (21), 5938–5939.

(38) Platel, R. H.; White, A. J. P.; Williams, C. K. Stereocontrolled Lactide Polymerisation Determined by the Nuclearity of the Yttrium Initiator. *Chem. Commun.* **2009**, *27*, 4115–4117.

(39) Hu, J.; Kan, C.; Wang, H.; Ma, H. Highly Active Chiral Oxazolinyl Aminophenolate Magnesium Initiators for Isoselective Ring-Opening Polymerization of *Rac*-Lactide: Dinuclearity Induced Enantiomorphic Site Control. *Macromolecules* **2018**, *51* (14), 5304–5312.

(40) Douglas, A. F.; Patrick, B. O.; Mehrkhodavandi, P. A Highly Active Chiral Indium Catalyst for Living Lactide Polymerization. *Angew. Chemie - Int. Ed.* **2008**, *47* (12), 2290–2293.

(41) Chisholm, M. H.; Patmore, N. J.; Zhou, Z. Concerning the Relative Importance of Enantiomorphic Site vs. Chain End Control in the Stereoselective Polymerization of Lactides: Reactions of (*R*,*R*-Salen)- and (*S*,*S*-Salen)-Aluminium Alkoxides $LAlOCH_2R$ Complexes (R = CH_3 and S-CHMeCl). *Chem. Commun.* **2005**, *1*, 127–129.

(42) Byers, J. A.; Bercaw, J. E. Kinetic Resolution of Racemic α-Olefins with Ansa-Zirconocene Polymerization Catalysts: Enantiomorphic Site vs. Chain End Control. *Proc. Natl. Acad. Sci. U. S. A.* **2006**, *103* (42), 15303–15308.

(43) Ovitt, T. M.; Coates, G. W. Stereoselective Ring-opening Polymerization of *Rac*-

Lactide with a Single-site, Racemic Aluminum Alkoxide Catalyst: Synthesis of Stereoblock Poly(Lactic Acid). *J. Polym. Sci. Part A Polym. Chem.* **2000**, *38* (S1), 4686–4692.

(44) Stasiw, D. E.; Luke, A. M.; Rosen, T.; League, A. B.; Mandal, M.; Neisen, B. D.; Cramer, C. J.; Kol, M.; Tolman, W. B. Mechanism of the Polymerization of *Rac*-Lactide by Fast Zinc Alkoxide Catalysts. *Inorg. Chem.* **2017**, *56* (22), 14366–14372.

(45) Spassky, N.; Wisniewski, M.; Pluta, C.; Borgne, A. Le. Highly Stereoelective Polymerization of *Rac*-(D,L)-Lactide with a Chiral Schiff's Base/Aluminium Alkoxide Initiator. *Macromol. Chem. Phys.* **1996**, *197* (9), 2627–2637.

(46) Ovitt, T. M.; Coates, G. W. Stereochemistry of Lactide Polymerization with Chiral Catalysts: New Opportunities for Stereocontrol Using Polymer Exchange Mechanisms. *J. Am. Chem. Soc.* **2002**, *124* (7), 1316–1326.

(47) Luke, A. M.; Peterson, A.; Chiniforoush, S.; Mandal, M.; Popowski, Y.; Sajjad, H.; Bouchey, C. J.; Shopov, D. Y.; Graziano, B. J.; Yao, L. J.; Cramer, C. J.; Reineke, T. M.; Tolman, W. B. Mechanism of Initiation Stereocontrol in Polymerization of Rac-Lactide by Aluminum Complexes Supported by Indolide-Imine Ligands. *Macromolecules* **2020**, *53* (5), 1809–1818.

(48) Kim, S. H.; Han, Y.-K.; Kim, Y. H.; Hong, S. I. Multifunctional Initiation of Lactide Polymerization by Stannous Octoate/Pentaerythritol. *Die Makromol. Chemie* **1992**, *193* (7), 1623–1631.

(49) Chisholm, M. H.; Gallucci, J. C.; Krempner, C. Ring-Opening Polymerization of L-Lactide by Organotin(IV)Alkoxides, $R_2Sn(OPr^i)_2$: Estimation of the Activation Parameters. *Polyhedron* **2007**, *26* (15), 4436–4444.

(50) Schwach, G.; Coudane, J.; Engel, R.; Vert, M. More about the Polymerization of

Lactides in the Presence of Stannous Octoate. *J. Polym. Sci. Part A Polym. Chem.* **1997**, *35* (16), 3431–3440.

(51) Hormnirun, P.; Marshall, E. L.; Gibson, V. C.; Pugh, R. I.; White, A. J. P. Study of Ligand Substituent Effects on the Rate and Stereoselectivity of Lactide Polymerization Using Aluminum Salen-Type Initiators. *Proc. Natl. Acad. Sci. U. S. A.* **2006**, *103* (42), 15343–15348.

(52) Ishii, R.; Nomura, N.; Kondo, T. Stereoselective Bulk Polymerization of Racemic Lactide for Stereoblock Poly(Racemic Lactide) Using an Achiral Aluminum Complex. *Polym. J.* **2004**, *36* (3), 261–264.

(53) Yu, X. F.; Zhang, C.; Wang, Z. X. Rapid and Controlled Polymerization of *Rac*-Lactide Using N,N,O-Chelate Zinc Enolate Catalysts. *Organometallics* **2013**, *32* (11), 3262–3268.

(54) Williams, C. K.; Breyfogle, L. E.; Choi, S. K.; Nam, W.; Young, V. G.; Hillmyer, M. A.; Tolman, W. B. A Highly Active Zinc Catalyst for the Controlled Polymerization of Lactide. *J. Am. Chem. Soc.* **2003**, *125* (37), 11350–11359.

(55) Umare, P. S.; Tembe, G. L.; Rao, K. V.; Satpathy, U. S.; Trivedi, B. Catalytic Ring-Opening Polymerization of L-Lactide by Titanium Biphenoxy-Alkoxide Initiators. *J. Mol. Catal. A Chem.* **2007**, *268* (1–2), 235–243.

(56) Kim, E.; Shin, E. W.; Yoo, I. K.; Chung, J. S. Characteristics of Heterogeneous Titanium Alkoxide Catalysts for Ring-Opening Polymerization of Lactide to Produce Polylactide. *J. Mol. Catal. A Chem.* **2009**, *298* (1–2), 36–39.

(57) Lv, W.; Wang, Y.; Wu, B.; Yao, Y.; Shen, Q. Synthesis, Structure, and Reactivity of Homodinuclear Lanthanide Complexes Bearing Salen-Type Schiff-Base Ligand. *Zeitschrift fur Anorg. und Allg. Chemie* **2012**, *638* (7–8), 1167–1172.

(58) Gu, W.; Xu, P.; Wang, Y.; Yao, Y.; Yuan, D.; Shen, Q. Synthesis and Characterization of Yttrium and Ytterbium Complexes Supported by Salen Ligands and Their Catalytic Properties for *Rac*-Lactide Polymerization. *Organometallics* **2015**, *34* (12), 2907–2916.

(59) Jianming, R.; Anguo, X.; Hongwei, W.; Hailin, Y. Review - Recent Development of Ring-Opening Polymerization of Cyclic Esters Using Aluminum Complexes. *Des. Monomers Polym.* **2014**, *17* (4), 345–355.

(60) Ajellal, N.; Carpentier, J. F.; Guillaume, C.; Guillaume, S. M.; Helou, M.; Poirier, V.; Sarazin, Y.; Trifonov, A. Metal-Catalyzed Immortal Ring-Opening Polymerization of Lactones, Lactides and Cyclic Carbonates. *Dalt. Trans.* **2010**, *39* (36), 8363–8376.

(61) Thomas, C. M. Stereocontrolled Ring-Opening Polymerization of Cyclic Esters: Synthesis of New Polyester Microstructures. *Chem. Soc. Rev.* **2010**, *39*, 165–173.

(62) Guillaume, S. M.; Kirillov, E.; Sarazin, Y.; Carpentier, J. F. Beyond Stereoselectivity, Switchable Catalysis: Some of the Last Frontier Challenges in Ring-Opening Polymerization of Cyclic Esters. *Chem. - A Eur. J.* **2015**, *21* (22), 7988–8003.

(63) Gupta, K. C.; Sutar, A. K. Catalytic Activities of Schiff Base Transition Metal Complexes. *Coord. Chem. Rev.* **2008**, *252* (12–14), 1420–1450.

(64) Lyubov, D. M.; Tolpygin, A. O.; Trifonov, A. A. Rare-Earth Metal Complexes as Catalysts for Ring-Opening Polymerization of Cyclic Esters. *Coord. Chem. Rev.* **2019**, *392*, 83–145.

(65) Wisniewski, M.; Borgne, A. Le; Spassky, N.; Le Borgne, A.; Spassky, N. Synthesis and Properties of (D)- and (L)-Lactide Stereocopolymers Using the System Achiral

Schiff's Base/Aluminium Methoxide as Initiator. *Macromol. Chem. Phys.* **1997**, *198* (4), 1227–1238.

(66) Hoops, S.; Gauges, R.; Lee, C.; Pahle, J.; Simus, N.; Singhal, M.; Xu, L.; Mendes, P.; Kummer, U. COPASI - A COmplex PAthway SImulator. *Bioinformatics* **2006**, *22* (24), 3067–3074.

(67) Miranda, M. O.; Deporre, Y.; Vazquez-Lima, H.; Johnson, M. A.; Marell, D. J.; Cramer, C. J.; Tolman, W. B. Understanding the Mechanism of Polymerization of ε-Caprolactone Catalyzed by Aluminum Salen Complexes. *Inorg. Chem.* **2013**, *52* (23), 13692–13701.

(68) Marlier, E. E.; Macaranas, J. A.; Marell, D. J.; Dunbar, C. R.; Johnson, M. A.; DePorre, Y.; Miranda, M. O.; Neisen, B. D.; Cramer, C. J.; Hillmyer, M. A.; Tolman, W. B. Mechanistic Studies of ε-Caprolactone Polymerization by (Salen)AlOR Complexes and a Predictive Model for Cyclic Ester Polymerizations. *ACS Catal.* **2016**, *6* (2), 1215–1224.

(69) Addison, A. W.; Rao, T. N.; Reedijk, J.; Van Rijn, J.; Verschoor, G. C. Synthesis, Structure, and Spectroscopic Properties of Copper(II) Compounds Containing Nitrogen-Sulphur Donor Ligands; the Crystal and Molecular Structure of Aqua[1,7-bis(N-methylbenzimidazol-2′-yl)-2,6-Dithiaheptane]Copper(II) Perchlorate. *J. Chem. Soc. Dalt. Trans.* **1984**, *7*, 1349–1356.

(70) Macaranas, J. A.; Luke, A. M.; Mandal, M.; Neisen, B. D.; Marell, D. J.; Cramer, C. J.; Tolman, W. B. Sterically Induced Ligand Framework Distortion Effects on Catalytic Cyclic Ester Polymerizations. *Inorg. Chem.* **2018**, *57* (6), 3451–3457.

(71) Hung, W. C.; Huang, Y.; Lin, C. C. Efficient Initiators for the Ring-Opening Polymerization of L-Lactide: Synthesis and Characterization of NNO-Tridentate

Schiff-Base Zinc Complexes. *J. Polym. Sci. Part A Polym. Chem.* **2008**, *46* (19), 6466–6476.

(72) Chen, H. Y.; Peng, Y. L.; Huang, T. H.; Sutar, A. K.; Miller, S. A.; Lin, C. C. Comparative Study of Lactide Polymerization by Zinc Alkoxide Complexes with a *β*-Diketiminato Ligand Bearing Different Substituents. *J. Mol. Catal. A Chem.* **2011**, *339* (1–2), 61–71.

(73) Buchard, A.; Bakewell, C. M.; Weiner, J.; Williams, C. K. Recent Developments in Catalytic Activation of Renewable Resources for Polymer Synthesis. In *Topics in Organometallic Chemistry: Organometallics and Renewables*; Meier, M. A. R., Weckhuysen, B. M., Brujinincx P. C. A., Eds.; Springer: Berlin Heidelberg, 2012; Vol. *39*.

(74) Dijkstra, P. J.; Du, H.; Feijen, J. Single Site Catalysts for Stereoselective Ring-Opening Polymerization of Lactides. *Polym. Chem.* **2011**, *2*, 520–527.

(75) Dagorne, S.; Normand, M.; Kirillov, E.; Carpentier, J. F. Gallium and Indium Complexes for Ring-Opening Polymerization of Cyclic Ethers, Esters and Carbonates. *Coord. Chem. Rev.* **2013**, *257* (11–12), 1869–1886.

(76) Sauer, A.; Kapelski, A.; Fliedel, C.; Dagorne, S.; Kol, M.; Okuda, J. Structurally Well-Defined Group 4 Metal Complexes as Initiators for the Ring-Opening Polymerization of Lactide Monomers. *Dalton Trans.* **2013**, *42*, 9007–9023.

(77) Hillmyer, M. A.; Tolman, W. B. Aliphatic Polyester Block Polymers: Renewable, Degradable, and Sustainable. *Acc. Chem. Res.* **2014**, *47* (8), 2390–2396.

(78) Hormnirun, P.; Marshall, E. L.; Gibson, V. C.; White, A. J. P.; Williams, D. J. Remarkable Stereocontrol in the Polymerization of Racemic Lactide Using Aluminum Initiators Supported by Tetradentate Aminophenoxide Ligands. *J. Am.*

Chem. Soc. **2004**, *126* (9), 2688–2689.

(79) Tang, Z.; Gibson, V. C. *Rac*-Lactide Polymerization Using Aluminum Complexes Bearing Tetradentate Phenoxy-Amine Ligands. *Eur. Polym. J.* **2007**, *43* (1), 150–155.

(80) Chisholm, M. H.; Gallucci, J. C.; Quisenberry, K. T.; Zhou, Z. Complexities in the Ring-Opening Polymerization of Lactide by Chiral Salen Aluminum Initiators. *Inorg. Chem.* **2008**, *47* (7), 2613–2624.

(81) Agatemor, C.; Arnold, A. E.; Cross, E. D.; Decken, A.; Shaver, M. P. Aluminium Salophen and Salen Initiators in the Ring-Opening Polymerisation of *Rac*-Lactide and *Rac-β*-Butyrolactone: Electronic Effects on Stereoselectivity and Polymerisation Rates. *J. Organomet. Chem.* **2013**, *745–746*, 335–340.

(82) Cross, E. D.; Allan, L. E. N.; Decken, A.; Shaver, M. P. Aluminum Salen and Salan Complexes in the Ring-Opening Polymerization of Cyclic Esters: Controlled Immortal and Copolymerization of *Rac-β*-Butyrolactone and *Rac*-Lactide. *J. Polym. Sci. Part A Polym. Chem.* **2013**, *51* (5), 1137–1146.

(83) Alcazar-Roman, L. M.; O'Keefe, B. J.; Hillmyer, M. A.; Tolman, W. B. Electronic Influence of Ligand Substituents on the Rate of Polymerization of ε-Caprolactone by Single-Site Aluminium Alkoxide Catalysts. *Dalt. Trans.* **2003**, *15*, 3082–3087.

(84) Wang, Y.; Ma, H. Exploitation of Dinuclear Salan Aluminum Complexes for Versatile Copolymerization of ε-Caprolactone and L-Lactide. *Chem. Commun.* **2012**, *48* (53), 6729.

(85) Cozzi, P. G. Metal-Salen Schiff Base Complexes in Catalysis: Practical Aspects. *Chem. Soc. Rev.* **2004**, *33* (7), 410–421.

(86) Chang, C. H.; Chuang, H. J.; Chen, T. Y.; Li, C. Y.; Lin, C. H.; Lee, T. Y.; Ko, B.

T.; Huang, H. Y. Di-Nuclear Zinc Complexes Containing Tridentate Imino-Benzotriazole Phenolate Derivatives as Efficient Catalysts for Ring-Opening Polymerization of Cyclic Esters and Copolymerization of Phthalic Anhydride with Cyclohexene Oxide. *J. Polym. Sci. Part A Polym. Chem.* **2016**, *54* (5), 714–725.

(87) Abbina, S.; Du, G. Zinc-Catalyzed Highly Isoselective Ring Opening Polymerization of *Rac*-Lactide. *ACS Macro Lett.* **2014**, *3* (7), 689–692.

(88) Schäfer, P. M.; Fuchs, M.; Ohligschläger, A.; Rittinghaus, R.; McKeown, P.; Akin, E.; Schmidt, M.; Hoffmann, A.; Liauw, M. A.; Jones, M. D.; Herres-Pawlis, S. Highly Active N,O Zinc Guanidine Catalysts for the Ring-Opening Polymerization of Lactide. *ChemSusChem* **2017**, *10* (18), 3547–3556.

(89) Honrado, M.; Otero, A.; Fernández-Baeza, J.; Sánchez-Barba, L. F.; Garcés, A.; Lara-Sánchez, A.; Rodríguez, A. M. Enantiopure N,N,O-Scorpionate Zinc Amide and Chloride Complexes as Efficient Initiators for the Heteroselective ROP of Cyclic Esters. *Dalt. Trans.* **2014**, *43* (45), 17090–17100.

(90) Roberts, C. C.; Barnett, B. R.; Green, D. B.; Fritsch, J. M. Synthesis and Structures of Tridentate Ketoiminate Zinc Complexes That Act as L-Lactide Ring-Opening Polymerization Catalysts. *Organometallics* **2012**, *31* (11), 4133–4141.

(91) Han, Y.; Feng, Q.; Zhang, Y.; Zhang, Y.; Yao, W. Ring-Opening Polymerization of *Rac*-Lactide by Mononuclear Zinc Complexes That Contain Chiral Tetra-Azane Ligands. *Polyhedron* **2017**, *121*, 206–210.

(92) von Frankland, E. Ueber Die Isolirung Der Organischen Radicale. *Justus Liebigs Ann. Chem.* **1849**.

(93) Lewiński, J.; Marciniak, W.; Lipkowski, J.; Justyniak, I. New Insights into the Reaction of Zinc Alkyls with Dioxygen. *J. Am. Chem. Soc.* **2003**, *125* (42), 12698–

12699.

(94) Labourdette, G.; Lee, D. J.; Patrick, B. O.; Ezhova, M. B.; Mehrkhodavandi, P. Unusually Stable Chiral Ethyl Zinc Complexes: Reactivity and Polymerization of Lactide. *Organometallics* **2009**, *28* (5), 1309–1319.

(95) Li, D.; Kagan, G.; Hopson, R.; Williard, P. G. Formula Weight Prediction by Internal Reference Diffusion-Ordered NMR Spectroscopy (DOSY). *J. Am. Chem. Soc.* **2009**, *131* (15), 5627–5634.

(96) Messman, J. M.; Storey, R. F. Real-Time Monitoring of the Ring-Opening Polymerization of *Rac*-Lactide with *in situ* Attenuated Total Reflectance/Fourier Transform Infrared Spectroscopy with Conduit and Diamond-Composite Sensor Technology. *J. Polym. Sci. Part A Polym. Chem.* **2004**, *42* (24), 6238–6247.

(97) Aubrecht, K. B.; Hillmyer, M. A.; Tolman, W. B. Polymerization of Lactide by Monomeric Sn(II) Alkoxide Complexes. *Macromolecules* **2002**, *35* (3), 644–650.

(98) Moravek, S. J.; Messman, J. M.; Storey, R. F. Polymerization Kinetics of *Rac*-Lactide Initiated with Alcohol/Stannous Octoate Using in Situ Attenuated Total Reflectance-Fourier Transform Infrared Spectroscopy: An Initiator Study. *J. Polym. Sci. Part A Polym. Chem.* **2009**, *47* (3), 797–803.

(99) Hanlan, J.; Skoog, D. A.; West, D. M. *Principles of Instrumental Analysis*; Cengage: Independence, KY, 2007.

(100) IC IR, React-IR Software. Mettler-Toledo AutoChem, Inc.: Columbus, OH 2008.

(101) Olis GlobalWorks, Spectral Global Fitting Analysis Software. OLIS, Inc.: Bogart, GA.

(102) Zell, M. T.; Padden, B. E.; Paterick, A. J.; Thakur, K. A. M.; Kean, R. T.; Hillmyer, M. A.; Munson, E. J. Unambiguous Determination of the ^{13}C and ^{1}H NMR

Stereosequence Assignments of Polylactide Using High-Resolution Solution NMR Spectroscopy. *Macromolecules* **2002**, *35* (20), 7700–7707.

(103) Gao, B.; Duan, R.; Pang, X.; Li, X.; Qu, Z.; Tang, Z.; Zhuang, X.; Chen, X. Stereoselective Ring-Opening Polymerization of *Rac*-Lactides Catalyzed by Aluminum Hemi-Salen Complexes. *Organometallics* **2013**, *32* (19), 5435–5444.

(104) Gao, B.; Duan, Q.; Li, Y.; Li, D.; Zhang, L.; Cui, Y.; Hu, N.; Pang, X. Stereoselective Ring-Opening Polymerization of *Rac*-Lactides Catalyzed by Titanium Complexes Containing N,N-Bidentate Phenanthrene Derivatives. *RSC Adv.* **2015**, *5* (18), 13437–13442.

(105) Marshall, E. L.; Gibson, V. C.; Rzepa, H. S. A Computational Analysis of the Ring-Opening Polymerization of Rac-Lactide Initiated by Single-Site *β*-Diketiminate Metal Complexes: Defining the Mechanistic Pathway and the Origin of Stereocontrol. *J. Am. Chem. Soc.* **2005**, *127* (16), 6048–6051.

(106) Börner, J.; Flörke, U.; Glöge, T.; Bannenberg, T.; Tamm, M.; Jones, M. D.; Döring, A.; Kuckling, D.; Herres-Pawlis, S. New Insights into the Lactide Polymerisation with Neutral N-Donor Stabilised Zinc Complexes: Comparison of Imidazolin-2-Imine vs. Guanidine Complexes. *J. Mol. Catal. A Chem.* **2009**, *316* (1–2), 139–145.

(107) Fliedel, C.; Vila-Viçosa, D.; Calhorda, M. J.; Dagorne, S.; Avilés, T. Dinuclear Zinc-N-Heterocyclic Carbene Complexes for Either the Controlled Ring-Opening Polymerization of Lactide or the Controlled Degradation of Polylactide under Mild Conditions. *ChemCatChem* **2014**, *6* (5), 1357–1367.

(108) Manna, C. M.; Kaur, A.; Yablon, L. M.; Haeffner, F.; Li, B.; Byers, J. A. Stereoselective Catalysis Achieved through *in situ* Desymmetrization of an Achiral Iron Catalyst Precursor. *J. Am. Chem. Soc.* **2015**, *137* (45), 14232–14235.

(109) Tabthong, S.; Nanok, T.; Sumrit, P.; Kongsaeree, P.; Prabpai, S.; Chuawong, P.; Hormnirun, P. Bis(Pyrrolidene) Schiff Base Aluminum Complexes as Isoselective-Biased Initiators for the Controlled Ring-Opening Polymerization of *Rac*-Lactide: Experimental and Theoretical Studies. *Macromolecules* **2015**, *48* (19), 6846–6861.

(110) Wang, Y.; Mehmood, A.; Zhao, Y.; Qu, J.; Luo, Y. Computational Studies on the Selective Polymerization of Lactide Catalyzed by Bifunctional Yttrium NHC Catalyst. *Inorganics* **2017**, *5* (3), 46.

(111) Robert, C.; Schmid, T. E.; Richard, V.; Haquette, P.; Raman, S. K.; Rager, M. N.; Gauvin, R. M.; Morin, Y.; Trivelli, X.; Guérineau, V.; Del Rosal, I.; Maron, L.; Thomas, C. M. Mechanistic Aspects of the Polymerization of Lactide Using a Highly Efficient Aluminum(III) Catalytic System. *J. Am. Chem. Soc.* **2017**, *139* (17), 6217–6225.

(112) Gu, X.; Zhang, Y.; Xu, Z. J.; Che, C. M. Iron(III)–Salan Complexes Catalysed Highly Enantioselective Fluorination and Hydroxylation of *β*-Keto Esters and N-Boc Oxindoles. *Chem. Commun.* **2014**, *50* (58), 7870–7873.

(113) Braun, M.; Fleischer, R.; Mai, B.; Schneider, M. A.; Lachenicht, S. The Regioisomeric Triphenylaminoethanols - Comparison of Their Efficiency in Enantioselective Catalysis. *Adv. Synth. Catal.* **2004**, *346* (4), 474–482.

(114) Kurahashi, T.; Fujii, H. One-Electron Oxidation of Electronically Diverse Manganese(III) and Nickel(II) Salen Complexes: Transition from Localized to Delocalized Mixed-Valence Ligand Radicals. *J. Am. Chem. Soc.* **2011**, *133* (21), 8307–8316.

(115) Bakewell, C.; White, A. J. P.; Long, N. J.; Williams, C. K. Scandium and Yttrium Phosphasalen Complexes as Initiators for Ring-Opening Polymerization of Cyclic

Esters. *Inorg. Chem.* **2015**, *54* (5), 2204–2212.

(116) Zhao, Y.; Truhlar, D. G. A New Local Density Functional for Main-Group Thermochemistry, Transition Metal Bonding, Thermochemical Kinetics, and Noncovalent Interactions. *J. Chem. Phys.* **2006**, *125* (19), 194101–194118.

(117) Zhao, Y.; Truhlar, D. G. Density Functionals with Broad Applicability in Chemistry. *Acc. Chem. Res.* **2008**, *41* (2), 157–167.

(118) Frisch, M. J. G.; Trucks, W.; Schlegel, H. B.; Scuseria, G. E.; Robb, M. A.; Cheeseman, J. R.; Scalmani, G.; Barone, V.; Mennucci, B.; Petersson, G. A.; Nakatsuji, H.; Caricato, M.; Li, X.; Hratchian, H. P.; Izmaylov, A. F.; Bloino, J.; Zheng, G.; Sonnenberg, J. L. Hada, M.; Ehara, M.; Toyota, K.; Fukuda, R.; Hasegawa, J.; Ishida, M.; Nakajima, T.; Honda, Y.; Kitao,O.; Nakai, H.; Vreven, T.; Montgomery, J. A.; Peralta, J. E.; Ogliaro, F.; Bearpark, M.; Heyd, J. J.; Brothers, E.; Kudin, K. N.; Staroverov, V. N.; Kobayashi, R.; Normand, J.; Raghavachari, K.; Rendell, A.; Burant, J. C.; Iyengar, S. S.; Tomasi, J.; Cossi, M.; Rega, N.; Millam, J. M.; Klene, M.; Knox, J. E.; Cross, J. B.; Bakken,V.; Adamo, C.; Jaramillo, J.; Gomperts, R.; Stratmann, R. E.; Yazyev, O.; Austin, A. J.; Cammi, R.; Pomelli, C.; Ochterski, J. W.; Martin, R. L.; Morokuma, K.; Zakrzewski, V. G.;Voth, G. A.; Salvador, P.; Dannenberg, J. J.;Dapprich, S.; Daniels, A. D.; Farkas, O.; Foresman, J. B.; Ortiz, J. V.; Cioslowski, J.; Fox, D. J. Gaussian 09, Revision D.01, *Gaussian, Inc*., Wallingford CT, 2016.

(119) Pople, J. A.; Schleyer, P. V.; Hehre, W. J.; Radom, L. *AB INITIO Molecular Orbital Theory*; 1986.

(120) Hehre, W. J.; Lathan, W. A. Self-Consistent Molecular Orbital Methods. XIV. An Extended Gaussian-Type Basis for Molecular Orbital Studies of Organic Molecules.

Inclusion of Second Row Elements. *J. Chem. Phys.* **1972**, *56* (11), 5255–5257.

(121) Clark, T.; Chandrasekhar, J.; Spitznagel, G. W.; Schleyer, P. V. R. Efficient Diffuse Function-augmented Basis Sets for Anion Calculations. III. The 3-21+G Basis Set for First-row Elements, Li–F. *J. Comput. Chem.* **1983**, *4* (3), 294–301.

(122) Andrae, D.; Häußermann, U.; Dolg, M.; Stoll, H.; Preuß, H. Energy-Adjusted Ab Initio Pseudopotentials for the Second and Third Row Transition Elements. *Theor. Chim. Acta* **1990**, *77* (2), 123–141.

(123) Zhao, Y.; Truhlar, D. G. The M06 Suite of Density Functionals for Main Group Thermochemistry, Thermochemical Kinetics, Noncovalent Interactions, Excited States, and Transition Elements: Two New Functionals and Systematic Testing of Four M06-Class Functionals and 12 Other Function. *Theor. Chem. Acc.* **2008**, *120*, 215–241.

(124) Marenich, A. V.; Cramer, C. J.; Truhlar, D. G. Universal Solvation Model Based on Solute Electron Density and on a Continuum Model of the Solvent Defined by the Bulk Dielectric Constant and Atomic Surface Tensions. *J. Phys. Chem. B* **2009**, *113* (18), 6378–6396.

(125) Marenich, A. V.; Jerome, S. V.; Cramer, C. J.; Truhlar, D. G. Charge Model 5: An Extension of Hirshfeld Population Analysis for the Accurate Description of Molecular Interactions in Gaseous and Condensed Phases. *J. Chem. Theory Comput.* **2012**, *8* (2), 527–541.

(126) Wei, J.; Riffel, M. N.; Diaconescu, P. L. Redox Control of Aluminum Ring-Opening Polymerization: A Combined Experimental and DFT Investigation. *Macromolecules* **2017**, *50* (5), 1847–1861.

(127) Jitonnom, J.; Molloy, R.; Punyodom, W.; Meelua, W. Theoretical Studies on

Aluminum Trialkoxide-Initiated Lactone Ring-Opening Polymerizations: Roles of Alkoxide Substituent and Monomer Ring Structure. *Comput. Theor. Chem.* **2016**, *1097*, 25–32.

(128) Jérôme, C.; Lecomte, P. Recent Advances in the Synthesis of Aliphatic Polyesters by Ring-Opening Polymerization. *Adv. Drug Deliv. Rev*. **2008**, *60* (9), 1056–1076.

(129) Stridsberg, K. M.; Ryner, M.; Albertsson, A. C. Controlled Ring-Opening Polymerization: Polymers with Designed Macromolecular Architecture. In *Advances in Polymer Science*. 2002, Vol. *157*

(130) Nomura, N.; Aoyama, T.; Ishii, R.; Kondo, T. Salicylaldimine-Aluminum Complexes for the Facile and Efficient Ring-Opening Polymerization of *ε*-Caprolactone. *Macromolecules* **2005**, *38* (13), 5363–5366.

(131) Stanford, M. J.; Dove, A. P. Stereocontrolled Ring-Opening Polymerisation of Lactide. *Chem. Soc. Rev*. **2010**, *39*, 486–494.

(132) MacDonald, J. P.; Shaver, M. P. Aluminum Salen and Salan Polymerization Catalysts: From Monomer Scope to Macrostructure Control. *ACS Symp. Ser.* **2015**, *1192*, 147–167.

(133) Wei, Y.; Wang, S.; Zhou, S. Aluminum Alkyl Complexes: Synthesis, Structure, and Application in ROP of Cyclic Esters. *Dalton Trans*. **2016**, *45*, 4471–4485.

(134) Stasiw, D. E.; Mandal, M.; Neisen, B. D.; Mitchell, L. A.; Cramer, C. J.; Tolman, W. B. Why so Slow? Mechanistic Insights from Studies of a Poor Catalyst for Polymerization of *ε*-Caprolactone. *Inorg. Chem.* **2017**, *56* (2), 725–728.

(135) Jin, R.; Liu, S.; Lan, Y. Distortion-Interaction Analysis along the Reaction Pathway to Reveal the Reactivity of the Alder-Ene Reaction of Enes. *RSC Adv.* **2015**, *5* (75), 61426–61435.

(136) Mandal, M.; Luke, A. M.; Dereli, B.; Elwell, C. E.; Reineke, T. M.; Tolman, W. B.; Cramer, C. J. Computational Prediction and Experimental Verification of ε-Caprolactone Ring-Opening Polymerization Activity by an Aluminum Complex of an Indolide/Schiff-Base Ligand. *ACS Catal.* **2019**, *9* (2), 885–889.

(137) Du, H.; Velders, A. H.; Dijkstra, P. J.; Zhong, Z.; Chen, X.; Feijen, J. Polymerization of Lactide Using Achiral Bis(Pyrrolidene) Schiff Base Aluminum Complexes. *Macromolecules* **2009**, *42* (4), 1058–1066.

(138) Rufino-Felipe, E.; Lopez, N.; Vengoechea-Gómez, F. A.; Guerrero-Ramírez, L. G.; Muñoz-Hernández, M. Á. Ring-Opening Polymerization of *Rac*-Lactide Catalyzed by Al(III) and Zn(II) Complexes Incorporating Schiff Base Ligands Derived from Pyrrole-2-Carboxaldehyde. *Appl. Organomet. Chem.* **2018**, *32* (6), e4315.

(139) Lee, C. L.; Lin, Y. F.; Jiang, M. T.; Lu, W. Y.; Vandavasi, J. K.; Wang, L. F.; Lai, Y. C.; Chiang, M. Y.; Chen, H. Y. Improvement in Aluminum Complexes Bearing Schiff Bases in Ring-Opening Polymerization of ε-Caprolactone: A Five-Membered-Ring System. *Organometallics* **2017**, *36* (10), 1936–1945.

(140) Black, D. S. C.; Craig, D. C.; Kumar, N.; Wong, L. C. H. Nickel(II) Complexes of Lmine Ligands Derived from 7-Formylindoles. *J. Chem. Soc. - Ser. Chem. Commun.* **1985**, *17*, 1172–1173.

(141) Liu, S. F.; Wu, Q.; Schmider, H. L.; Aziz, H.; Hu, N. X.; Popović, Z.; Wang, S. Syntheses, Structures, and Electroluminescence of New Blue/Green Luminescent Chelate Compounds: Zn(2-Py-in)$_2$(THF), BPh$_2$(2-Py-in), Be(2-Py-in)$_2$, and BPh$_2$(2-Py-Aza) [2-Py-in = 2-(2-Pyridyl)Indole; 2-Py-Aza = 2-(2- Pyridyl)-7-Azaindole]. *J. Am. Chem. Soc.* **2000**, *122* (15), 3671–3678.

(142) Mason, M. R.; Fneich, B. N.; Kirschbaum, K. Titanium and Zirconium Amido

Complexes Ligated by 2,2′-Di(3-Methylindolyl)Methanes: Synthesis, Characterization, and Ethylene Polymerization Activity. *Inorg. Chem.* **2003**, *42* (21), 6592–6594.

(143) Kingsley, N. B.; Kirschbaum, K.; Mason, M. R. Confirmation of Bridging N-Indolides in 3-Methylindole and Di- and Tri(3-Methylindolyl)Methane Complexes of Dimethyl-, Diethyl-, and Diisobutylaluminum. *Organometallics* **2010**, *29* (22), 5927–5935.

(144) Peng, K. F.; Chen, Y.; Chen, C. T. Synthesis and Catalytic Application of Magnesium Complexes Bearing Pendant Indolyl Ligands. *Dalt. Trans.* **2015**, *44* (20), 9610–9619.

(145) Houk, K. N.; Jabbari, A.; Hall, H. K.; Alemán, C. Why *δ*-Valerolactone Polymerizes and *γ*-Butyrolactone Does Not. *J. Org. Chem.* **2008**, *73* (7), 2674–2678.

(146) Igel-Mann, G.; Stoll, H.; Preuss, H. Pseudopotentials for Main Group Elements (IIIa through VIIa). *Mol. Phys.* **1988**, *65* (6), 1321–1328.

(147) Grimme, S.; Antony, J.; Ehrlich, S.; Krieg, H. A Consistent and Accurate Ab Initio Parametrization of Density Functional Dispersion Correction (DFT-D) for the 94 Elements H-Pu. *J. Chem. Phys.* **2010**, *132* (15).

(148) Adamo, C.; Barone, V. Toward Reliable Density Functional Methods without Adjustable Parameters: The PBE0 Model. *J. Chem. Phys.* **1999**, *110* (13), 6158–6170.

(149) Coates, G. W.; Moore, D. R. Discrete Metal-Based Catalysts for the Copolymerization of CO_2 and Epoxides: Discovery, Reactivity, Optimization, and Mechanism. *Angew. Chemie. - Int. Ed.* **2004**, *43* (48), 6618–6639.

(150) Drumright, R. E.; Gruber, P. R.; Henton, D. E. Polylactic Acid Technology. *Adv.*

Mater. **2000**, *12* (23), 1841–1846.

(151) Uhrich, K. E.; Cannizzaro, S. M.; Langer, R. S.; Shakesheff, K. M. Polymeric Systems for Controlled Drug Release. *Chem. Rev.* **1999**, *99* (11), 3181–3198.

(152) Le Borgne, A.; Vincens, V.; Jouglard, M.; Spassky, N. Ring-opening Oligomerization Reactions Using Aluminium Complexes of Schiff's Bases as Initiators. *Makromol. Chemie. Macromol. Symp.* **1993**, *73* (1), 37–46.

(153) Ovitt, T. M.; Coates, G. W. Stereoselective Ring-Opening Polymerization of Meso-Lactide: Synthesis of Syndiotactic Poly(Lactic Acid). *J. Am. Chem. Soc.* **1999**, *121* (16), 4072–4073.

(154) Radano, C. P.; Baker, G. L.; Smith, M. R. Stereoselective Polymerization of a Racemic Monomer with a Racemic Catalyst: Direct Preparation of the Polylactic Acid Stereocomplex from Racemic Lactide. *J. Am. Chem. Soc*. **2000**, *122* (7), 1552–1553.

(155) Majerska, K.; Duda, A. Stereocontrolled Polymerization of Racemic Lactide with Chiral Initiator: Combining Stereoelection and Chiral Ligand-Exchange Mechanism. *J. Am. Chem. Soc.* **2004**, *126* (4), 1026–1027.

(156) Zhong, Z.; Dijkstra, P. J.; Feijen, J. [(Salen)Al]-Mediated, Controlled and Stereoselective Ring-Opening Polymerization of Lactide in Solution and without Solvent: Synthesis of Highly Isotactic Polytactide Stereocopolymers from Racemic D,L-Lactide. *Angew. Chemie - Int. Ed.* **2002**, *41* (23), 4510–4513.

(157) Zhong, Z.; Dijkstra, P. J.; Feijen, J. Controlled and Stereoselective Polymerization of Lactide: Kinetics, Selectivity, and Microstructures. *J. Am. Chem. Soc.* **2003**, *125* (37), 11291–11298.

(158) Tang, Z.; Chen, X.; Pang, X.; Yang, Y.; Zhang, X.; Jing, X. Stereoselective

Polymerization of *Rac*-Lactide Using a Monoethylaluminum Schiff Base Complex. *Biomacromolecules* **2004**, *5* (3), 965–970.

(159) Alaaeddine, A.; Thomas, C. M.; Roisnel, T.; Carpentier, J. F. Aluminum and Yttrium Complexes of an Unsymmetrical Mixed Fluorous A lkoxy/Phenoxy-Diimino Ligand: Synthesis, Structure, and Ring-Opening Polymerization Catalysis. *Organometallics* **2009**, *28* (5), 1469–1475.

(160) Wei, Y.; Song, L.; Jiang, L.; Huang, Z.; Wang, S.; Yuan, Q.; Mu, X.; Zhu, X.; Zhou, S. Aluminum Complexes with Schiff Base Bridged Bis(Indolyl) Ligands: Synthesis, Structure, and Catalytic Activity for Polymerization of *Rac*-Lactide. *Dalton Trans.* **2019**, *48,* 15290–15299.

(161) Chisholm, M. H.; Gallucci, J. C.; Phomphrai, K. Comparative Study of the Coordination Chemistry and Lactide Polymerization of Alkoxide and Amide Complexes of Zinc and Magnesium with a *β*-Diiminato Ligand Bearing Ether Substituents. *Inorg. Chem.* **2005**, *44* (22), 8004–8010.

(162) Tian, J.; Hustad, P. D.; Coates, G. W. A New Catalyst for Highly Syndiospecific Living Olefin Polymerization: Homopolymers and Block Copolymers from Ethylene and Propylene. *J. Am. Chem. Soc*. **2001**, *123* (21), 5134–5135.

(163) Milano, G.; Cavallo, L.; Guerra, G. Site Chirality as a Messenger in Chain-End Stereocontrolled Propene Polymerization. *J. Am. Chem. Soc.* **2002**, *124* (45), 13368–13369.

(164) Dagorne, S.; Le Bideau, F.; Welter, R.; Bellemin-Laponnaz, S.; Maisse-François, A. Well-Defined Cationic Alkyl- And Alkoxide-Aluminum Complexes and Their Reactivity with ε-Caprolactone and Lactides. *Chem. - A Eur. J.* **2007**, *13* (11), 3202–3217.

(165) Lewiński, J.; Horeglad, P.; Wójcik, K.; Justyniak, I. Chelation Effect in Polymerization of Cyclic Esters by Metal Alkoxides: Structure Characterization of the Intermediate Formed by Primary Insertion of Lactide into the Al-OR Bond of an Organometallic Initiator. *Organometallics* **2005**, *24* (19), 4588–4593.

(166) Trofimoff, L.; Aida, T.; Inoue, S. Formation of Poly(Lactide) with Controlled Molecular Weight. Polymerization of Lactide by Aluminum Porphyrin. *Chem. Lett.* **1987**, *16* (5), 991–994.

(167) Jones, G. O. Contributions of Quantum Chemistry to the Development of Ring Opening Polymerizations and Chemical Recycling. *Tetrahedron* **2019**, *75* (14), 2047–2055.

(168) Bertini, Ivano; Luchinat, Claudio; Parigi, G. Chapter 8 - Two-Dimensional Spectra and Beyond. *Current Methods in Inorganic Chemistry*; 2001; Vol. *2*.

(169) Lu, J.; Ma, D.; Hu, J.; Tang, W.; Zhu, D. Nuclear Magnetic Resonance Spectroscopic Studies of Pyridine Methyl Derivatives Binding to Cytochrome C. *J. Chem. Soc. - Dalt. Trans.* **1998**, *13*, 2267–2273.

(170) Fang, J.; Yu, I.; Mehrkhodavandi, P.; Maron, L. Theoretical Investigation of Lactide Ring-Opening Polymerization Induced by a Dinuclear Indium Catalyst. *Organometallics* **2013**, *32* (23), 6950–6956.

(171) Xu, T. Q.; Yang, G. W.; Liu, C.; Lu, X. B. Highly Robust Yttrium Bis(Phenolate) Ether Catalysts for Excellent Isoselective Ring-Opening Polymerization of Racemic Lactide. *Macromolecules* **2017**, *50* (2), 515–522.

(172) Fang, J.; Tschan, M. J. L.; Roisnel, T.; Trivelli, X.; Gauvin, R. M.; Thomas, C. M.; Maron, L. Yttrium Catalysts for Syndioselective *β*-Butyrolactone Polymerization: On the Origin of Ligand-Induced Stereoselectivity. *Polym. Chem.* **2013**, *4* (2), 360–

367.

(173) Ligny, R.; Hänninen, M. M.; Guillaume, S. M.; Carpentier, J. F. Steric vs. Electronic Stereocontrol in Syndio- or Iso-Selective ROP of Functional Chiral β-Lactones Mediated by Achiral Yttrium-Bisphenolate Complexes. *Chem. Commun.* **2018**, *54* (58), 8024–8031.

(174) Sheldrick, G. M. SHELXT - Integrated Space-Group and Crystal-Structure Determination. *Acta Crystallogr. Sect. A Found. Crystallogr.* **2015**, *71* (1), 3–8.

(175) Sheldrick, G. M. A Short History of SHELX. *Acta Crystallogr. A.* **2008**, *64*, 112–122.

(176) Dolomanov, O. V.; Bourhis, L. J.; Gildea, R. J.; Howard, J. A. K.; Puschmann, H. OLEX2: A Complete Structure Solution, Refinement and Analysis Program. *J. Appl. Crystallogr.* **2009**, *42* (2), 339–341.

(177) Hübschle, C. B.; Sheldrick, G. M.; Dittrich, B. ShelXle: A Qt Graphical User Interface for SHELXL. *J. Appl. Crystallogr.* **2011**, *44* (6), 1281–1284.

(178) Hasegawa, T.; Kishida, H.; Nomura, N. A Practical Ortho-Rearrangement of Silyl Group of Ortho-Bromophenyl Silyl Ethers Using Magnesium(0). *Tetrahedron Lett.* **2017**, *58* (5), 455–457.

(179) Reich, H. J.; Goldenberg, W. S.; Gudmundsson, B. Ö.; Sanders, A. W.; Kulicke, K. J.; Simon, K.; Guzei, I. A. Amine-Chelated Aryllithium Reagents - Structure and Dynamics. *J. Am. Chem. Soc.* **2001**, *123* (33), 8067–8079.

(180) Harder, E.; Damm, W.; Maple, J.; Wu, C.; Reboul, M.; Xiang, J. Y.; Wang, L.; Lupyan, D.; Dahlgren, M. K.; Knight, J. L.; Kaus, J. W.; Cerutti, D. S.; Krilov, G.; Jorgensen, W. L.; Abel, R.; Friesner, R. A. OPLS3: A Force Field Providing Broad Coverage of Drug-like Small Molecules and Proteins. *J. Chem. Theory Comput.*

2016, *12* (1), 281–296.

(181) Becke, A. D. Density-Functional Exchange-Energy Approximation with Correct Asymptotic Behavior. *Phys. Rev. A* **1988**, *38* (6), 3098–3100.

(182) Ribeiro, R. F.; Marenich, A. V.; Cramer, C. J.; Truhlar, D. G. Use of Solution-Phase Vibrational Frequencies in Continuum Models for the Free Energy of Solvation. *J. Phys. Chem. B* **2011**, *115* (49), 14556–14562.

(183) Frisch, M. J., Trucks, G. W., Schlegel, H. B., Scuseria, G. E., Robb, M. A., Cheeseman, J. R., Scalmani, G., Barone, V., Petersson, G. A. Gaussian 16, Rev. C.01. *Gaussian, Inc.,* Wallingford, CT. 2016.

(184) Matsubara, K.; Terata, C.; Sekine, H.; Yamatani, K.; Harada, T.; Eda, K.; Dan, M.; Koga, Y.; Yasuniwa, M. Stereoselective Ring-Opening Polymerization of D,L-Lactide, Initiated by Aluminum Isopropoxides Bearing Tridentate Nonchiral Schiff-Base Ligands. *J. Polym. Sci. Part A Polym. Chem.* **2012**, *50* (5), 957–966.

(185) Gao, B.; Li, D.; Li, Y.; Duan, Q.; Duan, R.; Pang, X. Ring-Opening Polymerization of Lactide Using Chiral Salen Aluminum Complexes as Initiators: High Productivity and Stereoselectivity. *New J. Chem.* **2015**, *39* (6), 4670–4675.

(186) Sun, Z.; Duan, R.; Yang, J.; Zhang, H.; Li, S.; Pang, X.; Chen, W.; Chen, X. Bimetallic Schiff Base Complexes for Stereoselective Polymerisation of Racemic-Lactide and Copolymerisation of Racemic-Lactide with ε-Caprolactone. *RSC Adv.* **2016**, *6* (21), 17531–17538.

(187) Pang, X.; Duan, R.; Li, X.; Hu, C.; Wang, X.; Chen, X. Breaking the Paradox between Catalytic Activity and Stereoselectivity: *Rac*-Lactide Polymerization by Trinuclear Salen-Al Complexes. *Macromolecules* **2018**, *51* (3), 906–913.

(188) Chen, H. L.; Dutta, S.; Huang, P. Y.; Lin, C. C. Preparation and Characterization of

Aluminum Alkoxides Coordinated on Salen-Type Ligands: Highly Stereoselective Ring-Opening Polymerization of *Rac*-Lactide. *Organometallics* **2012**, *31* (5), 2016–2025.

(189) Tsuji, H. Poly(Lactide) Stereocomplexes: Formation, Structure, Properties, Degradation, and Applications. *Macromol. Biosci*. **2005**, *5* (7), 569–597.

(190) Orhan, B.; Tschan, M. J. L.; Wirotius, A. L.; Dove, A. P.; Coulembier, O.; Taton, D. Isoselective Ring-Opening Polymerization of *Rac*-Lactide from Chiral Takemoto's Organocatalysts: Elucidation of Stereocontrol. *ACS Macro Lett.* **2018**, *7* (12), 1413–1419.

(191) Wölfle, H.; Kopacka, H.; Wurst, K.; Preishuber-Pflügl, P.; Bildstein, B. On the Way to Biodegradable Poly(Hydroxy Butyrate) from Propylene Oxide and Carbon Monoxide via *β*-Butyrolactone: Multisite Catalysis with Newly Designed Chiral Indole-Imino Chromium(III) Complexes. *J. Organomet. Chem.* **2009**.

(192) Du, H.; Pang, X.; Yu, H.; Zhuang, X.; Chen, X.; Cui, D.; Wang, X.; Jing, X. Polymerization of *Rac*-Lactide Using Schiff Base Aluminum Catalysts: Structure, Activity, and Stereoselectivity. *Macromolecules* **2007**, *40* (6), 1904–1913.

(193) Gregson, C. K. A.; Blackmore, I. J.; Gibson, V. C.; Long, N. J.; Marshall, E. L.; White, A. J. P. Titanium–Salen Complexes as Initiators for the Ring Opening Polymerisation of Rac-Lactide. *J. Chem. Soc. Dalt. Trans.* **2006**, *25*, 3134–3140.

(194) Lee, J.; Kim, Y.; Do, Y. Novel Chlorotitanium Complexes Containing Chiral Tridentate Schiff Base Ligands for Ring-Opening Polymerization of Lactide. *Inorg. Chem.* **2007**, *46* (19), 7701–7703.

(195) Marchetti, F.; Pampaloni, G.; Pinzino, C.; Renili, F.; Repo, T.; Vuorinen, S. Ring Opening Polymerization of *Rac*-Lactide by Group 4 Tetracarbamato Complexes:

Activation, Propagation and Role of the Metal. *Dalt. Trans.* **2013**, *42* (8), 2792–2802.